UNIVERSITI TEKNOLOGI MARA

INTENSE RAINFALL ESTIMATION USING RADAR REFLECTIVITY FEATURE EXTRACTION FOR FLOOD FORECASTING

NOOR SHAZWANI OSMAN

PhD

April 2026

UNIVERSITI TEKNOLOGI MARA

INTENSE RAINFALL ESTIMATION USING RADAR REFLECTIVITY FEATURE EXTRACTION FOR FLOOD FORECASTING

NOOR SHAZWANI OSMAN

Thesis submitted in fullfillment
of the requirements for the degree of
Doctor of Philosophy
(Civil Engineering)

Faculty of Civil Engineering

April 2026

CONFIRMATION BY PANEL OF EXAMINERS

I certify that a Panel of Examiners has met on 14 November 2025 to conduct the final examination of Noor Shazwani binti Osman on her Doctor of Philosophy thesis entitled "Intense Rainfall Estimation using Radar Reflectivity Feature Extraction for Flood Forecasting" in accordance with Universiti Teknologi MARA Act 1976 (Akta 173). The Panel of Examiners recommends that the student be awarded the relevant degree. The Panel of Examiners was as follows:

Mazidah Mukri, PhD
Associate Professor
Faculty of Civil Engineering
Universiti Teknologi MARA
(Chairperson)

Fauzi Baharudin, PhD
Senior Lecturer
Faculty of Civil Engineering
Universiti Teknologi MARA
(Internal Examiner)

Badronnisa Yusuf, PhD
Associate Professor
Faculty of Engineering
Universiti Putra Malaysia
(External Examiner)

PROF. DR. HJH. ZURAEDA IBRAHIM
Dean
Institute of Postgraduates Studies
Universiti Teknologi MARA
Date: 16 April 2026

AUTHOR'S DECLARATION

I declare that the work in this thesis was carried out in accordance with the regulations of Universiti Teknologi MARA. It is original and is the results of my own work, unless otherwise indicated or acknowledged as referenced work. This thesis has not been submitted to any other academic institution or non-academic institution for any degree or qualification.

I, hereby, acknowledge that I have been supplied with the Academic Rules and Regulations for Post Graduate, Universiti Teknologi MARA, regulating the conduct of my study and research.

Name of Student	:	Noor Shazwani binti Osman
Student I.D. No	:	2021419378
Programme	:	Doctor of Philosophy (Civil Engineering) – EC950
Faculty	:	Civil Engineering
Thesis Title	:	Intense Rainfall Estimation using Radar Reflectivity Feature Extraction for Flood Forecasting

Signature of Student	:	
Date	:	April 2026

ABSTRACT

This thesis investigates the use of weather radar data for hydrological applications, specifically in rainfall estimation for flood forecasting, focusing on two major river basins in Selangor, Malaysia. Weather radar provides high-resolution rainfall estimates over large areas, addressing problems such as uneven rainfall distribution and limited rain gauge coverage. However, radar-based Quantitative Precipitation Estimation (QPE) is susceptible to errors caused by ground clutter, beam blockage, and signal attenuation. The research explores innovative techniques in radar QPE accuracy enhancement, including using artificial intelligence tools to classify rain types and improve the estimated rainfall values. Methodologies include the extraction of geometric characteristics from radar reflectivity images, including rain cell location, area, intensity, and orientation, which are then used for rainfall classification and machine learning applications. The K-Nearest Neighbor (KNN) algorithm is applied to classify radar-based rainfall into convective and stratiform categories. Despite some misclassifications due to overlapping feature characteristics, the KNN model achieves strong predictive performance with an Area Under the Curve (AUC) greater than 90%. In addition, an Artificial Neural Network (ANN) model is designed using the Levenberg-Marquardt algorithm and rain gauge data to improve the accuracy of radar-based QPE. The performance of the ANN-enhanced QPE model is evaluated using Root Mean Square Error (RMSE) and correlation metrics, showing a significant reduction in RMSE from 11.40 mm/h to 4.76 mm/h, thus enhancing the precision of radar-based rainfall estimates. The improved radar QPE model is then applied as input to an integrated flood forecasting system, employing the HEC-HMS hydrological model, with a novelty of merging process of the gridded-based QPE as sub-basin rainfall. The integrated system is applied for flood simulation in the Klang and Langat River Basins, with calibration results demonstrating that rain gauge data and ANN-calibrated QPE produces the highest correlation followed by uncalibrated radar QPE. The integration of calibrated radar QPE with hydrological models presents a promising approach for improving flood forecasting and predicting extreme weather events such as flash floods. This research contributes to advancements in radar hydrology, hybrid machine learning techniques for feature extraction, enhanced rainfall estimation methods, and improved radar-based rainfall-runoff models for better flood forecasting and warning systems in river basins in Malaysia.

ACKNOWLEDGEMENT

Praise be to the Almighty Allah for His blessings and guidance that enabled me to complete this thesis.

This research would not have been possible without the generous support and encouragement of many individuals. My deepest appreciation and love go to my husband, Amir Hafizuddin Markom, and my children, Adam Iskandar, Nuha, and Fathhan, for their unwavering support through the ups and downs of this journey. I am also deeply grateful to my beloved mother, my late father, my in-laws, and my siblings. Without their prayers, encouragement, and moral support, I would not have been able to persevere.

My sincerest gratitude goes to my supervisor, Prof. Ir. Ts. Dr. Wardah Tahir. I was extremely fortunate to have a supervisor who gave me the freedom to explore independently while consistently guiding me when I faltered. Her constructive feedback, unwavering patience, and continuous support helped me navigate numerous challenges and complete this thesis.

I would also like to express my heartfelt thanks to my co-supervisors, Assoc. Prof. Gs. Ts. Ir. Dr. Jazuri Abdullah and Prof. Dr. Nursuriati Jamil, for their valuable time, expertise, and insightful suggestions that significantly enriched my work. I deeply appreciate their guidance and contributions throughout this process.

A special thank you goes to Intan Shafeenar, whose friendship, support, and calm presence helped me remain rational and focused during the most challenging times. Her encouragement and care throughout the years have been a true source of strength.

To everyone who played a role in this journey, thank you from the bottom of my heart.

TABLE OF CONTENTS

LIST OF TABLES

LIST OF FIGURES

LIST OF SYMBOLS

Symbols	
A	Area
c	Speed of light
G	Antenna gain
i	Individual station
Ia	Initial abstraction
Kw	Refraction index factor
log	Logarithm
n	Number of stations
N_j	Number of Training Samples
P	Accumulated rainfall depth at time
Pe	Accumulated precipitation excess at time
P_j	Probability of the Sample
Pr	Average power returned
Pt	Power transmitted
r	Range
Rg	Rain gauge data
Rr	Radar data
S	Maximum retention
Tc	Concentration time
t_d	Delay time
Tlag	Lag time
w	Weight
x	Input
Z	Reflectivity factor
η	Learning rate
θ	Beam width
λ	Wavelength
μ	Momentum
τ	Pulse length

LIST OF ABBREVIATIONS

Abbreviations

AI	Artificial Intelligence
AMC	Antecedent Moisture Condition
ANN	Artificial Neural Network
ASC	American Standard Code
AUC	Area Under the Curve
BPN	Back Propagation Neural Network
CAPPI	Constant Plan Position Indicator
CE	Correlation Coefficient
CN	Curve Number
CNN	Convolutional Neural Networks
COE	Coefficient Of Efficiency
CORR	Pearson Correlation Coefficient
CSV	Comma Separated Values
DCNN	Deep Convolutional Neural Network
DEM	Digital Elevation Model
DID	Department of Irrigation and Drainage
DSD	Raindrop Size Distribution
DSMW	Digital Soil Map of the World
DT	Decision Trees
ELM	Extreme Learning Machine
ERR	Mean Standard Deviation
FAR	False Alarm Ratio
FFWS	Flood Forecasting and Warning System
FN	False Negatives
FP	False Positives
GD	Gradient Descent
GIS	Geographic Information Systems
GPCP	Global Precipitation Climatology Project
GPM	Global Precipitation Measurement

HEC-HMS	Hydrologic Engineering Center Hydrologic Modeling System
HEC-RAS	Hydrologic Engineering Center River Analysis System
HSG	Hydrologic Soil Group
IDW	Inverse Distance Weighting
IR	Infrared
KNN	K-Nearest Neighbor
LM	Levenberg-Marquardt
LSTM	Long Short-Term Memory
LUAS	Lembaga Urus Air Selangor
LULC	Land Use Land Cover
MAE	Mean Absolute Error
MAT	Microsoft Access Table
MATLAB	MATrix LABoratory
MBR	Mean Bias Ratio
ME	Mean Error
MET	Malaysian Meteorological Department
MLP	Multilayer Perceptron
MMD	Malaysian Meteorological Department
MRE	Mean Relative Error
NA	Not Available
NASH	Nash Sutcliffe Coefficient
NB	Normalized Bias
NE	Normalized Absolute Error
NEM	Northeast Monsoon
NetCDF	Network Common Data Form
NMB	Normalized Mean Bias
NSE	Normalised Standard Error
NSE	Nash-Sutcliffe Efficiency
NWP	Numerical Weather Prediction
PDF	Probability Density Functions
PRF	Pulse Repetition Frequency
PWRMS	Peak-Weighted Root Mean Square Error
QGIS	Quantum Geographic Information System

QPE	Quantitative Precipitation Estimation
RADAR	Radio Detection and Ranging
RAE	Relative Absolute Error
RaINS	Radar Integrated Nowcasting System
RBF	Radial Basis Function
RBNN	Radial Basis Neural Network
ResNet	Residual Networks
RF	Random Forests
RMSE	Root Mean Square Error
ROC	Receiver Operating Characteristic
SCS	Soil Conservation Service
SD	Standard Deviation
SGB	Stochastic Gradient Boosting
SGD	Stochastic Gradient Descent
SMA	Soil Moisture Accounting
SVM	Support Vector Machine
SVR	Support Vector Regression
SWM	Southwest Monsoon
SWMM	Storm Water Management Model
TN	True Negatives
TP	True Positives
TRMM	Tropical Rainfall Measuring Mission
WSR	Weather Surveillance Radar
WV	Water vapor
YSU	Yonsei University Scheme

CHAPTER 1
INTRODUCTION

1.1 Research Background

Flooding is one of the most frequent natural disasters in many countries around the world. Flooding occurs when water inundates normally dry places. In most cases, floods develop over the course of hours or even days, providing residents with sufficient time to either evacuate or prepare. There are also floods that occur suddenly and without warning, and these are typically referred to as flash floods. Flooding may occur due to natural factors such as intense monsoon rain, strong convective storms, and prolonged rainfall. Furthermore, human factors, such as urbanization, inadequate drainage systems, and deforestation, can also exacerbate the occurrence of floods (Zakaria et al., 2017). Flooding is categorized into several specific types (Tahir, 2024). These categories include fluvial floods, which occur in rivers; pluvial floods, which occur in any location; and coastal floods, which occur on land along the coast.

Malaysia is one of the countries commonly impacted by flooding due to its geographic location (Bukar et al., 2022). Malaysia experiences seasonal rainfall, with approximately 2440 mm of rain per year. However, some regions of the country receive different amounts of annual rainfall. This is due to seasonal variation in Malaysia, which is mainly influenced by the northeast monsoon and southwest monsoon (Tan, 2018). During the northeast monsoon, the eastern region in Peninsular Malaysia is affected by the massive floods due to the heavy and prolonged rainfall. The excessive amount of rainfall causes flooding, especially in riverine areas with low elevation.

The worst flood incidence in Malaysia for the past 30 years occurred in December 2014. The northeast monsoon distributed heavy rainfall across a significant area of Peninsular Malaysia, particularly in the states of Kelantan and Terengganu. The continuous rain continued until January 2015, resulting in over 1,750 mm of rain in some places. This rainfall was six times more than the normally recorded in December (Tahir, 2024). Many people lost their homes and belongings, and at least 21 people died in Kelantan, with additional casualties reported in other states. The floods were catastrophic, causing severe economic damage and affecting agriculture, businesses, and infrastructure.

Another worst flood scenario in Selangor had occurred in December 2021, where Tropical Depression 29W took an unexpected turn and dumped unprecedented volumes of rainfall onto the west coast of Peninsular Malaysia. This phenomena forms when a low-pressure area is accompanied by thunderstorms that produce a circular wind flow with maximum sustained winds below 39mph. Figure 1.1 displays a case study of one badly affected area, that is Taman Sri Muda during the flood event whereby there was a sudden and rapid water level rise due to the unusually high volumes of water flowing downstream. Many of the victims had complaint of not being warned early enough on the coming flood disaster. The flood disaster had claimed roughly 50 fatalities and displaced over 40,000 people, with total damages of approximately RM6.1 billion.

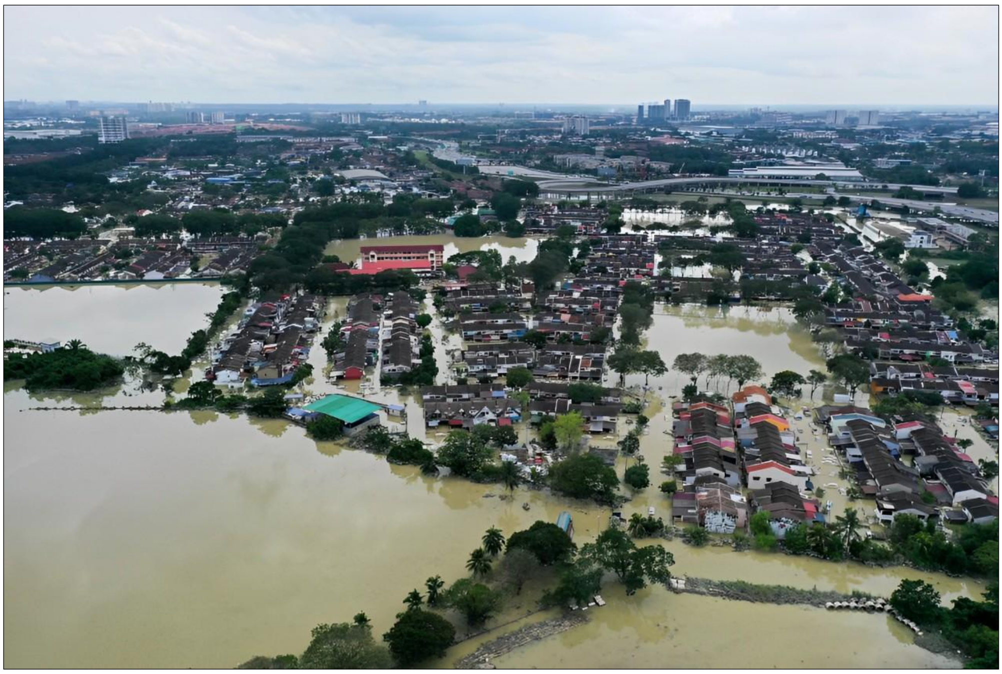

Figure 1.1 Flooding in Taman Sri Muda (Malaymail,2021)

Flooding significantly impacts large populations and disrupts their daily routines. Despite several mitigation measures put in place by Malaysia’s government, the country has witnessed this natural disaster for a long time. It has experienced numerous flood events recorded as far back as the late 1926 (Majid et al., 2021). According to reports from Department of Irrigation and Drainage (DID), Malaysia’s flood-prone areas cover about 30,000 km^2, or about 9% of the country's total land mass (Zakaria et al., 2017). Therefore, flood preparedness is critical to reducing damages and protecting lives from hazards. Accurate, dependable, and real-time rainfall measurement is essential in flood forecasting, management and mitigation.

1.1.1 The National Flood Forecasting and Warning System

Flood forecasting in Malaysia has advanced in recent years. The country has developed early warning systems, namely the National Flood Forecasting and Warning System (NaFFWS), which provides real-time data to the public through websites and mobile apps. The system integrates real-time and forecast data input, including rainfall observations, radar rainfall, river levels, and numerical weather prediction (NWP) model forecast into a central hydrological-hydraulic models to simulate river flows and flood levels. The system generates outputs in the form of flood forecasts and early warnings, delivered through dashboards, maps, and alert mechanisms to support timely decision-making and emergency response. NaFFWS performs well for larger river basins during the monsoon season, when rainfall is more widespread and predictable, allowing forecasts to extend up to several days ahead. The system also generates useful outputs such as predicted river levels, expected flood depth, and areas that may be affected. However, several challenges remain. Forecast accuracy can be reduced in areas with limited monitoring stations, and rainfall estimates from radar and NWP models still contribute to significant errors, especially during sudden and intense convective storms. Flash floods are particularly difficult to predict because they happen quickly in small catchments. The system also requires continuous calibration and high-quality data to ensure that the hydrological models remain accurate (Wijayarathne et al., 2021).

Overall, NaFFWS has strengthened Malaysia's flood forecasting system, but further improvements in data coverage, rainfall accuracy, and model refinement are still needed to increase reliability across the country. Advanced integrated models using artificial intelligence (AI) and machine learning could enhance predictions, as current models often struggle with rapid weather changes common in tropical areas. Enhancing public awareness and preparedness is also vital for reducing flood impacts. By addressing these issues, Malaysia can strengthen its flood resilience and better protect vulnerable communities (Sidek et al., 2021; Saad et al., 2024).

1.1.2 Radar Rainfall

The most critical data input for ensuring the reliability of NaFFWS is rainfall, obtained from rain gauges, weather radar, and numerical weather prediction (NWP) models (for longer forecasts). Compared to rain gauges and NWP forecast, radar technology offers continuous observations over wider areas with high temporal resolution. Despite various limitations, weather radar remains a powerful tool for rainfall estimation. Its optimal range coverage is typically within 40–180 km from the radar, where measurements are most reliable. By complementing traditional rain-gauge networks, radar provides a more comprehensive and timely understanding of rainfall patterns, thereby significantly improving the accuracy and lead time of flood forecasting. (Sokol et al., 2021; Met Office, 2023).

Radar emits pulses of electromagnetic waves that are reflected by precipitation, returning a signal to the radar surface. These reflectivity measurements, however, do not directly indicate rainfall amounts. To convert radar reflectivity (Z) into rainfall intensity (R), the Z-R relationship is applied. This relationship is typically expressed as a power law, $Z = aR^b$, where a and b are coefficients that depend on rainfall type, geographic location, and meteorological conditions. Z is proportional to $D^6$and R is proportional to D^3, where D represents the diameter of raindrops within a sampled volume (Ma et al., 2022). One widely used formulation, $Z = 200R^{1.6}$, was derived by Marshall and Palmer (Mahyun et al., 2021). However, no single Z-R relationship can accurately represent all rainfall events due to the variations in raindrop size distribution (DSD) across space, time, and storm type (Tahir et al., 2019). Therefore, selecting and validating an appropriate Z-R parameterization against rain gauge measurements is essential to improve the accuracy of radar-based rainfall estimates.

Radar rainfall data is particularly valuable for capturing convective rainfall, which exhibits significant spatial and temporal variability compared to rain gauge measurements (Sokol et al., 2021). Combining radar observations with rain gauge data and advanced models allows flood forecasting systems such as NaFFWS to generate more reliable predictions, enhancing public preparedness and reducing flood impacts.

1.2 Problem Statement

Weather radar has tremendous potential in hydrological applications, including flood forecasting, due to its ability to provide high spatial and temporal resolution rainfall information over a large area. Additionally, it offers a unique chance to enhance the observation of extreme rainfall events that trigger floods, debris flow, and landslides in complex terrain, a phenomenon that the typical rain gauge network sometimes struggles to detect. However, the indirect estimation of rainfall using radar is associated with various sources of error such as ground clutter, partial beam occultation, beam blockage, and attenuation effects (Hong and Gourley, 2017; Tahir et al., 2022). In addition, studies show that radar still underestimates extreme rainfall distribution due to factors such as integrated pathway attenuation and wet-radome conditions during heavy rainfall (Falconi and Marzano, 2019).

In the NaFFWS, weather radar–derived rainfall estimates (QPE) have provided essential high-resolution spatial inputs to hydrological and hydrodynamic models, complementing conventional rain-gauge observations. While existing bias-correction and gauge-radar calibration methods have improved radar rainfall performance, notable uncertainties remain due to range effects, terrain influences, and the nonlinear nature of convective rainfall processes. These limitations suggest that traditional correction approaches may be insufficient to fully represent the complex spatiotemporal relationships between radar observations and surface rainfall. Consequently, further studies employing data-driven techniques are warranted to better capture these nonlinearities, enhance radar rainfall accuracy, and ultimately strengthen the reliability of flood forecasting and early-warning outputs within NaFFWS.

A study by Kirsch et al. (2019) found that the use of separate stratiform and convective Z-R relationships can reduce the rainfall estimation error between 30% and 50%. Therefore, characterizing convective and stratiform rainfall from extracted features of radar reflectivity image, as well as optimally formulating Z-R relationships based on this classification, presents challenging and innovative tasks in this study. Furthermore, the development of AI-based radar QPE using the Artificial Neural Network (ANN) technique derived from the extracted radar image features will add novelty to this study. Traditional Z-R relationships and empirical methods often fail to capture the non-linear dynamics of rainfall, especially under conditions influenced by attenuation, varying drop size distributions, and spatial heterogeneity. ANN is introduced to overcome these limitations by learning complex, non-linear mappings from radar reflectivity to rainfall rate, thereby providing improved accuracy across different rainfall regimes. The efficiency of this model will then be evaluated by coupling enhanced ANN-based radar QPE with the rainfall-runoff modelling to improve the flood forecasting and warning system (FFWS) of the country.

1.3 Research Questions

These are some of the questions that support the relevance of conducting this research:

(1) How to classify between two distinct types of rainfall using extracted features of radar reflectivity images
(2) Does the newly derived Z-R relationship based on classified images improve the rainfall estimates?
(3) Can using Artificial Neural Networks (ANN) techniques improve the accuracy of radar rainfall estimation?
(4) What is the accuracy of flood forecasting by using the integrated model?

1.4 Research Objectives

The goal of this study is to develop an artificial intelligence-based quantitative precipitation estimation model derived from the extracted features of real-time radar reflectivity imagery in tropical intense rainfall regions specifically Klang and Langat River basins. The enhanced radar rainfall estimation model provides potential input to a coupled hydro-meteorological flood forecasting system. Therefore, the following specific objectives have been identified to achieve the aim of this study:

a) To classify between stratiform and convective rainfall types based on extracted features of radar reflectivity images using machine learning.
b) To formulate a new optimum Z-R relationship based on classified images for enhanced rainfall estimation.

c) To develop an enhanced radar QPE model using extracted radar reflectivity image features within an Artificial Neural Network (ANN) framework.
d) To implement a coupled framework integrating enhanced radar QPE with a hydrological rainfall–runoff model for flood forecasting applications.

1.5 Significance of Research

Significant contributions of the research are listed below:

a) Firstly, in terms of research impact, the findings will provide new knowledge or information on radar hydrology and feature extraction-machine learning techniques to academia and the public. Few studies have focused on feature extraction for rainfall estimations using radar reflectivity and machine learning algorithms, especially in the tropical monsoon zone.

b) Additionally, other regions can apply this new method of calculating rainfall estimates, lowering the cost of rain gauge installation and maintenance while also providing the government and industry with comprehensive coverage of rainfall measurement.

c) Advanced flood forecasting systems provide early warnings, allowing communities and authorities to prepare and take action, improving safety and reducing the impact of floods. These systems also raise public awareness about flood risks and the importance of preparedness.

d) Furthermore, an accurate flood forecasting enhances community preparedness by improving flood resilience strategies, including infrastructure reinforcement and public education. It also aids in adapting to climate change, informs strategic planning, and ensures efficient resource allocation for flood mitigation and recovery efforts.

e) Flood forecasting helps protect ecosystems by reducing flood damage to sensitive areas and provides economic benefits by minimizing losses to businesses, agriculture, and local economies through improved preparedness and control measures

1.6 Scope and Limitations

This study investigates two techniques that utilize extracted radar image features to enhance radar-derived quantitative precipitation estimates (QPE): Z-R relationship optimization and an artificial neural network (ANN)-based correction of radar rainfall estimates. The ANN-enhanced radar QPE is subsequently applied to flood forecasting. It should be noted that coupling the Z-R-optimized radar QPE with the rainfall-runoff model is not part of the study scope. Two case study areas are selected, namely the Langat River Basin and the Klang River Basin. Additionally, this study utilizes hourly data from rain gauges, flow gauges, and radar reflectivity measurements provided by Malaysia's Drainage and Irrigation Department (DID) and Meteorological Department (MMD) from November 2021 to August 2023, subject to data availability. The scope of study is grouped in four parts as shown in Figure 1.2.

Part I : Feature extraction of radar images and machine learning classifier.

a) Real-time radar reflectivity images were processed and analyzed by using Quantum Geographic Information System (QGIS).
b) MATLAB software was used to extract features from radar reflectivity images.
c) K-Nearest Neighbor (KNN) machine learning algorithm was chosen to classify two types of rainfall.

Part II: Z-R relationships modification.

a) The formulation of newly optimum Z-R relationship based on classified images were created.
b) The new improved Z-R relationship was compared to the existing Marshall Palmer relationship, and the performance was validated through statistical measurement.

Part III: Artificial Intelligence (AI)-based radar QPE model.

a) Artificial Neural Network (ANN) technique was used in the development of AI-based radar QPE model to enhance rainfall estimation.

b) MATLAB software uses data from extracted features of radar images to train the ANN model.

c) The performance of the ANN-based radar QPE was assessed through statistical verification.

Part IV: Flood forecasting using ANN-based radar QPE integrated with HEC-HMS model.

a) The Klang and Langat River basins catchment areas are modeled using a distributed rainfall-runoff system.

b) The ANN-based radar QPE model is coupled with the HEC-HMS rainfall runoff model as a hydro-meteorological flood forecasting system.

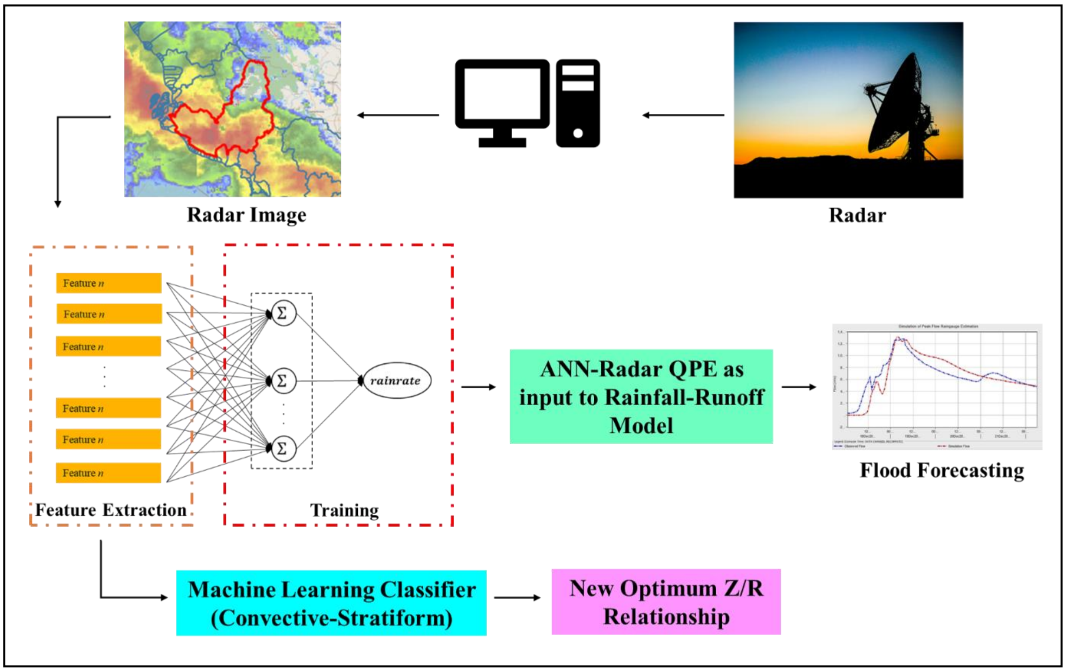

Figure 1.2 Improved Radar QPE Using Extracted Radar Reflectivity Image Features and Coupling ANN-Based Radar QPE with a Rainfall–Runoff Model

Since the performance of radar rainfall estimation depends on rain gauge measurements as observed data, it has been noted that some rain gauges installed at rainfall stations in the Klang and Langat River basins have failed to record any rainfall data. It is also found that there are missing data or gaps in the monthly datasets of hourly rainfall data. This issue can cause the rainfall station to be unreliable to be used for rainfall analysis. Among the possible reasons for this problem to occur are due to the lack of maintenance or inaccurate calibration of the equipment used to collect rainfall data. This problem can be a shortcoming for researchers where short data availability may affect the accuracy and reliability of rainfall analysis that will be done.

1.7 Thesis Structure

There are five chapters in the thesis. The first chapter comprises a broad introduction, problem statement, research questions, aims, and research importance. In addition, it describes the study's scope and limitations and implies the research's significance.

The second chapter provides basic information on weather radar, as well as a review of the literature on the application of radar rainfall and machine learning algorithms in previous research works. This chapter also explains the essential theories and concepts relevant to the subject.

Chapter 3 provides a full summary of the work completed to fulfil the study's objectives. This chapter also includes information about data collection, materials used, approach, and conceptual procedures.

Chapter 4 presents the results obtained from this study. This chapter elucidates the development of the radar reflectivity feature extraction algorithm, the classification of convective and stratiform rainfall, and the development of the new optimal Z-R relationship. This chapter also discusses and elaborates results on comparison, verification, and validation of ANN radar rainfall estimation models. The following section explains the application of the model in a coupled enhanced radar QPE with the rainfall-runoff model for flood forecasting.

Chapter 5 concludes the thesis and recommends further improvement to the study. The conclusions will accurately reflect the overall objectives of this research, interpreting the results from both the derivation work and the rainfall-runoff modelling sections.

CHAPTER 2
LITERATURE REVIEW

2.1 Introduction

This chapter reviews the literature relevant to this study. The chapter begins with a brief explanation of the basic meteorological process for rainfall classification.

Next, a more in-depth explanation of weather radar technology is included since estimating rainfall with weather radar is the main topic of the study. The definition, workings, classifications, and measurements of weather radar are provided together with the appropriate citations. The chapter covers studies done by the other researchers and gives important background information on the subjects.

The subsequent sections provide an overview of the feature extraction and classification of rainfall from real-time radar reflectivity images in tropical monsoonal region for enhanced radar rainfall estimates. The machine learning classifier used in this study is also discussed in this section, followed by the derivation of a new Z-R relationship for each rainfall category. In addition, the primary tool utilized in the model development for weather radar rainfall estimation, specifically the Artificial Neural Network (ANN), is also discussed. These sections include an analysis of the theoretical ideas and methodology of ANN, as well as a comprehensive assessment of the research conducted by others on the practical implementation of ANN in related domains.

Lastly, the chapter reviews the available rainfall-runoff modelling, which can potentially be coupled with the ANN-based rainfall estimation model to enhance the flood forecasting system. These chapter includes the previous work related to this research.

2.2 Rainfall Classification

Rainfall in general may be characterised by convective and stratiform regimes (Houze 2004). Vertical air movements are essential for the formation of clouds and significantly influence the type and quantity of rain that a cloud can ultimately produce.

According to Houze (1997), the dynamics and microphysics of convective and stratiform components of cloud systems are significantly different. Convective clouds are characterized by intense and localized storms that involve strong uplift movements, as depicted in Figure 2.1. Rainfall particles in convective clouds develop at the base and are propelled upward by strong vertical air movements until they either fall out of the updraft cores or get too large to be swept away (Rulfová and Kyselý, 2013). On the other hand, the stratiform cloud is characterized by modest vertical air movements, a creation phase that can last for a few hours, and the beginning of the growth process occurring at the top of the cloud. This type of rain, which falls over a large area and lasts for a long time, is associated with horizontal growth, meaning that it affects a larger area but generally has a lower intensity.

In addition, Houze (1997) states that convective components are driven by massive updrafts (5–10 ms-1 or more), whereas stratiform portions are controlled by lighter mesoscale ascents (<3 ms-1). According to Alpers and Melsheimer (2004), stratiform rain lasts longer than convective rain but is typically far less powerful and too uniform in space. In summary, convective rain type is usually considered heavy and high intensity, while stratiform rain is usually considered less intense (Shen et al., 2012; Sen Jaiswal et al., 2020).

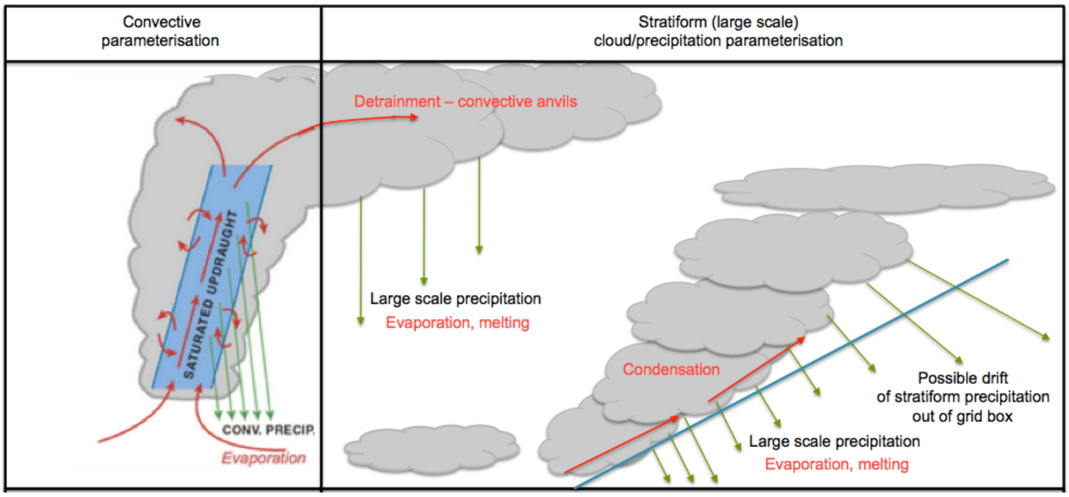

Figure 2.1 Convective versus Stratiform Rain (Zelman, 2019)

Simpson et al. (1988) introduced the concept of a separation between convective and stratiform precipitation, followed by Houze (1997), who provided a detailed analysis of this concept. Since then, several academics have proposed algorithms based on some parameters to separate rainfall into two components (Ulbrich and Lee, 2002; Bringi et al., 2003; Deo and Walsh, 2016).

According to the Malaysian scenario, the Department of Drainage and Irrigation (DID) classifies rainfall based on its intensity, as shown in Table 2.1. Convective rain exceeding 60 mm within a typical 2 to 4-hour period may lead to flash floods. In contrast, monsoon rains often last longer and involve heavy bursts that occur intermittently. The intensity of these rains can sometimes exceed several hundred millimeters in a single day (DID, 2022).

Table 2.1
Rainfall Intensity Categorization

Category	Rainfall intensity (mm/h)
Light	1-10
Moderate	11-30
Heavy	31-60
Very Heavy	>60

(Source: DID, 2022)

2.3 Rain gauge Network

Rain gauge networks have historically been the primary method for measuring rainfall in Malaysia. Rain gauges come in various forms, including graduated cylinders, weighing gauges, tipping buckets, and basic buried pit collectors. A rain gauge is considered a ground-truth measurement of rainfall because it detects rain falling directly to the ground. When measuring rainfall at a specific location over a short period, this method is considered one of the most accurate (Wood et al., 2000).

A rain gauge is essentially a set of cylindrical vessels placed in the open to collect rain. There is a correlation between the exposure conditions of the rain gauge and the amount of rainfall it collects. Standard guidelines have been established to ensure that rain gauges reliably represent the rainfall in the surrounding area. The device must have a horizontal catch surface, and the ground should be level when setting up the rain gauge (Vokoun and Moravec, 2022). The unit of measurement for rainfall is millimeters per hour.

Figure 2.2 illustrates a typical tipping bucket rain gauge in Malaysia. The gauge consists of an electric transmitter, a triangle bucket, and a collector. The gauge collects rainfall and then channels it to the tipping bucket. The collector will tip and empty itself if the water weight inside it increases by 0.2 mm. After each tip, the gauge records the water level and then releases it from its base. Each time the bucket tips, it forms an electrical contact and records an electronic signal (Lanza et al., 2022).

Figure 2.2 Tipping Bucket Rain Gauge (InfoBanjir JPS Selangor, 2008)

In recent years, the rain gauge has demonstrated good accuracy in monitoring rainfall, but several issues require improvement. Rain gauges are reliable for measuring rainfall at specific locations, but their spatial distribution is sparse in remote areas, particularly in mountainous terrain, leading to insufficient spatial resolution for accurate rainfall pattern mapping (Dhiram and Wang, 2016). Sene (2024) investigated how rainfall flows around the gauge during strong gusts, leading to inaccuracies. Besides that, poor maintenance can also cause mechanical errors in the rain gauge due to sand, insects, falling leaves, vegetation growing around the gauge, and other obstructions (Hwang et al., 2020).

In addition, operational hydrology produces rainfall data through the spatial interpolation process and displays it as a spatial rainfall map. Point rainfall data is transformed into spatial rainfall data, enabling the determination of water availability in a watershed and the dissemination of early flood warning information to the public via a flood forecasting model or system. Typically, catchment or areal rainfall is used to measure the spatial rainfall data (Salleh et al., 2019; Asmat et al., 2021). Rainfall data from multiple stations within a catchment area is used to compute the catchment rainfall. Therefore, the sufficiency and dependability of the rainfall data collected from each station in the station network have a major impact on the accuracy of the catchment rainfall. Additionally, the proper placement of the station to measure the amount of rainfall that reaches the ground determines the sufficiency and dependability of the rainfall data (Cheng et al., 2008; Urban and Strug, 2021; Jamaluddin et al., 2022).

2.4 Weather Radar System

2.4.1 Working principles of radar

The term 'RADAR' is an acronym for 'Radio Detection and Ranging'. During World War II, this technology was used for military purposes. Scientists observed noise in the echoes returned during radar operations due to weather conditions like rain, snow, and sleet. Since then, scientists have continued to investigate and study weather radar (Sokol et al., 2021). The basic principle of radar is to emit electromagnetic signals, transmit pulses, and measure the reflected pulses. Four main components of a radar system are the transmitter (which emits electromagnetic radiation), the antenna (which concentrates the radiation and captures some of the backscattered radiation), the receiver (which collects the backscattered radiation and converts it to a low-frequency signal), and the display system (Collier, 2000). Figure 2.3 shows a diagram of the radar system.

Figure 2.3 Radar System (Roshni, 2014)

2.4.2 Type of weather radar

2.4.2.1 Conventional Radar

Conventional radar is effective in measuring precipitation using reflectivity and echoes. Prior to the 1980s, precipitation was measured with conventional radars to analyze weather patterns. It can display the intensity of a storm, but only in relation to precipitation. Conventional radar is useful in predicting the intensity of precipitation, hook echoes, and bow echoes, which are indicators of tornadoes and thunderstorms. However, these conventional radars can misinterpret data by reflecting non-precipitation signals, and severe storms may occur without a detectable signal, making conventional radar ineffective. Raghavan (2013) stated that while conventional radar is useful for tracking rainfall through reflectivity and echoes, it is not as precise as Doppler radar for detecting storms.

2.4.2.2 Doppler Radar

Doppler radar is an upgrade over conventional weather radar due to its ability to detect the slight frequency shift in the returning pulse (Brown, 2013). After the National Severe Storms Laboratory began experimenting with the Doppler effect on its radar in 1964, it emerged as a vital tool for forecasting and storm preparation. Weather forecasters typically use it to determine the velocity, direction, and speed of objects such as precipitation drops. Additionally, a similar study by Brown et al. (2016), who identified the three fundamental variables of Doppler radar namely spectrum width, Doppler velocity, and radar reflectivity which further supports this conclusion.

Doppler weather radar is a remote sensing device that can distinguish not only the type of particles, such as rain, snow, and hail, but also their intensity and motion. This radar also enables the identification of severe weather conditions. For instance, a tornado could be the cause if precipitation particles alternate between moving toward and away from the radar at close range (Cox and Ackerman, 2022).

Weather radar emits microwave energy pulses that target objects, most commonly clouds. The radar measures the energy that bounces back from these objects, providing information about them, as illustrated in Figure 2.4. It can measure the size, quantity, speed, and direction of rainfall within a radius of about 100 miles from its location. Variability in the radar energy reflected from the object indicates the potential for a large volume of precipitation. Ultimately, the transmitted signal is transformed into the rate of rainfall.

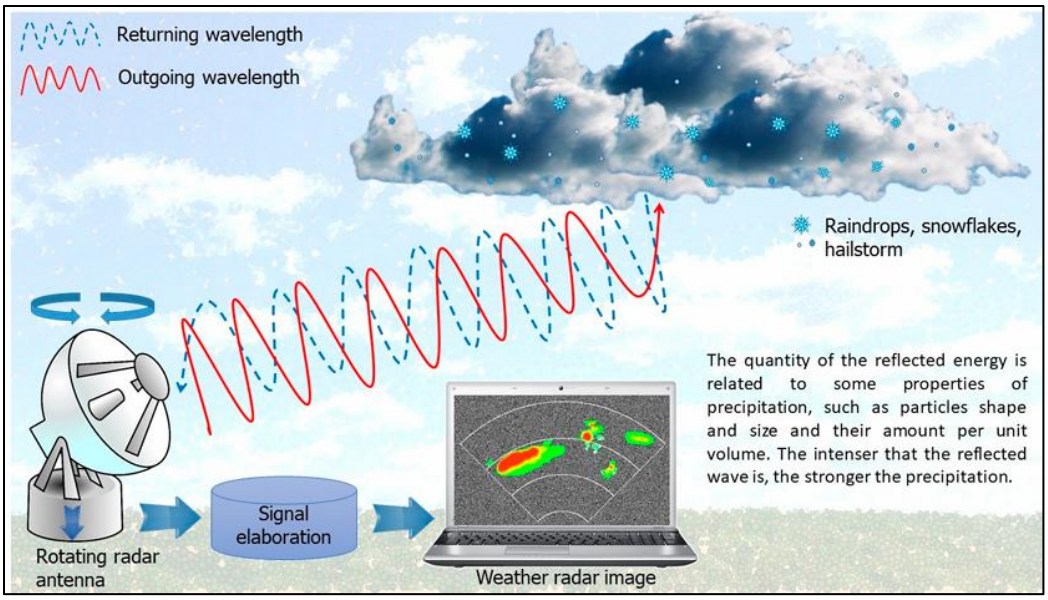

Figure 2.4 Weather Radar Principle of Function (Binetti et al., 2022)

Figure 2.5 illustrates the fundamental components of the Doppler radar system. The radar signal processor directs the transmitter, which produces microwave pulses, to the duplexer. The duplexer is a nonlinear microwave circuit that amplifies the signal and eliminates the microwave carrier frequency by sending the signal to the antenna and the backscattered signals to the receiver. The signal processor then digitizes and processes the output signal, controlling the transmitter's timing, pulse width, and pulse repetition frequency (PRF). The user's workstation and radar product generator receive the output data, as depicted in Figure 2.5, and create three-dimensional meteorological data sets. The operator must adjust the transmitter timing, the scan method, and, if necessary, the polarization settings based on the products of interest. The range, r, the distance between radar and target, is determined by the delay time, t_d, the signal needs to travel to and back from the target at c, the speed of light (Doviak and Zrnic, 2014):

$$r = t_d c / 2 \tag{2.1}$$

The pulse length, τ, and the duration of the transmitted radiation determine the range resolution, $\Delta r = \tau c/2$. An average pulse length is $1\mu s$, which is equivalent to 300 meters in space. Since a signal return must be received before the subsequent pulse is transmitted, the PRF determines the range $r_{\max}$ up to which measurements can be made with certainty (Skolnik, 2008).

$$r_{max} = t_{d,max}\, c/2 = c\ /\ 2(PRF) \tag{2.2}$$

The reflectivity, Z ,of a target is calculated from the received power P_R. This power relies on radar technical features, propagation conditions, target distance, and reflectivity Z. The equation governing the power returned from the reflected power transmitted by radar and the reflectivity factor, Z , is given as (Doviak et al., 1994):

$$P_r = \frac{\pi^3 c}{2^{10} \ln 2} \frac{P_t G^2 \tau \theta^2}{\lambda^2} \frac{|K_w|^2 Z}{r^2} \tag{2.3}$$

where;

Pr = Average power returned

Pt = Power transmitted

G = Antenna gain

Kw = Refraction index factor

θ = Beam width

τ = Pulse length

λ = Wavelength

r = Range

Z = Reflectivity factor

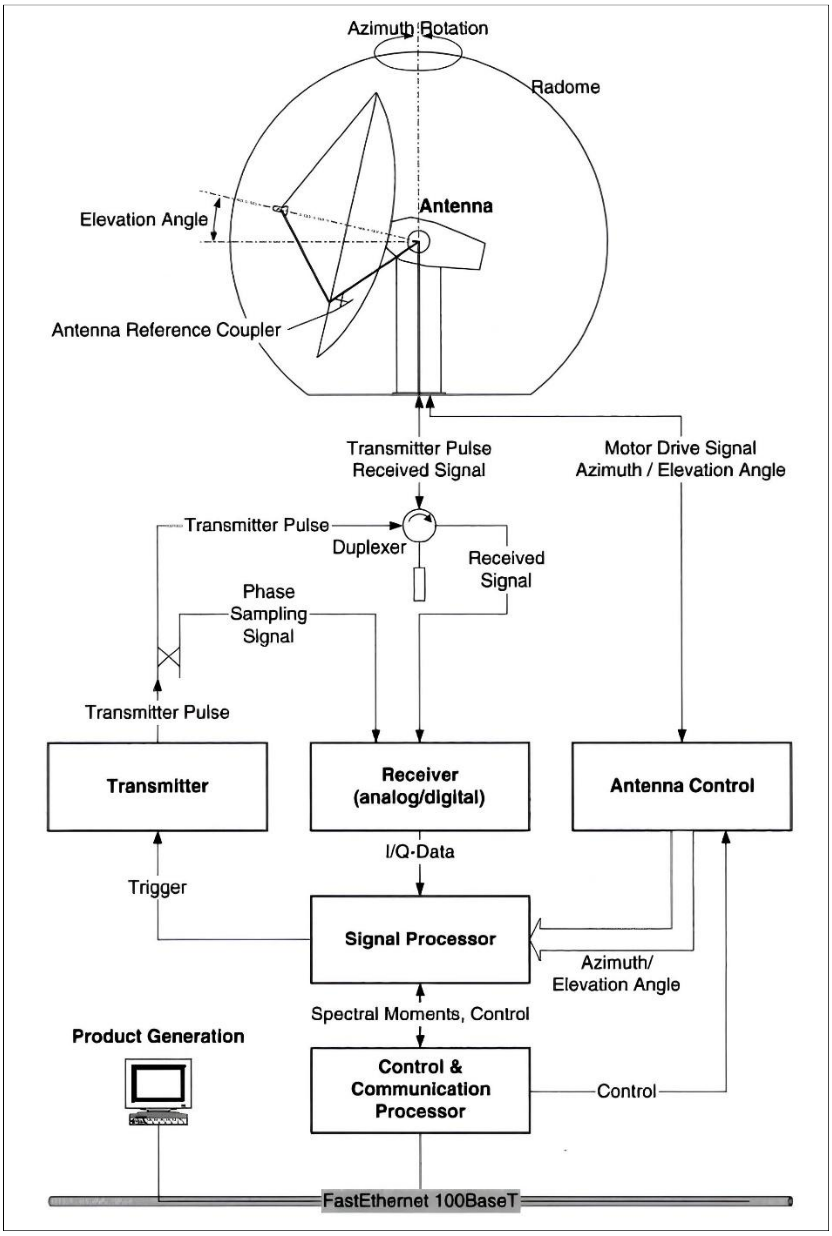

Figure 2.5 Basic Component of A Doppler Radar System (Meischner,2005)

2.4.2.3 Doppler Radar in Malaysia

Every station in Malaysia is equipped with a Doppler radar due to its ability to detect rainfall intensity, which is measured in decibels (dBZ). Doppler radar can be classified into two types: single-polarimetric and dual-polarimetric radar. Single-polarimetric or 'single-pol' radar transmits and receives a single polarization, usually in the same direction, resulting in a horizontal-horizontal (HH) or vertical-vertical (VV) configuration. Dual-polarimetric or 'dual-pol' radar transmits and receives pulses in both horizontal and vertical orientations. This allows forecasters to obtain a better understanding of the size, shape, and range of targets by measuring them in both horizontal and vertical directions.

Figure 2.6 shows that Malaysia operates 18 Doppler weather radars, including S-band, C-band, and X-band radars. Furthermore, Table 2.1 describes the characteristics of these radars in Malaysia. The S-band radar operates at a frequency of 2–4 GHz and a wavelength of 8–15 cm, providing coverage over a radius of up to 300 km and being useful for weather observation in all conditions. Meanwhile, C-band radar serves the same function as S-band radar but is limited to short-range weather observation and requires less power. This radar operates between 4 and 8 GHz, with a wavelength of 4 to 8 cm. On the other hand, X-band radar is more effective at detecting smaller particles, such as tiny water vapor and light precipitation. It has a limited range of up to 100 km and operates at a wavelength of 2.5–4 cm and a frequency of 8–12 GHz.

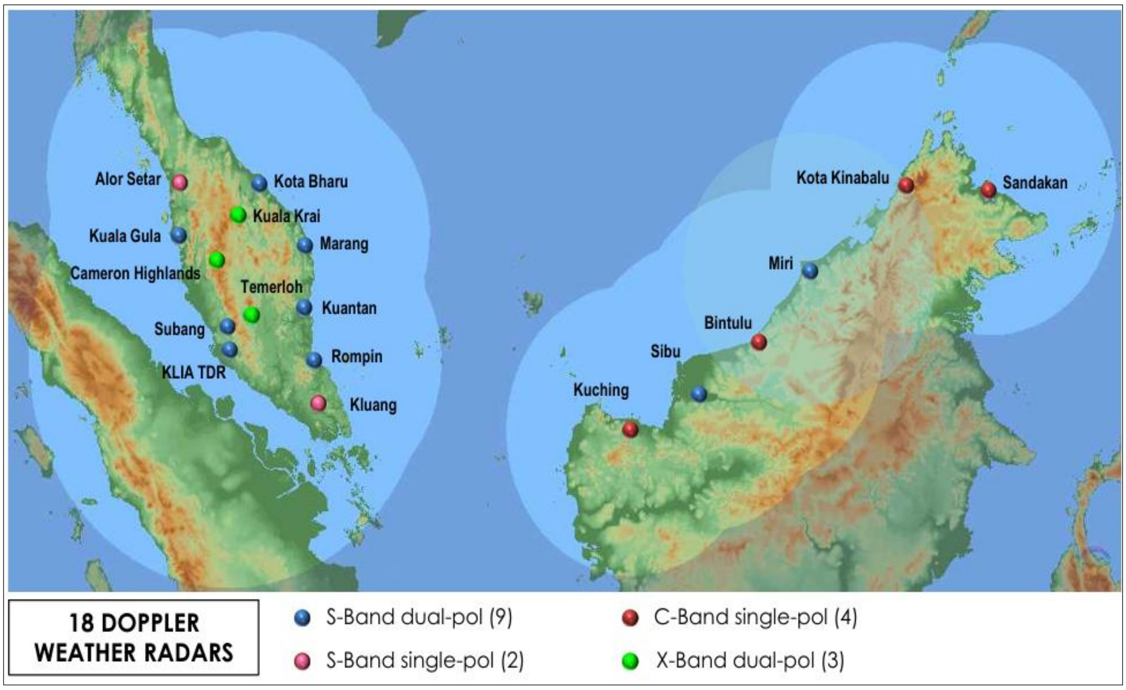

Figure 2.6 The Distribution of Radar Network in Malaysia (MET Malaysia, 2024)

Table 2.2
Radar Characteristics in Malaysia

Type of Radar	S-band (dual polarization)	S-band	C-band	X-band (dual polarization)
Frequency (MHz)	2705-2900	2801-2850	5602-5625	9375-9430
Peak Power (kW)	640-850	525-660	250	150
Pulse Length (μs)	0.5-2.0	0.8-2.0	0.8-1.8	0.5-2.0
Pulse Repetition Frequency (Hz)	250-1000	250-600	250-740	960-1000
Antenna Diameter (m)	8.4	8.4	4.2	2.4
Beam Width (º)	1	2	1.7	1
Detection Range (km)	300	300	300	100

(Source: MET Malaysia,2024)

2.5 Quantitative Precipitation Estimation (QPE)

QPE is a technique for estimating the amount of rainfall that has fallen at a specific point or over a large area. QPEs are essential in the development of meteorological, hydrological, and geological hazard alerts. Hydrological models that coupled with radar-derived quantitative precipitation estimations (QPEs) have become a competitive alternative to rain gauges in the modern era due to recent developments in radar equipment, data processing, and numerical modelling (Osman & Tahir, 2024).

2.5.1 Radar Integrated Nowcasting System (RaINS)

Developed by the Hong Kong Observatory and operationalized by MET Malaysia since August 2017, RaINS has become the primary tool for issuing thunderstorm warnings by MET Malaysia. RaINS is a nowcasting system that uses inputs from Numerical Weather Prediction (NWP) models, including maximum vertical dBZ, and observed radar data from 18 Malaysian Meteorological Department (MMD) radar stations. NWP forecasts future atmospheric conditions by solving partial differential equations, with ensembles generated from NWP models. The NWP model often struggles to accurately capture the initial precipitation distribution, while radar-based nowcasting is more effective for predicting rainfall over shorter time scales.

However, over longer time scales, NWP surpasses radar nowcasting due to better resolution of larger dynamical flows. To combine their strengths, the RaINS framework integrates the SWIRLS methodology with NWP. These models enhance flood forecast accuracy and reliability by linking meteorological and hydrological data (Trinh et al., 2023; Ozkaya, A., 2023).

2.5.2 RaINS Data Processing

Radar data, in the form of Constant Plan Position Indicator (CAPPI) at 2 km in dBZ, is combined using inverse distance weighting (IDW). The NWP blending utilizes maximum vertical reflectivity from MMD-WRF-ARW forecasts, which are produced hourly for up to 137 hours. These forecasts use GFS 0.25° data as a boundary condition with three-way nesting (9 km, 3 km, and 1 km). Besides, the Yonsei University Scheme (YSU) is used for the planetary boundary.

Furthermore, the blending process uses quantile mapping and phase correction to align the NWP image with the radar image before combining them to produce RaINS. The 1 km resolution NWP grid is merged with the 833 m radar grid through bilinear interpolation, resulting in a new grid with 833 m resolution. In addition, to optimize nowcast results, time-varying and hyperbolic tangent functions are applied, with their formulas provided in equations 2.4 and 2.5 (Seed et al., 2013; Hung et al., 2023):

$$(\mathrm{t}) = \mathrm{g} \times \mathrm{a} \times \frac{(\beta - \alpha)}{2}[1 + \tanh(\mathrm{y}(\mathrm{t} - 9))] \tag{2.4}$$

$$\mathrm{QPF}_{\mathrm{RaINS}} = (1 - \mathrm{w(t)})1 \times \mathrm{RADAR}^{\mathrm{EXTRAPOLATION}} + \mathrm{w(t)} \times \mathrm{NWP} \tag{2.5}$$

RaINS data is stored in netCDF format and converted into HDF5 format, containing four variables: Latitudes, Longitudes, Time, and Zradar. NetCDF is used for array-oriented scientific data, while HDF5 is designed for storing and organizing large, complex datasets efficiently. Besides, Python scripts are used to read, manipulate, and extract radar data, converting it into human-readable values stored in CSV files. These reflectivity values are then plotted against latitude and longitude on a geo-referenced map of Malaysia using Panoply software.

2.6 Estimation of Rainfall Intensity (R) from Reflectivity Factor (Z)

Weather radar indirectly estimates rainfall intensity (R) using the reflectivity factor, Z. The most common Z-R relationship is a power law expressed as $Z=aR^b$ where a and b are coefficients that depend on space and time. The relationship is based on the fact that the radar reflectivity factor, Z and the rain rate, R, are related through the raindrop size distribution (DSD) (Ma et al., 2022). Z is proportional to Di^6 , where D is the diameters of individual raindrops in a sample volume, while R is proportional to Di^3. The widely known Z-R relationship, $Z=200R^{1.6}$, was derived by Marshall & Palmer (Mahyun et al., 2021). However, no universal Z-R relationship truly represents all rainfall events, as the DSD has ambiguous characteristics and varies significantly in both space and time (Tahir et al., 2019).

The radar equation already mentions the radar reflectivity factor, which is a meteorological parameter determined by the number and size of particles in a sample volume (Marshall and Palmer, 1948). Due to the huge range of magnitudes (from 0.001 mm^6/mm^3 for fog, to 36 000 000 mm^6/m^3 for softball-sized hail), the radar reflectivity is convenient to express in decibels (dB) unit or dBZ as follows:

$$dBZ = 10\ log_{10} \frac{Z}{m^6/m^3} \tag{2.6}$$

where dBZ is the logarithmic radar reflectivity factor and *Z* is the linear radar reflectivity factor in mm^6/mm^3. The relationship between rain rate (R) in unit mm/h and radar reflectivity factor (Z) in unit m^6/m^3 is commonly described as empirical power-law relationship (Atlas, 1964):

$$Z = aR^b \tag{2.7}$$

where *a* and *b* are empirically derived constants. In reality, the radar reflectivity is measured and used to calculate the rain rate*, R,* hence the equation mostly appropriate written as (Battan, 1973):

$$R = AZ^B \tag{2.8}$$

where A and B are again empirical constants. Many values are possible for both a and b although b does not vary as much as a, as described in Table 2.3. In this study, the Marshall & Palmer Z-R equation is used because it is widely recognized as the standard reference for converting radar reflectivity into rainfall estimates. It provides stable performance for widespread and long-duration rainfall, which commonly occurs in Malaysia during the monsoon seasons. In addition, this equation is the default setting applied by the Met Malaysia and many operational weather radar systems, making it a practical and consistent choice for daily operations (Fulton et al., 1998; Peng et al., 2022).

Table 2.3
Several Parameters a and b depend on the Type of Rainfall or Cloud

Parameter a	Parameter b	Relationship	Type of cloud
200	1.6	Marshall Palmer	Stratiform precipitation
250	1.2	Rosenfeld	Convective precipitation
400	1.4	Laws and Parsons	Stratiform precipitation
300	1.5	Joss and Waldvogel	Stratiform precipitation

(Source: Ahmad et al., 2017)

2.7 Radar Reflectivity Image

Each pixel in a radar image represents the number of backscattered waves received from the surface of a specific object (Batool et al., 2020). An imaging radar functions similarly to a flash camera by recording the returned signal (radar echoes). Some imaging radar systems generate microwaves with wavelengths ranging from 1 cm to 1 meter, which are longer than the wavelengths used to detect rain and snow in weather radars. Imaging radar technology is useful for recording surface characteristics in any situation, whether day or night, and under various weather conditions, due to the longer wavelength's ability to penetrate the atmosphere and clouds without causing disturbance (Smith, 2012).

Radar images can provide details on the physical and biological characteristics of the surface terrain, as well as its shape. They have long been used in geological studies to identify structural features that are made visible by the terrain's topography (Stepanian et al., 2014). Radar images use a color code to indicate the intensity of precipitation in specific areas. It is important to note that radar images cannot determine the type of precipitation, but they can show the location and intensity of precipitation based on when the image is generated. Figure 2.7 shows that magenta represents stronger precipitation, whereas blue represents lighter precipitation. Since there is no snow in Malaysia, the blue color indicates light rain.

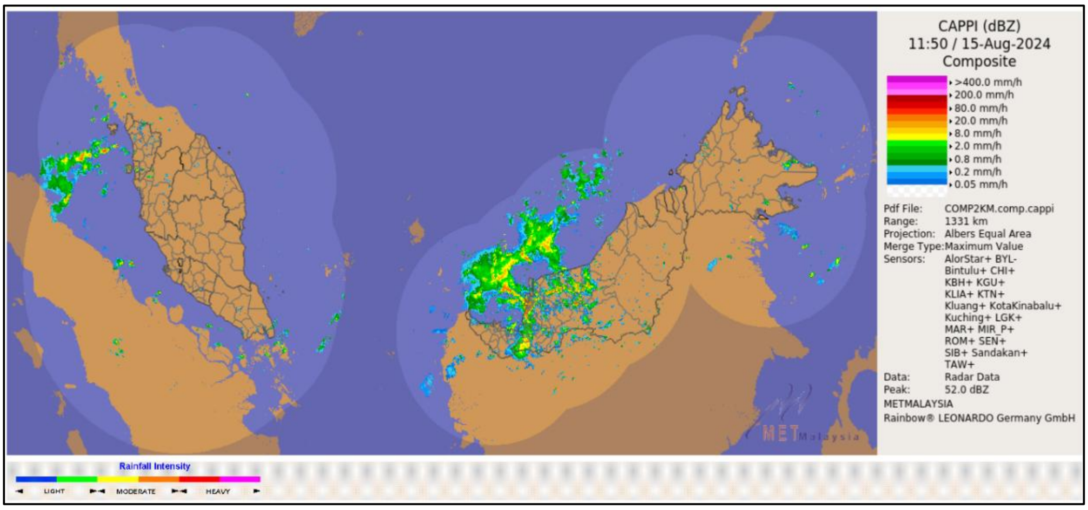

Figure 2.7 Radar Image Display on the MMD Website (MET Malaysia, 2024)

2.7.1 Reviews on Rainfall Classification using Radar Reflectivity Images

Since the late 1940s, when weather radar first became available, the term 'stratiform' has been used to describe precipitation as shown in radar data displays. Stratiform precipitation has a layered structure in vertical cross-sections of radar reflectivity because it is relatively homogeneous in the horizontal plane. It often displays a distinct layer of high reflectivity known as the 'bright band' (Battan, 1975; Houze, 2004). In contrast, convective rainfall appears on radar as 'cells,' as defined by Byers and Braham (1949). These cells are horizontally localized patches or cores of intense radar reflectivity.

Radar meteorologists have developed a tradition of speaking of radar echoes as convective or stratiform, according to whether they form patterns of vertically oriented intense cores or horizontal layers (Rigo and Llasat , 2004; Karklinsky & Morin, 2006; Llasat et al., 2007; Barnolas et al., 2010; Djafri and Haddad, 2014; Peleg et al., 2018). The process for classifying precipitation as "convective" or "stratiform" involves three key steps called “texture algorithms”. First, a reflectivity threshold (typically between 40 and 45 dBz) is applied to identify pixels with high confidence as "convective," based on the fact that convective rain rates are generally more intense than stratiform rain (Llasat and Rigo, 2002). Second, a pixel not exceeding the "convective" threshold is labeled as "convective" if its reflectivity value significantly differs from the mean background reflectivity, accounting for gradients in convective precipitation areas. Lastly, if adjacent pixels are classified as "convective," the analyzed pixel is also considered "convective," even if it doesn't meet the previous criteria, to include pixels at the borders of convective systems. After applying these three requirements, any pixel not meeting one of them is classified as "stratiform".

The classification of radar echoes into "convective" and "stratiform" types is a foundational concept in radar meteorology, with several studies proposing structured methods for this distinction. A commonly used approach involves a three-step texture algorithm based on reflectivity thresholds, background variability, and spatial continuity. While this method is widely accepted, its reliance on fixed reflectivity thresholds (typically 40–45 dBZ) may limit its applicability across diverse climatic and radar settings. The second step, which compares pixel reflectivity to the background field, enhances sensitivity to convective features but is influenced by the spatial scale used for background estimation. The inclusion of neighboring pixels as a classification factor helps maintain spatial coherence but may lead to the overextension of convective regions.

Overall, while the algorithm is operationally effective, its binary classification may fail to capture the full spectrum of precipitation types, particularly mixed or transitional cases. Emerging approaches, such as probabilistic and machine learning models, are being explored to address these limitations and improve classification accuracy.

2.8 Radar Limitations

Radar observations provide a good spatial representation of precipitation, but they are burdened with a wide spectrum of errors from different sources, each characterized by specific properties and spatial and temporal structures. Weather radar estimates rainfall intensity (R) by measuring the power of electromagnetic pulses backscattered by raindrops, called reflectivity (Z). The variability in raindrop size distribution and microphysical processes during rainfall formation contributes significantly to uncertainty and bias in rainfall estimates. According to Tahir et al. (2019), rainfall estimation worsens as the signal is attenuated with distance from the radar station.

Weather radar data errors stem from hardware issues (such as electronics instability, antenna accuracy, and signal processing), radar beam geometry and scan strategy (including beam broadening and increasing distance from the radar due to Earth's curvature), and non-meteorological echoes (such as ground clutter, electromagnetic interference, measurement noise, and biological objects), all of which significantly affect precipitation estimation (Krajewski et al., 2011; Gauthreaux and Diehl, 2020: Kou et al., 2024). Additionally, some researchers have found that radar errors arise from beam blockage by terrain (e.g., mountains), signal attenuation by rain (especially heavy rain), and anomalous propagation due to atmospheric temperature gradients, which cause the radar beam to follow an unusual path, leading to return signals from greater distances (Bech et al., 2007; Gu et al., 2011; Lee and Kim, 2017).

2.8.1 Reviews on Radar QPE Calibration Methods

High-quality weather radar data is crucial for hydrological applications. As mentioned in Section 2.8, radar measurements provide a good spatial representation of precipitation but are subject to several sources of error. Radar errors are difficult to diagnose and, as a result, challenging to completely eliminate. The development of more efficient quality control techniques has been driven by advancements in image processing and increased computational capabilities. Data from various measurement systems, particularly rain gauge networks, are used to enhance radar-based QPE by adjusting or combining multiple sources. To improve accuracy, radar data are adjusted based on rain gauge observations, which are assumed to provide more accurate point values (Mecklenburg et al., 2005; Bruen and O'Loughlin, 2014; Ali et al., 2021; Yousefi et al., 2023). While rain gauge observations are often considered ground truth data, their reliability and spatial representation are limited. Gauge adjustment largely depends on the distribution of the rain gauge network and real-time availability, which can be scarce and irregular, especially in complex terrain.

Table 2.4 shows the summary of the radar QPE calibration methods and performance evaluations. The enhancement of radar QPE started with the adoption of alternative methods aimed at reducing the uncertainty in the Z–R relationship, which is the primary source of bias in radar rainfall estimates. Besides, space-based rainfall products serve as valuable tools for large-scale hydrogeological and climate studies, with satellite-based precipitation measurements regarded as a viable substitute for ground-based data (Karbalaee et al., 2017; Chen et al., 2019). However, challenges persist due to limitations in parametric retrieval algorithms, as well as gaps in temporal and spatial sampling, especially for light rainfall or extreme events. Additionally, machine learning approaches for QPE present a promising alternative for enhancing radar-based QPE due to their simplicity (Roslan et al., 2021; Zhang et al., 2021; Shin et al., 2021). Nevertheless, the time required for computations to develop QPE models can vary depending on the machine learning algorithm used and may need to be adjusted before implementation. It is strongly recommended that the accuracy of these methods be evaluated in polarimetric radar systems to better assess the effectiveness of machine learning algorithms in future rainfall retrieval applications.

Additionally, ground-based weather radar systems, specifically dual-polarization radar systems, have demonstrated significant advantages in conducting high-resolution precipitation surveys over large areas in a very short time frame. Dual-polarization systems have been installed in the National Weather Service Next Generation Radar network to improve quantitative precipitation estimation, hydrometeor classification, and other capabilities. Numerous studies advocate for the use of dual-polarization radar variables as direct inputs to rainfall estimation equations, not only to ensure a high degree of data quality (Simpson and Fox, 2018; Voormansik et al., 2020; Shin et al., 2021). However, the effectiveness of these methods can be reduced under certain conditions such as beam blockage, signal attenuation, or complex terrain, all of which may distort radar observations. Their performance may also vary with precipitation type, drop size distribution, and the presence of mixed-phase hydrometeors. While dual-polarization radar represents a significant advancement in meteorological observation, its full potential depends on the refinement of estimation techniques and continuous validation against ground-based measurements. Emerging approaches, including machine learning and adaptive correction methods, show promise in addressing current limitations and improving the reliability of precipitation estimates.

Table 2.4

Radar QPE Calibration Methods (Osman & Tahir, 2024)

Articles	Optimization Approach	Performance Measurement Method	Country
Giangrande et al. (2014)	ZR variability	Bias Correction, RMSE	New York
Boodoo et al. (2015)	ZR variability	RMSE, NMB, NSE, CORR	Canada
Bringi et al. (2011)	ZR variability	MAE, NASH, Bias Correction	UK
Ramli et al. (2011)	Rainfall classification	MAE, RMSE, Bias Correction	Malaysia
Tahir et al. (2014)	Kalman Filtering	CC	Malaysia
Yahya et al. (2012)	Kalman Filtering	CC, RMSE	Malaysia
Tahir et al. (2012)	ZR variability	MAE	Malaysia
Zhao and Su (2019)	ZR variability	SD, ERR, CC	China
Zhang et al. (2021)	Deep learning algorithm QPENet	CC, RMSE, NB, NE, Bias ratio	China
Handoyo et al. 2021	Kraemer approach	RMSE	Indonesia
Song et al. (2021)	Quantile matching method	MAE, RMSE, CC	China
Shin et al. (2021)	ML (regression tree and random forest))	RMSE, MAE, Bias Correction, CC, COE	China
Zhang et al. (2020)	ZR variability	MBR, CC, MAE	USA
Biswas et al. (2020)	Parsivel Disdrometer data from two NOAA Physical Sciences Division (PSD)	DSD Characteristics	USA
Chen et al. (2019)	Bayesian approach, MFB and LB correction	RMSE, MAE, CC	USA
Wolfensberger et al. (2021)	Random forest algorithm	RMSE, Bias Correction	Switzerland
Gou et al. (2018)	Reflectivity Threshold (RT) and Storm Cell Identification and Tracking (SCIT) algorithms	Bias Correction, MAE, CC, RMSE	China
Yang et al. (2017)	Terrain-based weighted random forests (TWRF) method	Bias Correction, RMSE, MAE, MB, CC	China

Wardhana et al. (2017)	Mean Field Bias Correction (MFB) and static adjustment	RMSE	Indonesia
Yang et al. (2016)	Rainfall Classification (Fuzzy Logic algorithm)	Bias Correction, RAE, RMSE	China
Zhang et al. (2014)	Radar, rain gauge, and an orographic precipitation (merging radar)	RMSE	USA
Delrieu et al. (2014)	Geostatistical technique	Bias Correction, CC	France
Wang and Chandrasekar (2010)	ZR variability	Bias Correction, NSE	USA
Jang et al. (2012)	"Sorting and moving average" (SMA) method	RMSE, Bias Correction	Korea
Cifelli et al. (2011)	Hydrometeor identification (HID)	RMSE, NB, CC	USA
Zhang and Qi (2010)	ZR variability	RMSE	USA
He et al. (2013)	Levenberg-Marquardt Algorithm (LMA) with Jacobian matrix updating	RMSE	Denmark
Ali et al. (2020)	Mean Field Bias (MFB)	MAE, FAR	Indonesia
Voormansik et al. (2020)	ZR variability	NASH, RMSE, NMB, CC	Estonia
Montopoly et al. (2017)	ZR variability	CC, RMSE, NASH, NB	Italy
Hanchoowong et al. (2012)	Kringing technique, geostatistical technique	RMSE	Thailand
Wijayarathne et al. (2020)	ZR variability	CC, Bias Correction, RMSE	Canada
Rafieeinasab et al. (2015)	Fisher estimation	RMSE	USA
Wang et al. (2014)	ZR variability	MB, RMSE, CC	USA
Karbalaee et al. (2017)	PERSIANN-CCS algorithm; satellite Probability Matching Method	Bias Correction, CC, RMSE	USA
Wang et al. (2013)	ZR variability	Simulations using drop size distribution (DSD) and drop shape relation (DSR) observations	Taiwan
Calvetti et al. (2017)	An algorithm, Spirec,	CC, RMSE	Brazil

	used to blend rain gauges, radar mosaic data, satellite by using Poisson's equation		
Pauthier et al. (2018)	Merging technique (radar and rain gauge data) based on Krigine with external drift (KED)	NASH, RMSE	France
Shin et al. (2019)	Random forest, stochastic gradient boosted model, extreme learning machine method	RMSE	Korea
Gou et al. (2019)	ZR variability	MAE, RMSE, CC	China
Martinaitis et al. (2020)	Multi radar multi sensor system (MRMS)	MBR, ME, MAE, CC	USA
Chen et al. (2021)	Integrate S- and C-Band Dual polarization radars	RMSE	Taiwan
Husnoo et al. (2021)	Real time adaptive algorithm uses a neural network	CC, RMSE, Bias Correction	UK

SD: standard deviation; ERR: mean standard deviation; CORR: Pearson correlation coefficient; RMSE : root mean square error; MAE: mean absolute error; MBR: mean bias ratio; ME: mean error; CC: correlation coefficient; NASH: Nash Sutcliffe coefficient; MRE: mean relative error; NMB: normalized mean bias; FAR: false alarm ratio; NB: normalized bias; NSE: normalised standard error; RAE: relative absolute error; COE: coefficient of efficiency; NE: normalized absolute error

The previous sections describe in detail the radar characteristics, limitations, error and calibration techniques. The following section will review relevant research and provide the theoretical background on the primary tools applied in the study which are feature extraction technique, rainfall classification (convective vs. stratiform) using machine learning, optimization of Z-R relationship and Artificial Neural Networks (ANN).

2.9 Feature extraction of rainfall characteristics from radar images

Feature extraction is the process of converting raw images into a simplified form to aid in decision-making, such as pattern detection, classification, or recognition. This technique is crucial as it enables machine learning models and other algorithms to process data more effectively and accurately. By eliminating noise and removing redundant or irrelevant data, feature extraction allows machine learning programs to focus on the most important and relevant information. Feature extraction of radar image is initially performed by classifying rainfall characteristics using segmentation methods into two categories: stratiform and convective. On the other hand, weather radar data provide detailed insights into the spatial structures of rain fields, offering information that was previously unavailable from traditional rain gauge networks. This data is essential for enhancing our understanding of rainfall and hydrometeorological systems, as demonstrated in previous studies.

Research into rain cell characterization has evolved significantly, with studies contributing diverse methods and perspectives shaped by regional and climatic contexts. Féral et al. (2000) employed elliptical geometry to define rain cells, focusing on their orientation and axis dimensions. While this approach provided a simplified geometric interpretation, it may not fully capture the irregularity of natural convective structures. Theusner and Hauf (2004) extended this work by examining the spatial characteristics of convective rain cells in post-frontal environments over Germany, highlighting diurnal variations and introducing a temporal dynamic that earlier geometric models lacked. In a contrasting climate zone, Karklinsky and Morin (2006) introduced additional parameters such as central location, area, and integrated rainfall intensity, reflecting a more detailed and comprehensive approach. Their study emphasized that regional climatic conditions substantially influence rain cell behavior, challenging the comparability of findings across diverse settings.

May and Ballinger (2007) addressed this variability by comparing convective cells across different seasonal regimes, showing that cell size, height, and duration vary between continental and oceanic conditions. This comparative approach provided valuable insights but also highlighted the complexity of defining universal convective characteristics. Capsoni et al. (2008) added to this complexity by demonstrating that the choice of rain intensity thresholds significantly influences rain cell statistics, raising concerns about methodological consistency across studies. Meanwhile, Barnolas et al. (2010) applied GIS tools to analyze rain cell geometry in the western Mediterranean, improving spatial accuracy and illustrating the advantages of modern geospatial techniques in rainfall analysis.

In a more practical approach, Liu et al. (2016) reduced rainfall data into feature matrices to support landslide risk modeling, categorizing rainfall into components such as evaporation, infiltration, and runoff. This shift from descriptive characterization to functional application reflects a growing interest in the practical implications of rainfall analysis. Although several alternative feature extraction techniques are cited in the literature, there remains a lack of comparative evaluations to guide best practices (Dixon and Wiener, 1993; Johnson et al., 1998; Bonelli and Marcacci, 2008; Peleg et al., 2018). Collectively, these studies reveal a progression from simple geometric models to more complex, context-specific, and application-oriented analyses. However, they also highlight persistent gaps in methodological standardization and cross-regional validation that future research should aim to address.

Conversely, this study explores the application of pixel-based analysis techniques to radar reflectivity images, particularly in the context of the tropical monsoon region, which has not been extensively investigated. The task of extracting features of convective and stratiform rainfall from radar reflectivity, especially when applied to the unique characteristics of the tropical region, is both challenging and novel. In addition, developing an optimal rainfall estimation model using machine learning techniques based on radar reflectivity data presents a significant opportunity for advancement. The extracted features from the radar images will serve as input for a machine learning classifier, which will be used to train an ANN model for enhanced radar-based QPE.

2.10 Rainfall classification by using machine learning algorithm

Stratiform and convective rainfall are linked to distinct cloud physical processes, thermodynamic influences, vertical structures, and types of precipitation. Differentiating between convective and stratiform systems is valuable for meteorological research and weather forecasting. However, a clear boundary between these two types of precipitation does not exist. Several studies have advanced the classification of convective and stratiform precipitation using remote sensing data combined with machine learning techniques. Anagnostou (2004) introduced a neural network-based method for classifying reflectivity measurements from ground-based volume scanning radar, trained and validated using data from 18 Weather Surveillance

Radar (WSR88D) Doppler radar sites across the southern United States. While the approach demonstrated potential, it also revealed limitations in classification performance, with an overall 4 percent overestimation of stratiform and a 27 percent underestimation of convective rain areas. This underestimation of convective precipitation is particularly significant, as convective systems often drive localized hydrometeorological extremes and therefore require precise identification.

In comparison, Islam et al. (2015) adopted a spectral approach using passive microwave satellite data. Their study applied machine learning algorithms to distinguish between stratiform and convective rain regimes using only calibrated brightness temperatures from the Tropical Rainfall Measuring Mission (TRMM) microwave imager. Although the method successfully identified rain types with good accuracy, its reliance solely on spectral parameters may limit its ability to capture the vertical structure of clouds and the microphysical processes essential for accurate classification, especially in convective environments.

Lazri and Ameur (2018) expanded these efforts by applying a combination of support vector machines, artificial neural networks, and random forests to classify precipitation types using spectral features derived from SEVIRI satellite imagery. Their use of multiple algorithms improved classification performance by combining the strengths of different machine learning techniques. This multi-model approach is beneficial for operational applications that require broad spatial coverage and frequent updates. However, while the integration of several models can increase accuracy, it also introduces greater computational demands and complexity, which may pose challenges in real-time or resource-limited settings.

Yang et al. (2019) used the K-nearest neighbor (KNN) machine learning algorithm to classify precipitation types. The KNN method effectively identifies the location and extent of both stratiform and convective systems. These findings indicate that KNN can accurately classify nearly all stratiform precipitation and the majority of convective precipitation types, highlighting its strong potential for classifying precipitation types. The strength of KNN lies in its simplicity and intuitive proximity-based classification. However, the algorithm's sensitivity to the selection of hyperparameters, such as the number of neighbors and the choice of distance metric, introduces potential variability in performance. Moreover, its instance-based nature can lead to increased computational costs when applied to large datasets, and the method's effectiveness across diverse climatological conditions remains insufficiently tested.

Foth et al. (2021) present two micro rain radar-based methods to differentiate between stratiform and convective precipitation. One method uses probability density functions (PDFs) combined with a confidence function, while the other employs an ANN for classification. Both methods produce similar results, but the ANN approach is more definitive, as it can also identify an inconclusive class, thereby enhancing the reliability of the stratiform and convective classifications. Nevertheless, the implementation of ANN models can be computationally intensive, and the training process typically requires extensive, well-labelled datasets to generalize effectively. The study would benefit from a more detailed analysis of model performance under varied precipitation intensities and types, especially in more complex convective scenarios.

Wang et al. (2021) developed and tested a precipitation separation method using a support vector machine (SVM) on a C-band polarimetric weather radar in Taiwan. The proposed method integrates input variables with the SVM, which was trained using typical stratiform and convective precipitation events. The results indicate that the SVM-based approach outperforms the traditional separation index method, highlighting the value of integrating multiple input features. Importantly, the study introduces a flexible prototype framework that accommodates additional variables, such as differential phase, to further enhance classification accuracy. This adaptability represents a practical advantage for real-time radar systems. However, the study's reliance on events from a single region limits its generalizability, and the robustness of the method across different radar systems or climatic zones is not fully addressed.

2.10.1 K-Nearest Neighbor (KNN) Algorithm

In this study, the K-nearest neighbor (KNN) algorithm is used to classify precipitation types, as a study by Yang et al. (2019) demonstrates its strong potential for such classification. Moreover, KNN algorithm saves training samples during the training phase and processes them upon receiving test samples (Sun and Huang, 2010). To ensure accurate classification, a larger, balanced set of training samples is required. Since stratiform precipitation typically covers a larger area than convective precipitation, there is often an imbalance in the number of grid points for each type. To address this, the training samples are balanced by randomly selecting precipitation samples and reconstructing the set with a 1:1:1 ratio of stratiform, convective, and other types of precipitation (Taunk et al., 2019; Yang et al., 2019; Nasrullah et al., 2024).

To classify a sample, the distance between the sample and all the training samples is first calculated. Afterward, the k nearest training samples with the smallest distances are selected. These k training samples have same influence factor, and the probability of classifying the sample as type j is determined as follows:

$$P_j = \frac{N_j}{k} \tag{2.9}$$

where P_j represents the probability of the sample being classified as type j, and N_j is the number of training samples labeled as type j among the k-nearest neighbors. The classification result is type j when the Pj value is maximized.

2.11 Z-R Relationship

The Z-R relationship is essential for accurate quantitative precipitation estimation (QPE). The rain rate (R), derived from this relationship, plays a key role in many hydrological processes, including rainfall-runoff modeling, catchment capacity calculation, flood forecasting, agricultural irrigation, and other hydrological applications. Therefore, converting the radar reflectivity factor (Z) into rain rate is a vital step for improving precipitation estimates in radar-based hydrology systems. To achieve the highest accuracy in radar rainfall measurements, it is important to select the most appropriate Z-R equation. Numerous Z-R equations have been developed based on factors such as rainfall type (stratiform or convective), geographic location (high or low latitudes), and other meteorological conditions. The validity of these equations is typically evaluated by comparing radar estimates with rain gauge data.

The Z-R relationship is based on the fact that the radar reflectivity factor (Z) and the rain rate (R) are both dependent on the raindrop size distribution (DSD) (Ma et al., 2022). Specifically, Z is proportional to Di^6 , where D represents the diameter of individual raindrops in a sample volume, while R is proportional to Di^3. The most common Z-R relationship is a power law, typically expressed as:

$$Z=aR^b \tag{2.10}$$

where a and b are coefficients that depend on space and time. In the 1940s, Marshall and Palmer introduced an exponential model to characterize the DSD, which later became known as the M-P distribution. This model forms the basis for the classical Z-R relationship, commonly expressed as $Z = 200R^{1.6}$, where Z is the radar reflectivity factor and R is the rainfall rate. However, the parameters of the Z-R relationship are not constant and tend to vary depending on regional and climatic conditions. These variations are primarily due to differences in raindrop microphysics, such as raindrop size and concentration. Therefore, selecting suitable Z-R parameters is essential for enhancing the reliability of QPE (Ciach and Krajewski, 1999; Kato and Maki, 2009; Wei and Liu, 2022).

Many researchers have developed methods to improve the Z-R relationship by classifying rainfall into distinct categories to address these limitations (Yabin et al., 2015; Xie et al., 2020; Zeng et al., 2021; Lavanya and Kirankumar, 2021; Ghada et al., 2022; Kovalchuk et al., 2023). A commonly used approach for enhancing QPE is the rainfall classification method, which utilizes radar echo characteristics to distinguish between rainfall types, such as convective and stratiform. Stratiform and convective rainfall, for instance, have distinct DSDs, with stratiform rain generally consisting of smaller and more uniform raindrops, while convective rain tends to include larger and more variable drops. This distinction in DSDs directly influences the radar reflectivity factor and its relationship to rainfall rate. As a result, applying a single, universal Z-R relationship across all rainfall types can lead to significant inaccuracies in precipitation estimation (Alfieri et al., 2010; Ramli, 2015; Tahir et al., 2019).

Different Z-R relationships are therefore applied to each rainfall type, as these categories exhibit significantly different raindrop size and concentration characteristics (Chumchean et al., 2006; Zhang et al., 2008; Bangsawan et al., 2022). Consequently, using different Z-R relationships for each type of rainfall improves the accuracy of QPE, which in turn enhances the reliability of forecasts and practical applications. Furthermore, these relationships can be dynamically adjusted based on real-time radar observations, increasing their ability to capture rapid changes in precipitation intensity and storm development.

2.12 Artificial Neural Network (ANN)

Machine learning techniques, including Artificial Neural Networks (ANN), decision trees (DT), random forests (RF), and other approaches, have proven highly effective in solving various forecasting problems, such as rainfall prediction. These methods identify relationships between independent and dependent variables using sample data, without relying on prior assumptions like linearity (Chen et al., 2019). In this study, ANNs are employed due to their ability to model non-linear relationships and extract patterns from complex atmospheric remote sensing data (Karbalaee et al., 2017). ANNs are inspired by the structure of the human neuron-synaptic network. Recently, there has been growing interest in using machine learning and remote sensing data for Quantitative Precipitation Estimation (QPE) (Roslan et al., 2021; Zhang et al., 2021;Li et al., 2023;Lu et al., 2023; Huangfu et al., 2024).

ANN is a mathematical model made up of nodes and layers that can map complex nonlinear processes. The typical structure of an ANN includes an input layer, one or more hidden layers, and an output layer (Dewangan et al., 2023; Schmidgall et al., 2024). One of the most widely used types of neural network is the feedforward neural network, which consists of layers of parallel processing units known as neurons. The input layer receives the variables that influence the output, while the output layer represents the model's predictions. Between these layers, there may be one or more hidden layers. Neurons in each layer are connected to neurons in the subsequent layer by weights, denoted as 'w', which are adjusted during training. The networks are organized and optimized through training methods, making it easier to develop specific applications (Zou et al., 2009). Figure 2.8 illustrates a three-layer neural network consisting of three neurons in input layer, three neurons in hidden layer and one neuron in output layer, with the interconnection weights between layers of neurons.

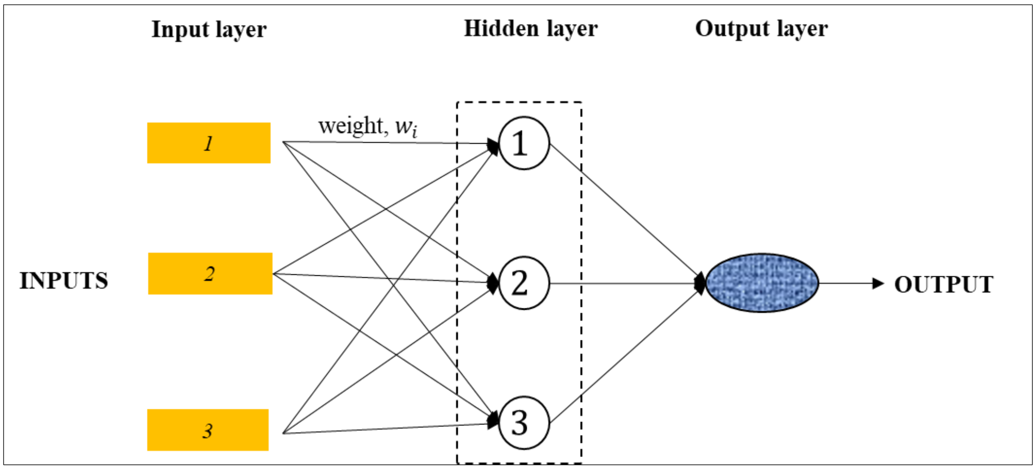

Figure 2.8 Architecture of A Three-Layer Neural Network

2.12.1 ANNs Training Algorithm

In ANNs, training involves adjusting the network's weights to reduce prediction errors. It is a process in which an ANN repeatedly processes a training set (input–output data pairs), adjusting the values of its weights based on a predefined algorithm to enhance its performance. This process generally includes two primary steps: forward propagation, where inputs pass through the network to produce outputs, and backpropagation, where the error is calculated and used to update the weights using an optimization algorithm. Some of the optimization algorithms used with backpropagation include Gradient Descent (GD), Stochastic Gradient Descent (SGD), Conjugate Gradient, Quasi-Newton methods, Momentum, and Levenberg-Marquardt (LM). In this study, the training algorithms employed are backpropagation and the Levenberg-Marquardt algorithm.

2.12.1.1 Backpropagation Algorithm

The Neural Networks package offers various training techniques, including the Back Propagation Neural Network (BPN), which is effective in estimating a wide range of functions. This technique outperforms numerical differentiation in efficiency (Buscema, 1998). The backpropagation algorithm was initially developed by Paul Werbos in 1974 and later independently rediscovered by Rumelhart and Parker (Mehrotra et al., 1996) . Since then, it has become widely used as a learning algorithm in feedforward multilayer neural networks.

The back-propagation algorithm provides a method for adjusting the weights, w_{ij}, in a feedforward network to learn a set of input-output training pairs. It is a supervised learning technique where the output error is propagated back through the network, modifying the connection weights to reduce the error between the network's output and the target output, as illustrated in Figure 2.9.

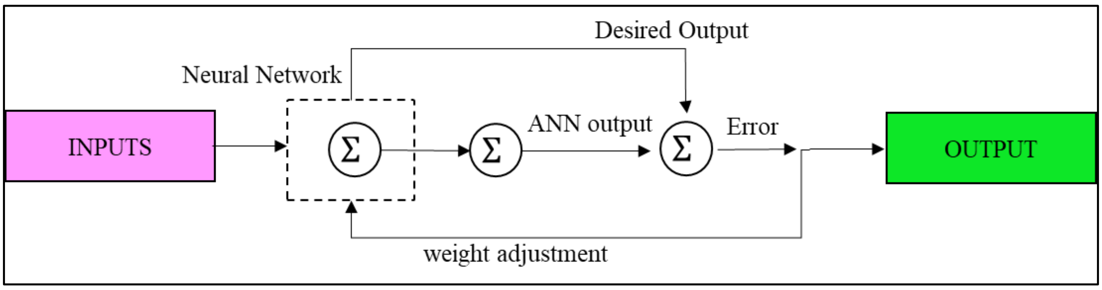

Figure 2.9 Illustration of A Backpropagation ANN Algorithm

Artificial neural networks have been widely studied for classification and optimization problems. Multilayer neural networks employ backpropagation as the training algorithm. In the backpropagation algorithm, the weights in the network are adjusted by moving in the negative direction of the gradient of the sum of squared errors with respect to the weight variables. Let the input be represented by vector x, the weights by vector w, the network output by o, and the desired output by vector od. The error vector is defined as e = o - od. The weights in a backpropagation neural network are then updated as follows:

$$w_{t-1} = w_t - \eta \frac{1}{2} \frac{\partial e^t e}{\partial x} \tag{2.11}$$

Here, η is referred to as the learning rate. To speed up the learning process, some studies recommend using a momentum parameter, μ (Haykin, 1999; Kevin and Paul, 2005). With the momentum parameter, the weights are updated using the following rule:

$$w_{t-1} = w_t - \eta \frac{1}{2} \frac{\partial e^t e}{\partial x} + \mu(w_t - w_{t-1}) \tag{2.12}$$

The learning process can be improved to enhance the performance of the prediction system. Therefore, this study employs the Levenberg-Marquardt algorithm during the learning phase of BPN.

2.12.1.2 Levenberg-Marquardt algorithm

The Levenberg-Marquardt (LM) algorithm is specifically designed to minimize sum-of-squares error functions (Aldrich, 2002; Gavin 2019). It is a modified version of the Gauss-Newton method (Haykin, 1999). In the Gauss-Newton method, the weights for neural network training are updated using the following rule:

$$w_{n+1} = w(n) - \left(J(n)^T J(n)\right)^{-1} J(n)^T e(n) \tag{2.13}$$

In this context, J denotes the Jacobian matrix, defined as:

$$J = \begin{bmatrix} \frac{\partial e_1}{\partial w_1} \frac{\partial e_1}{\partial w_2} \cdots \frac{\partial e_1}{\partial w_m} \\ \frac{\partial e_2}{\partial w_1} \frac{\partial e_2}{\partial w_2} \cdots \frac{\partial e_2}{\partial w_m} \\ \vdots \quad \vdots \quad \vdots \quad \vdots \\ \frac{\partial e_n}{\partial w_n} \frac{\partial e_n}{\partial w_n} \cdots \frac{\partial e_n}{\partial w_m} \end{bmatrix} \tag{2.14}$$

The Levenberg-Marquardt adaptation to the Gauss-Newton method is:

$$w_{n+1} = w(n) - (J(n)^T J(n) + \mu I)^{-1} J(n)^T e(n) \tag{2.15}$$

As is commonly understood, the learning parameter, μ, represents the step size for adjusting the actual output towards the desired output. In the standard Levenberg-Marquardt (LM) method, μ is a constant value. This parameter ensures that matrix inversion always yields a valid result. The value of μ is determined by evaluating the sum of squared errors. If the error decreases, μ is divided by a scalar θ; conversely, if the error increases, μ is multiplied by the scalar θ;

$$\theta = 0.01(e^t e) \tag{2.16}$$

Since e is a k×1 matrix, $e^T e$ is a 1× 1 scalar, making $[JTJ + \mu I]$ invertible. As a result, when the actual output is far from the desired output, or when errors are large, the system converges to the desired output with larger steps. Conversely, when the error is small, the actual output approaches the desired output with more gradual steps. This helps to significantly reduce error oscillation.

2.12.2 Review on ANN-based Radar QPE in Rainfall Forecasting

ANN models are universal approximators, making them well-suited for modeling the dynamic and nonlinear behavior of hydrological systems. For over 20 years, ANNs have been increasingly used in river forecasting, which involves modeling streamflow and rainfall-runoff (Abrahart et al., 2012). ANNs are capable of handling qualitative, incomplete, and ambiguous data, and are recognized for their resilience and fault tolerance. When properly trained with historical data, ANN models are known to perform effectively in various hydrological applications.

ANNs are commonly used to address problems involving nonlinear and complex relationships. This parallel computing system connects multiple artificial neurons to simulate the brain's neural network (Nogales and Benalcázar, 2023). ANNs excel at learning and generalizing, enabling them to tackle problems that would be difficult or impossible to solve with traditional approximation methods. Additionally, ANNs provide an alternative approach to overcoming the limitations of physically based, conceptual, and numerical models (Santos et al., 2023). Beyond serving as powerful tools for accurate prediction and modeling of complex processes, ANNs can also offer valuable insights into the process being modeled by evaluating the model and understanding the learned relationships. Furthermore, ANN-based solutions often outperform other methods, such as conceptual and physically based models. Nevertheless, despite their strengths in predictive accuracy and adaptability, ANNs often lack transparency and require large amounts of high-quality data. Issues such as overfitting and high computational cost can also hinder their practicality. Therefore, while ANNs represent a valuable modeling tool, their limitations must be considered when selecting appropriate methods for real-world applications.

Xiao and Chandrasekar (1997) developed a neural network technique to estimate ground-level precipitation using radar observations. They evaluated the effectiveness of the neural network method using data collected from various storms. At that time, neural networks were typically multilayer perceptron (MLP) networks, which took a considerable amount of time to train and were not ideal for long-term applications (spanning months to years). In a later study, a novel adaptive Radial Basis

Function (RBF) neural network was created to calculate rainfall from radar data based on horizontal reflectivity profiles. Alqudah et al. (2013) used radar reflectivity as input and rain gauge data as the target to assess the accuracy of rainfall estimates generated by RBF neural networks. However, while these studies show progress in model design and performance, they do not fully address persistent challenges such as model interpretability, generalization to new storm types, and data quality variability. More recent work should continue to build on these foundations by integrating hybrid modeling techniques and incorporating uncertainty analysis to improve both accuracy and reliability in operational settings.

Shin et al. (2021) conducted a study to assess the feasibility of using stochastic gradient boosting (SGB), extreme learning machine (ELM), and random forest (RF) in QPE models. The results indicated that the machine learning (ML)-based QPE models outperformed traditional Z–R relationship-based models, particularly in cases of extreme rainfall. The successful implementation of RF-based models by Yang et al. (2017) and Wolfensberger et al. (2021), which minimized the need for extensive radar data pre-processing, further reinforces the operational potential of ML techniques. Furthermore, since neural networks are among the most popular and effective machine learning algorithms, many meteorologists have begun exploring their use to model the relationship between reflectivity (Z) and rainfall (R) (Mahdianpari et al., 2018; Mosavi et al., 2018; Yo et al., 2021). However, while the effectiveness of these models is promising, it is important to recognize that their performance often depends heavily on data quality, regional characteristics, and event-specific variability.

Generally, ANN models solve a problem by adjusting the weights according to the internal representation of relationships between variables. This adjustment occurs during the training process to minimize the error between the output of the artificial neural network and the actual data. Therefore, the aim of this study is to enhance rainfall estimation through an ANN model that integrates machine learning. Additionally, this study will make a novel contribution, as no established method currently exists for improving QPE through feature-based intensity characterization of radar images in Malaysia, especially considering the unique conditions of the tropical monsoon region.

2.13 Flood Modelling

Flood modeling involves using mathematical and computational methods to simulate and predict the behaviour of floodwaters under different conditions. The main purpose of flood modeling is to assess flood risks, provide early warnings, and develop effective flood control strategies. These models can simulate the flow of water across land surfaces, estimate flood coverage, and evaluate the impact of various flood management techniques. Flood modeling typically considers various factors such as rainfall, river flow, topography, land use, and climate to predict flood behavior.

There are several types of flood models available, each designed for different aspects of flood prediction and management. Some commonly used models include the Hydrologic Engineering Center Hydrologic Modeling System (HEC-HMS), Hydrologic Engineering Center River Analysis System (HEC-RAS), Storm Water Management Model (SWMM), FLOOD-FLUX, and RiverWare. In this study, HEC-HMS was selected for flood modeling due to its ability to simulate hydrological processes comprehensively, its ease of use, flexibility, and low cost. The model's compatibility with GIS, its support for various hydrological methods, and its proven success in real-world applications make it a reliable and popular choice for many flood modeling situations.

2.13.1 Rainfall–runoff model: HEC-HMS Model

Flooding is a frequent natural disaster in Malaysia, causing significant damage. An accurate flood forecasting system is crucial for improving preparedness, reducing property damage, saving lives, and supporting rescue efforts. One of the key strategies to lessen the impact of flood disaster is by flood modelling, which is especially beneficial in flood risk management and decision making (Azad et al., 2019). Researchers worldwide have developed numerous rainfall-runoff models to provide the most accurate predictions for rainfall-runoff processes. In this study, HEC-HMS model version 4.9 will be utilized. The HEC-HMS software, developed by the US Army Corps of Engineers, simulates precipitation and runoff processes within river basin systems, specifically designed to model the precipitation-runoff dynamics of dendritic watershed systems.

Various data sources are used in rainfall-runoff modeling, including soil type, digital elevation models (DEMs), and land use land cover (LULC) data (Ramly and Tahir, 2016; Sahu et al., 2023). The HEC-HMS model offers multiple infiltration loss parameterizations, but only the gridded curve number (CN) method allows for spatially distributed infiltration calculations (Chu and Steinman, 2009). Infiltration capacity is represented by a parameter known as the curve number (CN), which is derived from the Soil Conservation Service (SCS).

The CN method is used to estimate storm runoff in an area based on factors such as land use, soil type, land cover, and hydrologic soil group (Mishra and Singh, 2013). Soil groups are categorized according to the soil's type and infiltrability. The infiltration loss method is based on empirical equations that divide rainfall into infiltration and runoff components. In this study, the Soil Moisture Accounting (SMA) loss method in HEC-HMS was combined with canopy and surface methodologies to model infiltration losses as shown in Figure 2.10. The canopy represents the presence of vegetation within a sub-basin and is primarily used for continuous simulations in HEC-HMS. All rainfall is trapped by the canopy until its storage capacity is reached.

After passing through the canopy, excess precipitation reaches the soil surface. The surface method in HEC-HMS represents ground depressions where water collects once the soil's pores are filled to its field capacity. Runoff occurs when the precipitation rate exceeds the soil's infiltration rate and the storage in these depressions is depleted. The values for canopy and surface storage were determined through the analysis of land use and DEM maps.

HEC-HMS is an advanced hydrologic modeling software that offers a good balance between moderate processing time and reasonable accuracy, in contrast to more complex hydrodynamic models. Rainfall-runoff models help improve our understanding of hydrological processes, from the atmosphere to surface water systems, by providing solutions through simulation. Due to the complexity of hydrologic systems, advanced methods are required to address key tasks in engineering hydrology. The primary goal of a rainfall-runoff model is to study these processes and integrate the necessary inputs to generate the desired outputs. It serves as an approximation of the actual system, using available tools to simulate measurable hydrologic processes.

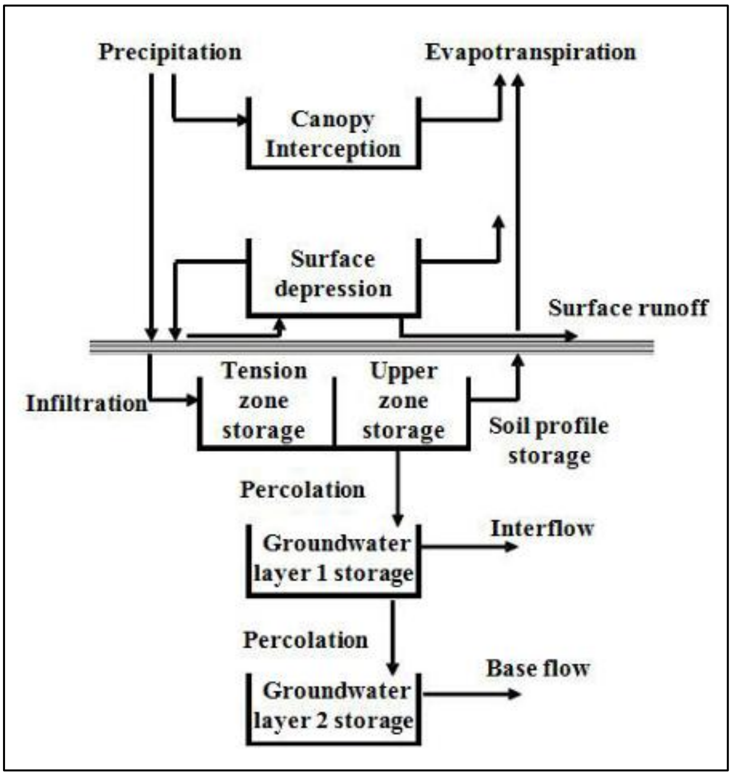

Figure 2.10 HEC-HMS Model Structure (Wallner et al., 2012)

2.13.2 Reviews on HEC-HMS Model Application

The HEC-HMS has been widely adopted in hydrological research due to its conceptual framework, deterministic structure, and semi-distributed modeling approach. Its ability to simulate direct discharge from precipitation events has made it particularly valuable in flood modeling and watershed-scale analysis. Numerous international studies have demonstrated the model’s adaptability; however, a critical evaluation reveals both its strengths and limitations in practice.

One of the primary strengths of HEC-HMS is its successful integration with other modeling tools and spatial analysis platforms. For example, Barbosa et al. (2019) applied HEC-HMS alongside HEC-RAS and Geographic Information Systems (GIS) to analyze the floodplains of the Zab Besar River in Turkey, reporting high correlation after calibration and validation. Similarly, Martin et al. (2012) combined HEC-HMS with HEC-GeoHMS and ArcMap to estimate surface runoff, showcasing the model’s compatibility with spatial datasets and tools. These studies highlight the model’s flexibility in diverse geographic contexts and its utility in generating accurate hydrological predictions when properly calibrated.

Nevertheless, several limitations emerge when analyzing these applications more critically. In regions where calibration data are scarce or of low quality, the model's performance often deteriorates. This is evident in the work of El Afandi et al. (2013), who applied HEC-HMS to the Sampean Baru basin in Indonesia, yielding a negative Nash-Sutcliffe Efficiency (NSE) value of -0.2. Such a value indicates that the model performs worse than a simple average of observed flows, suggesting poor model fit. Similarly, in the Bantimurung sub-watershed study, despite integrating soil texture maps and GIS tools, only moderate R^2 and NSE values (0.595 and 0.456 respectively) were achieved reinforcing concerns about data limitations and the need for more rigorous calibration (Rizal et al., 2023).

Further complexities arise in studies involving remote sensing data, especially in ungauged or data-scarce basins. Sapountzis et al. (2021) evaluated the effectiveness of satellite-based precipitation datasets such as GPM-IMERG in predicting flash flood events. While rain gauge-calibrated models provided more reliable outputs, uncalibrated satellite data failed to capture peak discharges accurately. Though regression-based extrapolation improved performance ($R^2 > 0.65$), this method introduces its own uncertainties and assumptions, which were not fully addressed in the reviewed studies. These findings underscore the necessity of combining ground-based observations with remote sensing to enhance model accuracy, particularly for flood risk assessments in ungauged catchments.

Additionally, while studies such as Oleyiblo and Li (2010) report satisfactory results from HEC-HMS in Chinese basins, the review lacks critical engagement with the model's internal assumptions, including those related to baseflow estimation, infiltration processes, and temporal resolution of rainfall inputs. These factors can significantly affect the model's realism, especially in regions with complex hydrological responses or highly variable climatic conditions.

Furthermore, several previous studies have highlighted the effectiveness of the HEC-HMS model for flood simulation. In a 2019 study, Ademe et al. (2020) used the HEC-HMS model to predict flooding in the Lake Tana basin watershed in Ethiopia, finding that the model successfully replicated flood events. In their assessment of drainage structure failure at the Akaki river crossing, Guduru et al. (2023) concluded that HEC-HMS accurately estimated design discharge. Additionally, Gunatilakhe et al. (2020) conducted an event-based streamflow simulation analysis of the Seethawaka

River in Sri Lanka. Their findings indicated that the model developed in their study effectively simulated peak discharges and the timing of their occurrence, supported by statistical parameters and graphical analysis. However, these studies often focus on model output without addressing underlying uncertainties, input data quality, or calibration methods. Moreover, the lack of comparison with alternative or data-driven models restricts a broader assessment of HEC-HMS's relative strengths.

Malaysia is a tropical country with high humidity and copious rainfall, amounting to an average of 2000–4000 mm annually. In certain years, the rainfall can exceed this range, particularly during extreme rainfall events that often lead to flooding in various regions during the monsoon seasons (Loi, 1996). Given this, it is essential to develop a policy for evaluating flood discharge. Runoff is heavily influenced by various factors, so selecting the most suitable model with minimal input data requirements, a straightforward structure, and realistic accuracy is crucial. In a study by Ramly and Tahir (2016), the HEC-HMS model was used, along with rain gauge and DEM data, to simulate the rainfall-runoff process in the upper Klang-Ampang River basin, a flood-prone area near Malaysia's capital. The results demonstrated a reasonable level of accuracy, as evidenced by a Nash-Sutcliffe coefficient of 0.86. Nevertheless, while the NSE suggests strong agreement between observed and simulated flows, the study lacks discussion on model limitations, calibration methods, or data sensitivity, which are essential for evaluating the model's reliability in varied flood scenarios.

Additionally, Adnan et al. (2014) highlighted the significant impact of land use changes on flood behavior in the River Kelantan catchment, noting increases in peak flow and runoff volume due to urban and agricultural expansion. Their findings underscore the importance of integrating land use planning with hydrological modeling to support flood mitigation, particularly in monsoon-prone regions like Malaysia. However, while the study identifies trends in runoff behavior, it does not quantify the modeling uncertainties or evaluate the hydrological model used, limiting its predictive application.

In a more technical comparison, Sukairi et al. (2023) evaluated HEC-HMS against the RRI model in the Sungai Lebir basin. HEC-HMS consistently outperformed RRI in both calibration and validation stages, showing strong NSE values (e.g., 0.858 and 0.821) and better streamflow accuracy. However, the extreme negative NSE value (-9.806) during one calibration phase raises concerns about parameter sensitivity and model setup. Despite post-optimization improvements, this variability suggests a need for careful calibration and validation procedures when applying HEC-HMS. Notably, several studies have observed a tendency for HEC-HMS to underestimate peak flows, which poses a risk in flood-prone areas where accurate peak prediction is critical (Romali et al., 2018; Ramly et al., 2020; Azam et al., 2021). This systematic underestimation highlights a key limitation of the model and signals the importance of using supplementary validation methods or conservative design margins in flood assessments.

In summary, while HEC-HMS has proven suitable for simulating streamflow in Malaysia, its application in flood analysis requires caution due to known tendencies to underpredict peak flows and the model's sensitivity to calibration quality. Further comparative studies and model refinement are essential to ensure reliable flood forecasting under changing land use and climate conditions.

2.14 Summary

Most previous studies have relied on gauged rainfall data or satellite imagery for rainfall estimates and forecasting, as shown in Table 2.5. While satellite-based precipitation estimation provides near-global coverage and long-term datasets, it has limitations in resolving small-scale convective structures and intense tropical rainfall. In contrast, radar-based rainfall classification offers high spatial and temporal resolution and is particularly effective for identifying convective rain cells, but its coverage is limited and susceptible to measurement errors. Nevertheless, there is limited research on using machine learning, particularly ANN and feature extraction, for rainfall estimation from radar reflectivity. The application of these techniques for detailed pixel-based analysis of radar reflectivity images, especially under the unique conditions influenced by the tropical monsoon region, has not been explored. Extracting features of convective and stratiform rainfall from radar reflectivity, as well as optimally developing a rainfall estimation model using machine learning techniques based on radar reflectivity image data, presents both a challenging and novel task.

Table 2.5

Summary of Literature Review

References	Findings/Methods
Huang et al., (2019)	There are notable differences in the rain cell development mechanisms and thermodynamic processes between convective and stratiform precipitation.
Yuter and Houze, (1997)	Convective rainfall is primarily driven by strong, narrow updrafts (5–10 ms^{-1} or higher), whereas stratiform rainfall is influenced by weaker mesoscale ascents (<3 ms^{-1}).
Kirsch et al., (2019)	The use of stratiform and convective Z–R relationships reduce the estimation error between 30% and 50%.
Penide et al., (2013)	Less than 3% of stratiform rain rates are above the classical threshold of 10mm h^{-1} and 90% of all the stratiform points are associated with a rain rate below 4.6mm h^{-1}
Jaiswal et al., (2020)	Attempted to differentiate between convective and stratiform events based on parameters that have been obtained from Tropical Rainfall Measuring satellite (TRMM) data.
Rigo and Llasat, (2004)	A grid point in Z field is identified as the convective center if its value is larger than 40 dBZ or exceeds.
Powell et al., (2016)	Introduced a new approach that can identify shallow convection embedded within large stratiform regions, and those isolated shallow and weak convections.
Yin et al., (2023)	Estimating rainfall intensity using an image-based deep learning model.
Orescanin et al., (2021)	Developed one deep learning algorithm which adopts a Bayesian form of Residual Networks (ResNet) architectures to extract the information from PMW observations vectors and identify convective and stratiform structural rainfall type.
Nielsen et al., (2024)	Merging weather radar data and opportunistic rainfall sensor data to enhance rainfall estimates.

Choi and Kim (2020)	Proposed rain-type classification from microwave satellite observations using deep neural network segmentation
Seela et al., (2021); Chen et al., (2022); Teng et al., (2022); Wu et al., (2022)	Studies have classified the precipitation into stratiform, convective and transition regions based on DSD characteristics retrieved from polarimetric radar which may obtain extra information about raindrops' size, shape and orientation, through transmitting and receiving electromagnetic waves along the horizontal and vertical directions
Cramer et al., (2017)	Radial Basis Neural Network (RBNN) and Support Vector Regression (SVR) are among the two top machine learning techniques that produce good rainfall prediction results using data from around Europe and USA.
Poornima and Pushpalatha, (2019); Aswin et al., (2018); Kumar et al., (2022); Caseri et al., (2022); Yao et al., (2020); Cao et al., (2022)	Long Short-Term Memory (LSTM) is a variation of Recurrent Neural Network and has been applied to predict rainfall in India and worldwide with data from Global Precipitation Climatology Project (GPCP) and satellite data.
Yin et al., (2023); Weesakul et al., (2018); Yang et al., (2019); Han et al., (2021); Wei and Hsieh, (2020); Yo et al., (2021); Mahdianpari et al., (2018); Li et al., (2023); Huangfu et al., (2024)	Deep Convolutional Neural Network (DCNN) shown very good rainfall forecasting result in rainfall estimation from different country.
Sehad et al., (2017)	Implement novelty in SVM based technique to improve rainfall estimation over the Mediterranean region.
Lu et al., (2023)	Studied on QPE in the Tianshan mountains based on

	machine learning.
Karklinsky and Morin, (2006)	Studied focuses on spatial features of convective rain cells in southern Israel where the climate ranges from Mediterranean to hyper-arid.
Peleg and Morin, (2012)	Extract the details about rain cell characteristics from high-resolution weather radar data and examines the spatiotemporal characteristics of convective rain cells over the eastern Mediterranean.
Chen et al., (2019)	Introduced an innovative machine learning framework for remote sensing precipitation estimation to produce rainfall estimation using satellite data.
Mekonnen et al., (2023)	Studied the accuracy of satellite and reanalysis rainfall estimates over Africa.
Sadeghi et al., (2019)	Applying convolutional neural networks (CNNs) together with the infrared (IR) and water vapor (WV) channels from geostationary satellites for estimating precipitation rate.
Garba et al., (2024)	Studied the performance evaluation of satellite-based rainfall estimation across climatic zones in Africa.
Wang et al., (2021)	Examines the capability of three statistical and machine learning methods to rainfall forecasting over the tropical pacific ocean using Global Precipitation Measurement (GPM) satellite radar.

Furthermore, the effectiveness of using the novel radar rainfall estimation technique in flood forecasting models has not yet been explored. Most previous studies applying the HEC-HMS model have relied on extensive rain gauge networks for time series data input (Ramly et al., 2022). However, studies comparing simulated flow outputs using both rain gauge and radar data are rare, particularly in Malaysia, despite several initiatives on radar QPE research (Wardah et al., 2011; Wardah et al., 2012). Moreover, the integration of gridded radar QPE data with the HEC-HMS model has not been widely explored. This research aims to address these gaps, focusing on evaluating these factors in the context of hydrologic analysis for Malaysia.

CHAPTER 3
RESEARCH METHODOLOGY

3.1 Introduction

This chapter reviews the detailed methodology and procedures for the study, covering the background of the study area, data collection methods, and the overall methodology.

Firstly, the chapter begins with the acquisition and processing of both weather radar and rain gauge data. The Malaysian Meteorological Department (MMD) provided the Radar Integrated Nowcasting System (RaINS) for weather radar data, while the Department of Drainage and Irrigation (DID) supplied the rain gauge datasets for 2021 until 2023. The chapter also explains the derivation of feature extraction algorithms for radar reflectivity images, considering different types of rainfall. Following that, this chapter describes the methodology that employs a machine learning classifier to categorize convective and stratiform rainfall based on extracted features of radar reflectivity images. An optimization approach was implemented to develop new Z/R relationships based on the classified rainfall types.

Next, the chapter describes the development of a radar-based QPE model using the artificial neural network (ANN) technique. The final part of the methodology focuses on applying the radar-based rainfall estimation technique in a flood forecasting system using HEC-HMS. Figure 3.1 concisely illustrates the overall methodology of the research.

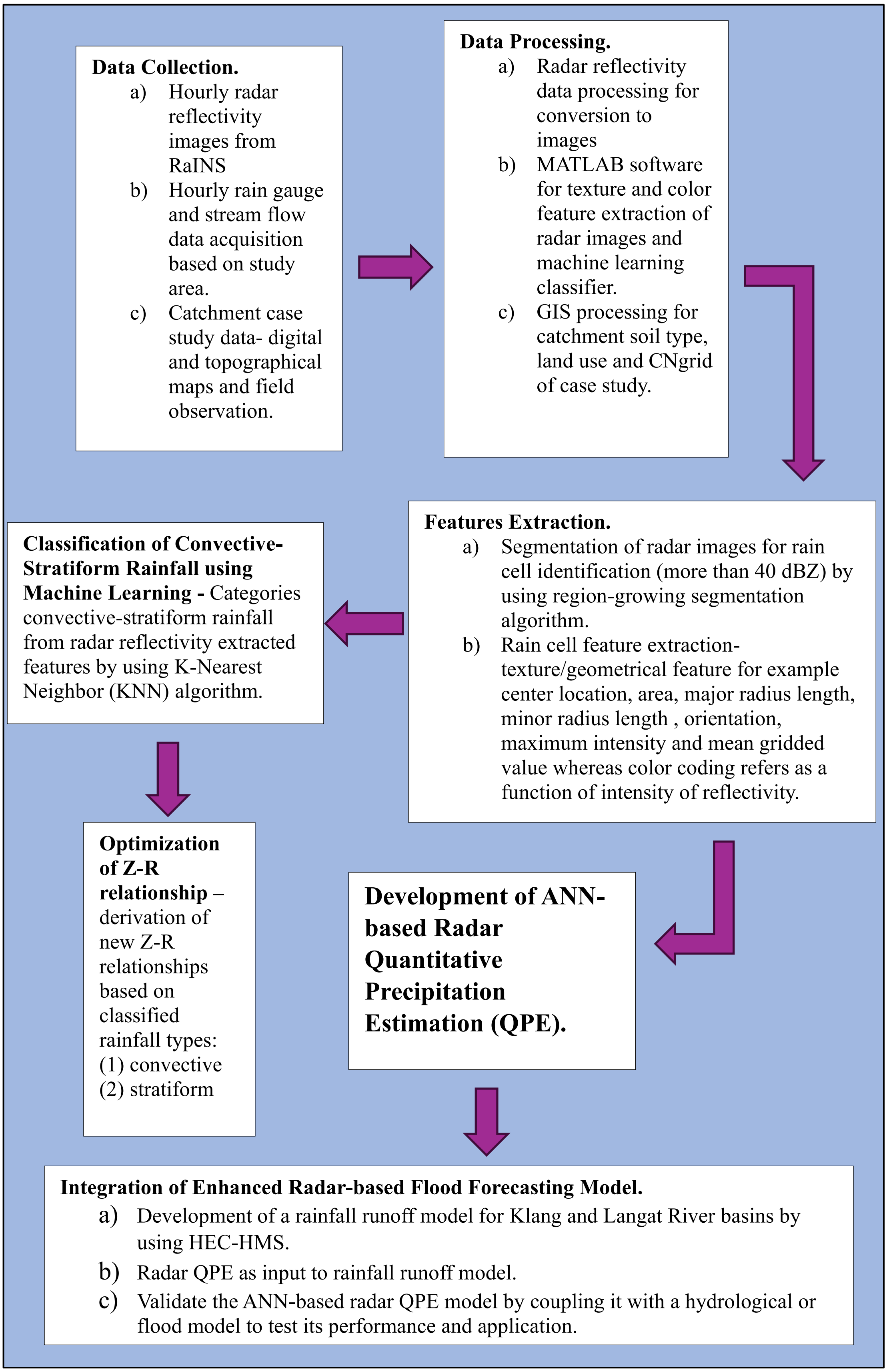

Figure 3.1 Research Methodology

3.2 Case Study Area

Malaysia is located in Southeast Asia and has a humid tropical climate. It is situated near the equator, with latitudes ranging from 1° to 7° north and longitudes from 99° to 120° east. Malaysia receives significant amounts of rainfall due to localized thunderstorms, as well as extremely high convective rainfall resulting from its maritime location.

Malaysia experiences two monsoon seasons that affect rainfall patterns in Peninsular Malaysia: the Northeast Monsoon (NEM), from November to March, and the Southwest Monsoon (SWM), from May to September (Xiang, 2020). During the SWM, Peninsular Malaysia typically experiences drought, which is considered a dry phase. In contrast, the NEM is the primary period of intense rainfall on the east coast of Peninsular Malaysia, including Johor, Kelantan, Terengganu, and Pahang. However, the western part of Peninsular Malaysia encounters substantial rainfall during the intermonsoon season, which spans from April to October (Sang et al., 2015). As a result of convective precipitation with extreme intensity, urban areas may experience flash flooding.

In addition, tropical cyclones can occasionally trigger flooding and landslides in Malaysia. A significant flood disaster occurred on December 17, 2021, when nearly every state in Peninsular Malaysia, as well as those on both the eastern and western coasts, experienced rainfall for four consecutive days. Selangor, the central state that includes Kuala Lumpur, was one of the most severely affected by the floods. The main reason for the drastic shifts in weather in the Klang Valley is the ongoing impact of global climate change. Typhoon Rai and Tropical Depression 29W intensified the effects of the monsoon, causing rainfall to extend further west than usual. This may have contributed to the 2021 flood disaster.

The Langat and Klang River basins were selected as study locations due to the significant flood disaster that occurred in December 2021, as illustrated in Figure 3.2. This tragedy highlighted the importance of remaining vigilant and prepared for floods, especially as global climate change significantly impacts Malaysia's weather patterns.

The Langat River valley is located in the southern and southeastern parts of Selangor, between latitudes 02°40′152″ N and 3°16′15″ N, and longitudes 101°19′20″ E to 102°1′10″ E. The Langat River flows through an area of approximately 1,815 km^2 and has multiple tributaries, the main ones being the Beranang, Lui, and Semenyih rivers. It is 78 km long and has a catchment area of 2350 km^2. The average annual rainfall and evapotranspiration in this basin are 2145 and 1500 mm, respectively, indicating a tropical climate. Despite being one of Malaysia's most significant catchments, the basin presents an advantageous case study for an integrated water resource policy system that involves various stakeholders and decision-makers, particularly concerning issues of flooding, water pollution, and water scarcity.

On the other hand, the Klang River Basin lies between latitudes 2°55'N and 3°25'N and longitudes 101°20'E and 101°50'E. It covers approximately one-third of Selangor State and has a catchment area of 1,288.4 km^2 on the western coast of Peninsular Malaysia. The Klang River basin includes Kuala Lumpur, one of Malaysia's most important cities, as well as the highly urbanized and industrialized towns of Petaling Jaya, Shah Alam, and Klang. This region has recently experienced significant expansion and growth. Periodic flooding has long been a serious impediment to efficient land use and living conditions in Klang. Approximately 14% of the Klang Valley's administrative area (234,347 ha) is vulnerable to flooding (Kim Loi, 1996). The basin experiences roughly 1900-2600 mm of rainfall each year, with the majority falling during the NEM, the SWM, and the two inter-monsoon months (April and October). Consequently, whenever there is a prolonged period of heavy rainfall in the catchment area, there is a risk of flooding in the Klang River Basin (Sezer et al., 2011).

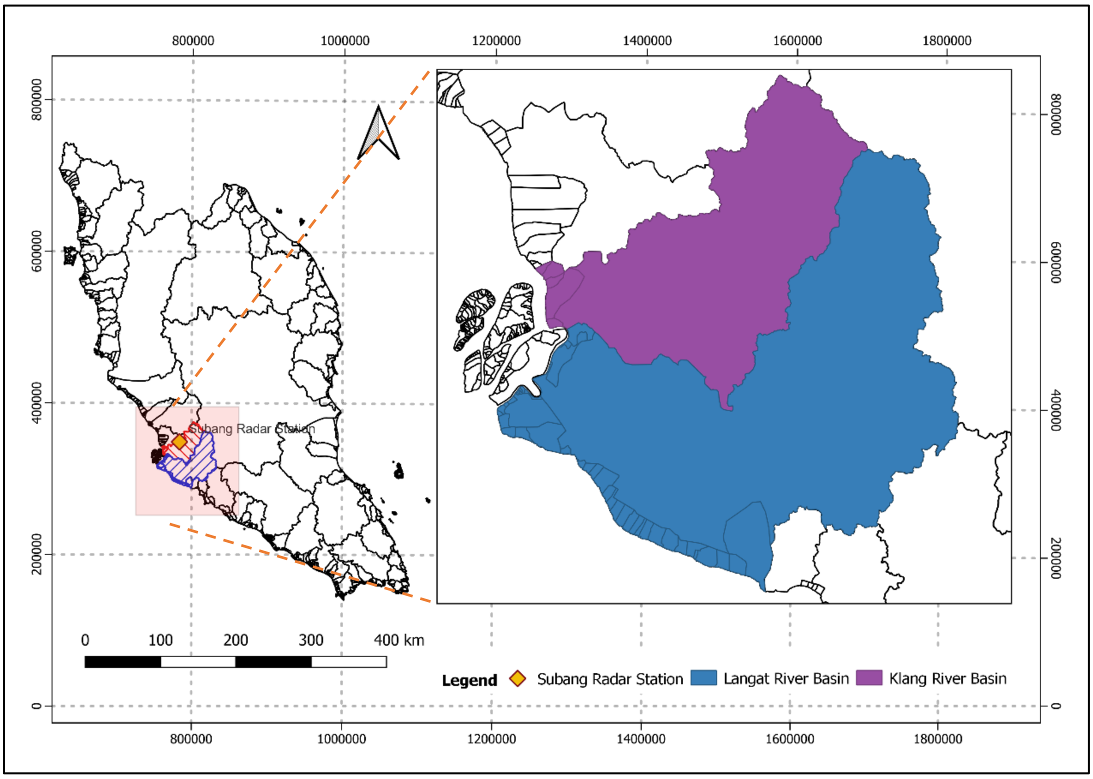

Figure 3.2 Langat and Klang River Basin Map

3.3 Data Acquisition and Processing

This section outlines the methods used to acquire and process the secondary data for the study. Weather radar data were sourced from the Malaysian Meteorological Department (MMD), while hydrological data, including rainfall data from rain gauges and streamflow, were provided by the Department of Irrigation and Drainage (DID). Additional data, such as digital and topographical maps related to the catchment case study, were obtained from relevant websites.

Several software tools and applications were utilized for data acquisition, processing, and analysis, such as Quantum Geographic Information System (QGIS), MATLAB, and HEC-HMS. The following sections describe in detail the radar data acquisition and processing.

3.3.1 Weather Radar

The nearest Doppler weather radar to the research region is located at Latitude 3.120 °N and Longitude 101.55 °E, with an altitude of 32 m, near Subang Airport in

Selangor, as illustrated in Figure 3.3. The Subang Weather Radar employs an S-band radar with a maximum horizontal coverage of 300 kilometers. Initially, radar rainfall intensity could not be directly measured from the data. These raw datasets were obtained from the Malaysian Meteorological Department (MMD) at ten-minute interval. The LINUX operating system transforms the raw data into a readable text format in a.txt file, converting the unit of radar reflectivity from decibels to millimeters per hour.

The raw radar data are stored in a format known as Constant Altitude Plan Position Indicator (CAPPI). Since each CAPPI file represents a 10-minute scan, six files are required to generate one hour of radar-based rainfall data. The 10-minute interval radar data were converted to hourly rainfall in a few steps. First, radar reflectivity (Z) from each scan was converted to rainfall rate (R) (mm/h) using the Marshall & Palmer Z-R relationship (as adopted by the Met Malaysia). Next, the mean hourly radar rainfall is calculated by converting each 10-minute radar rainfall intensity (mm/h) into rainfall depth by multiplying it by $\frac{10}{60}$hour, summing the six 10-minute depths within the hour to obtain the hourly rainfall total, and, if required, expressing this total as the mean hourly rainfall intensity (mm/h), which is numerically equal to the hourly rainfall depth for a one-hour period. The final hourly rainfall data were checked for quality and, if needed, adjusted using rain gauge measurements.

Figure 3.3 Subang Doppler Radar (Tahir et al., 2022)

3.3.1.1 Radar Integrated Nowcasting System (RaINS)

Radar composite products, referred to as the Radar Integrated Nowcasting System (RaINS), are produced by mathematically combining data from different radars stations. The products for Peninsular Malaysia are derived by interpolating data from 18 radar stations across the Peninsula into a single grid using the inverse distance weighted (IDW) technique, as explained in Chapter 2. The maximum re-gridded reflectivity data from the 18 radar stations constitutes the final product, which is obtained from the weather radar system of the Malaysian Meteorological Department (MMD) (Yik et al., 2018). The radar reflectivity is converted to rain rate using the Marshall-Palmer equation and used as the rainfall input.

The uncalibrated RaINS data used for this study were collected between December 2021 and August 2023. The selected data were screened for outliers and missing values. Outliers were identified when the rainfall values were too high, too low, or clearly unrealistic compared to nearby stations. These abnormal values were either corrected using data from nearby stations or removed if they could not be fixed. For missing values, small gaps were filled using interpolation or by referring to the nearest reliable station. If the missing periods were too long to estimate accurately, those parts of the data were excluded from the analysis. The chosen rainfall events represent a wide range of annual precipitation quantities, including an unprecedented flood disaster. RaINS data are provided in both Microsoft Excel and ASC file formats, with the ASC file representing radar rainfall images. The RaINS data in Excel format consist of radar rainfall that has been computed to the nearest pixels of the corresponding rain stations using Python (Tahir et al., 2022). These data are presented as hourly rainfall measurements, categorized by rainfall station numbers, before the selection of specific stations. As for the ASC file data, the real-time rainfall observations is shown in Figure 3.4. The radar data in ASC format (Figure 3.5) are then processed using QGIS software to prepare the input needed for this analysis.

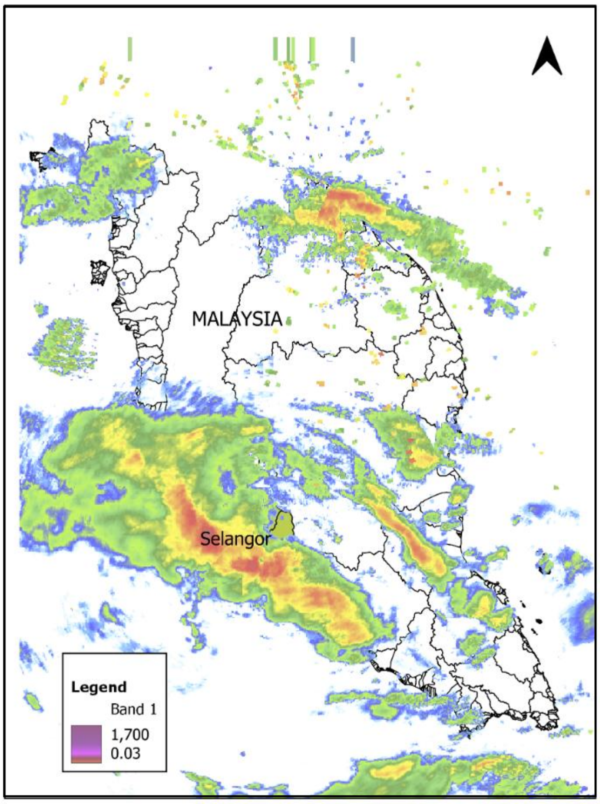

Figure 3.4 Radar display

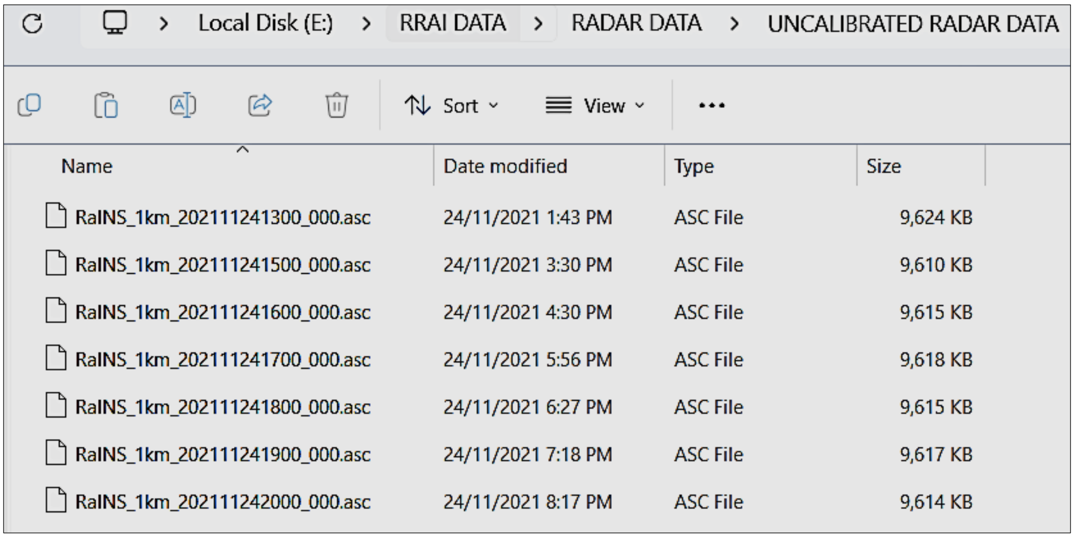

Figure 3.5 File Extension in ASC format

3.3.1.2 Radar Reflectivity Image Processing

The radar reflectivity image from MMD covers the entire area of Malaysia. Therefore, in this study, the first step is to extract the radar reflectivity image for the specific regions of the Klang and Langat river basins using QGIS software, as shown in Figure 3.6.

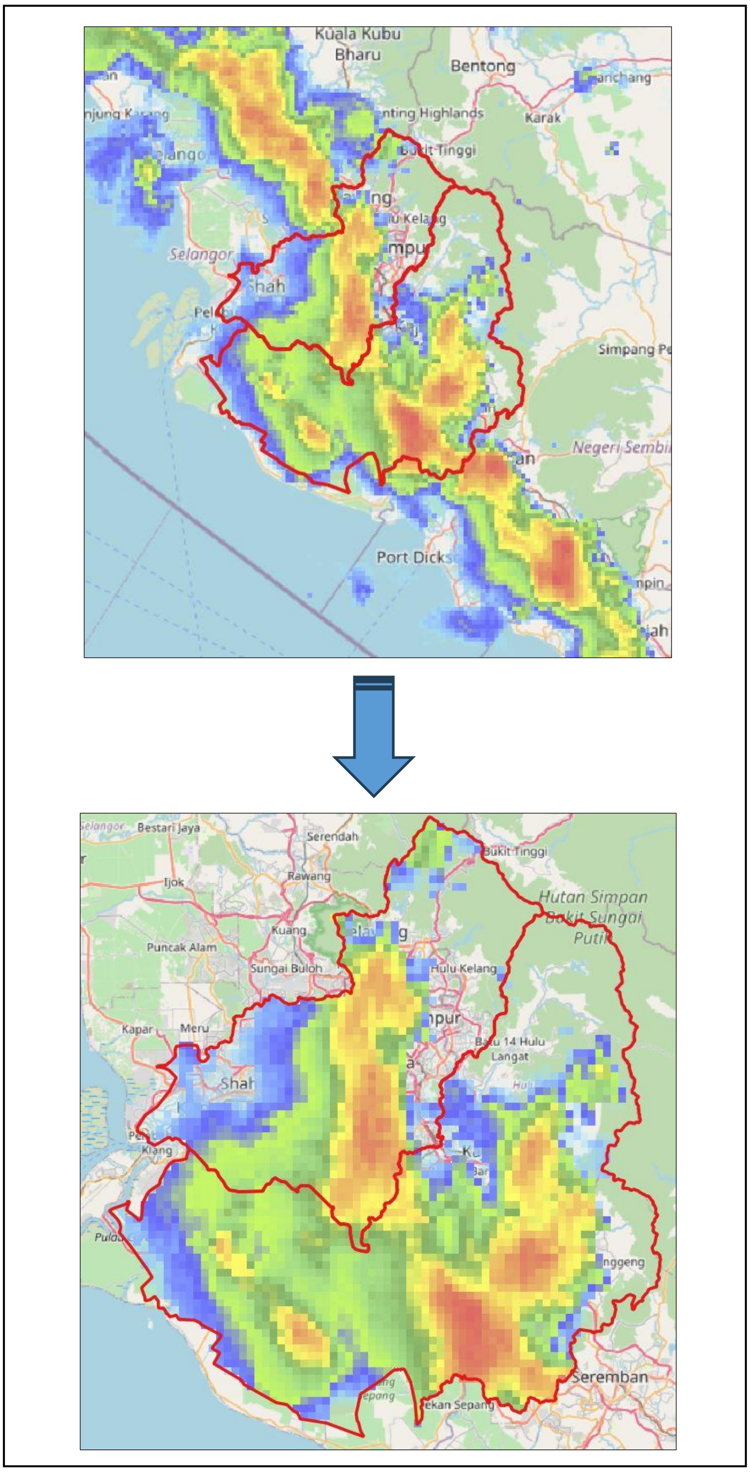

Figure 3.6 Radar Image Delineation for Klang and Langat River Basin

3.3.2 Rainfall and Streamflow Data

The selection of rainfall stations was based on both the availability of rain gauge data and RaINS data, which were managed by the DID and MMD, respectively. This means that only rainfall stations with data available at the same temporal and spatial scale for both the rain gauges and RaINS radar were selected for this analysis. Rainfall data were collected from 38 rain gauge stations located in the Klang and Langat River Basins, and hydrological data, such as streamflow data, were obtained from the Hydrology Division of the DID. The rainfall stations used in this study are listed in Table 3.1 and illustrated in Figure 3.7.

Table 3.1
List of Rainfall Station for Klang and Langat River Basin

No	Station_Name	Longitude	Latitude
1	Sg Ampang Kg Lembah Jaya	101.7909	3.148075
2	Sg Damansara Batu 3	101.5539	3.075611
3	Sg. Klang di Bandar Klang	101.4448	3.048056
4	Bukit Antarabangsa	101.7727	3.183694
5	Sg. Gombak di Batu 10	101.7267	3.267279
6	Sg Damansara Kg Melayu Subang	101.5409	3.150055
7	Sg. Penchala di Kg. Gandhi	101.6214	3.076444
8	Kg. Rantau Panjang	101.4132	3.049139
9	Kota Damansara	101.578	3.156392
10	Puncak Antheneum	101.7658	3.182472
11	Sg Penchala Jalan 222	101.6344	3.09652
12	Ayer Hitam Puchong	101.5804	2.979611
13	Sg Rasau Pulau Meranti	101.6394	2.969105
14	IOI Puchong Jaya	101.6214	3.04275
15	Sg. Klang di Puchong Drop	101.5974	3.019527
16	Selayang Baru	101.6663	3.250222
17	Sg. Batu di Batu Caves	101.6802	3.236266
18	Taman Sentosa	101.4701	3.001619
19	Taman Botani	101.4976	3.093046
20	Sg. Kayu Ara di Taman Mayang	101.5964	3.112277

21	Sg. Klang di Taman Sri Muda	101.5345	3.037722
22	Sg. Damansara di TTDI Jaya	101.5542	3.096944
23	Sg. Langat di Batu 12	101.7978	3.093388
24	Sg. Langat di Batu 15	101.8347	3.136888
25	Sg. Langat di Bukit Changgang	101.6419	2.813472
26	Sg. Langat di Dengkil	101.6814	2.855777
27	Genting Peres	101.9232	3.14025
28	Sg. Langat di Jenderam Hilir	101.7283	2.896966
29	JPS Hulu Langat	101.7637	2.936064
30	Sg. Langat di Pekan Kajang	101.7861	2.992694
31	Sg. Balak di Kg. Baru Balakong	101.7488	3.027667
32	Sg. Semenyih di Kg. Pasir	101.8661	3.013444
33	Sg. Langat di TNB Pangsun	101.8759	3.209638
34	Pekan Banting	101.5085	2.810653
35	Empangan Semenyih	101.8806	3.07861
36	Sg. Langat di JPS Sg. Manggis	101.5428	2.825278
37	Sg. Semenyih di Rinching	101.8219	2.915194
38	Ladang Bute	101.7473	2.75341

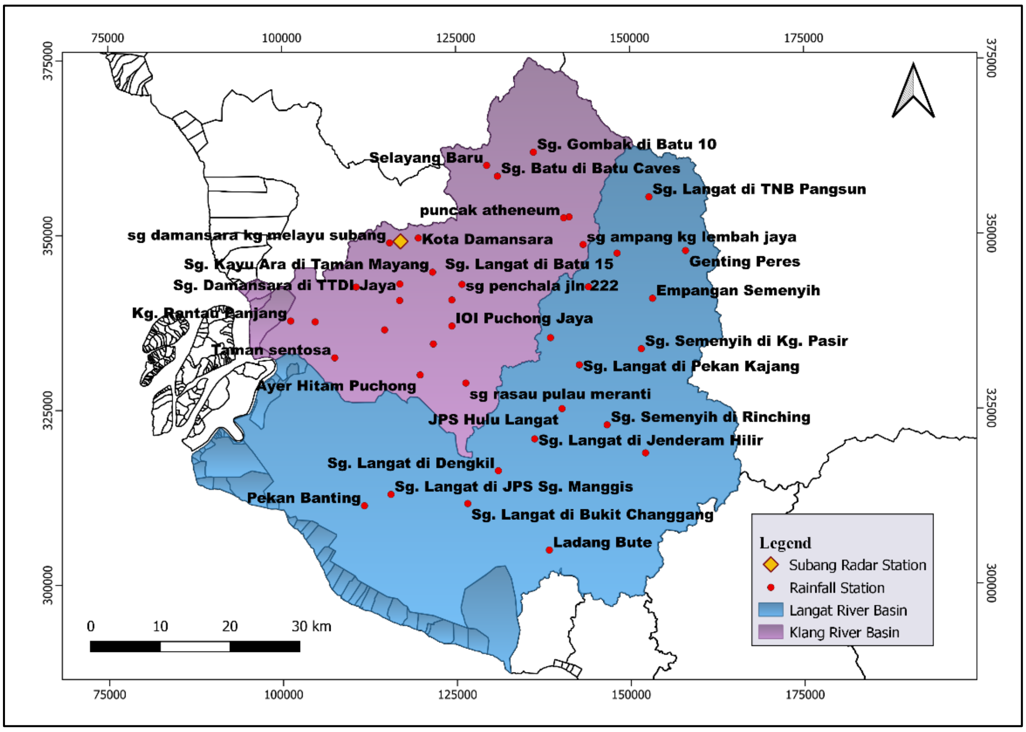

Figure 3.7 Raingauge Station in Klang and Langat River Basin

3.4 Mean Areal Rainfall Estimation

Mean areal rainfall estimation is used to determine the average rainfall depth across a specific region. This is crucial for applications such as hydrological modeling, water resource management, flood forecasting, and climate studies, as it provides a more comprehensive representation of precipitation over a large area, rather than relying on data from a single point of rain gauge. Essentially, it helps researchers gain a better understanding of rainfall patterns and their impacts on a given area.

There are three primary methods used to calculate the average depth of rainfall over a specific catchment area for any given time period. These methods are arithmetic mean method, Thiessen polygon method, and isohyetal method. Each method offers a unique approach for estimating the average rainfall, considering factors such as spatial distribution, rainfall patterns, and the location of rainfall measurement stations. The arithmetic mean method assumes an equal weight for all stations, while the Thiessen polygon and isohyetal methods consider the spatial variability of rainfall by using geometric or contour-based techniques to better reflect local conditions.

The Thiessen polygon method was chosen in this study because it provides better accuracy compared to the arithmetic mean method and is simpler than the isohyetal method (Kumar et al., 2021). The Thiessen polygon method assumes that each precipitation gauge is assigned a different weight, unlike the arithmetic method where all gauges are treated equally.

$$P_{avg} = \sum_{i=1}^{m} w_i P_i \tag{3.1}$$

where $\sum_{i=1}^{m} w_i = 1$. The Thiessen polygon method simplifies to the arithmetic mean method if $w_i = \frac{1}{m}$. In the Thiessen polygon method,

$$w_i = \frac{A_i}{A_T} \tag{3.2}$$

where;

A_T = Total basin or watershed area,

A_i = Area defined by Thiessen polygons, To determine A_i, start by joining the locations of adjacent stations with straight lines. Next, draw the perpendicular bisectors to these lines, as shown in Figure 3.8. Then, define the polygons that enclose each station and calculate the area of each polygon.

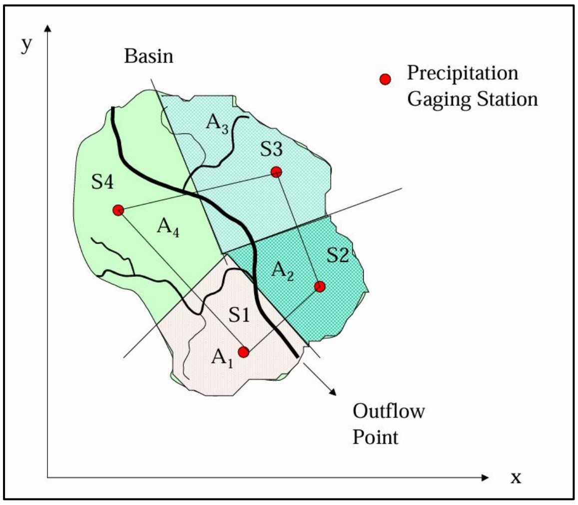

Figure 3.8 Thiessen Polygon Method (Olawoyin and Acheampong, 2017)

3.5 Feature Extraction of Radar Images

Feature extraction is a critical step in machine learning and data analysis, where the goal is to identify and isolate the most relevant information from raw data. In the case of image files, this process involves converting the visual data into numerical features that can be processed by machine learning algorithms. By focusing only on the most significant features, feature extraction helps to reduce the complexity of the model, making it easier to interpret and faster to compute. This selection process also enhances the performance of machine learning algorithms by eliminating noise and irrelevant data. The extracted features are then used to build a more concise and informative dataset, which can be applied to a wide range of tasks, including classification, clustering, and prediction. MATLAB software is utilized in this process, with part of the script presented in Figure 3.9. In the context of this study, the results of the feature extraction from radar images will serve as the input for an ANN-based model, which will be used for rainfall classification, specifically distinguishing between stratiform and convective rainfall types.

```
close all;
I=imread('C:\MATLAB\PM1712212100.tif');
Ib=imbinarize(I,180/255);%threshold remove background;noise
Ih=imfill(Ib,'holes');% automatically remove holes by
region filling
Io=bwareaopen(Ih,40,4); %remove area pixel less than 40,by
4-connectivity
Il=bwlabel(Io,4);
nsegment=max(max(Il));%counted number of segments
Ir=label2rgb(Il);%different colour different segment
imshow(Ir);
s = regionprops(Il, 'Centroid');
hold on
for k = 1:numel(s)
    c = s(k).Centroid;
    text(c(1), c(2), sprintf('%d', k), ...
        'HorizontalAlignment', 'center', ...
        'VerticalAlignment', 'middle'); %labelling numbers
                                         for every segment
end
hold off
stats=regionprops(Il,'all'); %features for all statistics

%stats =
regionprops('table',Il,'Centroid',...'MajorAxisLength','Min
orAxisLength');
%centers = stats.Centroid;
%diameters = mean([stats.MajorAxisLength
stats.MinorAxisLength],2);
%radii = diameters/2;
%area=regionprops(Il,'Area');
```

Figure 3.9 MATLAB Script for Extracting Features from Radar Images

3.5.1 Image Segmentation

The identification of rain cells involves several steps, with convective rain cells being partially detected through the use of segmentation techniques. Each radar image, initially captured in polar coordinates, is transformed into a Cartesian grid where the resolution is set to 1.0 x 1.0 km² per pixel. This means each pixel in the radar image represents an area of 1 km × 1 km on the ground. This conversion enables the image to be segmented into distinct rain segments (clusters of pixels representing rain). The first step in this process is to convert the original radar image into a binary image, as shown in Figure 3.10. This binary representation highlights areas where rainfall intensity exceeds a predefined threshold, marking the locations of significant rainfall in two dimensions. The specific threshold used here is approximately 40 dBZ, which ensures that only the convective portion of the rainfall, characterized by higher intensity, remains for further analysis. This threshold has been widely adopted in previous studies, such as those by Rigo and Llasat (2004), Karklinsky and Morin (2006), Kyznarová and Novak (2009), Barnolas et al. (2010), and Peleg et al. (2018), among others, to isolate the convective rain cells from stratiform rain and improve the accuracy of rain cell identification.

Convective structures in radar images are identified based on their connectivity. To achieve this, the 'four nearest neighbors' algorithm is employed to define and configure the individual rain cells. According to this method, two convective pixels are considered part of the same convective structure if they are adjacent to each other either vertically (above or below), horizontally (to the right or left), or in the same plane. However, pixels that are diagonally adjacent are not considered connected, even if they share the same intensity or type. In this study, a total of 720 radar images were analyzed, resulting in the detection of 559 precipitation structures, 210 of which were identified as convective structures based on data availability. This approach allows for the effective isolation of convective rainfall areas, which are crucial for understanding the characteristics of rainfall in a given region (Féral et al., 2000; Barnolas et al., 2010).

Additionally, segments containing rain cells with an area smaller than 16 km^2 are excluded from further analysis. Since each pixel is 1 km^2, a rain cell would need to cover at least 16 pixels to be included in the analysis. This threshold is chosen to eliminate very small cells, which are often linked to anomalous radar echoes or noise, and to focus on the more significant and reliable rain cells. Furthermore, if any isolated pixels, or 'spurs,' are detected within the segmented areas, they are assigned a null value to avoid skewing the results. Alternative methods for segmenting and identifying rain cells can be found in the broader literature, as mentioned in Chapter 2. An example of the segmentation process is shown in Figure 3.10(e), where the rain cell segments are clearly delineated by different colors, highlighting the areas successfully identified as rain cells.

3.5.1.1 Accuracy assessment

The performance of the results is evaluated by comparing the estimated areal rainfall with the data obtained from rain gauges, using the arithmetic average method (3.3). This approach involves calculating the mean rainfall values across all local stations within the study area. This method is used in areas where rainfall is evenly distributed because it gives all stations equal weight regardless of their proximity or other variables.

$$\bar{P} = \frac{1}{n}\sum_{i=1}^{n} P_i \quad (3.3)$$

where $\bar{P}$ = average rainfall

P = rainfall value at individual station

i = individual station

n = number of stations

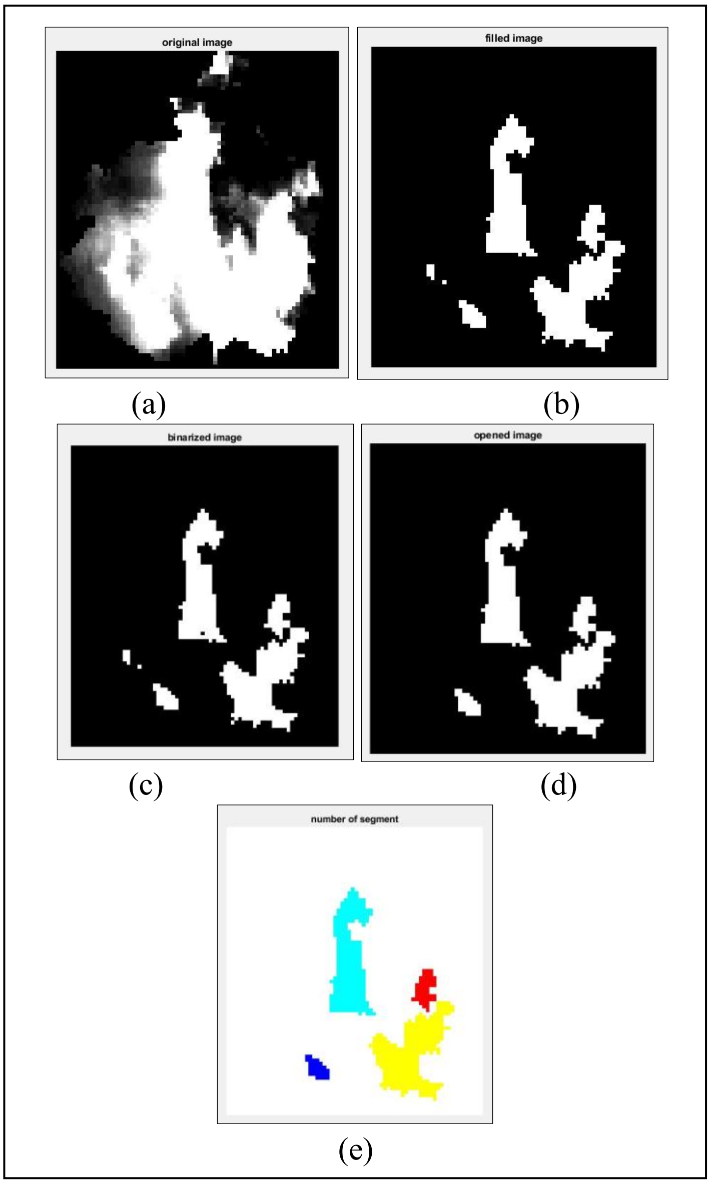

(a) (b) (c) (d) (e)

Figure 3.10 Description of the Segmentation Process, for the Event of 01 February 2023 at 17:00 UTC: (a) Reflectivity Radar Data Map in Tiff Format, (b) Binary Image, (c) Region Filling to Remove Holes Found in the Image, (d)Images Opened to Remove Pixels Less than 40 dBZ, and (e) Number of Rain Cell Segments Captured.

3.5.2 Rain Cell Features

The next step is the feature extraction procedure for the rain cells, where various characteristics of each segment are derived. In this study, convective structures are represented using ellipses. In weather radar applications, elliptical representations are preferred for connective and spatial structures because they align with the circular radar scanning geometry and effectively convey the continuity of precipitation fields (Saltikoff et al., 2019) . For each segment, an ellipsoid is fitted to the data, and the major and minor axes are determined. The major axis represents the longest path, which is measured from the center of the segment, while the minor axis is oriented perpendicular to the major axis. This approach allows for a better understanding of the shape and orientation of the convective structures (Peleg et al., 2018). Additional features of each segment include the central location of the ellipsoid, the area (in km²), the lengths of the major and minor radius (in km), and the cell orientation, which is defined by the major radial angle in degrees relative to the west-east direction (with positive angles measured counterclockwise). Moreover, the maximum and mean gridded intensities (in mm/h) are also extracted. Each grid cell represents an areal rainfall intensity value (mm/h) derived from radar reflectivity using a Z-R relationship. Maximum and mean gridded rainfall intensities were derived at each time step by spatial aggregation of radar-derived rain rates over the storm domain, following the methodology of Peleg et al. (2018). These characteristics are visualized in Figure 3.11, providing a detailed representation of the rain cell features.

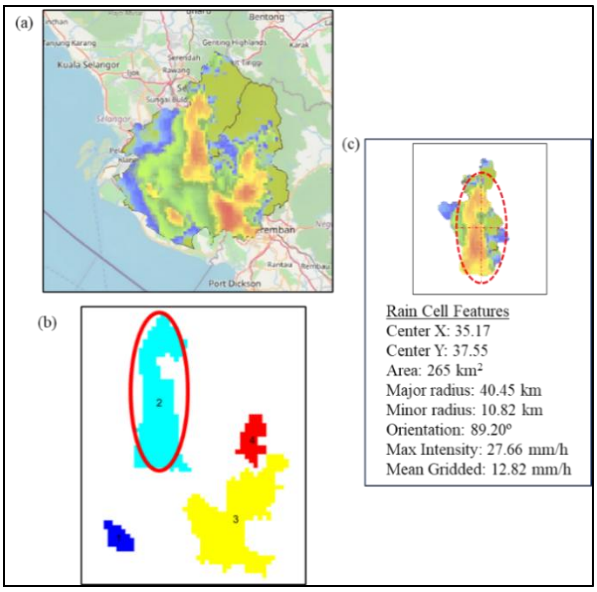

Figure 3.11 Feature Extraction Process for A Single Radar Map

3.6 Classification of Convective-Stratiform Rainfall using Machine Learning

3.6.1 K-Nearest Neighbor Method (KNN)

KNN is often described as a 'lazy learner' because it does not immediately learn from the training data. Instead, it stores the dataset and only performs computations when making predictions. Figure 3.12 illustrates the K-nearest neighbor model. KNN classifies a new data point by analyzing its nearest neighbors. The red diamonds represent Category 1, and the blue squares represent Category 2. The new data point looks at the closest neighbors (marked with circles). Since most of the nearby points are blue squares (Category 2), KNN assigns the new point to Category 2.

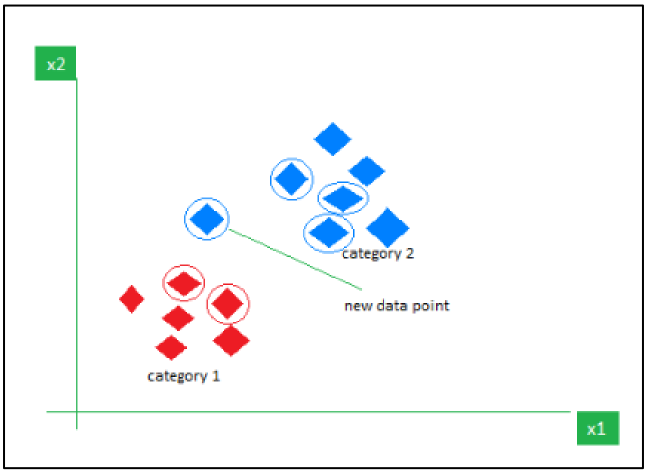

Figure 3.12 An Illustration of K-Nearest Neighbor Model (Kartik, 2025)

Classifying different precipitation types using KNN requires that the variables employed in the classification exhibit clear and significant differences between types. The next section describes the steps and procedure involved in the KNN method.

3.6.1.1 Selection of features

Radar reflectivity values constitute the first feature. Rainfall classification into different types based on radar reflectivity follows these criteria: (1) rainfall is categorized as stratiform when the radar reflectivity is below 40 dBZ, and (2) rainfall is classified as convective when the radar reflectivity exceeds 40 dBZ. These classifications are supported by studies from Rigo and Llasat (2004), Karklinsky and Morin (2006), Barnolas (2010), Djafri and Haddad (2014), and Peleg et al. (2018).

Radar reflectivity, denoted as Z and measured in decibels (dBZ), is a crucial parameter that indicates the intensity of the returned radar signal from raindrops. This measurement is closely linked to the raindrop size distribution (DSD) within a specific radar sample volume. Furthermore, radar reflectivity can be inverted to estimate the rain rate (R), typically expressed in millimeters per hour (mm/h). The relationship between reflectivity and rain rate has been extensively studied and well-established in the literature (Fraile and Fernández-Raga, 2009; Roslan et al., 2021).

In this study, the reflectivity values in dBZ are converted into rainfall using the Marshall-Palmer equation, as applied by the Malaysian Meteorological Department (MMD). Reflectivity, denoted as *Z*, is expressed in dBZ. The decibel (dB) is a unit originally developed to represent power ratios, as shown in the following equation (Tahir et al., 2022):

$$\text{dB} = 10 \log[P1/P2] \tag{3.4}$$

where *P1* and *P2* represent the two power levels being compared, and the log is to the base 10.

Reflectivity can be mathematically represented as;

$$Z(\text{dBZ}) = 10 \log [z/[1\text{mm}^6/\text{m}^3]] \tag{3.5}$$

where z represents the backscattered power measured by the radar. Using Marshall-Palmer equation adopted by the MMD;

$$z = 200 \text{ R}^{1.6} \tag{3.6}$$

Thus, to determine the rainfall intensity, R, at Z = 40 dBZ;

$$z = \text{antilog } (40/10)$$
$$R = (z/200) \wedge (1/1.6)$$
$$= 11.53 \text{ mm/h}$$

Based on this, it can be concluded that rainfall with an intensity of $R < 11.53$ mm/h is classified as stratiform rainfall, while rainfall with $R \geq 11.53$ mm/h is classified as convective rainfall in context of radar reflectivity images.

Additionally, Roslan et al. (2021) established three distinct rainfall intensity categories for monsoon rainfall in Malaysia, which are as follows: low rain ($0.3 < R < 3.2$ mm/h), medium rain ($3.2 \leq R < 13$ mm/h), and high rain ($R \geq 13$ mm/h). These classifications are particularly relevant in the context of Malaysia's climate. The mean gridded rainfall intensity, derived from the feature extraction of radar images, constitutes the second feature. Rainfall is then classified into two categories (stratiform and convective) based on the rainfall intensity thresholds mentioned earlier. This classification helps maintain the quality and accuracy of the reflectivity data.

3.6.1.2 Training and Classification

In this study, two variables (radar reflectivity and mean gridded intensity) are utilized as classification features in the K-nearest neighbors (KNN) algorithm. These variables are incorporated into the KNN algorithm during the training process. First, an optimal value for k (the number of nearest neighbors) is selected to ensure accurate classification. Once the optimal k is determined, the feature values of the sample to be classified are input into the KNN algorithm.

Next, the standardized Euclidean distance between the sample and each training sample stored in the KNN model is computed. This distance calculation allows the algorithm to evaluate the similarity between the sample and its neighbors. The class that corresponds to the majority of the k nearest neighbors is then assigned as the predicted classification for the sample. For the training process, MATLAB is used to implement the KNN algorithm. A sample of the corresponding script, which outlines this process, is shown in Figure 3.13.

```
% Train a classifier
% This code specifies all the classifier options and trains the classifier.
classificationKNN = fitcknn(...
    predictors, ...
                                response, ...
    'Distance', 'Euclidean', ...
    'Exponent', [], ...
    'NumNeighbors', 1, ...
    'DistanceWeight', 'Equal', ...
    'Standardize', true, ...
    'ClassNames', categorical({'convective'; 'stratiform'}));

% Create the result struct with predict function
predictorExtractionFcn = @(t) t(:, predictorNames);
knnPredictFcn = @(x) predict(classificationKNN, x);
trainedClassifier.predictFcn = @(x)
knnPredictFcn(predictorExtractionFcn(x));

% Add additional fields to the result struct
trainedClassifier.RequiredVariables = {'CenterX', 'CenterY', 'Area',
'MajorRadius', 'MinorRadius', 'Orientation', 'MaxIntensity',
'MeanIntensity'};
trainedClassifier.ClassificationKNN = classificationKNN;
trainedClassifier.About = 'This struct is a trained model exported from
Classification Learner R2017b.';
trainedClassifier.HowToPredict = sprintf('To make predictions on a new
table, T, use: \n  yfit = c.predictFcn(T) \nreplacing ''c'' with the name of
the variable that is this struct, e.g. ''trainedModel''. \n \nThe table, T,
must contain the variables returned by: \n  c.RequiredVariables \nVariable
formats (e.g. matrix/vector, datatype) must match the original training
data. \nAdditional variables are ignored. \n \nFor more information, see <a
href="matlab:helpview(fullfile(docroot, ''stats'', ''stats.map''),
''appclassification_exportmodeltoworkspace'')">How to predict using an
exported model</a>.');

% Extract predictors and response
% This code processes the data into the right shape for training the
% model.
inputTable = trainingData;
predictorNames = {'CenterX', 'CenterY', 'Area', 'MajorRadius',
'MinorRadius', 'Orientation', 'MaxIntensity', 'MeanIntensity'};
predictors = inputTable(:, predictorNames);
response = inputTable.RainfallType;
isCategoricalPredictor = [false, false, false, false, false, false, false,
false];

% Perform cross-validation
partitionedModel = crossval(trainedClassifier.ClassificationKNN, 'KFold',
5);

% Compute validation predictions
[validationPredictions, validationScores] = kfoldPredict(partitionedModel);

% Compute validation accuracy
validationAccuracy = 1 - kfoldLoss(partitionedModel, 'LossFun',
'ClassifError');
```

Figure 3.13 MATLAB Script for KNN Algorithm

3.7 Determination of Z-R relationship for Convective-Stratiform Rain Types

For each classified rain type, a new Z-R relationships is derived using a statistical method via Solver Analysis, where the error between radar data and rain gauge data is minimized. The simplex algorithm is applied in the optimization of selected rainfall data, which estimates the system parameters and identifies potential interactions. The smallest difference between radar and rain gauge data is achieved by employing the simplex algorithm. In this approach, the optimization of the Z-R relationship is carried out using Equation 3.7. First, both radar data and rain gauge data are categorized according to rainfall classifications (convective and stratiform). The rainfall rates are then converted into log Z (for radar data) and log Rg (for gauge data) as shown in Equation 3.8.

$$Z = aR^b \tag{3.7}$$

$$\log Z = \log a + b * \log R \tag{3.8}$$

$$\log R = \frac{\log Z - \log a}{b} \tag{3.9}$$

$$\log Rg = \log(Raingauge) \tag{3.10}$$

To use the Solver Analysis method, the initial values of log a and coefficient b are assumed to be 1 before the optimization process begins. In this step, log R is calculated using the formula above, with log a set to 1 and b set to 1. Next, the error between log R and log Rg is computed by subtracting the values, followed by squaring the error, as shown in Equation 3.12.

$$Error = \log Rg - \log R \tag{3.11}$$

$$Error^2 = (\log Rg - \log R)^2 \tag{3.12}$$

Next, constraints are set for the values of log a and b based on previous research. According to studies by Chumchean (2004), the coefficients a and b, each have their own limitations. After considering the characteristics of these coefficients, it was determined that the suitable limitations for a and b are 2.7 and 1.9, respectively, which align with the rainfall classes in Malaysia's climate (Ramli et al., 2011). Several trials were conducted with the radar and gauge dataset for the selected case study. The results from these trials showed improved performance in terms of statistical measurements, including bias, mean error, and root mean square error.

In this method, Solver Analysis finds the optimal values for log a and b in the equation that minimizes the difference between log Rg and log R. The iteration continues until the objective function is met, which corresponds to the lowest sum of squared errors. Statistical measurements such as mean absolute error (MAE) and root mean square error (RMSE) are used to evaluate the performance of the improved Z-R relationship.

$$MAE = \frac{1}{n}\sum_{i=1}^{N}\left|Rg - Rr\right| \tag{3.13}$$

$$RMSE = \sqrt{\frac{1}{n}\sum_{i=1}^{N}(Rg - Rr)^2} \tag{3.14}$$

where;
n = number of samples
Rg=Rain gauge data
Rr= Radar data

3.8 Development of ANN-based Radar QPE

3.8.1 Data Processing

A novel approach in this study is an attempt to estimate mean areal rainfall from the features extracted from radar images using Artificial Neural Network (ANN). In this context, the feature extraction derived from radar images serves as the input layer for the subsequent ANN analysis, as mentioned in Section 3.5. The features are based on eight distinct characteristics of the radar images: the central location of the ellipsoid, the total area (in km^2), the lengths of the major and minor axes (in km), the orientation of the radar cell, the maximum intensity, and the mean gridded intensities (measured in mm/h).

To facilitate the ANN training process, a Microsoft Access Table (MAT) file is created in MATLAB, which holds the input data. This file is of size 210 by 8, where each row represents a different sample, and each of the eight columns corresponds to one of the aforementioned features.

In addition to the input data, the ANN model also requires target values for training, validation, and testing phases. These target values are stored in another MAT file, this one sized 210 by 1, where each entry contains the true rainfall value obtained from rain gauge measurements. The network will attempt to learn the relationship between the radar-based features and the corresponding rainfall measurements in order to predict future rainfall patterns accurately.

3.8.2 Methods

The flow diagram for the ANN process is illustrated in Figure 3.14. Initially, the radar images are analyzed to extract relevant features of the rain cells, which are characterized by eight distinct attributes. Once the extraction process is completed, the resulting data is prepared for input into the network. Following this, the next critical step is to partition the data into three subsets: training, validation, and testing. This is a standard practice to ensure that the model is trained effectively, with 60% of the data used for training, 20% for validation, and the remaining 20% for testing. The division of the data ensures that the subsets are balanced and appropriately represent the full dataset, facilitating an unbiased evaluation of the model's performance. The data division process is performed with attention to ensure that the subsets are of equal size, providing consistency and reliability during the training and evaluation stages.

The next step in the process involves the development of a multilayer feedforward neural network using the feedforwardnet function. This network architecture consists of a single hidden layer. The number of neurons within the hidden layer plays a crucial role in determining the network's responsiveness and its ability to capture patterns in the data. If the network has too few neurons, it may fail to adequately model the underlying relationships, leading to underfitting. On the other hand, an excessive number of neurons can cause the network to become overly complex, potentially resulting in overfitting, where the model performs well on training data but fails to generalize to new, unseen data. For this study, the network is configured with 6 neurons in the hidden layer, as depicted in Figure 3.15. The number of neurons in the output layer is determined by the size of the target vector, which corresponds to the number of desired output values the network needs to predict.

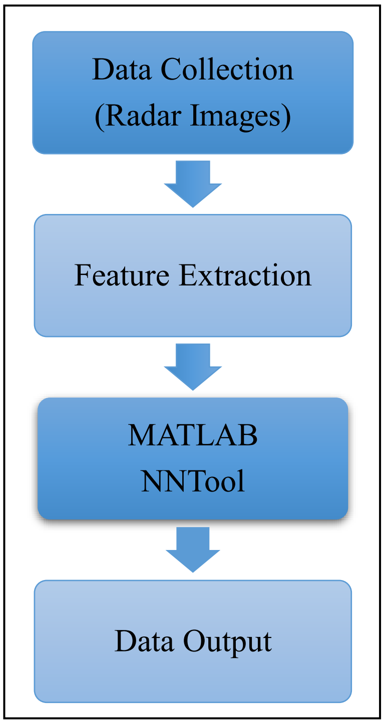

Figure 3.14 ANN Process Flow

To achieve optimal performance, the network has undergone a manual optimization process. The Levenberg-Marquardt (LM) algorithm has been specifically selected for this optimization. Known for its efficiency, the LM algorithm is one of the fastest training methods available, though it typically demands more memory compared to other training algorithms. Despite its higher memory requirements, the LM algorithm was chosen because of its superior reliability in predicting the desired parameter, in this case, the rain rate. This is particularly beneficial when the initial value of the parameter is significantly different from the expected reflectivity value, as the LM method can still produce accurate predictions. Moreover, the Levenberg-Marquardt algorithm is particularly adept at handling inversion problems. In contrast to other algorithms, the LM method is able to process inversions more quickly, which significantly enhances its performance in scenarios that involve complex parameter estimation. These advantages make the LM algorithm a preferred choice for applications requiring quick and reliable parameter predictions, such as the one outlined in Roslan et al. (2021).

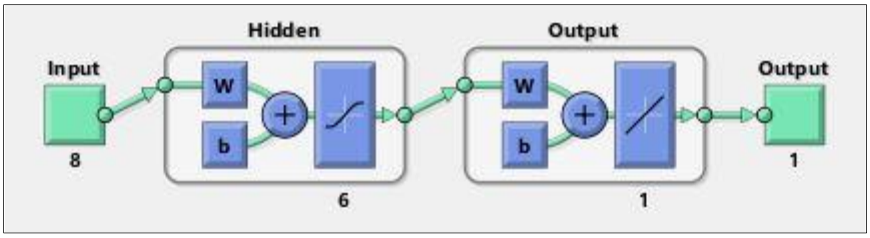

Figure 3.15 ANN Architecture

The primary objective of the ANN model is to accurately estimate rainfall amounts based on a set of targeted data. This targeted data is derived from the mean areal rainfall rate values collected from raingauge observations provided by the DID, and it is calculated for each individual rain cell area. After the training phase is completed, the performance of the network is assessed to determine its effectiveness. If necessary, adjustments are made to improve the model's performance. These adjustments may include refining the training process, altering the network architecture, or modifying the input data to enhance the network's accuracy. The specific neural network structure employed for this model and part of the script are illustrated in Figure 3.16 and Figure 3.17.

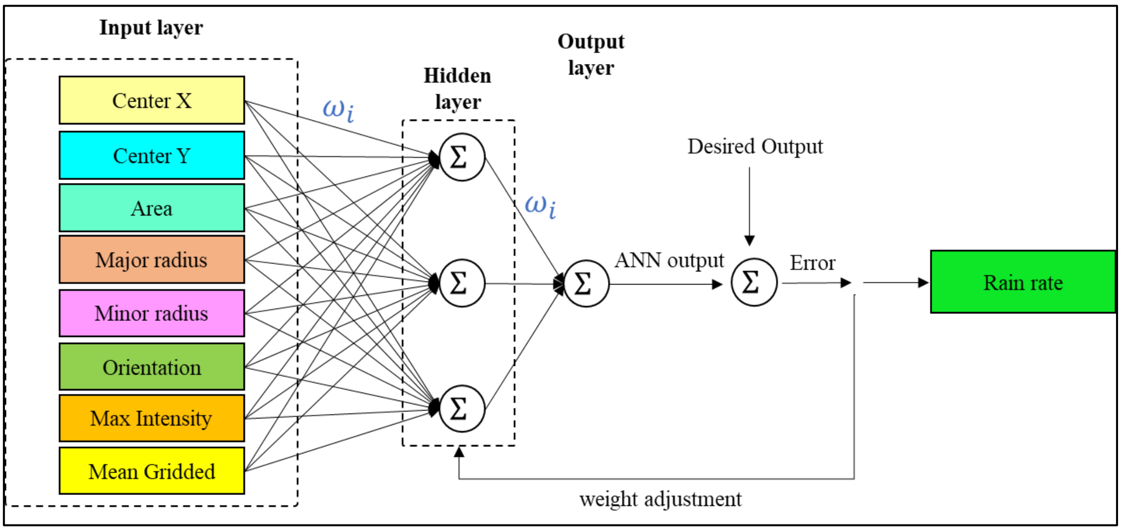

Figure 3.16 Model Neural Network Architecture

```matlab
% Created 08-Dec-2023 09:32:19

%   RainsInput - input data.
%   RainsTarget - target data.

x = RainsInput;
t = RainsTarget;

% Choose a Training Function
% For a list of all training functions type: help nntrain
% 'trainlm' is usually fastest.
% 'trainbr' takes longer but may be better for challenging problems.
% 'trainscg' uses less memory. Suitable in low memory situations.
trainFcn = 'trainlm';  % Levenberg-Marquardt backpropagation.

% Create a Fitting Network
hiddenLayerSize = 6;
net = fitnet(hiddenLayerSize,trainFcn);

% Choose Input and Output Pre/Post-Processing Functions
% For a list of all processing functions type: help nnprocess
net.input.processFcns = {'removeconstantrows','mapminmax'};
net.output.processFcns = {'removeconstantrows','mapminmax'};

% Setup Division of Data for Training, Validation, Testing
% For a list of all data division functions type: help nndivision
net.divideFcn = 'dividerand';  % Divide data randomly
net.divideMode = 'sample';  % Divide up every sample
net.divideParam.trainRatio = 80/100;
net.divideParam.valRatio = 10/100;
net.divideParam.testRatio = 10/100;

% Choose a Performance Function
% For a list of all performance functions type: help nnperformance
net.performFcn = 'mse';  % Mean Squared Error

% Choose Plot Functions
% For a list of all plot functions type: help nnplot
net.plotFcns = {'plotperform','plottrainstate','ploterrhist', ...
    'plotregression', 'plotfit'};

% Train the Network
[net,tr] = train(net,x,t);

% Test the Network
y = net(x);
e = gsubtract(t,y);
performance = perform(net,t,y)

% Recalculate Training, Validation and Test Performance
trainTargets = t .* tr.trainMask{1};
valTargets = t .* tr.valMask{1};
testTargets = t .* tr.testMask{1};
trainPerformance = perform(net,trainTargets,y)
valPerformance = perform(net,valTargets,y)
testPerformance = perform(net,testTargets,y)

% View the Network
view(net)

% Plots
% Uncomment these lines to enable various plots.
%figure, plotperform(tr)
%figure, plottrainstate(tr)
%figure, ploterrhist(e)
%figure, plotregression(t,y)
%figure, plotfit(net,x,t)

% Deployment
% Change the (false) values to (true) to enable the following code blocks.
% See the help for each generation function for more information.
if (false)
    % Generate MATLAB function for neural network for application
    % deployment in MATLAB scripts or with MATLAB Compiler and Builder
    % tools, or simply to examine the calculations your trained neural
    % network performs.
    genFunction(net,'myNeuralNetworkFunction');
    y = myNeuralNetworkFunction(x);
end
if (false)
    % Generate a matrix-only MATLAB function for neural network code
    % generation with MATLAB Coder tools.
    genFunction(net,'myNeuralNetworkFunction','MatrixOnly','yes');
    y = myNeuralNetworkFunction(x);
end
if (false)
    % Generate a Simulink diagram for simulation or deployment with.
    % Simulink Coder tools.
    gensim(net);
end
```

Figure 3.17 MATLAB Script for ANN Analysis

3.8.3 Model Validation

The performance of the ANN-Radar QPE model is evaluated using two key metrics for deterministic continuous variables: the root mean square error (RMSE) and the correlation coefficient (r). These metrics help assess the accuracy of the model's predictions. The calculations for these metrics are provided in equations (3.4) and (3.5), where *G* represents gauge rainfall, *R* denotes radar rainfall, and *i* refers to the number of rainfall stations.

$$RMSE = \sqrt{\frac{1}{n}\sum_{i=1}^{n}(G_i - R_i)^2} \tag{3.15}$$

$$r = \frac{n(\sum xy) - (\sum x)(\sum y)}{\sqrt{[n\sum x^2 - (\sum x)^2][n\sum y^2 - (\sum y)^2]}} \tag{3.16}$$

where, $G_i = x, R_i = y$.

3.9 Application of ANN-based Radar QPE as Input to HEC-HMS Flood Forecasting Model

The research employs the HEC-HMS rainfall-runoff hydrological model to simulate flood forecasting with input from the radar QPE. The process of developing the hydro-meteorological flood forecasting model for the Klang and Langat River basins using the HEC-HMS model version 4.9 is shown in Figure 3.18. This process begins with the preparation and integration of the input data required for the HEC-HMS model. For this study, the input data are rainfall data from rain gauge, radar QPE and newly developed ANN-enhnaced radar QPE. This rainfall data is then fed into the hydrological or rainfall-runoff model. The model is crucial in providing accurate rainfall inputs, which are essential for simulating flood events and forecasting flood behaviour in the basin.

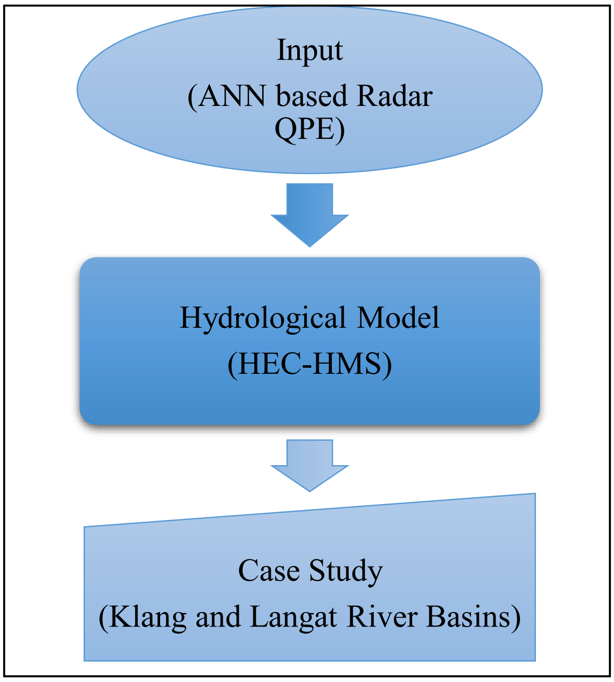

Figure 3.18 Hydro-Meteorological Flood Modeling Process Flow

3.9.1 Data Processing

This section presents a comprehensive approach for systematically collecting and organizing the data required for spatial hydrological modeling within the defined basin. In this study, both rain gauge data and radar QPE were integrated into the modeling process, with a focus on hourly precipitation data specifically for the Klang and Langat River basins. As shown in Figure 3.19, radar imagery corresponding to each subbasin within the basin is displayed. To compute the average rainfall for each subbasin, the study employs the Quantum Geographic Information System (QGIS) software to calculate the mean value of gridded pixel data for each respective subbasin.

The study adopts the arithmetic mean analysis method for the rain gauge data (Equation 3.3), which involves computing the mean areal rainfall for each subbasin by averaging the rainfall measurements obtained from multiple rain gauge points distributed across the catchment area. This method ensures a comprehensive representation of the rainfall over the entire subbasin area.

In addition, the study utilizes specialized tools to facilitate the modeling process, such as Arc Hydro and HEC Geo-HMS, both of which are extensions of Geographic Information Systems (GIS). These tools were employed to prepare and process the necessary spatial and temporal data required for the hydrological modeling. Furthermore, additional spatial datasets, such as land use and soil maps, were generated. The curve number grid, a key component for calculating runoff, was also derived based on these spatial datasets, providing essential input for hydrological simulations.

Finally, once all the necessary data were prepared, the basin model was imported into the Hydrologic Engineering Center's Hydrologic Modeling System (HEC-HMS) software. This step enabled further analysis and simulation of hydrological processes, allowing for a deeper understanding of the basin's behavior under various rainfall conditions.

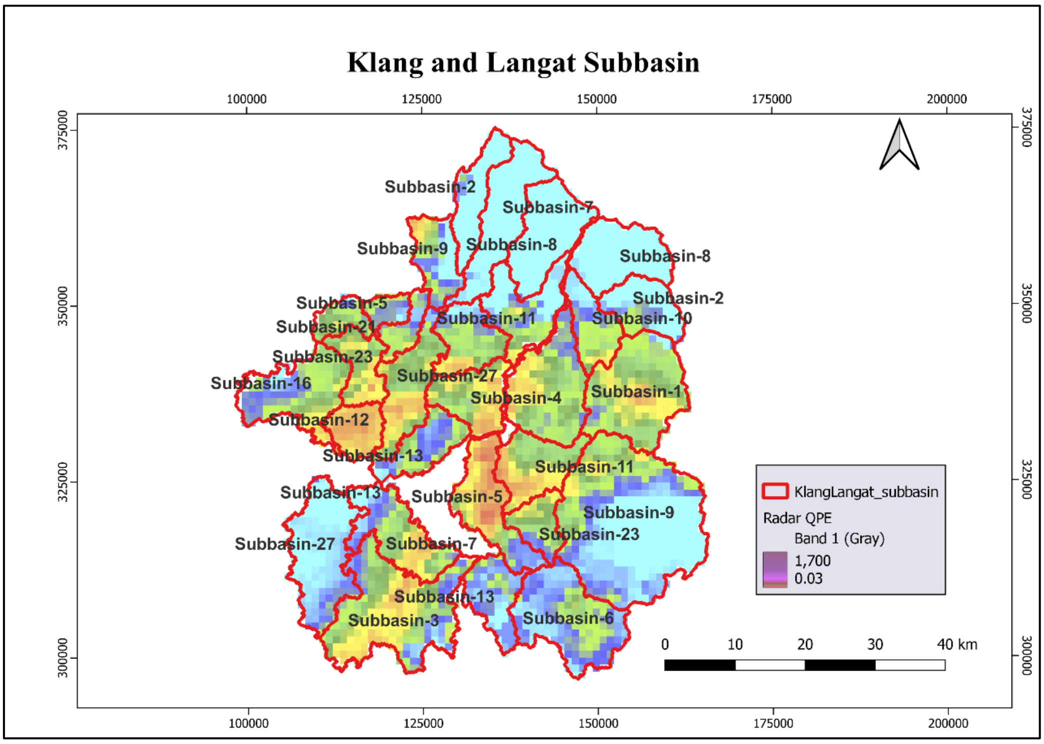

Figure 3.19 Distributed Subbasin of Radar QPE

3.9.1.1 Digital Elevation Model (DEM)

A topographic map, as illustrated in Figure 3.20, represented by a Digital Elevation Model (DEM) with a resolution of 30 meters or less, is essential for accurately determining the elevation at each point within the study area. The DEM serves as a critical tool for the delineation of catchments and the creation of river cross-sections, enabling precise hydrological analysis. Traditionally, manually delineating a watershed area from a topographic map can be both labor-intensive and susceptible to errors, which can affect the overall accuracy of the analysis. To overcome these limitations, the basin model is developed using an automated extraction process powered by the DEM. This process involves executing several computational operations that streamline and enhance the accuracy of the watershed delineation, significantly reducing the potential for human error and saving time.

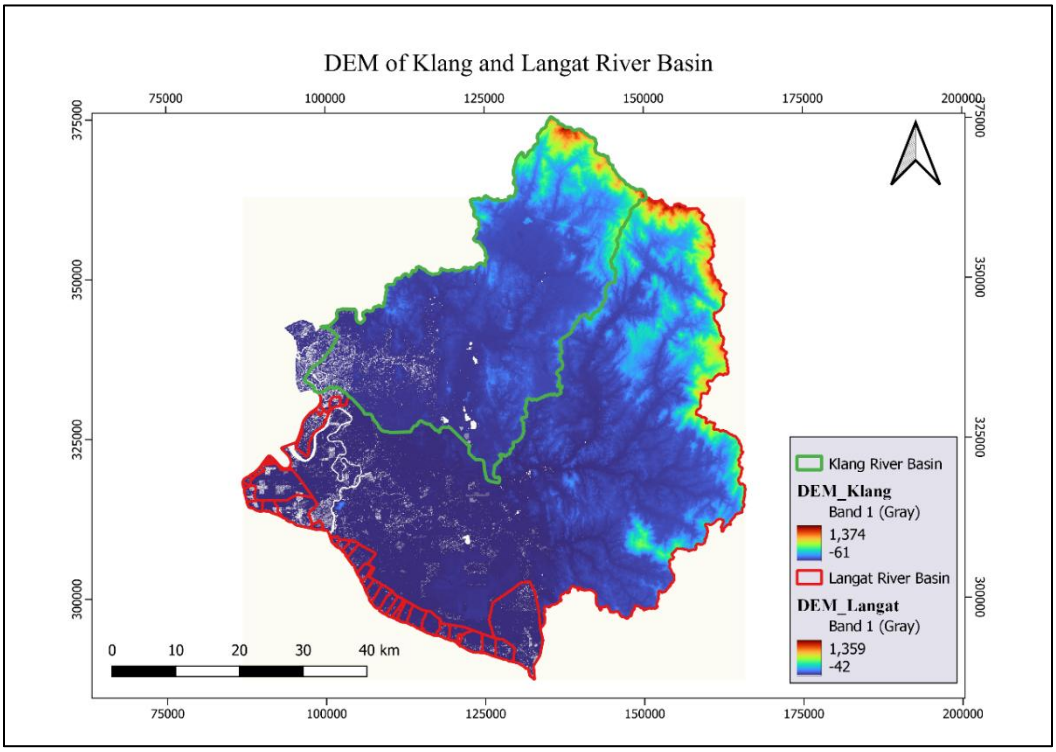

Figure 3.20 Digital Elevation Model for the Klang and Langat River Basins

3.9.1.2 Soil Map

The soil map plays a crucial role in determining the hydrological properties of a catchment area and is essential for further defining the Curve Number (CN) value. It provides detailed information on the different soil types present within the basin, each corresponding to a specific area. These soil types are vital for understanding the catchment's ability to absorb and transmit water, which directly influences runoff calculations. The soil map can be sourced from the Digital Soil Map of the World (DSMW) website, which offers comprehensive global soil data. In this study, the soil map of the Klang and Langat River basins, as shown in Figure 3.21, are used to categorize and assess the various soil types across the region, enabling more accurate hydrological modeling and CN value determination.

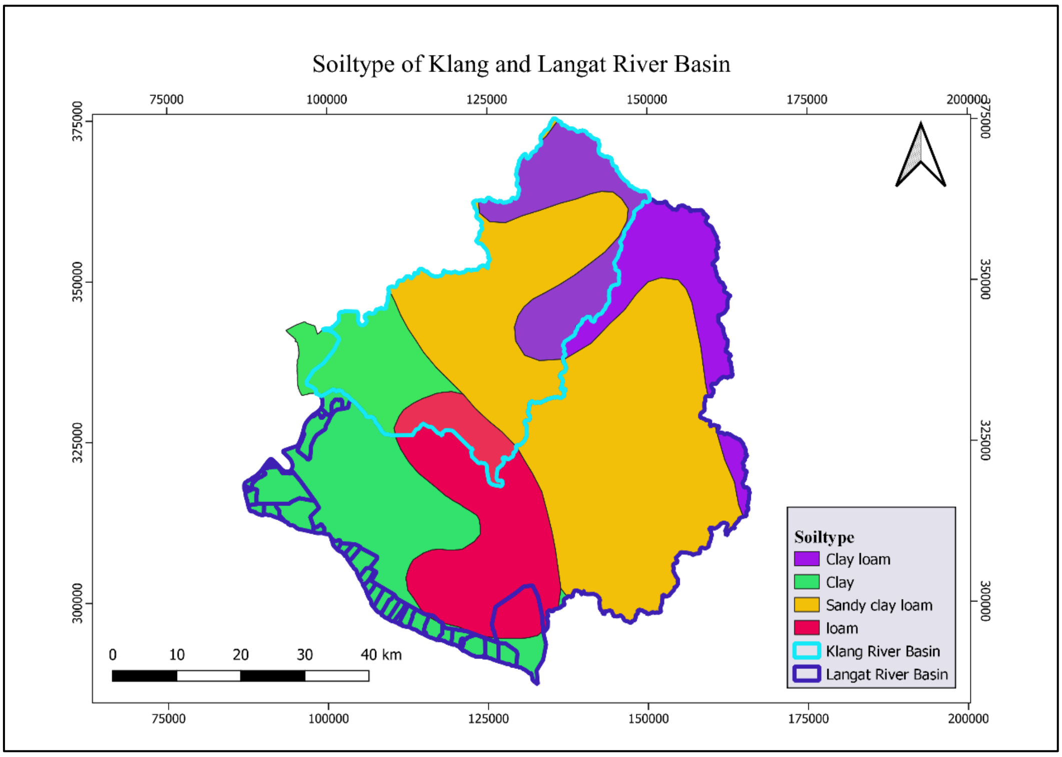

Figure 3.21 Hydrologic Soil Group (HSG) for the Klang and Langat River Basins

The Soil Conservation Service (SCS) method employs a hydrological classification system to group soils based on their estimated infiltration potential. This classification categorizes soils into four distinct groups: A, B, C, and D. Group A represents soils with high infiltration rates, meaning they allow water to seep through rapidly; Group B consists of soils with moderate infiltration rates; Group C includes soils with slow infiltration rates; and Group D represents soils with extremely slow infiltration rates, which are less permeable and tend to generate more runoff.

Furthermore, the transition from general soil classification to the SCS hydrological classification takes soil texture into account. The texture is determined by the proportion of sand, clay, and loam in the soil composition, as this information is crucial for accurately assessing the soil's ability to absorb water and, in turn, for determining the runoff coefficient. The specific information for these soil components is provided in Table 3.2. Based on the analysis of the soil map, it is evident that the dominant soil class in the Klang River basin is Class D, indicating that the majority of the soils have slow infiltration rates. As a result, these soils are more prone to higher runoff, which can impact water management and flood risk in the area.

Table 3.2
Soil Texture Classes

SNUM	COUNTRY	Texture	Hydrological Group
4284	MALAYSIA	clay-loam	D
4324	MALAYSIA	clay	C
4464	MALAYSIA	sandy-clay-loam	D
4552	MALAYSIA	loam	D

3.9.1.3 Land Use Map

The land use map is a crucial tool for determining the Curve Number (CN) of a catchment, which is calculated in relation to the soil type of the area. This map can be obtained from the Land Use and Land Cover (LULC) website, which provides comprehensive data for countries worldwide. However, for this analysis, only the datasets corresponding to areas connected to the study region for the year 2021 were downloaded. To integrate this data into the study, the land use information was imported as shapefiles into ArcGIS, ensuring that the entire study region was adequately covered. The land use distribution within the Klang and Langat River catchment is depicted in Figure 3.22. Additionally, Table 3.3 presents the land use class definitions for the Klang and Langat watershed, based on the ESRI classification system (ArcGIS, 2021). The table includes only the relevant class numbers and their corresponding class names to focus on the land use categories pertinent to the study area.

Table 3.3

Land Use Classification

Class Number	Class Name
1	water
2	forest
4	mangrove swamp
5	crops
7	built area
8	bare ground
10	cloud
11	rangeland

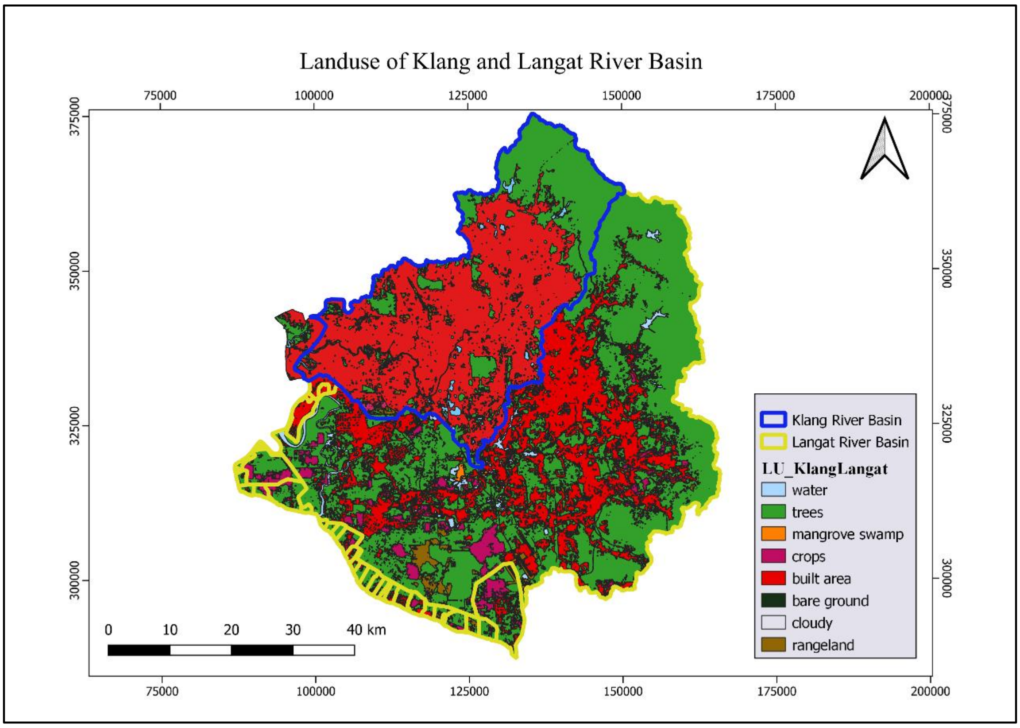

Figure 3.22 Land Use for the Klang and Langat River Basins

3.9.1.4 CN-Lookup Table

The lookup table is designed to contain CN values corresponding to different combinations of land use and soil group classifications. The purpose of this table is to provide a detailed reference for determining the CN value linked to each specific combination of land use and hydrological group. In this particular scenario, the SCS curve values derived from the literature will be used (Rosli, 2021). Table 3.4 shows a comprehensive summary of the CN lookup table, which has been constructed by integrating the different land use classes with their corresponding hydrological groups (HSG). This table serves as an essential tool for accurately assessing runoff potential based on the unique characteristics of each land use and soil type combination within the study area.

Table 3.4

Initial CN Values for Land Use and Hydrological Soils Group

Land use	HSG			
	A	B	C	D
Water	100	100	100	100
Forest	25	55	70	77
Rangeland	66	77	88	94
Bare ground	72	82	88	90
Built area	77	85	90	92
Mangrove swamp	77	80	83	86
Crops	65	75	82	85

3.9.1.5 CN Grid

The HEC-GeoHMS tool, integrated within the ArcGIS software platform, is used to generate the Curve Number (CN) grid for the study area. This tool utilizes several key datasets, including the Digital Elevation Model (DEM) of the basin, the CN-Lookup table, and the combined results of land use and soil type data. The final CN map for the Klang and Langat watershed are shown in Figure 3.23 and Figure 3.24. In this study, the Soil Conservation Service Curve Number (SCS-CN) method is selected as the loss approach for each sub-basin within the Klang and Langat watershed. This method is used to estimate potential runoff following a rainfall event by considering the complex interactions between soil type, land use, and hydrologic soil conditions.

The antecedent moisture condition (AMC) is an important factor in this method, as it reflects the moisture levels in the soil before a rainfall event occurs. AMC represents different soil moisture conditions based on prior precipitation. AMC I is applied in cases where the basin has experienced minimal rainfall before the event, indicating dry soil conditions. AMC III, on the other hand, is used for basins that have received significant precipitation prior to the modeled event, resulting in saturated or near-saturated soil conditions. AMC II is considered the average or typical moisture condition and is most commonly used in modeling applications. Equations 3.17 and 3.18 demonstrate how adjustment factors are applied to the CN values under AMC II conditions in order to adjust the CN values for conditions corresponding to AMC I and AMC III (Tranceto, 2015).

$$AMCI = \frac{4.2 \times AMCII}{10-(0.058 \times AMCII)} \quad (3.17)$$

$$AMCIII = \frac{23 \times AMCII}{10+(0.13 \times AMCII)} \quad (3.18)$$

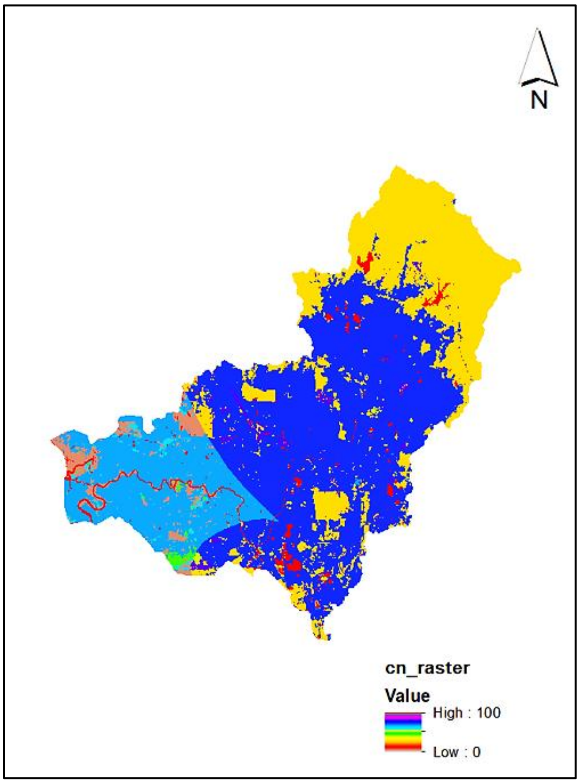

Figure 3.23 CN Map of Klang River Basin

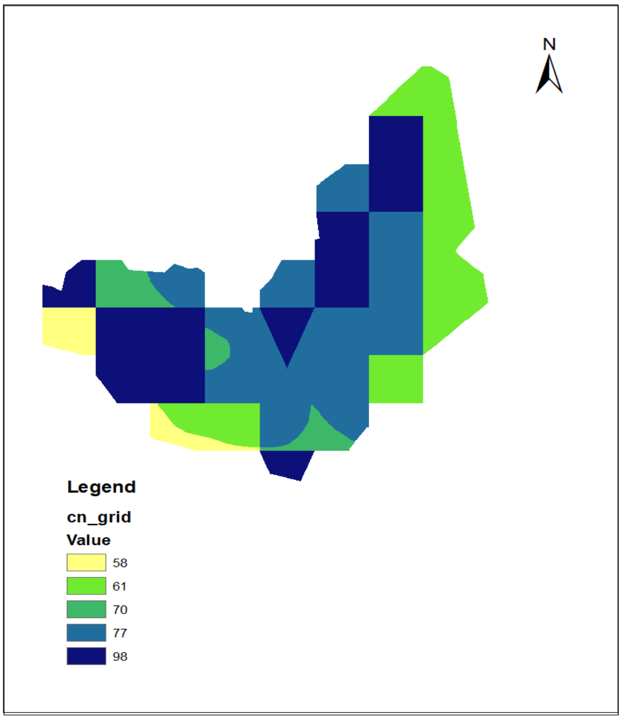

Figure 3.24 CN Map of Langat River Basin

3.9.2 HEC- HMS Rainfall Runoff Modeling

The HEC-HMS model is highly regarded and widely used in hydrological research due to its ability to accurately simulate runoff for both short- and long-duration rainfall events. Its popularity is further attributed to its intuitive user interface, which makes it accessible for a wide range of users (Tassew et al., 2019; Daide et al., 2021). The model consists of several key components that work together to simulate hydrological processes. These include the basin model, which represents the catchment area (as illustrated in Figure 3.25 and Figure 3.26); the meteorological model, which processes weather data; control specifications, which manage simulation settings; and time series data inputs, which provide temporal data for rainfall, temperature, and other relevant variables (Fleming, 2004).

For the meteorological model, the input data consisted of observed rainfall and streamflow data. These data were essential for accurately modeling the hydrological response of the basin to precipitation events. In addition, the control requirements component governs the overall simulation parameters, including the start and end dates of the simulation period, as well as the time step used in the model's calculations. For this study, the model was configured with a simulation period from December 18, 2021, to December 22, 2021, and a time step of one hour, allowing for a detailed analysis of the runoff response over that time frame.

In this study, the SCS-CN (Soil Conservation Service-Curve Number) loss method was employed to estimate the initial runoff resulting from a specific or designed rainfall event. This method calculates the accumulated rainfall excess, which is influenced by several key factors, including soil type, land use, cumulative precipitation, and antecedent moisture conditions. The antecedent moisture condition refers to the soil moisture present prior to the rainfall event, which significantly impacts the runoff response. The relationship between these factors and the calculated runoff is described in Equation 3.19, which provides the mathematical formulation for determining the rainfall excess based on these variables (Mishra and Singh, 2003).

$$P_e = \frac{(P - I_a)^2}{P - I_a + S} \tag{3.19}$$

where *Pe*=accumulated precipitation excess at time t,

P =accumulated rainfall depth at time t,

I_a=the initial abstraction (0.2S),

S =potential maximum retention.

The maximum retention (*S*) is related to the characteristics of the watershed through the dimensionless Curve Number (CN), as shown in Equation 3.20.

$$S = 25400 - \frac{254 \times CN}{CN} \tag{3.20}$$

The SCS-CN is a parameter used to represent the combined effects of the key characteristics of a catchment area. These characteristics include factors such as land use, soil type, and hydrological conditions, all of which influence runoff. For transforming excess precipitation into runoff, the SCS Unit Hydrograph model was chosen. This model is widely used to convert the excess rainfall into a hydrograph that represents the runoff response over time. In this approach, the primary input required is the lag time (Tlag), which refers to the time interval between the center of mass of the excess rainfall and the peak of the resulting runoff hydrograph. This lag time is determined by the concentration time (Tc), which is the time it takes for runoff from the entire catchment to reach the outlet. The relationship between lag time and concentration time is described in Equation 3.21, which mathematically defines how the catchment's characteristics influence the timing of runoff peak.

$$Tlag = 0.6Tc \tag{3.21}$$

where the variables Tlag and Tc represent time intervals measured in minutes.

The Muskingum method, introduced by McCarthy, has been selected as the routing technique for this study (Ismail et al., 2020). This approach allows for the calculation of the downstream outflow hydrograph of a river or channel by using the upstream inflow hydrograph as input. To apply the Muskingum method, two key parameters are required: the travel time of the flood wave (k) through the routing reach, and the dimensionless weighting factor (x), which represents the degree of attenuation of the flood wave as it moves downstream. The value of x indicates how the flood wave's intensity diminishes as it flows through the channel.

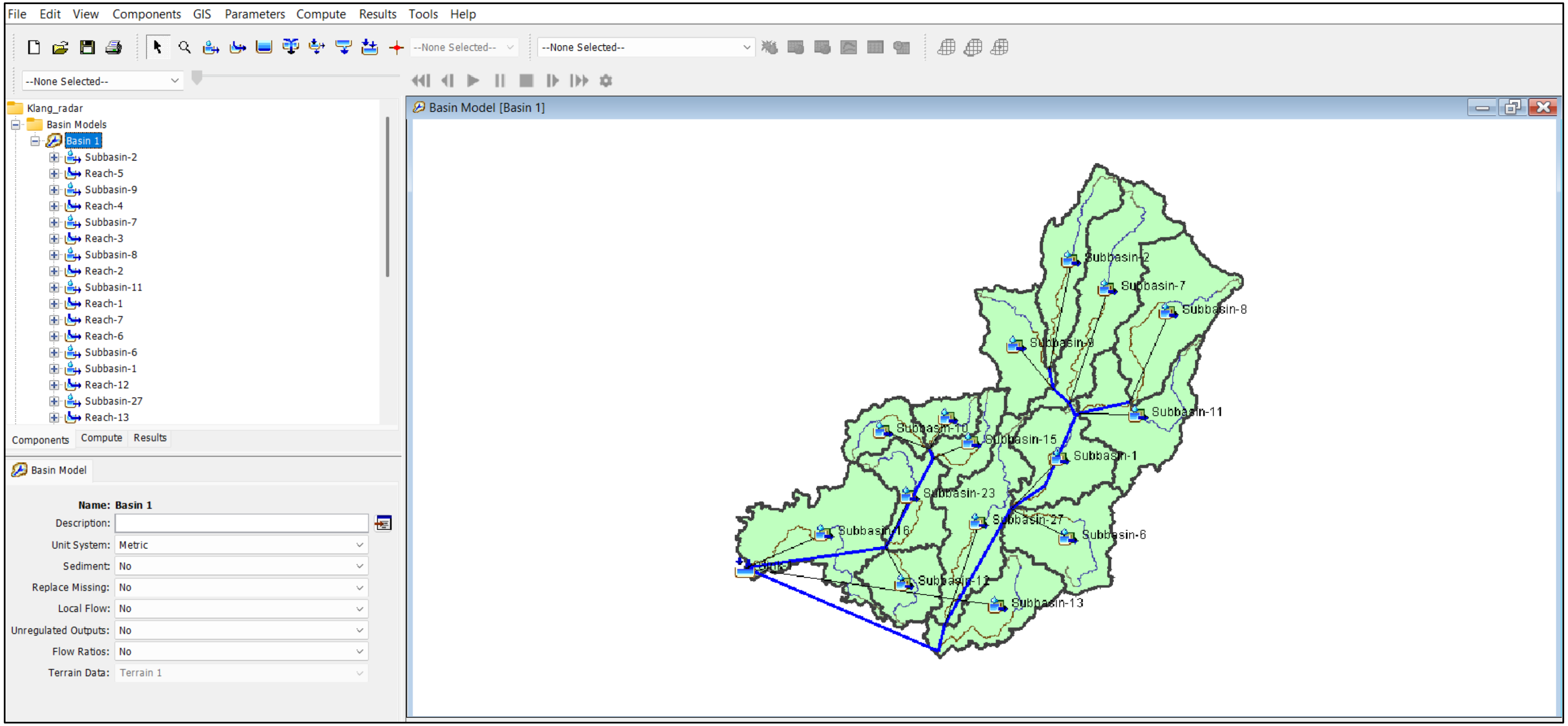

Figure 3.25 HEC-HMS Rainfall-Runoff Model for the Klang River Basin Catchment

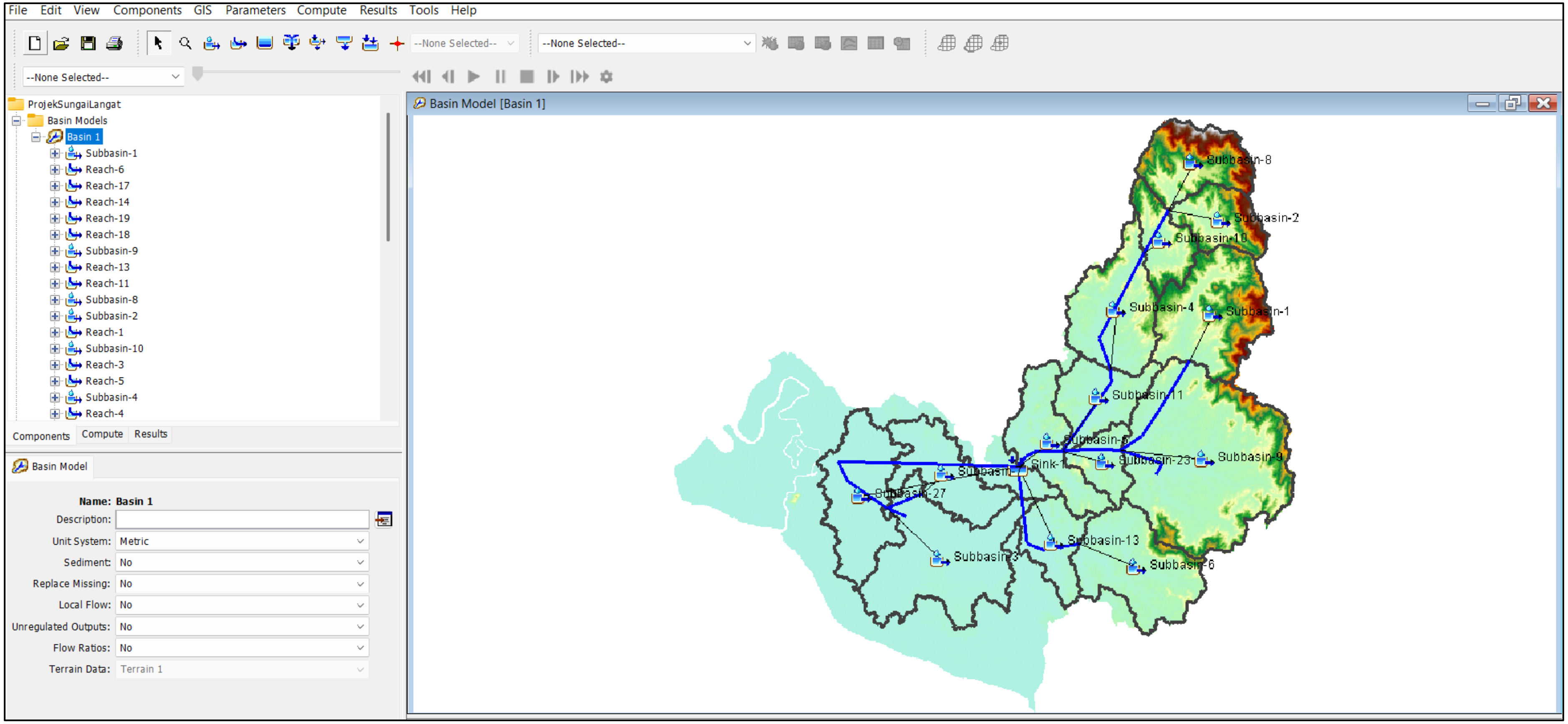

Figure 3.26 HEC-HMS Rainfall-Runoff Model for the Langat River Basin Catchment

Typically, to calibrate the Muskingum model and fine-tune its parameters, measured discharge hydrographs are utilized. These observed hydrographs provide real-world data that allow for the adjustment of the routing parameters to more accurately reflect the dynamics of the channel's flow. This calibration process is crucial for ensuring the reliability and accuracy of the model's predictions for downstream flow behavior (Birkhead and James, 2002).

3.9.2.1 Model Calibration

Both manual and automatic calibration techniques were utilized to fine-tune the parameters of the HEC-HMS model. In many hydrological modeling studies, sensitivity analysis is an essential step to identify the key variables that significantly influence model performance and determine the level of precision required for parameter calibration. For this study, the sensitivity factors were selected based on their effect on critical model outputs, such as peak discharge and total runoff volume, which are vital for accurately simulating flood events.

To optimize the calibration process, the model was evaluated using the Peak-Weighted Root Mean Square Error (PWRMS) objective function. This method was chosen due to its simplicity and its ability to effectively measure the discrepancy between simulated and observed values, particularly in terms of peak discharge, which is crucial for flood analysis (Hawkins et al., 2008). During the calibration process, various watershed parameters such as the curve number (CN), lag time (Tlag), baseflow, and initial abstraction, were adjusted as needed to achieve the best possible match between the model's predictions and the observed data.

3.9.3 Model Validation

Next, the performance of the model, along with the selected loss and transform methods, was evaluated by comparing the observed streamflow data to the simulated values produced by the model. This comparison was conducted using several statistical evaluation metrics to quantify the model's accuracy and reliability. The statistical criteria used include the coefficient of determination (R^2), which measures the proportion of variance in the observed data explained by the model; the percent bias (PBIAS), which quantifies the average tendency of the model to overestimate or underestimate streamflow; the Nash-Sutcliffe Efficiency (NSE), which evaluates how well the model's predictions match the observed values; and the Root Mean Square Error to Standard Deviation Ratio (RSR), which provides an indication of the model's overall prediction accuracy by comparing the magnitude of the error to the variability in the observed data. By utilizing these metrics, the study aims to assess the strengths and limitations of the model's ability to simulate streamflow accurately under varying conditions.

$$R^2 = [\frac{\frac{1}{M}\sum_{k=1}^{M}[(Q_S)_k-\overline{Q_S}][(Q_O)_k-\overline{Q_O}]}{\sqrt{\frac{1}{M}\sum_{k=1}^{M}[(Q_S)_k-\overline{Q_S}]^2}\sqrt{\frac{1}{M}\sum_{k=1}^{M}[(Q_O)_k-\overline{Q_O}]^2}}]^2 \tag{3.22}$$

$$PBIAS = \frac{\sum_{k=1}^{n}[(Q_O)_k-(Q_S)_k]}{\sum_{k=1}^{n}(Q_O)_k} \times 100\% \tag{3.23}$$

$$NSE = 1 - \frac{\sum_{k=1}^{n}[(Q_O)_k-(Q_S)_k]^2}{\sum_{k=1}^{n}[(Q_O)_k-\overline{Q_O}]^2} \tag{3.24}$$

$$RSR = \frac{\sqrt{\sum_{k=1}^{n}[(Q_O)_k-(Q_S)_k]^2}}{\sqrt{\sum_{k=1}^{n}[(Q_O)_k-\overline{Q_O}]^2}} \tag{3.25}$$

where, *(Qo)k*, *(Qs)k* are the k^{th} observed and simulated discharges respectively; $\overline{Q_O}$ = mean observed discharge; *n* is the total number of reference data points.

3.10 Summary

This chapter outlines the methodology used in the study, including an overview of the study area, data collection methods, and the overall approach. It begins with the acquisition and processing of weather radar data from the Malaysia Meteorological Department (MMD) and rain gauge data from the Department of Drainage and Irrigation (DID) for the years 2021 to 2023. The chapter also discusses the development of feature extraction algorithms for radar reflectivity images, considering different rainfall types. Next, a machine learning classifier is employed to differentiate between convective and stratiform rainfall based on the extracted features. Subsequently, an optimization approach is applied to create new Z/R relationships for the classified rainfall types.

Another novelty in the research methodology involves using an Artificial Neural Network (ANN) model to enhance the radar QPE rainfall estimation, with the extracted features serving as inputs. The final part of the methodology applies the distributed sub-basin mean radar-based rainfall estimation in a flood forecasting system using HEC-HMS software. Several statistical analyses, including R^2, correlation coefficient (r), RMSE, and NSE, are conducted in this study to assess the performance and accuracy of both the ANN-based radar QPE model and the HEC-HMS model.

CHAPTER 4
RESULTS AND DISCUSSION

4.1 Introduction

The chapter presents and discusses the research findings, encompassing results from the rainfall classification model using features extracted from the radar image, optimum Z-R relationship for each rain type, ANN-based radar QPE model development and its application to the HEC-HMS rainfall-runoff model. The chapter begins with the performance analysis of radar QPE as an alternative to gauged rainfall. The results include a correlation analysis to compare the accuracy between rain gauge data and the raw radar QPE.

This chapter also discusses the derivation of pixel-based radar QPE images for the Klang and Langat River basins using QGIS software. The features of these radar images were extracted based on recorded rainfall events. Next, results from the optimal machine learning classifier for categorizing convective and stratiform rainfall based on the extracted features of radar reflectivity images are presented, followed by the results on the newly derived Z-R relationship for each rainfall category. Subsequently, the findings from the development of a novel radar QPE enhancement model based on an Artificial Neural Network (ANN) are presented.

Finally, the chapter describes the application of the ANN-enhanced radar QPE, as input to a rainfall-runoff model to simulate flood forecasting. The integrated flood forecasting model was developed for the case study basin using HEC-HMS software. The results of the integrated model are presented and discussed in this chapter.

4.2 Basin Mean Areal Rainfall Comparison

This section demonstrates the mean areal rainfall estimation for the Klang River basin to compare the accuracy between radar QPE and rain gauge data. Rain gauge data measures rainfall at specific locations, and point rainfall data is transformed into spatial rainfall data, providing a better representation of rainfall over the catchment by calculating the mean rainfall from multiple stations within the catchment area.

On the other hand, weather radar has the capability to monitor rainfall over a much larger area, thereby offering significantly broader spatial coverage compared to traditional measurement methods. Moreover, weather radar provides detailed spatial data about various meteorological conditions with high temporal resolution, allowing for real-time observation of rainfall dynamics. However, one key limitation is that radar does not directly measure the actual rainfall amount. Instead, it captures the intensity of radar reflectivity, which represents the amount of energy reflected by precipitation particles. This data requires further processing and enhancement to accurately estimate rainfall amounts, as reflectivity alone does not directly correlate to the volume of precipitation.

In this study, the mean areal rainfall was calculated using the Thiessen polygon method for the rainfall events from 17 December 2021 to 19 December 2021. In addition, a total of 17 rainfall stations were used to calculate the mean areal rainfall over the catchment. The Thiessen polygon method was chosen in this study as it provides better accuracy compared to the arithmetic mean method (Hasni et al., 2024). This method uses a graphical technique to calculate weights based on the relative areas of each measurement station within the Thiessen polygon network as shown in Figure 4.1. Areal rainfall estimation is obtained by aggregating the individual station weights and multiplying them by the corresponding rainfall amounts at each station as explained in Chapter 3. The area and station weights for the Thiessen polygon calculation were derived using QGIS analysis as shown in Table 4.1.

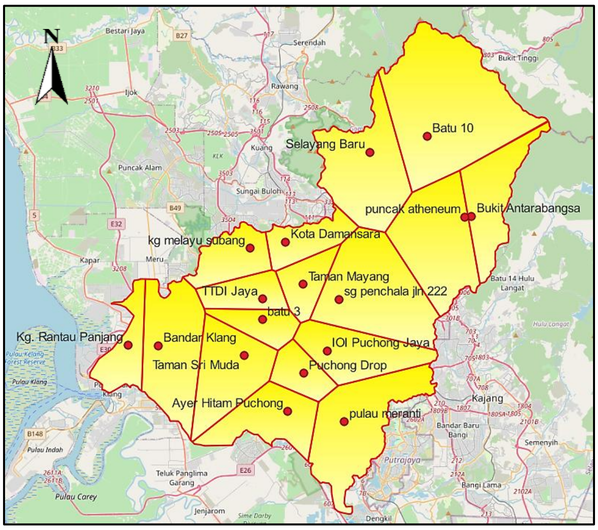

Figure 4.1 Thiessen Polygon for Klang River Basin

Table 4.1

Areal Rainfall Estimation using Thiessen Polygon

No	Station Name	Area (km^2)	Thiessen weight
1	Batu 3	30.462	0.02
2	Bandar Klang	98.825	0.08
3	Bukit Antarabangsa	69.839	0.05
4	Batu 10	204.689	0.16
5	Kg Melayu Subang	45.265	0.03
6	Kg. Rantau Panjang	39.832	0.03
7	Kota Damansara	39.318	0.03
8	Puncak Atheneum	107.524	0.08
9	Sg Penchala	126.497	0.1
10	Ayer Hitam Puchong	64.887	0.05
11	Pulau Meranti	113.145	0.09
12	IOI Puchong Jaya	69.683	0.05
13	Puchong Drop	30.859	0.02
14	Selayang Baru	108.874	0.08
15	Taman Mayang	33.157	0.03
16	Taman Sri Muda	79.713	0.06
17	TTDI Jaya	34.675	0.03

The results of comparing the uncalibrated radar QPE with rainfall measurements from rain gauges at the mean areal basin are presented in Figure 4.2. This comparison reveals that some of the uncalibrated radar data tend to underestimate the rainfall amounts. Possible reasons for this discrepancy could include errors in the radar reflectivity measurements, limitations in the radar's ability to capture certain rainfall characteristics, or discrepancies due to the spatial and temporal differences between the two data sources. Nevertheless, despite these underestimations, radar data usually shows a strong correlation with rain gauges because both capture precipitation, and their overall patterns tend to match. The correlation analysis, as depicted in Figure 4.3, indicates a good correlation between the mean areal radar QPE data and the mean areal rainfall gauge measurements (r=0.8). The correlation indicates how accurately the radar detects rainfall events, though it may still miss certain details in specific areas or situations. As a result, the radar data requires further enhancement to improve its accuracy. To address this, an Artificial Neural Network (ANN) analysis is employed. The ANN is used to refine the radar QPE by leveraging its ability to model complex, non-linear relationships between the radar reflectivity data and the actual rainfall amounts. This advanced machine learning technique helps correct the inherent inaccuracies in the radar measurements, providing more reliable and precise precipitation estimates.

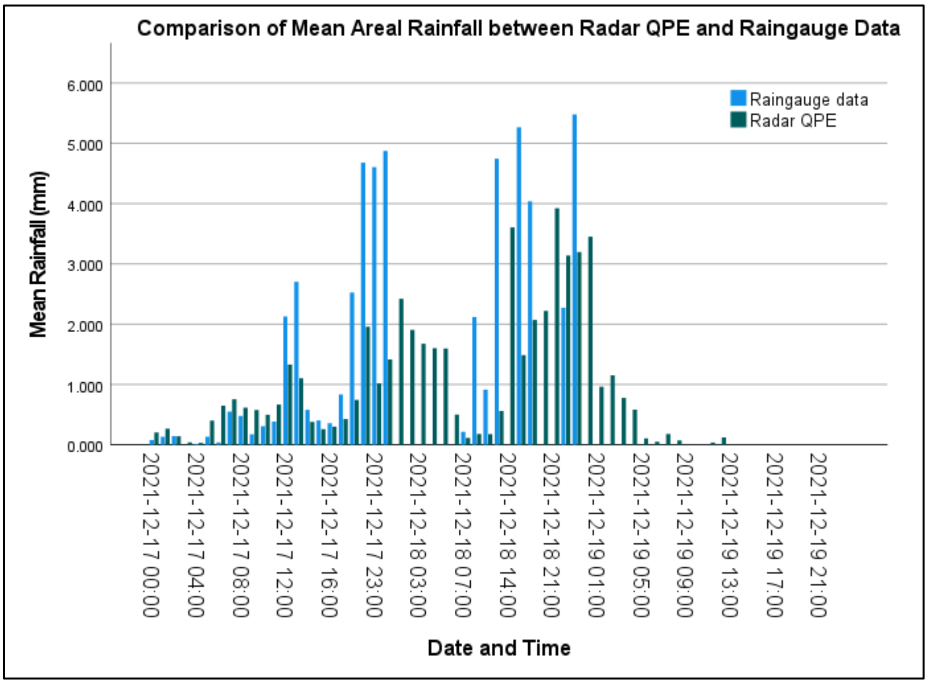

Figure 4.2 Uncalibrated Radar QPE versus Rain Gauge Measurements Comparison

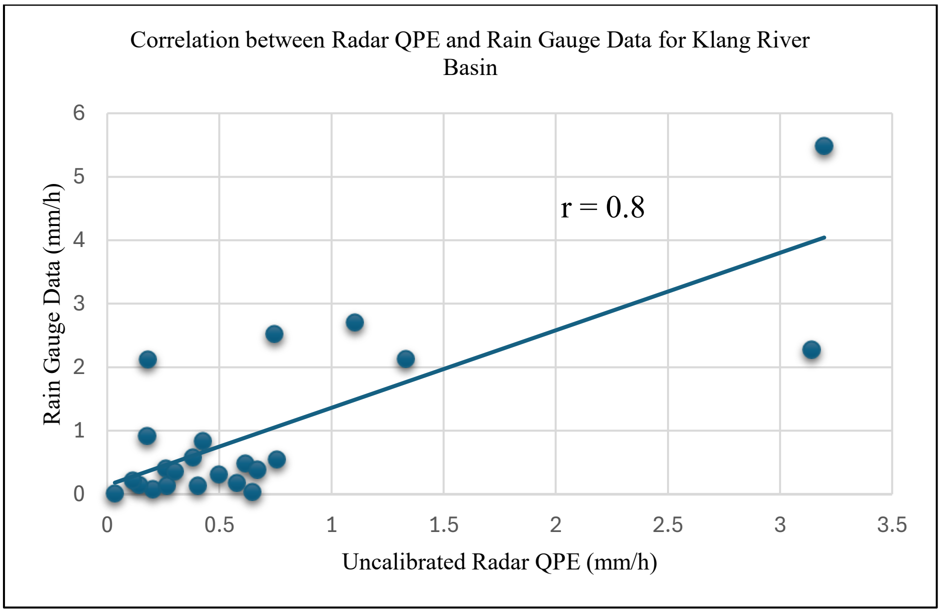

Figure 4.3 Scatter Diagram of the Correlation between Mean Areal Radar QPE and Mean Areal Rainfall Gauge Data

4.3 Rainfall Classification

4.3.1 General Classification

The Department of Drainage and Irrigation (DID) has classified rainfall categories for Malaysian conditions based on their intensity, as shown in Table 4.2. Convective rainfall exceeding 60 mm within a typical time frame of 2 to 4 hours may lead to flash floods.

Table 4.2
Rainfall Intensity Categorization (One Hour)

Category	Light	Moderate	Heavy	Very Heavy
Rainfall intensity (mm/h)	1-10	11-30	31-60	>60

(Source: DID, 2022)

4.3.2 Rainfall Classification based on Radar Reflectivity Images

Radar imagery typically uses a color scale to represent the intensity of precipitation in different areas, as described in Chapter 2. Meteorologists specializing in radar analysis often categorize precipitation based on its structure into two types: convective or stratiform. These classifications are based on the vertical and horizontal arrangement of precipitation patterns observed in the radar data. Convective rainfall is associated with intense, vertically oriented precipitation cores, while stratiform rainfall is characterized by more widespread, horizontally layered patterns.

Rainfall classification based on radar reflectivity relies on specific thresholds. Precipitation is generally considered stratiform when reflectivity is below 40 dBZ, indicating lighter, steady rainfall, while convective rainfall occurs when reflectivity exceeds 40 dBZ, corresponding to heavier, more intense precipitation often associated with thunderstorms (Rigo and Llasat, 2004; Karklinsky and Morin, 2006; Barnolas, 2010; Djafri and Haddad, 2014; Peleg et al., 2018). This classification system enables meteorologists to better understand rainfall intensity and dynamics, supporting weather forecasting and storm prediction.

In tropical regions, radar reflectivity is particularly reliable for distinguishing convective and stratiform rainfall due to the frequent occurrence of intense convective storms. Convective rainfall is characterized by strong vertical motion and larger raindrops, producing high reflectivity values, whereas stratiform rainfall typically shows weaker reflectivity signatures. Although the 40 dBZ threshold is commonly adopted, reflectivity in tropical environments can be influenced by monsoon conditions, storm organization, and microphysical processes, suggesting that regional calibration may enhance classification accuracy (Tokay and Short, 1996; Schumacher and Houze, 2003).

4.4 Radar Images Processing

The uncalibrated radar QPE map, stored as a raster file, was further processed using a Geographic Information System (GIS) application, as shown in Figure 4.4. The Langat and Klang River basins were chosen as the focal study areas due to the devastating flood disaster that occurred in December 2021. The data used in this study, which were derived from the uncalibrated RaINS system, span the period from December 2021 to August 2023. To ensure the quality of the data, the selected rainfall records were carefully screened to identify and remove any outliers or missing values. The chosen rainfall events encompass a broad spectrum of annual precipitation amounts, including those associated with the unprecedented flood disaster.

In total, 720 radar images were analyzed as part of this study. From these images, 559 precipitation structures were detected, with 210 of them identified as convective structures based on the available data. Figure 4.5 illustrates the radar image processing of several selected rainfall events, offering a visual representation of the analysis conducted. The remaining results are provided in the Appendix.

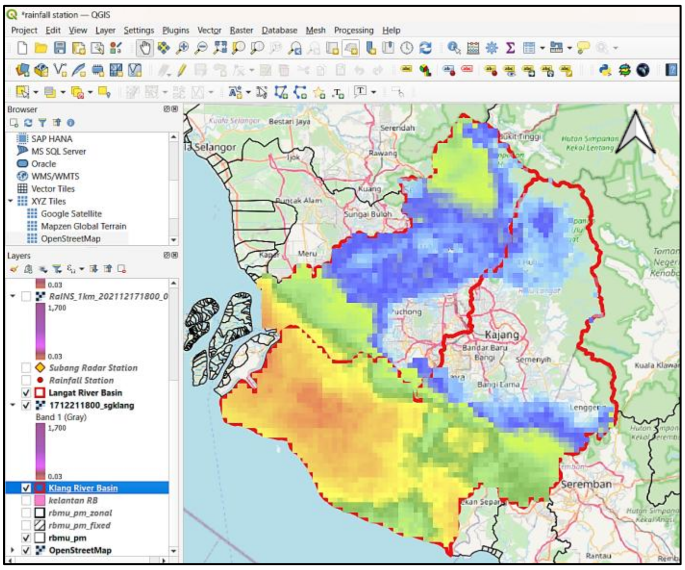

Figure 4.4 The Radar Reflectivity Map Processed in QGIS Software

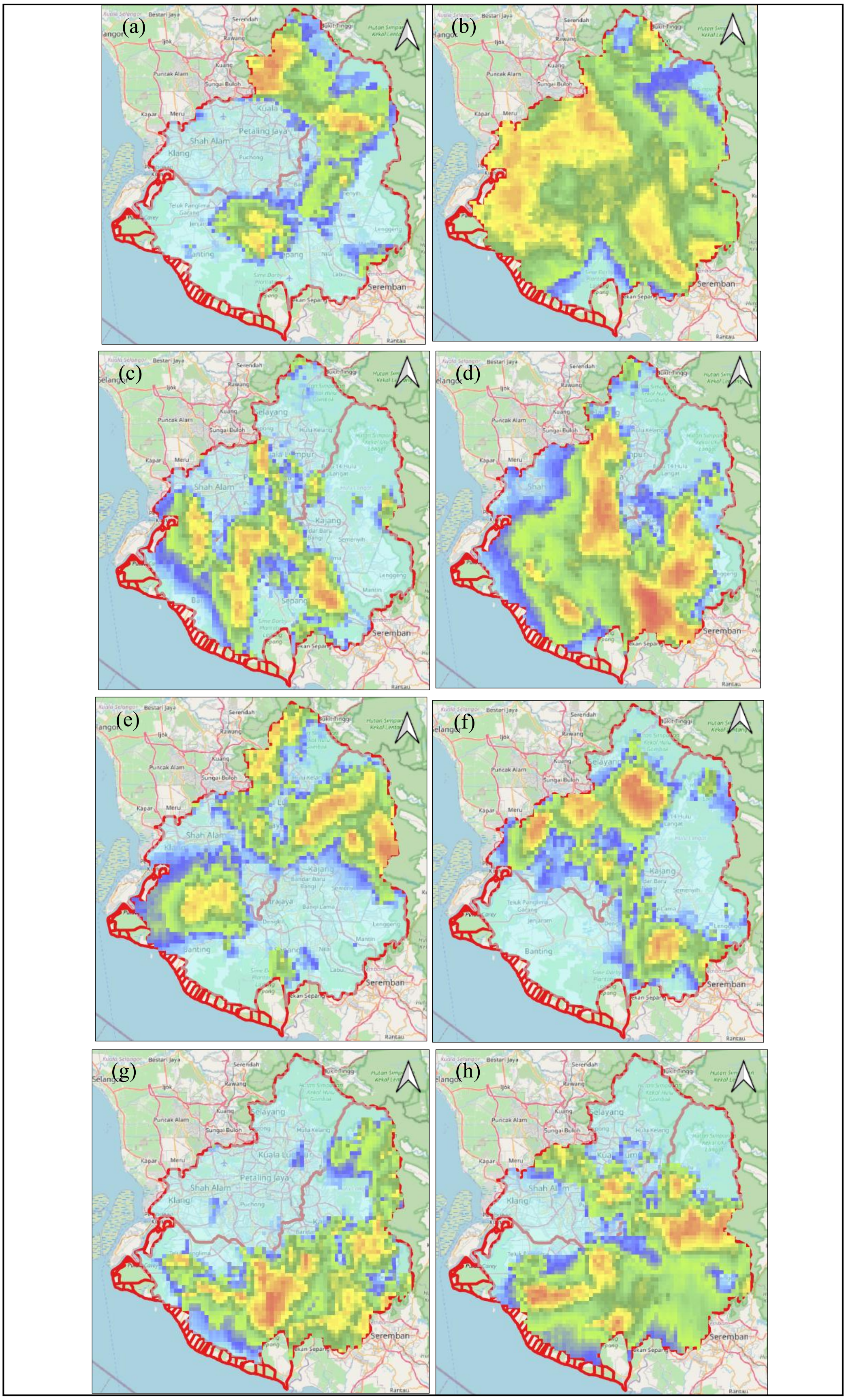

Figure 4.5 Radar Images for Selected Rainfall Events: (a) 23/08/22 at UTC 17:00, (b) 02/12/22 at UTC 22:00, (c) 01/02/23 at UTC 16:00, (d) 01/02/23 at UTC 17:00, (e) 11/02/23 at UTC 15:00, (f) 23/06/23 at UTC 15:00, (g) 24/06/23 at UTC 14:00, and (h) 24/06/23 at UTC 15:00

4.5 Feature Extraction of Radar Images

4.5.1 Image segmentation

Image segmentation refers to the technique of dividing a digital image into distinct regions or segments, where each segment corresponds to a specific part of the image with similar characteristics. In the context of this study, the original radar QPE map is segmented to identify rain cells, where different regions are color-coded to represent distinct segments as shown in Figure 4.6. One of the simplest methods for performing image segmentation is image thresholding. This approach involves setting a specific threshold value based on the pixel intensity of the image, allowing for the separation of certain features from the background.

In this case, the threshold is set at approximately 40 dBZ, which ensures that only areas representing convective rainfall, characterized by higher radar reflectivity values, are considered. These regions correspond to intense precipitation, such as thunderstorms or heavy rainfall. Figure 3.10 in Chapter 3 provides a concise illustration of the segmentation process. The results of this segmentation are visually presented in Figure 4.7, where the different rain cells are clearly identified and distinguished from one another based on the defined threshold. The remaining data is included in the Appendix.

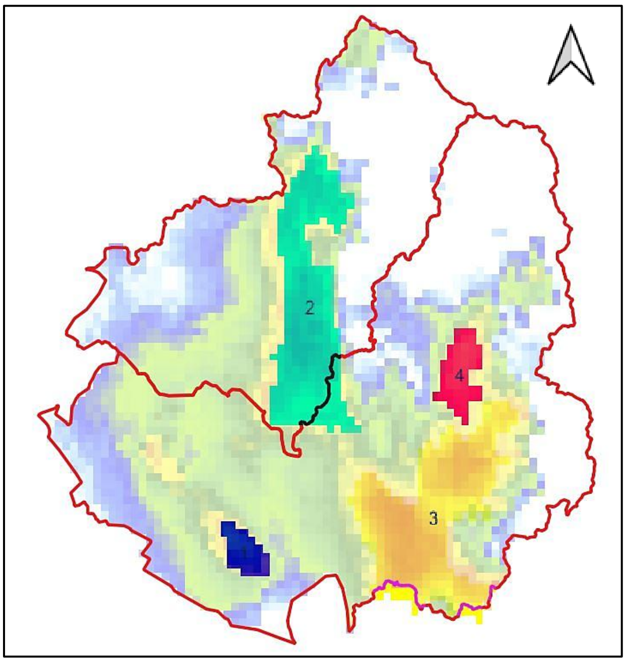

Figure 4.6 Different Rain Cells Color-Coded to Illustrate Distinct Segments

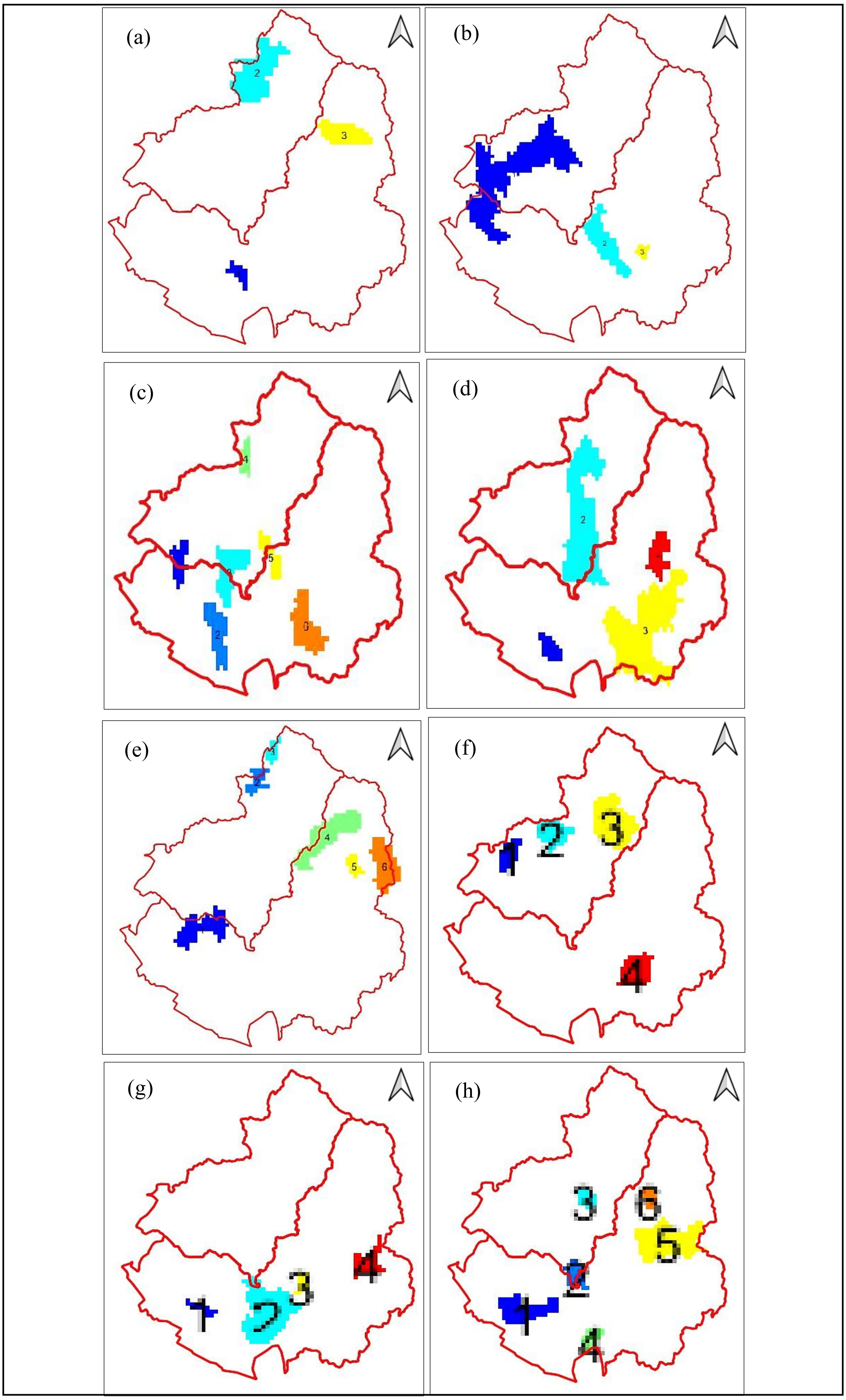

Figure 4.7 Image Segmentation of Selected Rainfall Events: (a) 23/08/22 at UTC 17:00, (b) 02/12/22 at UTC 22:00, (c) 01/02/23 at UTC 16:00, (d) 01/02/23 at UTC 17:00, (e) 11/02/23 at UTC 15:00, (f) 23/06/23 at UTC 15:00, (g) 24/06/23 at UTC 14:00, and (h) 24/06/23 at UTC 15:00.

4.5.2 Rain Cell Feature Extraction

The process of rain cell feature extraction involves deriving several features for each identified segment. Features are extracted from each fitted ellipse, including the center location (cell centroid), which represents the spatial position of the rain cell. The area of each cell is calculated in square kilometers to quantify its spatial extent. Additionally, the lengths of the major and minor axes are determined to describe the size and elongation of the cell. The orientation angle of the major axis is also computed, measured counterclockwise from the west-east direction, providing information on the alignment of the rain cell.

Furthermore, rainfall intensity characteristics are extracted, including the maximum and mean rainfall intensities within each cell, expressed in millimeters per hour. Maximum intensity represents the highest rainfall rate detected within an individual rain cell. It is derived by examining all radar pixels associated with the cell and identifying the maximum rainfall value among them, which reflects the peak intensity of the convective structure. In contrast, the mean gridded value represents the average rainfall intensity over a regular spatial grid covering the study area. This value is obtained by overlaying a fixed grid resolution on the radar image and averaging the rainfall values of all pixels within each grid cell. When a rain cell extends across multiple grid cells, its pixels contribute to the mean calculation of their respective grids. While maximum intensity captures localized extreme rainfall, the mean gridded value gives an average rainfall over an area, making it easier to compare different events and match with rain gauge data (Schleiss et al., 2020; Hydrologic Engineering Center, 2025)

Table 4.3 presents the results of rain cell feature extraction based on the rainfall events shown in Figure 4.7, while the remaining results are provided in the Appendix. The extracted features represent the attributes of rain cell structures detected during several rainfall or flood events. The chosen events range from moderate to very heavy rainfall, as stated in Table 2.1 of Chapter 2.

Next, the extracted data acts as the necessary input for training an Artificial Neural Network (ANN) model to improve the accuracy and effectiveness of radar QPE. Furthermore, these features also serve as the required input for a machine learning-based rainfall type classifier model. This classifier model will be capable of predicting different types of rainfall, such as convective and stratiform rain, based on the features derived from radar reflectivity maps.

Table 4.3
Feature Extraction of Radar Images for the Selected Rainfall Event between 2021 and 2023.

Date _Time	Cell Features								
	Rain cell	Center X	Center Y	Area, km^2	Major Radius, km	Minor Radius, km	Orientation, degree	Max Intensity, mm/h	Mean Gridded Value, mm/h
230822_17:00	1	32.56	62.56	16	7.35	3.53	-53.37	15.56	9.32
	2	36.82	15.50	105	17.39	8.97	59.64	24.17	13.92
	3	56.89	29.94	53	13.31	5.33	-13.08	23.97	11.58
021222_22:00	1	21.83	39.66	477	49.42	22.51	43.28	16.93	9.32
	2	50.95	61.92	128	26.24	8.09	-61.30	15.36	8.70
	3	63.13	64.81	16	5.31	4.55	77.04	10.81	8.12
010223_16:00	1	16.28	49.07	29	10.11	4.40	85.19	15.40	8.95
	2	25.94	63.90	51	15.47	4.97	-76.28	17.10	9.62
	4	33.19	27.24	21	8.90	3.33	86.17	16.76	11.19
	5	39.68	47.82	28	12.23	3.77	-61.05	17.78	10.57
	6	48.70	62.19	69	14.93	7.33	-69.62	24.43	12.50
010223_17:00	2	35.17	37.55	265	40.45	10.82	89.20	27.66	12.82
	3	52.66	64.05	305	29.67	19.00	59.39	45.72	17.26
	4	56.41	46.14	49	11.82	6.05	82.13	20.97	11.04
110223_15:00	1	20.69	51.94	67	16.01	7.48	21.92	12.40	8.46
	2	34.48	15.61	23	8.27	4.91	63.15	11.70	8.75
	3	38.38	8.06	16	7.28	3.22	70.57	12.72	9.01
	4	52.08	29.16	100	22.61	6.75	39.44	19.76	11.45
	6	66.54	36.43	67	14.34	6.62	-79.41	26.62	14.40
230623_15:00	1	17.16	32.81	37	10.02	4.95	66.68	25.97	14.28
	2	28.89	27.15	54	9.54	7.92	-11.00	21.80	11.39
	3	44.69	24.33	121	15.11	10.67	-64.63	31.38	16.60
	4	50.69	63.55	62	10.49	7.95	46.61	22.69	11.91
240623_14:00	1	20.38	62.13	16	9.45	2.60	-24.59	13.33	9.24
	2	36.28	63.50	149	18.07	12.53	80.84	34.59	14.91
	3	44.82	55.35	17	6.80	3.63	76.59	27.12	13.07
	4	61.29	49.76	42	11.10	7.46	55.08	14.76	9.69
240623_15:00	1	20.61	63.12	69	16.93	6.33	3.50	30.21	14.53
	2	34.00	54.69	32	8.22	5.62	-64.35	16.89	10.29
	3	36.90	34.90	20	5.85	4.57	-34.48	19.40	11.66
	4	38.17	70.09	23	7.22	4.58	44.05	24.19	11.62
	5	58.32	45.86	139	19.56	10.42	4.88	26.51	13.83

The accuracy of each rain segment is evaluated by comparing it with rain gauge data from the DID as shown in Figure 4.8. The mean gridded value and maximum intensity are compared with the mean areal rainfall from the 'ground-truth' rain gauges data, indicating the actual rainfall values (Militino et al., 2018). This demonstrates the strength of the relationship between gauge-measured rainfall and radar rainfall estimates, as shown in Table 4.4. The strength of the relationship between gauge-measured rainfall and radar rainfall estimates is observed through statistical agreement, indicated by a strong linear correspondence, high correlation coefficients, and reduced discrepancies between radar-derived and gauge-observed values. This consistency demonstrates the capability of the radar-based estimates to reliably represent the spatial and intensity characteristics of observed rainfall (Villarini and Krajewski, 2010).

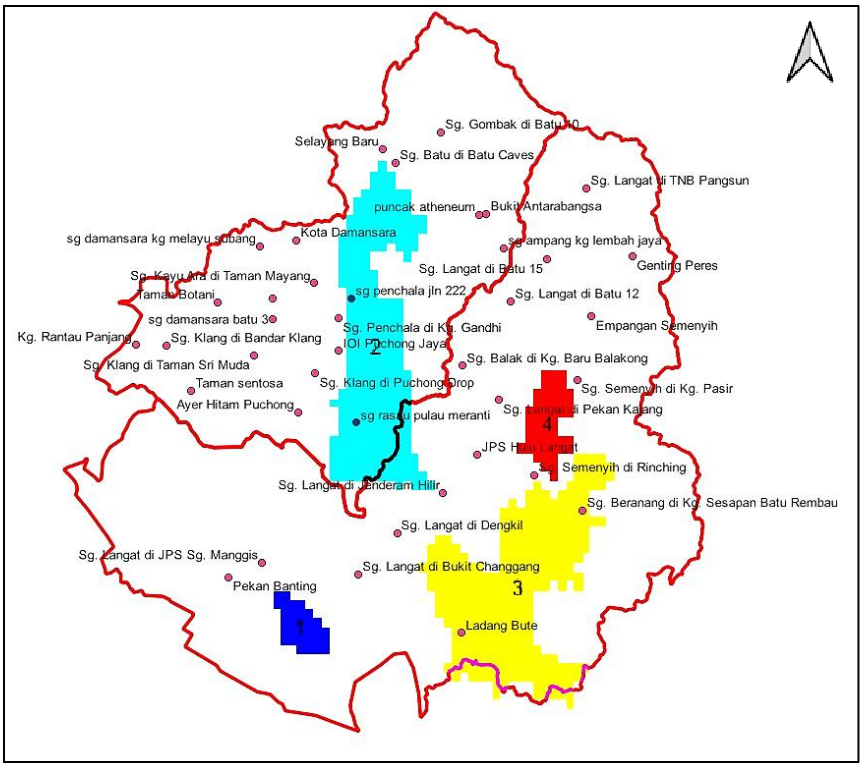

Figure 4.8 Rain Segment versus Areal Mean Gauge Value

Figures 4.9 and 4.10 illustrate the correlation between the mean gridded value and maximum rainfall intensity in both radar QPE and rainfall gauge data. The results show a moderately strong positive relationship, with correlation values of 0.81 and 0.82, respectively. The analysis also indicates that some rain cell segments are not located near a rainfall station. For areas without a nearby station, the value is recorded as ‘not available’ (NA), which is one of the limitations due to insufficient data. Additionally, the observation reveals that in many cases, the radar rainfall estimates are underestimated compared to the gauged rainfall.

ff

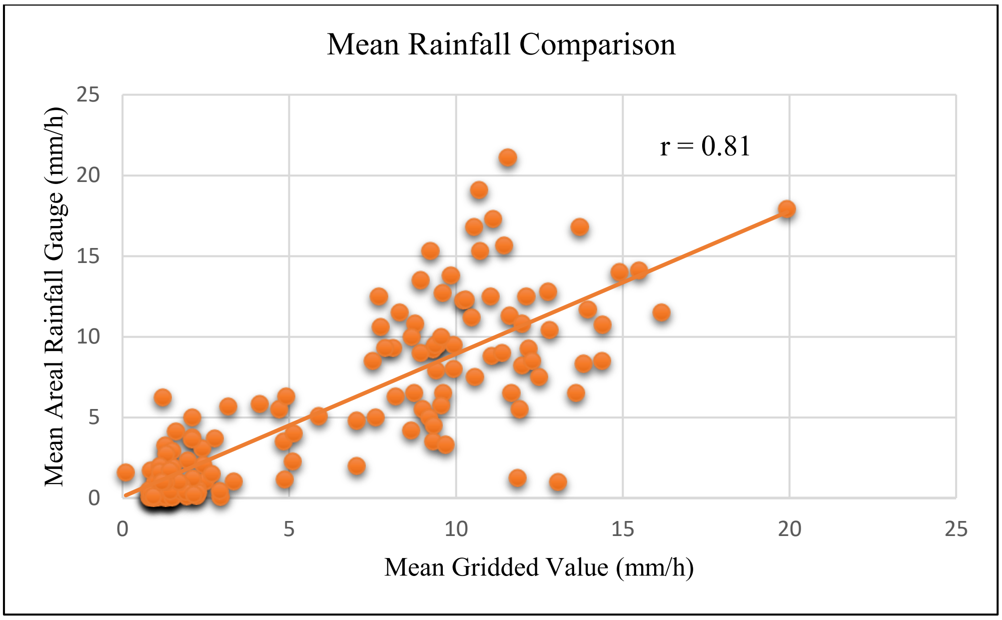

Figure 4.9 Radar-Gauge Comparison in Mean Intensity

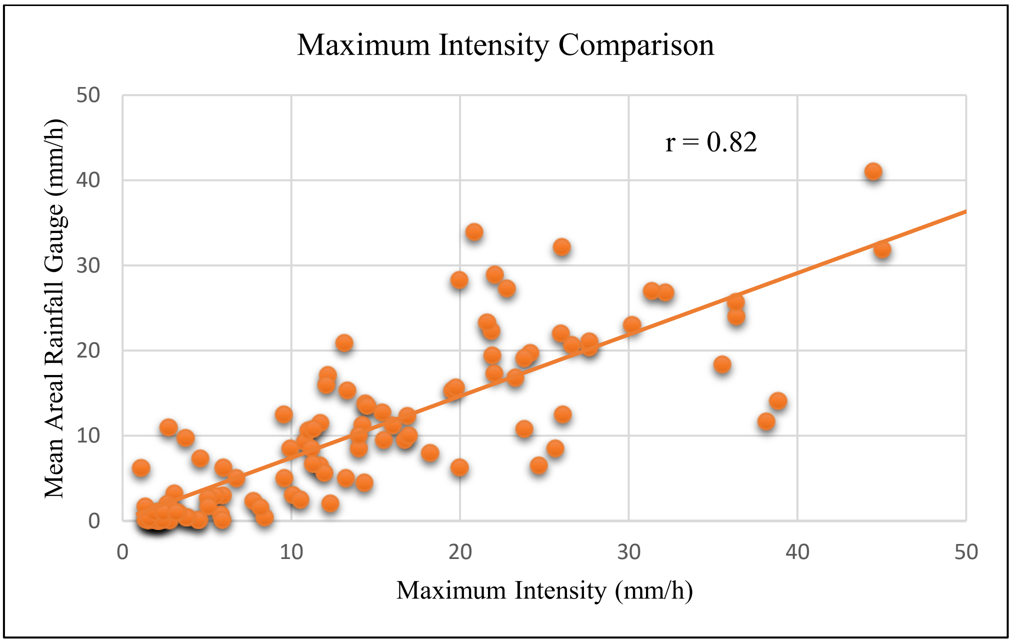

Figure 4.10 Radar-Gauge Comparison in Maximum Intensity

Table 4.4
Comparison of Two Features with the Mean Areal Rainfall Gauges for Selected Rain Events between 2021 and 2023

Maximum Intensity (mm/h)	Mean Gridded Value (mm/h)	Mean Areal Rainfall Gauge (mm/h)	Maximum Intensity (mm/h)	Mean Gridded Value (mm/h)	Mean Areal Rainfall Gauge (mm/h)
20.86	11.31	33.9	25.29	2.77	3.68
32.18	11.05	26.8	24.69	3.73	9.2
26.64	11.39	20.7	22.32	2.93	8.74
21.85	10.80	22.3	37.43	5.89	5.06
24.17	13.92	19.7	19.00	2.58	8.07
9.59	7.22	17	1.00	0.71	9.96
22.06	10.55	28.9	4.23	1.68	16.33
52.12	16.17	11.5	44.95	7.88	9.3
31.97	13.72	16.8	14.00	2.42	8.5
19.55	10.73	15.3	0.89	0.71	7.75
22.38	11.61	11.3	3.74	0.97	9.74
11.72	8.32	11.5	2.74	1.21	11
21.61	10.40	23.3	19.98	4.91	6.3
26.06	13.34	32.2	9.94	2.23	8.5
27.69	11.96	20.38	21.80	11.39	9
28.24	12.77	12.78	31.38	16.60	27
14.26	9.38	28.43	13.33	9.24	15.3
27.66	12.82	10.4	38.18	13.96	11.7
20.97	11.04	12.5	36.36	16.47	25.7
9.56	7.69	12.5	14.38	9.85	13.8
11.70	8.75	6.5	22.05	11.12	17.30
19.76	11.45	15.67	22.78	11.29	27.3
26.62	14.40	10.75	16.73	9.94	9.5
34.93	12.53	26.5	16.04	10.47	11.2
21.91	10.22	12.25	9.61	7.60	5
28.13	14.38	8.5	11.32	8.78	10.8
36.40	13.86	24	31.01	12.18	9.25
11.03	7.74	10.6	16.96	8.68	10
24.92	11.07	8.8	25.66	12.29	8.5
23.81	10.70	19.1	14.49	8.94	13.5
21.91	2.80	19.405	20.85	9.56	5.75
45.05	4.36	31.89	15.41	9.60	12.7
5.98	1.21	6.25	24.66	13.60	6.5
12.20	2.09	3.62	15.48	9.38	9.5
3.07	1.28	3.25	38.85	15.49	14.1
30.82	2.47	9.7	18.23	9.94	8
14.21	2.10	11.3	19.70	9.81	44.5
6.76	2.10	5	12.09	8.57	16
25.28	5.14	4	13.16	9.61	20.9
13.32	1.61	4.14	23.28	10.54	16.8
11.95	3.17	5.67	23.83	11.98	10.8
22.67	4.91	9.33	14.00	9.56	10

4.6 Classification of Rainfall using K-Nearest Neighbor Algorithm

Figure 4.11 illustrates a scatter plot showing the relationship between mean intensity and maximum intensity of radar rainfall. In this plot, the blue points represent convective rainfall, while the red points indicate stratiform rainfall. The plot demonstrates that the K-Nearest Neighbor (KNN) algorithm effectively classifies the rainfall based on the selected features, as the majority of data points are correctly categorized into their respective classes. Nevertheless, it is important to note that there are a few instances where the algorithm misclassifies certain points. These misclassifications suggest that while the KNN method is largely successful in distinguishing between convective and stratiform rainfall, there may be some overlap or ambiguity in the feature space that leads to occasional errors in classification.

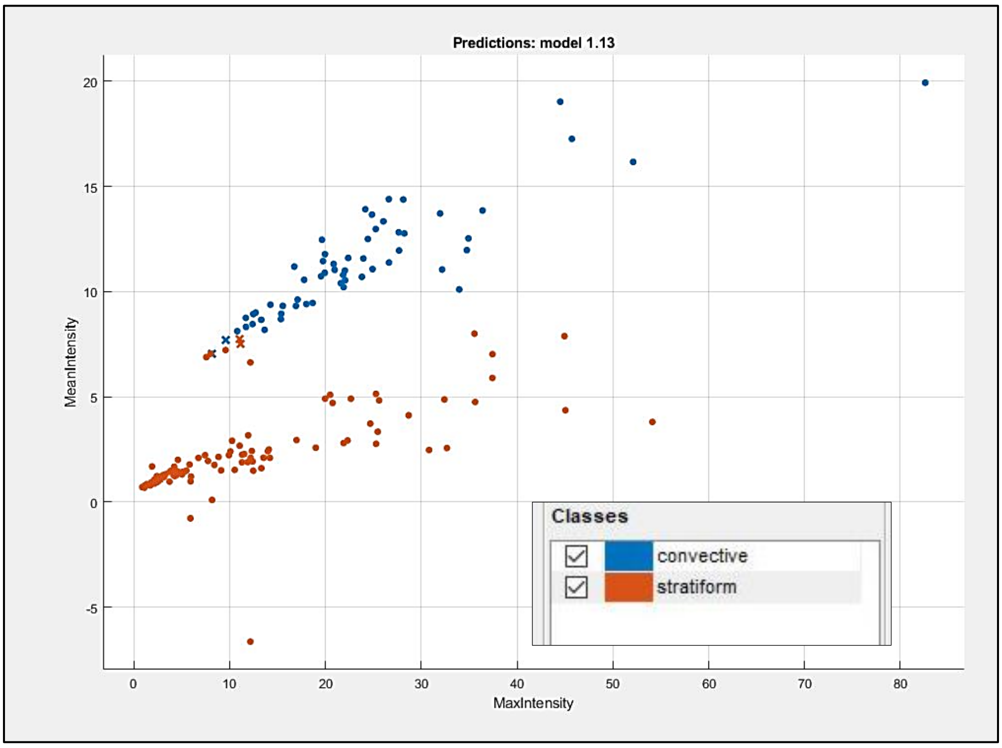

Figure 4.11 Mean Intensity versus Maximum Intensity

A confusion matrix is a graphical representation used to evaluate the performance of a classification model by comparing its predicted labels to the true labels of the dataset. This matrix helps in analyzing how well the model has learned from the training data and provides insight into the types of errors the model may be making. As shown in Table 4.5, the confusion matrix consists of four key components: true positives (TP), true negatives (TN), false positives (FP), and false negatives (FN). These values indicate the accuracy of the model's predictions, with TP representing correctly predicted positive cases, TN for correctly predicted negative cases, FP for incorrectly predicted positive cases, and FN for incorrectly predicted negative cases. The results of the confusion matrix for this model are depicted in Figure 4.12, where the counts are as follows: 55 true positives (TP), 143 true negatives (TN), 2 false positives (FP), and 2 false negatives (FN). These values provide a clear summary of the model's prediction performance, allowing for a deeper understanding of its strengths and weaknesses.

Table 4.5

Confusion Matrix Summary (Susmaga, 2004)

Category	Description
True Positives (TP)	It represents the count of true positive cases, where the model correctly predicts a positive label
True Negatives (TN)	It represents the count of true negative cases, where the model correctly predicts a negative label.
False Positives (FP)	It represents the count of false positive cases, where the model incorrectly predicts a positive label for a negative case.
False Negatives (FN)	It represents the count of false negative cases, where the model incorrectly predicts a negative label for a positive case.

In addition, accuracy of the confusion matrix is one of the most commonly used metrics for assessing the performance of a classification model. As defined in Equation 4.1, accuracy represents the proportion of correctly classified instances out of the total number of instances. In simpler terms, it measures how frequently the model makes correct predictions overall.

$$
\begin{aligned}
Accuracy &= \frac{TP+TN}{TP+FP+TN+FN} \\
&= \frac{55+143}{55+2+143+2} \\
&= 0.98
\end{aligned}
\tag{4.1}
$$

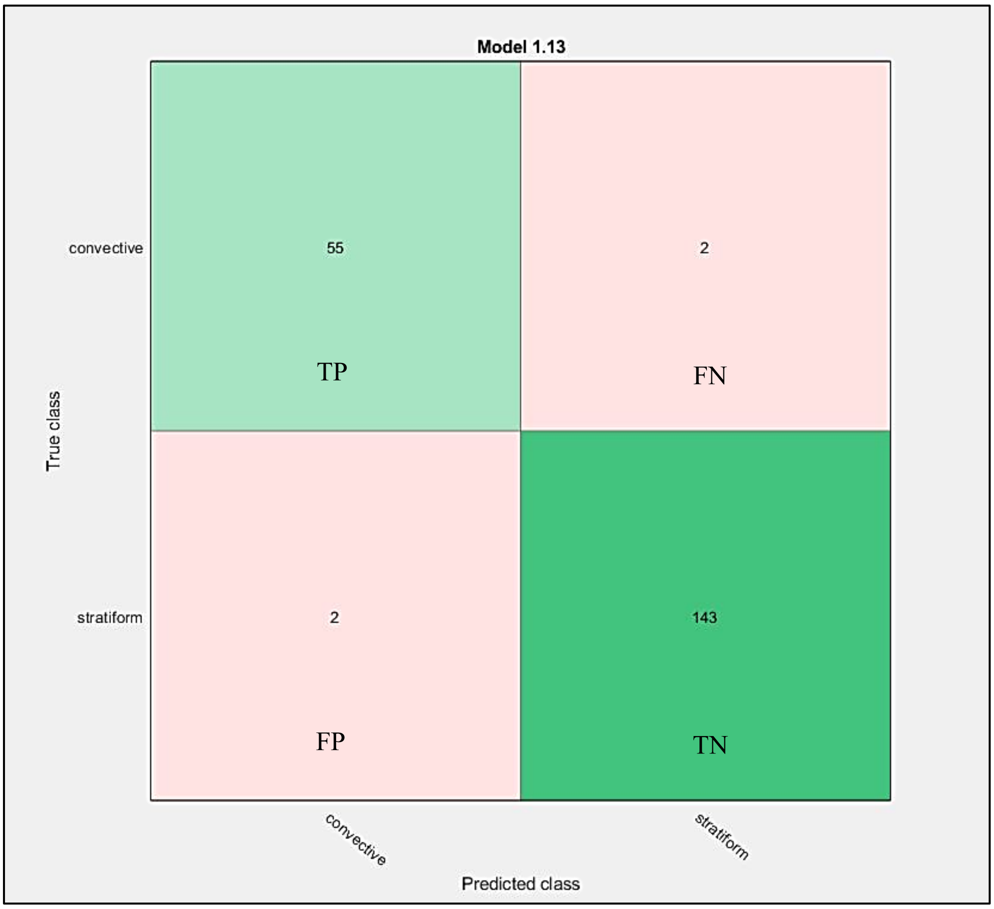

Figure 4.12 The Confusion Matrix of Rainfall Classification

Figure 4.13 illustrates that a higher value of the Area Under the Curve (AUC) indicates a better-performing classifier. The AUC score of the model is more than 90%, which is considered an excellent result. The more the Receiver Operating Characteristic (ROC) curve of a model moves toward the (0.0, 1.0) point (representing the ideal classifier) the better the model's ability to predict correctly across all classification thresholds (Flach, 2019). This highlights the model's overall predictive strength, with a curve closer to the top-left corner indicating superior performance.

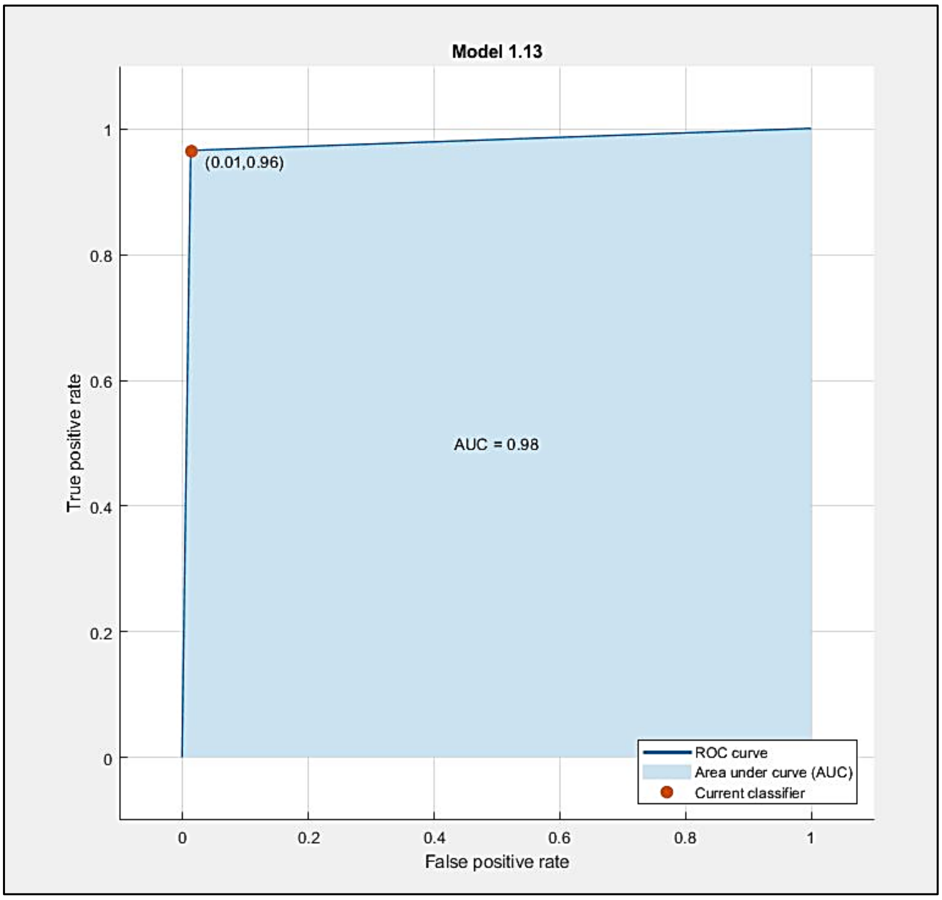

Figure 4.13 Graph of ROC Curve

4.7 Optimization of Z-R Relationship

Currently, the Subang Doppler radar uses the traditional Marshall-Palmer equation ($Z=200R^{1.6}$) to convert reflectivity into rainfall rate in millimetres per hour . A comparison with rain gauge observations shows that some of the radar data is underestimated (Figure 4.2). Therefore, it is essential to implement a new Z-R relationship to improve accuracy. An optimization approach has been applied to establish new Z-R relationships for stratiform rainfall (<40 dBZ) and convective rainfall (>40 dBZ). The classification is essential for assessing rainfall rates in terms of error measurement.

The new Z-R relationships were determined using a statistical method called Solver Optimization Analysis, which reduced the error between radar data and gauge data. Currently, the Malaysian Meteorological Department (MMD) uses the Z-R equation derived from the Marshall-Palmer relationship, where $Z=200R^{1.6}$. The newly determined Z-R relationship for the Klang and Langat River Basins is shown in Table 4.6 below.

The new Z-R relationship, $Z=158R^{1.9}$, was modified through solver analysis. The results revealed a reduction in measurement error and an improvement in hourly rainfall data accuracy, with a 44% difference between new Z-R and gauge data as shown in Figure 4.14. Meanwhile, the best Z-R relationship achieved from optimization work for convective rainfall with an intensity greater than 40dBZ is $Z=40R^{1.9}$. Compared to rain gauge data, the results obtained with this new Z-R were much better than those using $Z=200R^{1.6}$. The new Z-R equation improved the results, reducing the discrepancy between the gauge data and the new Z-R to 34% as illustrated in Figure 4.15.

Table 4.6

New Z-R Relationships for Klang and Langat River Basin

Rainfall Classification	Current Z/R equation	Newly modified Z/R equation
Stratiform	$Z=200R^{1.6}$	$Z= 158R^{1.9}$
Convective	$Z=200R^{1.6}$	$Z= 40R^{1.9}$

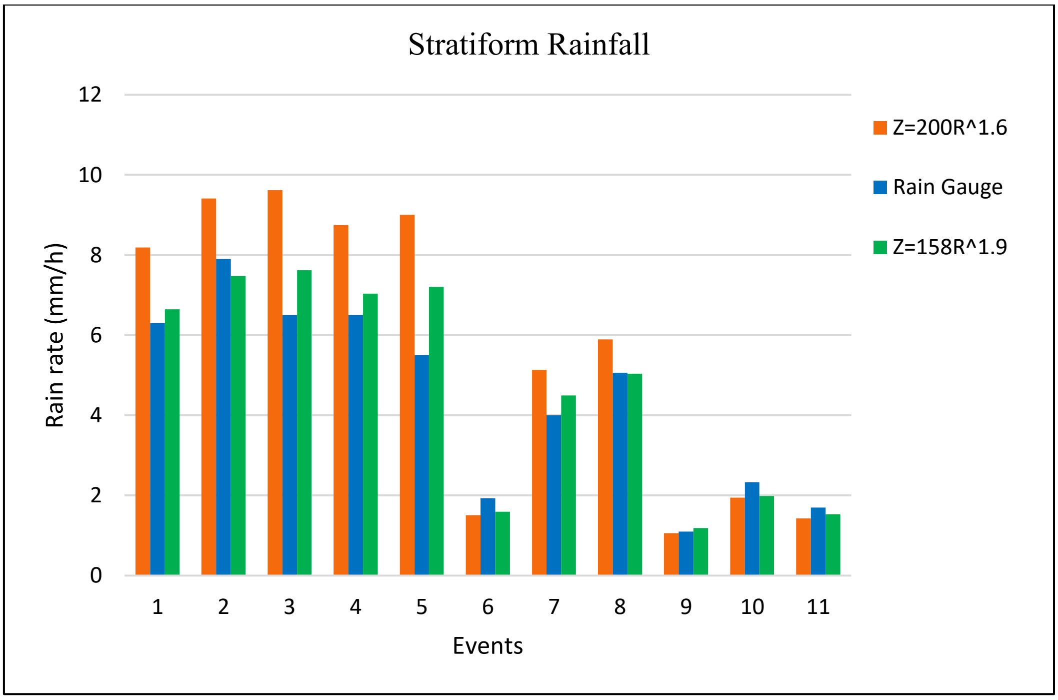

Figure 4.14 Comparison of Z-R Relationships for Stratiform Rainfall

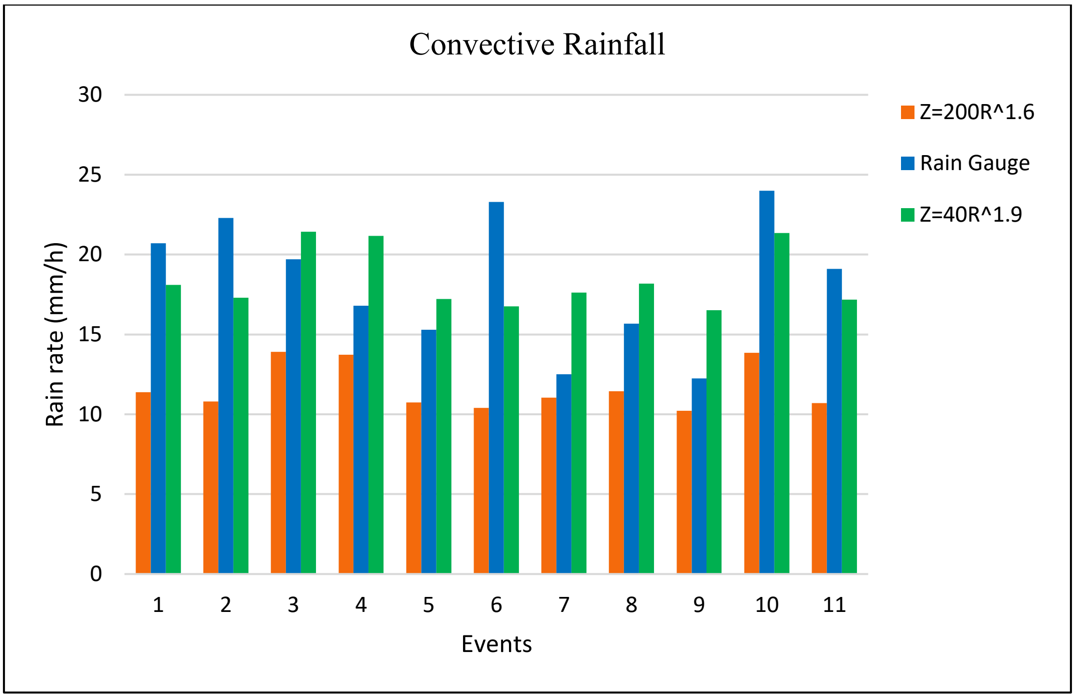

Figure 4.15 Comparison of Z-R Relationships for Convective Rainfall

4.7.1 Validation of New Z-R Relationships

Table 4.7 shows the statistical measurements of error for stratiform and convective rainfall categories. From the table, it is evident that stratiform rainfall exhibits a smaller reduction in error compared to convective rainfall. Applying the new Z-R relationships reduces the MAE for stratiform rainfall from 2.26 to 2.16, and for convective rainfall, the MAE decreases from 8.92 to 7.09. The RMSE values also decrease for both stratiform and convective rainfall, from 3.11 to 2.93 and from 11.25 to 8.24, respectively. These lower RMSE values suggest that the new Z-R relationships lead to more accurate predictions and provide a better fit to the data.

Table 4.7
Statistical Measurement for Different Z/R Relationships

Category	Z/R	MAE	RMSE
Stratiform	$Z=200R^{1.6}$	2.26	3.11
	$Z=158R^{1.9}$	2.16	2.93
Convective	$Z=200R^{1.6}$	8.92	11.25
	$Z=40R^{1.9}$	7.09	8.24

4.8 Development of ANN-based Radar QPE

Radar data often encounters limitations and discrepancies because of differences in spatial and temporal resolution, which can affect the accuracy of rainfall measurements. These discrepancies arise when radar observations and other data sources, such as ground-based measurements, are not perfectly aligned in terms of location and time. As a result, the radar data may not fully capture certain rainfall characteristics, leading to inaccuracies. To address these challenges, an Artificial Neural Network (ANN) analysis is applied. The ANN helps refine the radar data by learning complex patterns in the data, effectively enhancing its accuracy and providing more reliable rainfall estimates.

Table 4.8

Input and Output Variables to the ANN Model

Input	Output
Center X	
Center Y	
Area (km^2)	
Major Radius (km)	Radar rain rate (mm/h)
Minor Radius (km)	
Orientation (degree)	
Maximum Intensity (mm/h)	
Mean Gridded Value (mm/h)	

The ANN model is structured to enhance radar QPE, with rain cell features extracted from radar images acting as inputs as shown in Table 4.8. These features pass through an input layer and a hidden layer, which performs computations using a feedforward neural network approach. During training, the ANN adjusts the weights and biases between neurons to optimize its performance, resulting in more accurate hourly rainfall estimates. These adjustments fine-tune the network’s ability to predict rainfall by learning complex relationships between the input data and the output. Once the network is built and trained, its performance is rigorously tested and validated using various evaluation metrics to ensure its reliability and accuracy in making predictions such as mean squared error (MSE). The performance is determined through a performance plot, which displays the value of the performance function against the iteration number. This plot includes the training, validation, and test performances. As shown in Figure 4.16, the plot illustrates the errors for training, validation, and test sets. The best validation performance occurred at iteration 10, and the network at this iteration is returned.

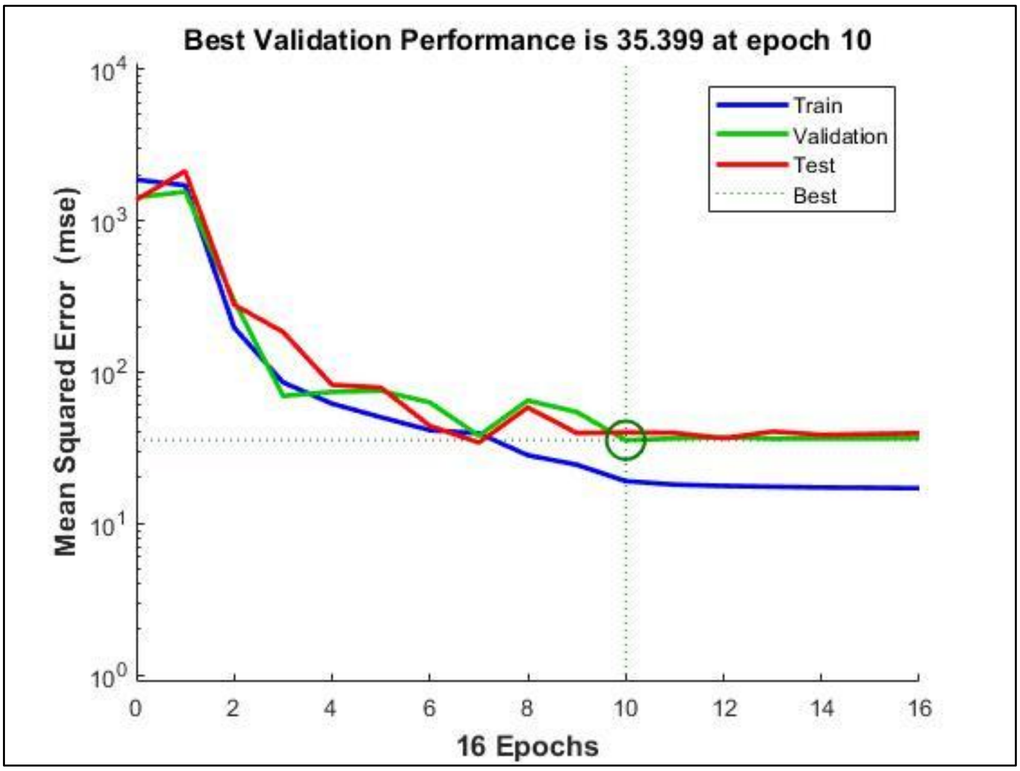

Figure 4.16 Performance Plot of ANN Model

Figure 4.17 presents an error histogram that illustrates the distribution of network errors. The histogram distinguishes between different datasets: the training data is represented by blue bars, the validation data by green bars, and the testing data by red bars. As shown in the figure, the majority of significant errors are concentrated around zero, indicating that the model is generally performing well with small errors. This is a positive sign, as it suggests that the network's predictions are mostly accurate. Furthermore, it can be observed that the instances of larger errors decrease sharply as the error values move away from zero at both ends of the error range.

The Levenberg-Marquardt (LM) algorithm was selected as the training method to achieve optimal performance in the ANN model. Although it requires more memory compared to other algorithms, it is highly efficient and reliable, particularly for predicting rain rates (Roslan et al., 2021; Suprajitno, 2022). The LM algorithm is especially effective when initial parameter values are far from the expected reflectivity, as it can still make accurate predictions, and it is well-suited for handling inversion problems, processing them more quickly than other methods in complex parameter estimation scenarios. During training, LM minimizes the error between predicted and observed rainfall by combining the fast convergence of the Gauss–Newton method with the stability of gradient descent, dynamically adjusting step sizes to efficiently reduce the mean squared error. It was chosen over standard gradient descent and Bayesian regularization because it converges faster, handles the nonlinear relationships in rainfall-runoff and QPE correction effectively, and provides a good balance between training speed and predictive accuracy (Aghelpour et al., 2022).

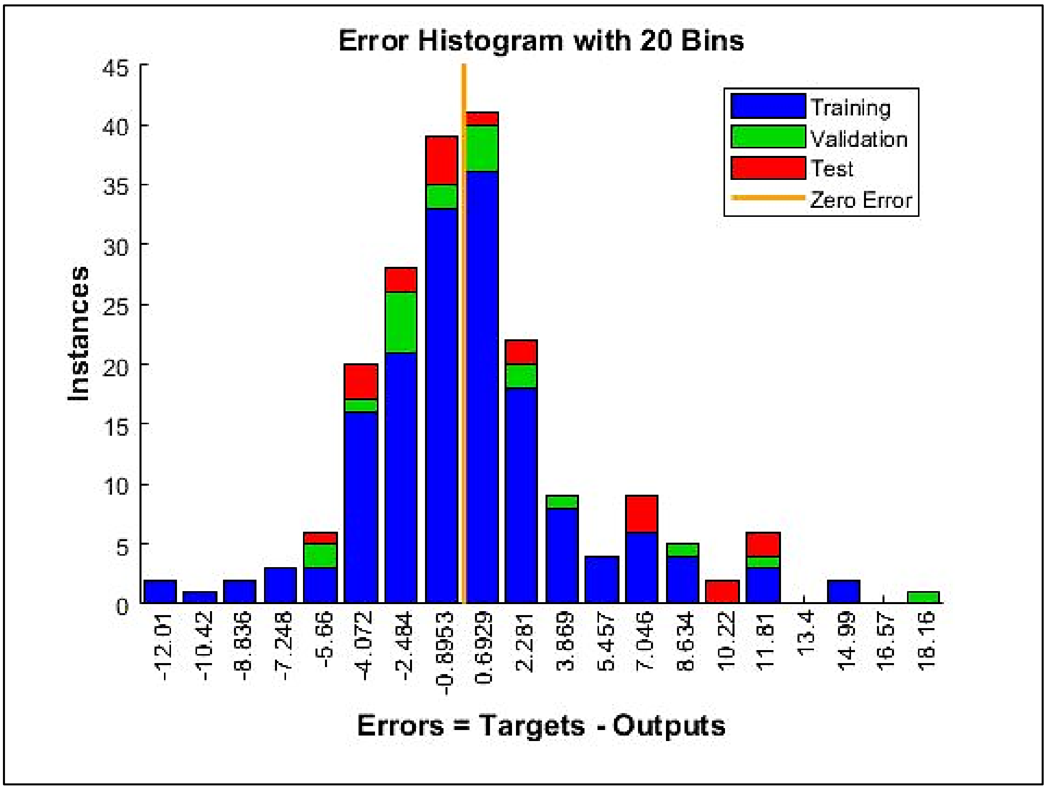

Figure 4.17 Error Histogram of Network Distribution

Figure 4.18 presents a scatter plot that illustrates the relationship between the model's predicted radar QPE and the observed rainfall. In an ideal scenario, the data points should align along a 45-degree line, where the predicted values exactly match the observed rainfall values. The plot demonstrates a relatively strong fit for each dataset, with the overall result yielding an R value of 0.9. This high correlation coefficient indicates a strong relationship between the model's predicted values and the observed data, suggesting that the model's predictions are generally accurate.

While ANNs can enhance radar-based rainfall estimates, they have several limitations, including the risk of overfitting, strong dependence on high-quality data, limited generalization across regions or time periods, and low interpretability, as well as high computational demands for real-time applications. Nevertheless, there is room for improvement, as the network can be retrained to refine its predictions further. There are several strategies that can be implemented to improve the ANN model's accuracy (Laskar and Majumder, 2015; Abdolrasol et al., 2021). First, before each training session, the network should be reset with newly initialized weights and biases to ensure that the model starts from a fresh state, preventing any bias from previous training runs. Second, the number of hidden neurons in the network can be gradually increased. This allows the model to capture more complex patterns and improve its ability to generalize. Furthermore, the size of the training dataset should be expanded incrementally. By providing the model with more diverse training examples, it can learn more robust representations of the data. Similarly, the number of input features may also be increased over time to incorporate more relevant information that could enhance the model's predictive power. Furthermore, periodically adjusting or modifying the training algorithm (such as changing the learning rate or the optimization technique) also can help the network converge more efficiently, leading to better performance.

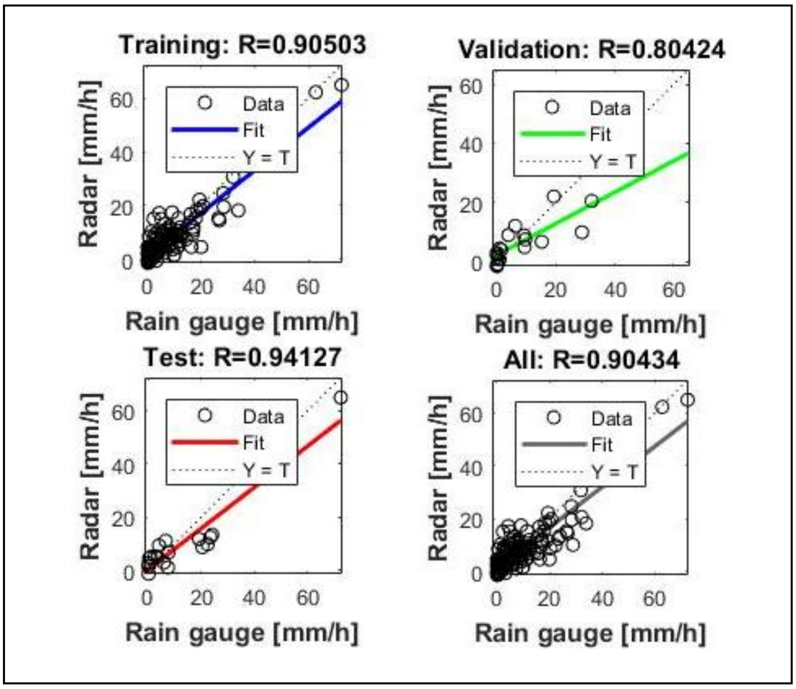

Figure 4.18 Scatter Plot Showing Correlation between Observed Rainfall and ANN Based-Radar QPE

4.8.1 Model Validation

The effectiveness of the ANN-enhanced Radar QPE model was evaluated through the root mean square error (RMSE) and the correlation coefficient (r). An RMSE approaching zero indicates that the predicted rainfall values are very close to the observed data, reflecting high accuracy, while a high correlation demonstrates that the model effectively captures the temporal and spatial patterns of rainfall. Together, low RMSE and high correlation indicate that the ANN-based radar QPE correction is both precise and consistent, making it reliable for hydrological and flood forecasting applications (Legates and McCabe, 1999).

As presented in Table 4.9, the results show a significant improvement in the model's performance, with RMSE reducing from 11.40 mm/h to 4.76 mm/h after applying the ANN. This reduction represents a substantial improvement in predictive accuracy, indicating that the corrected rainfall estimates are much closer to observed values. RMSE is widely used in hydrological model evaluation to quantify the average discrepancy between simulated and observed data, with values closer to zero reflecting better model fidelity and reduced error in forcing inputs, such as rainfall, for runoff simulations (Razeghi et al., 2026). In rainfall-runoff modeling and flood forecasting, more accurate rainfall input directly improves discharge and hydrograph predictions because hydrological models are highly sensitive to precipitation intensity. This leads to better calibration, enhanced reliability of peak discharge estimates, and more trustworthy operational forecasts. Improved RMSE also typically correlates with higher confidence in model performance across calibration and validation periods, which is essential for water resource management and decision-making (Sharma and Sharma, 2025).

This indicates that the ANN significantly enhanced the accuracy of the radar-based precipitation estimates. In addition to the RMSE analysis, the relationship between radar QPE and rainfall measurements from gauges was further explored through scatter plots illustrating the correlation coefficient both before and after the ANN implementation, as shown in Figure 4.19 and Figure 4.20. In addition, Figure 4.21 presents a plot comparing the rainfall gauge data to the ANN-enhanced radar QPE, with the 95% confidence interval. Overall, the use of ANN in hourly radar rainfall estimation yielded highly satisfactory results, with the correlation coefficient (r) ranging from 0.55 to 0.92. This wide range of correlation values demonstrates a strong positive relationship between the ANN-enhanced Radar QPE estimates and the rain gauge data, showcasing the ANN model's ability to significantly refine the radar-based precipitation estimates and improve their alignment with observed rainfall data.

Table 4.9

Performance Measurement of ANN-Radar QPE

	Radar QPE	ANN-Radar QPE
RMSE	11.40	4.76
Correlation coefficient, r	0.55	0.92

Further analysis in Table 4.10 reveals a reduction in the standard deviation after applying the ANN model, dropping from 11 to 9. A lower standard deviation which closer to 1 or below suggests that the data points are more tightly grouped around the mean, indicating reduced variability and greater consistency in the model's predictions. Figure 4.22 also highlights that the mean value of the radar QPE after the ANN application is lower compared to the pre-ANN mean, further supporting the model's refinement in estimating rainfall rates. A lower MSE is indicative of better model performance, with zero MSE indicating perfect accuracy, as there would be no difference between the predictions and the observed data (Das et al., 2004).

Table 4.10

Descriptive Statistics of Radar QPE Model

Radar intensity

	N	Mean	Std. Deviation	Std. Error	95% Confidence Interval for Mean		Minimum	Maximum
					Lower Bound	Upper Bound		
Before ANN	202	7.1594	11.05345	.77772	5.6258	8.6929	.02	72.48
After ANN	202	6.7378	9.38099	.66004	5.4363	8.0393	-1.51	64.97
Total	404	6.9486	10.24083	.50950	5.9470	7.9502	-1.51	72.48

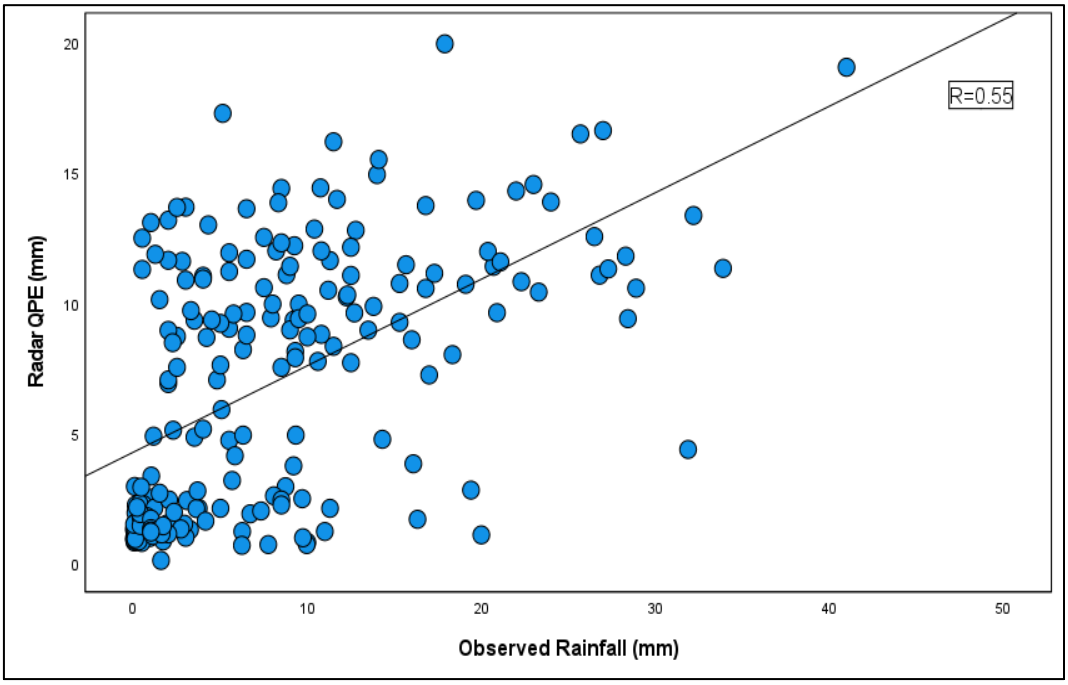

Figure 4.19 Correlation between Observed Rainfall and Radar QPE

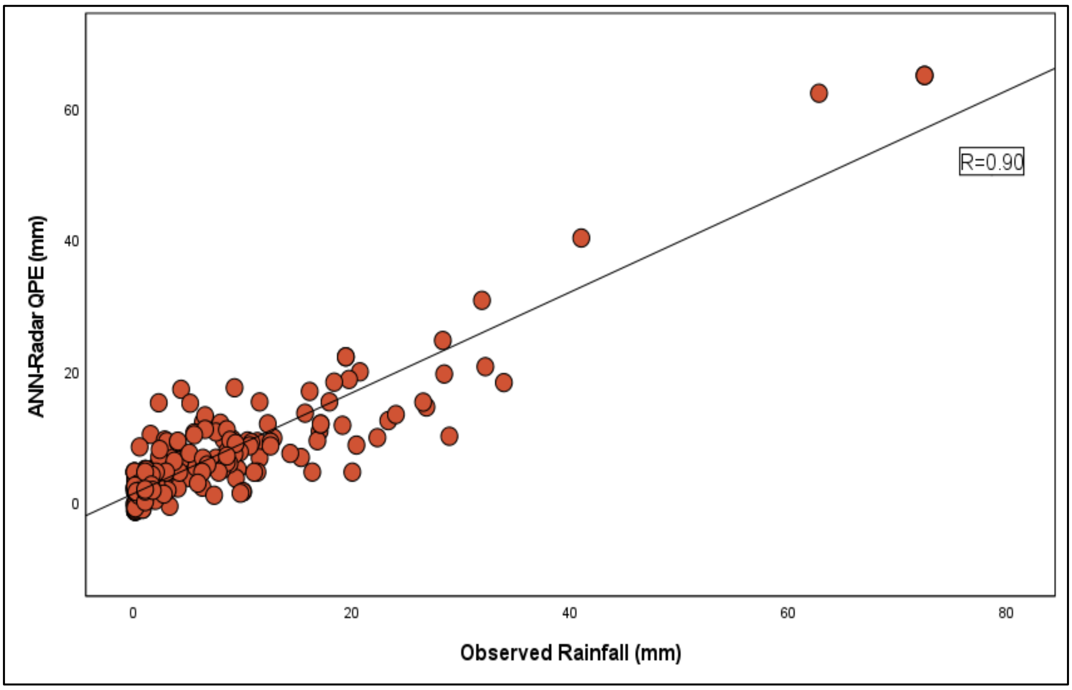

Figure 4.20 Correlation between Observed Rainfall and ANN-Enhanced Radar QPE

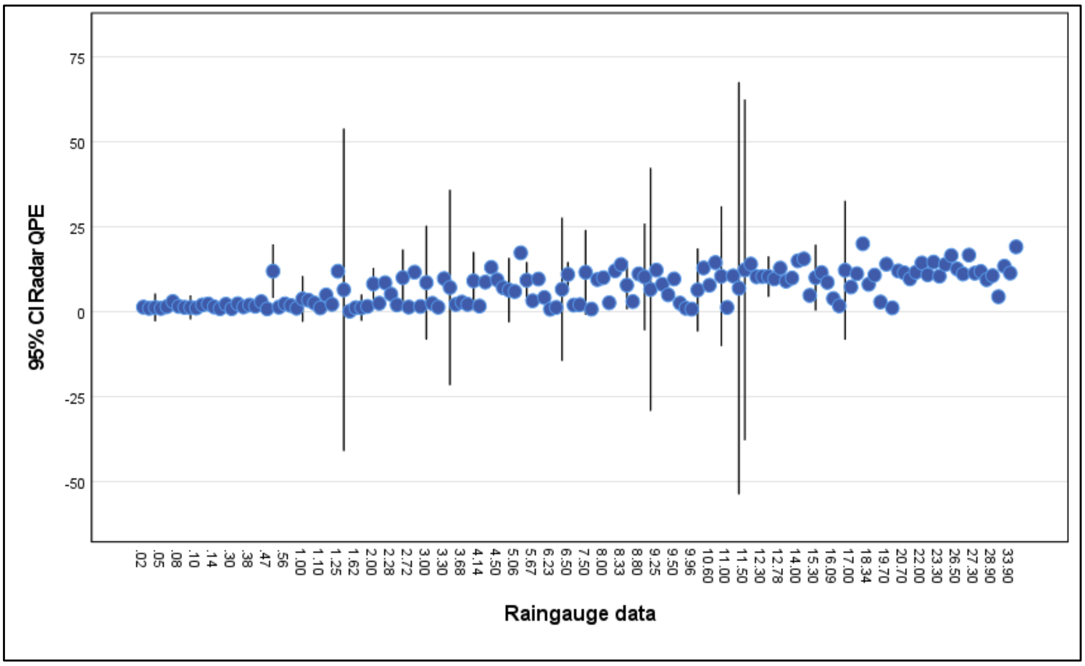

Figure 4.21 Raingauge Data Plotted against the ANN-Enhanced Radar QPE

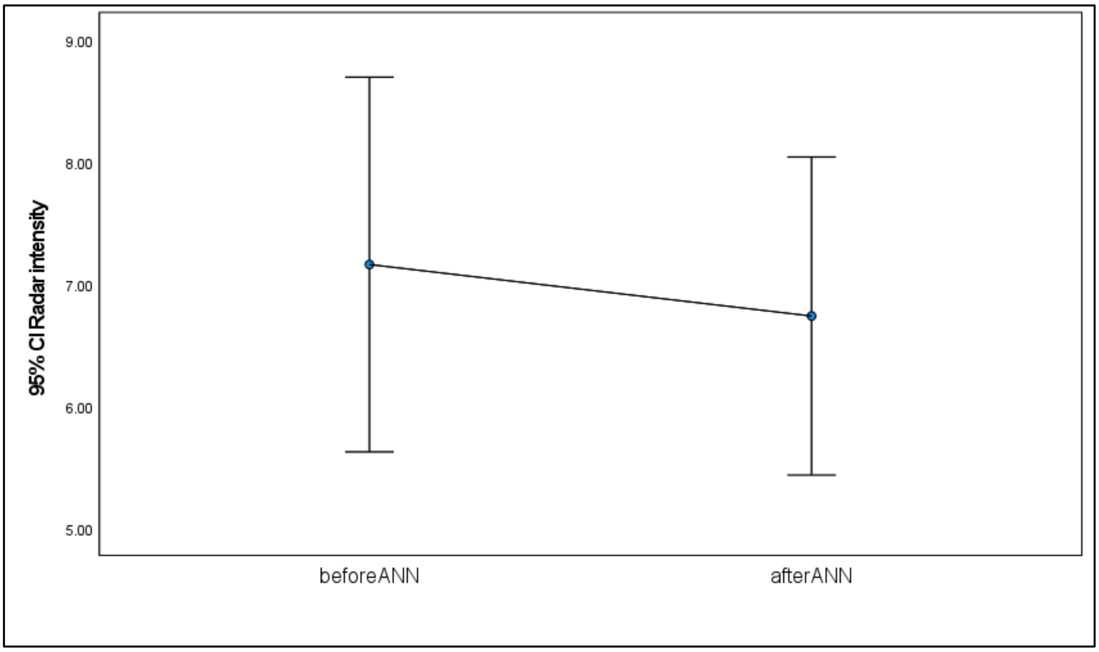

Figure 4.22 Interval Plot Before versus After ANN Application

4.9 Rainfall Runoff Model Development using HEC-HMS Model

In the development of an enhanced radar-based flood forecasting model, the HEC-HMS model was selected due to its simplicity and suitability, as outlined in Chapter 2. The rainfall-runoff model was successfully executed and optimized for the simulation period from December 18, 2021, to December 22, 2021, using an hourly time interval. Notably, during this period, a significant flood event occurred within the Klang and Langat River basins, providing a relevant case for the model's testing and validation. The basin characteristics were incorporated into the HEC-HMS model, and the pre-processing steps for the basin model were thoroughly discussed in Section 3.9 of the methodology. The subsequent sections of this study will present the simulation results, which are based on various rainfall inputs, including data from rain gauge, radar QPE, and the newly developed ANN-based radar QPE, offering a comprehensive evaluation of model performance.

4.9.1 Watershed Parameter

HEC-HMS is a lumped-parameter hydrological model that simulates the behavior of a watershed as a single unit, both for input and output. In a lumped model, the entire watershed is treated as one aggregated entity, where physical and hydrological processes such as rainfall, runoff, and infiltration are averaged across the entire area. Table 4.11 and Table 4.12 presents the different watershed factors utilized in the calibration of the model. For instance, there is notable spatial variation in the Curve Number (CN) values across the watershed. The weighted average of the CN values ranges from 80.0 to 91.6, reflecting the variability in land use, soil type, and hydrological conditions within different areas of the watershed. In addition, Subbasin-16 stands out as having the steepest basin slope within the watershed, with a gradient of 29.4%. Furthermore, Figure 4.23 and Figure 4.24 illustrates the results of the sub-basin schematic diagram generated during the HEC-HMS modeling process, providing a visual representation of the watershed's spatial layout and the distribution of hydrological parameters.

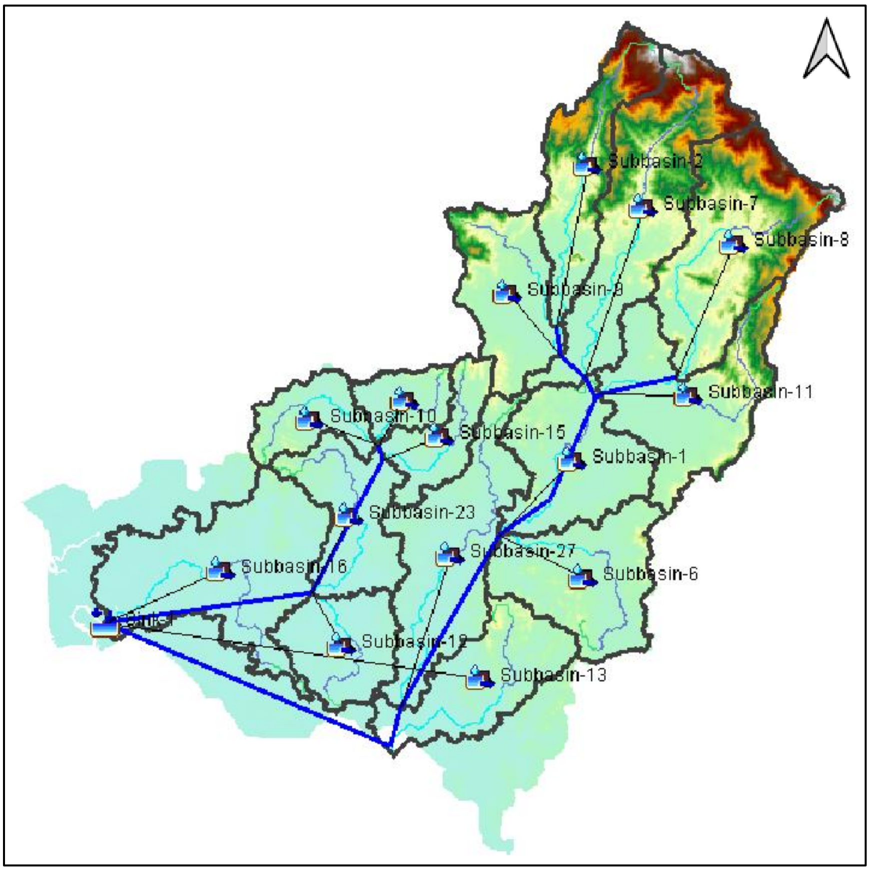

Figure 4.23 HEC-HMS Sub-basins Map for Klang River Basin

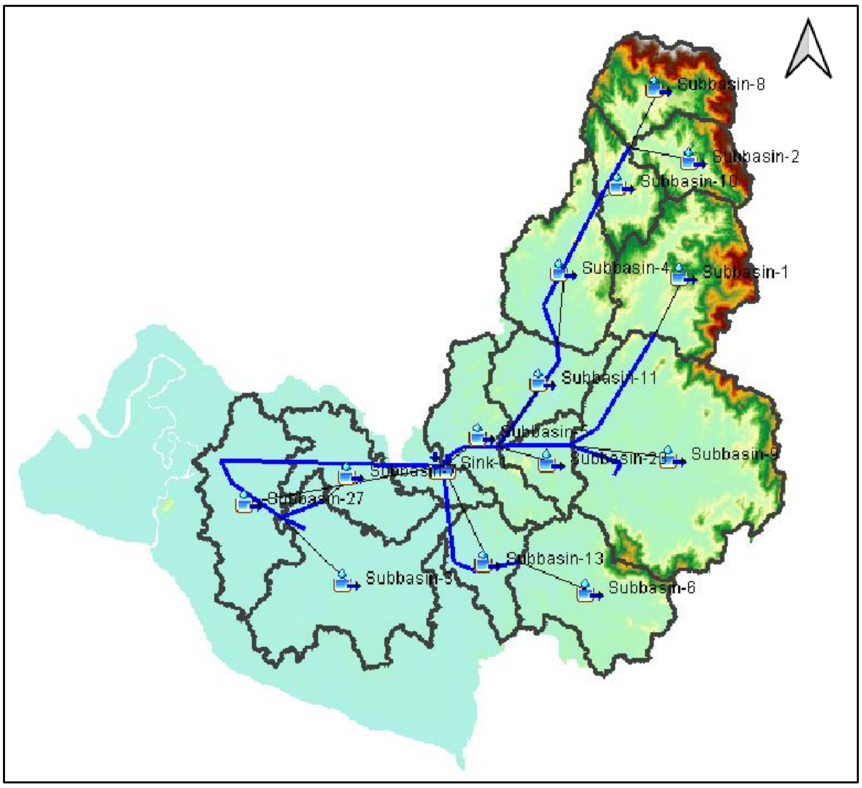

Figure 4.24 HEC-HMS Sub-basins Map for Langat River Basin

Table 4.11
Watershed Parameters Generated by HEC-GeoHMS for Klang River Basin

Sub-basin	Area (km^2)	Lag Time (min)	Basin Slope (%)	CN
Subbasin-1	77.8	115.0	13.2	91.2
Subbasin-10	34.6	94.7	14.6	88.8
Subbasin-11	97.0	146.6	17.7	87.9
Subbasin-12	51.3	129.2	6.7	90.2
Subbasin-13	70.9	156.0	11.8	88.6
Subbasin-15	35.5	222.7	7.8	90.5
Subbasin-16	127.9	115.5	29.4	88.3
Subbasin-2	72.4	203.2	10.5	81.8
Subbasin-23	60.5	224.0	9.0	90.5
Subbasin-27	103.4	93.7	13.2	91.6
Subbasin-5	25.2	83.6	13.2	87.7
Subbasin-6	82.8	136.4	12.9	90.1
Subbasin-7	124.2	173.5	26.9	82.6
Subbasin-8	116.3	148.1	28.9	80.0
Subbasin-9	67.9	108.9	16.5	87.9

Table 4.12
Watershed Parameters Generated by HEC-GeoHMS for Langat River Basin

Sub-basin	Area (km^2)	Lag Time (min)	Basin Slope (%)	CN
Subbasin-1	177.9	116.5	38.8	61.7
Subbasin-9	387.2	32.5	28.4	96.9
Subbasin-8	109.7	107.0	12.0	94.4
Subbasin-2	74.3	160.1	31.1	79.9
Subbasin-10	66.9	147.8	8.9	63.5
Subbasin-4	147.6	200.8	21.4	76.8
Subbasin-11	90.2	238.6	4.4	87.5
Subbasin-23	49.9	260.7	4.2	70.3
Subbasin-7	110.8	121.9	34.2	77.0
Subbasin-3	227.8	96.1	34.0	86.7
Subbasin-6	164.8	155.8	11.5	80.4
Subbasin-27	151.3	87.9	14.7	68.0
Subbasin-5	108.0	94.8	13.5	91.4
Subbasin-13	73.0	116.5	38.8	75.5

4.9.2 Rain Gauge Data Input

Figure 4.25 presents a hydrograph comparing runoff simulations based on rain gauge data. The blue line represents the observed streamflow recorded at the Rantau Panjang and Dengkil stations, while the red line illustrates the streamflow simulated by the model. The comparison indicates that the rainfall–runoff model successfully captures the general pattern of the observed streamflow, as the simulated flow closely follows the overall trends of the measured data.

However, Figure 4.26 shows the results of a test simulation in which the simulated peak flow for the Klang River Basin is 905.2 m^3/s, which is significantly lower than the observed peak flow of 1286.4 m^3/s. The errors in the total runoff volume and peak flow are 37.5% and 29.6%, respectively, as shown in Table 4.13.

Similarly, for the Langat River Basin, the simulated peak flow is 480.6 m^3/s, compared to the observed peak flow of 643.2 m^3/s. The corresponding errors are 35.7% for the total runoff volume and 25.3% for the peak flow, as presented in Table 4.14. These discrepancies indicate a relatively high deviation between the simulated and observed results, highlighting the need for further model refinement. Therefore, a calibration (optimization) and validation procedure was applied to improve the model's accuracy. This process, described in the following subsection, aims to fine-tune the model parameters to reduce errors and enhance agreement between simulated and observed streamflow.

(a)

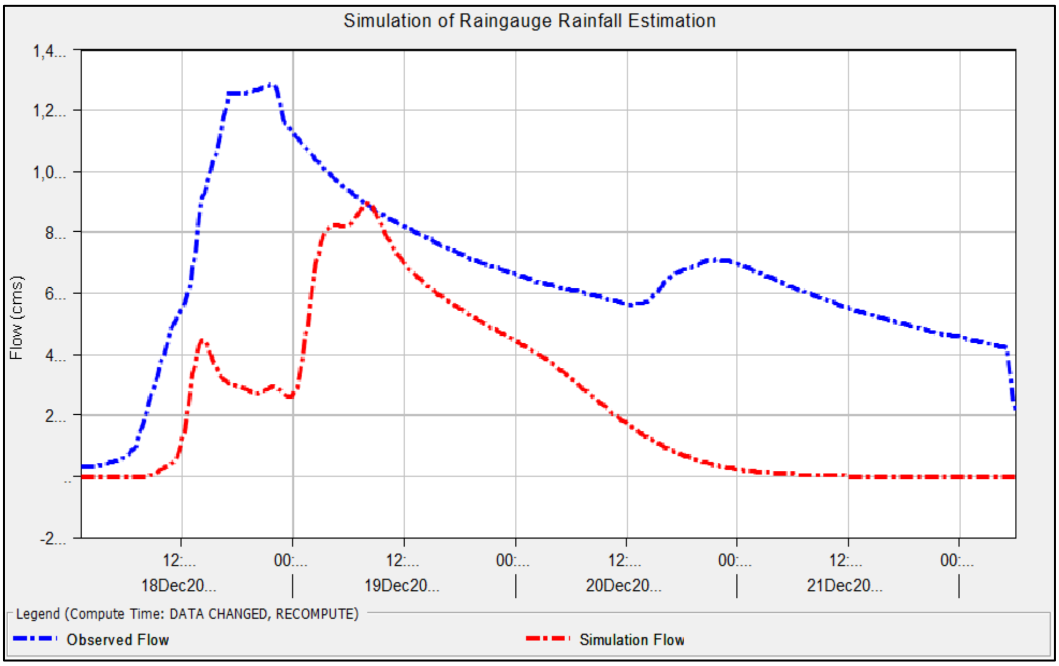

(b)

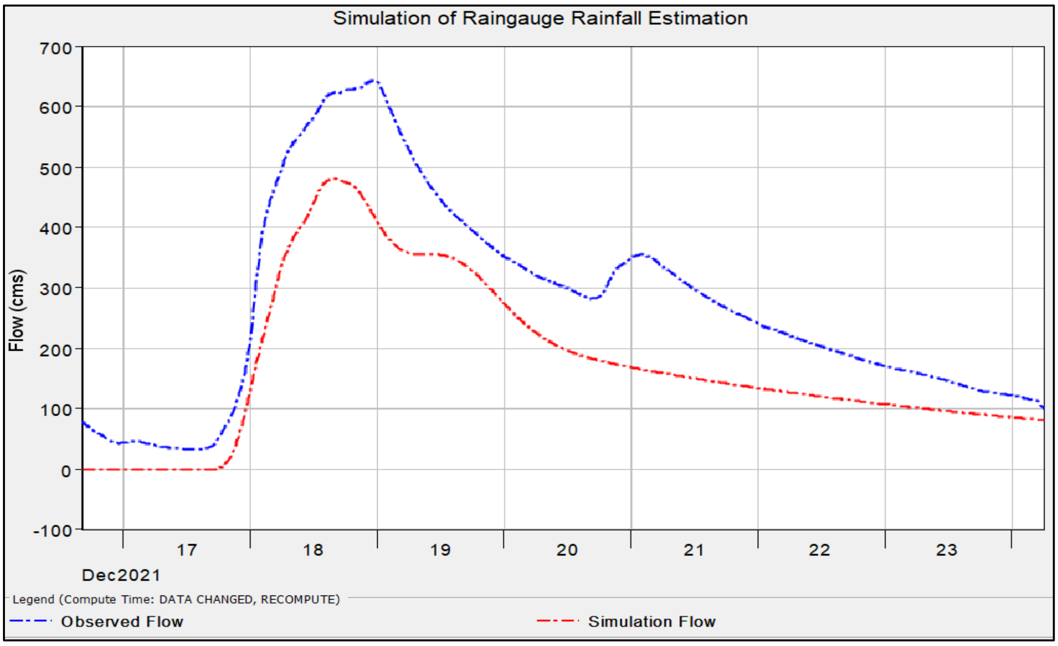

Figure 4.25 HEC-HMS Simulation Results using Rain Gauge Data; (a) Klang River Basin, (b) Langat River Basin

(a)

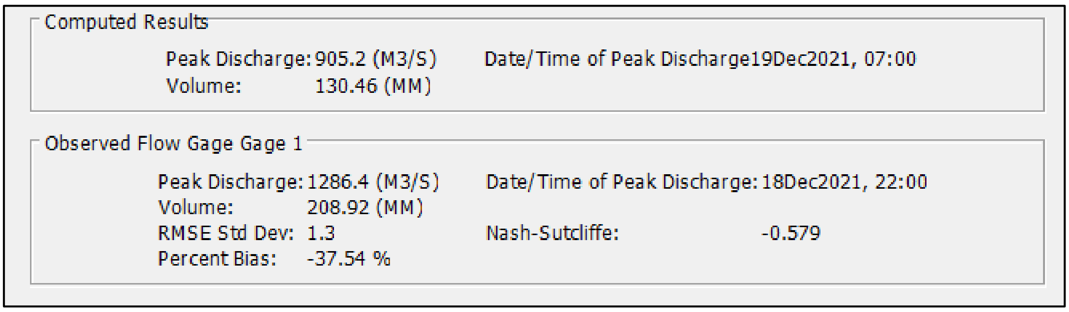

(b)

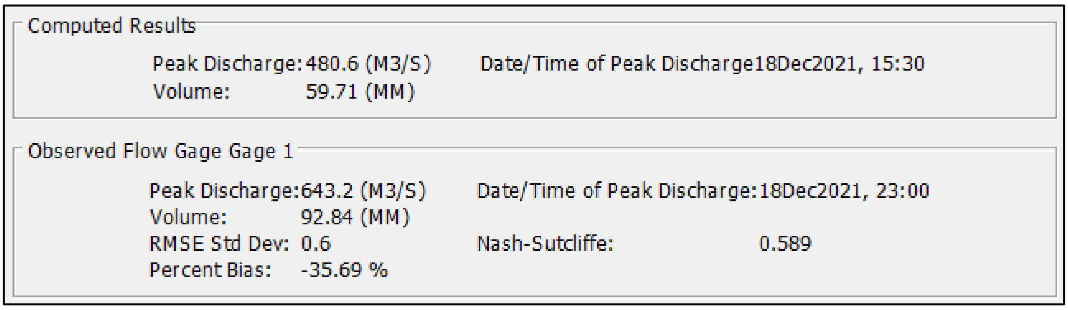

Figure 4.26 Summary of the Simulation Results; (a) Klang River Basin, (b) Langat River Basin

4.9.3 Radar QPE Input

Figure 4.27 illustrates a hydrograph comparing runoff simulations generated using radar QPE as the input data. The model successfully replicates the general shape of the hydrograph, indicating that the simulated flow closely follows the observed runoff pattern. Figure 4.28 presents the results of a test simulation, where the simulated peak flow for the Klang River Basin is 981.1 m^3/s, which is notably lower than the observed peak flow of 1286.4 m^3/s. The errors in the total runoff volume and peak flow are 22.8% and 23.7%, respectively.

For the Langat River Basin, the simulated peak flow is 338.9 m^3/s, compared to the observed peak flow of 643.2 m^3/s. The corresponding errors are 59.7% for the total runoff volume and 47.3% for the peak flow. These relatively high error values indicate a significant discrepancy between the simulated and observed results, suggesting that the current model configuration does not adequately represent the hydrological response of the basins. Therefore, a calibration process is necessary to improve model performance.

(a)

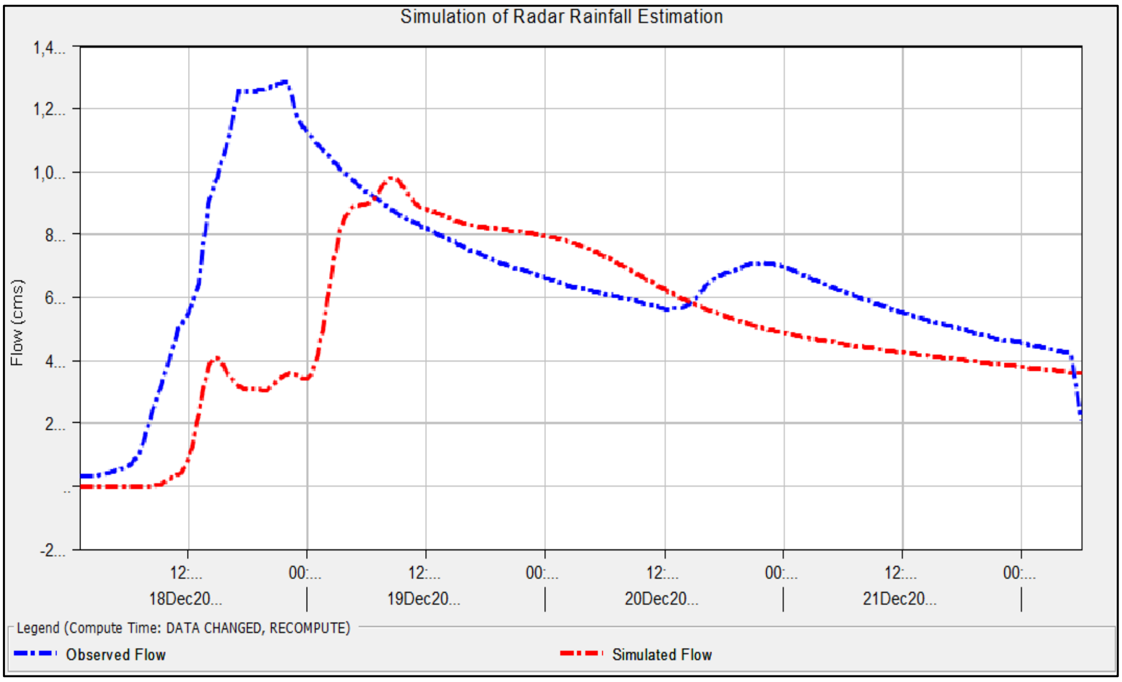

(b)

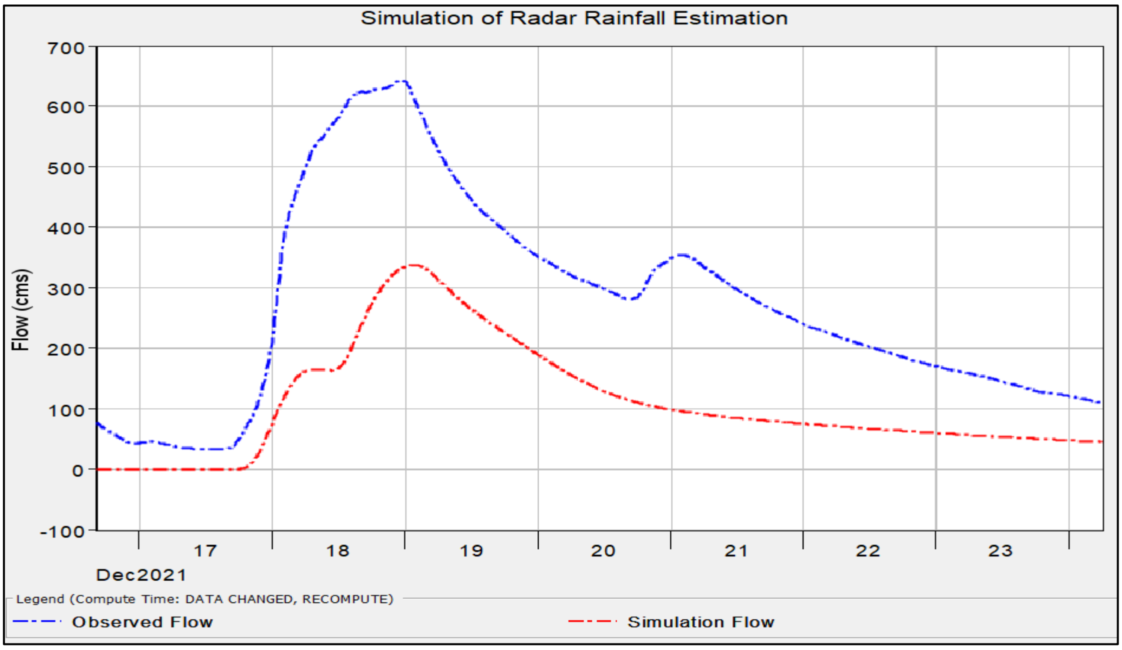

Figure 4.27 HEC-HMS Simulation Results using Radar QPE; (a) Klang River Basin, (b) Langat River Basin

(a)

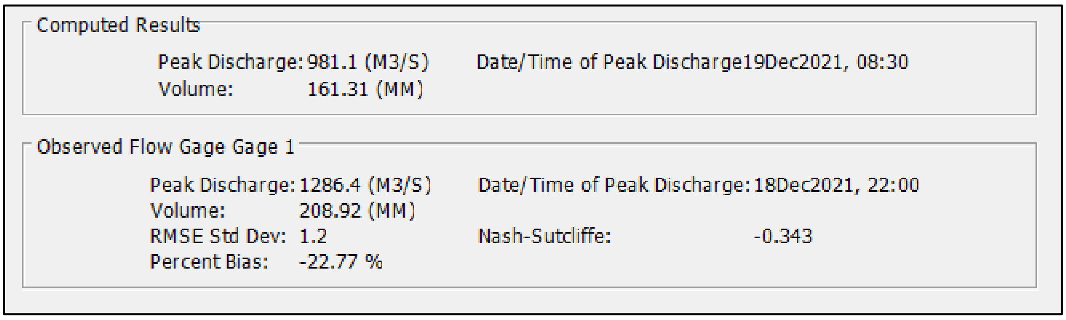

(b)

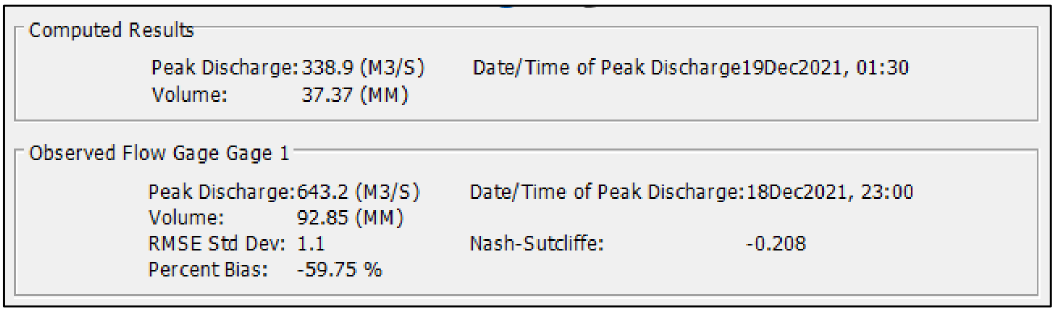

Figure 4.28 Summary of the Simulation Results; (a) Klang River Basin, (b) Langat River Basin

4.9.4 ANN-based Radar QPE Input

Figure 4.29 presents a hydrograph comparing runoff simulations obtained using the ANN-based radar QPE. The model effectively reproduces the streamflow, showing good agreement with the observed hydrograph patterns. Figure 4.30, however, presents the results of a test simulation in which the simulated peak flow for the Klang River Basin is 1049.7 m³/s, which is lower than the observed peak flow of 1286.4 m³/s. The model errors for total runoff volume and peak flow are 21.7% and 18.4%, respectively, as reported in Table 4.13.

For the Langat River Basin, the simulated peak flow is 1031.7 m³/s, exceeding the observed peak flow of 643.2 m³/s. The corresponding errors are 28.1% for total runoff volume and 60.4% for peak flow as shown in Table 4.14. These discrepancies indicate that, despite improvements introduced by the ANN-based radar QPE, the model still requires calibration to further reduce errors and improve agreement between simulated and observed streamflow.

(a)

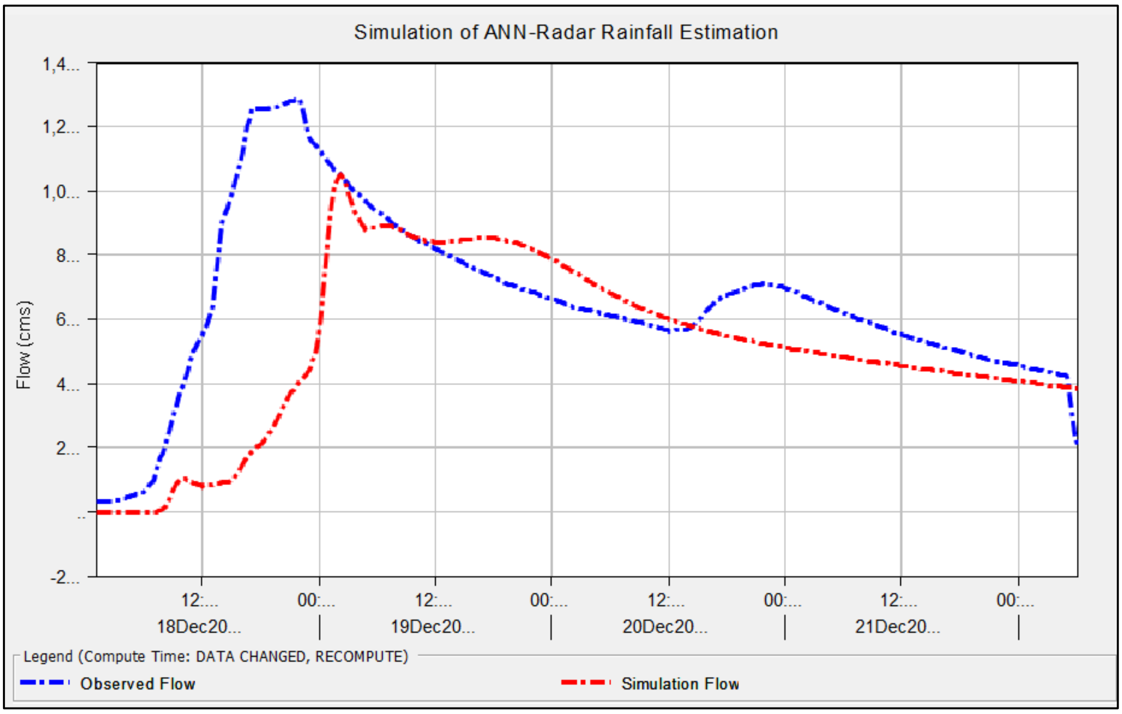

(b)

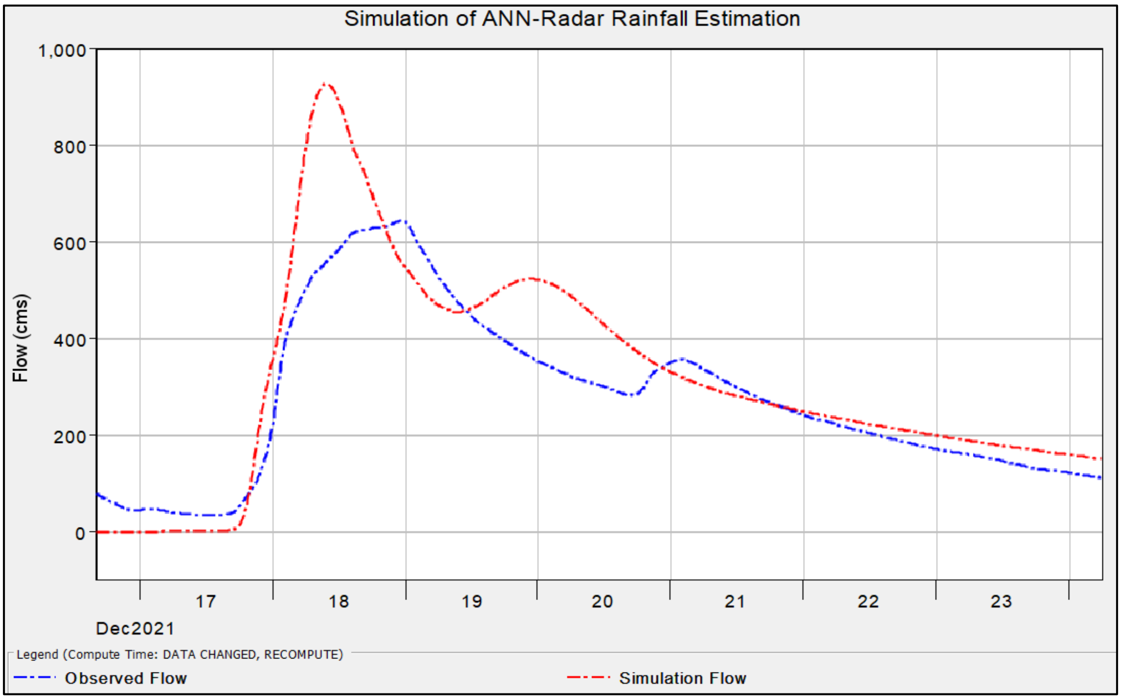

Figure 4.29 HEC-HMS Simulation Results using ANN-based Radar QPE; (a) Klang River Basin, (b) Langat River Basin

(a)

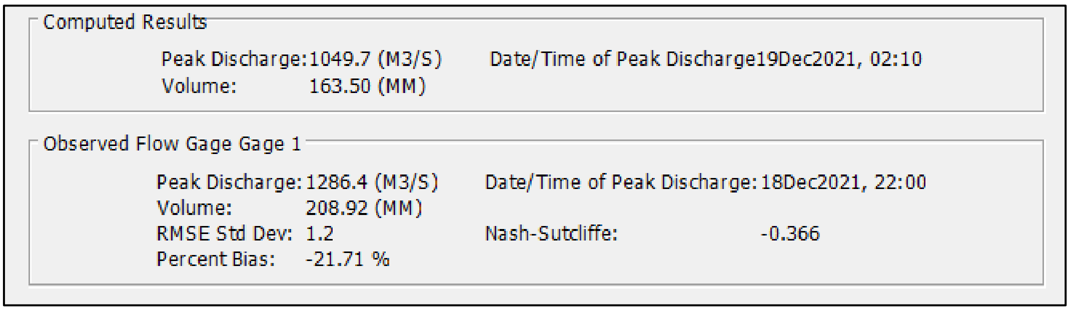

(b)

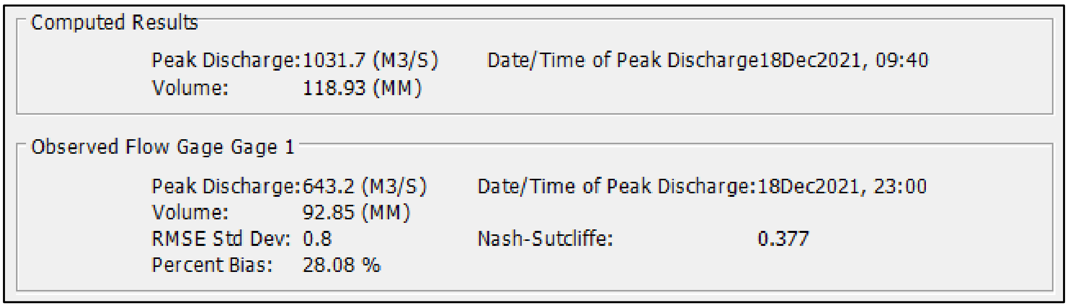

Figure 4.30 Summary of the Simulation Results; (a) Klang River Basin, (b) Langat River Basin

Table 4.13

Simulated and Observed Peak Discharges, Total Volume, and their Evaluation Criteria before Calibration for Klang River basin

	Total volume (mm)			Peak discharge (m^3/s)			R^2	NSE	PBIAS (%)	RSR
	Simulated	Observed	RE	Simulated	Observed	RE				
Rain gauge	130.5	208.9	-37.5	905.2	1286.4	-29.6	0.3	-0.6	-37.5	1.3
Radar QPE	161.3	208.9	-22.8	981.1	1286.4	-23.7	0.2	-0.3	-22.7	1.2
ANN-Radar QPE	163.5	208.9	-21.7	1049.7	1286.4	-18.4	0.2	-0.3	-21.7	1.2

RE: relative error; R^2 : correlation coefficient; NSE: Sutcliffe Efficiency; PBIAS: percent bias; RSR: Root mean square error-standard deviation ratio

Table 4.14

Simulated and Observed Peak Discharges, Total Volume, and their Evaluation Criteria before Calibration for Langat River basin

	Total volume (mm)			Peak discharge (m^3/s)			R^2	NSE	PBIAS (%)	RSR
	Simulated	Observed	RE	Simulated	Observed	RE				
Rain gauge	59.7	92.8	-35.7	480.6	643.2	-25.3	0.5	0.6	-35.7	0.6
Radar QPE	37.37	92.8	-59.7	338.9	643.2	-47.3	0.4	-0.2	-59.7	1.1
ANN-Radar QPE	118.9	92.8	28.1	1031.7	643.2	60.4	0.5	0.4	28.1	0.8

RE: relative error; R^2 : correlation coefficient; NSE: Sutcliffe Efficiency; PBIAS: percent bias; RSR: Root mean square error-standard deviation ratio

4.9.5 Model Calibration (Optimization)

A sensitivity analysis was performed to identify the most influential parameters affecting model accuracy. The sensitivity analysis indicates that, while the flood travel time (k) exhibits minimal sensitivity, lag time (Tlag) and Curve Number (CN) exert strong control over model accuracy by regulating runoff timing and runoff volume, respectively. Small variations in Tlag significantly affect peak timing errors, whereas changes in CN directly influence effective rainfall, leading to substantial errors in peak discharge and total runoff volume. To refine the model's accuracy, the values of these parameters were adjusted within a range of +10% to -10%. This modification considered acceptable according to the guidelines established by Sardoii et al. (2012).

Figures 4.31, 4.32, and 4.33 illustrate the hydrographs comparing the runoff simulations using rain gauge data, radar QPE, and ANN-based radar QPE after model calibration for the Klang River basin. The shape of the hydrograph was accurately reproduced in the model output, with both the overall shape and peak time closely matching the observed data. In Figure 4.31, the runoff simulation using rain gauge data shows that the computed volume was 216.3 mm, which is very close to the observed volume of 216.0 mm. Additionally, the observed peak discharge on December 19, 2021, was approximately 1286.4 m^3/s, while the computed peak discharge was about 1313.7 m^3/s, resulting in an acceptable percent error of 2.1%.

Additionally, the computed volume discharged by radar QPE (218.2 mm) is slightly higher than the observed volume (216.0 mm), as shown in Figure 4.32. The simulation result indicates that the computed peak discharge (1284.2 m^3/s) on December 19, 2021, was slightly underestimated compared to the observed peak discharge (1286.4 m^3/s), resulting in a percent error of 0.2%. On the other hand, Figure 4.33 illustrates the runoff simulation using ANN-based radar QPE. The results show that the computed volume was 216.2 mm, which is closed to the observed volume of 216.0 mm. In addition, the observed peak discharge on December 19, 2021, was approximately 1286.4 m^3/s, while the computed peak discharge was about 1304.0 m^3/s, resulting in an accepted percent error of 1.4%.

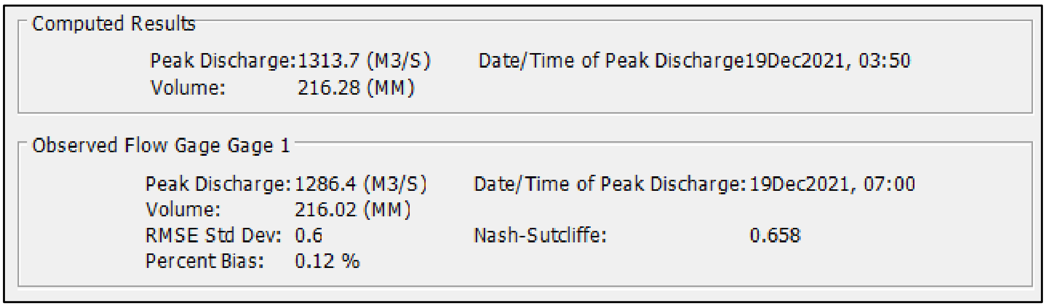

Computed Results

Peak Discharge: 1313.7 (M3/S) Date/Time of Peak Discharge19Dec2021, 03:50
Volume: 216.28 (MM)

Observed Flow Gage Gage 1

Peak Discharge: 1286.4 (M3/S) Date/Time of Peak Discharge: 19Dec2021, 07:00
Volume: 216.02 (MM)
RMSE Std Dev: 0.6 Nash-Sutcliffe: 0.658
Percent Bias: 0.12 %

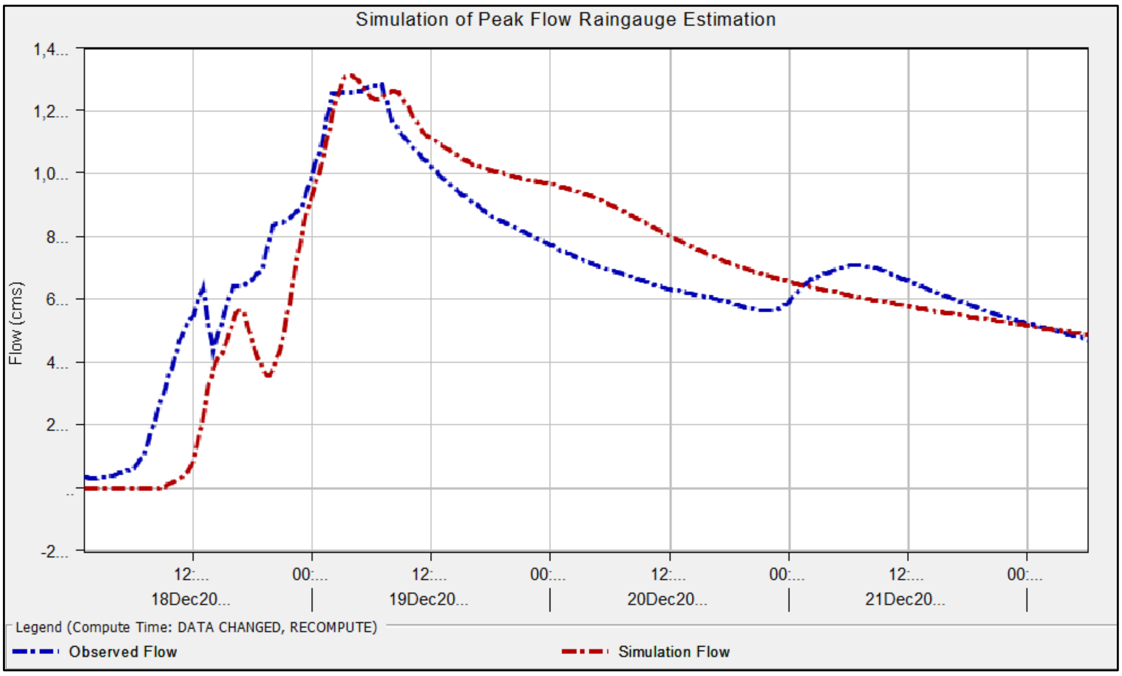

Figure 4.31 Simulated and Observed Hydrograph using Rain Gauge Data after Calibration for Klang River Basin

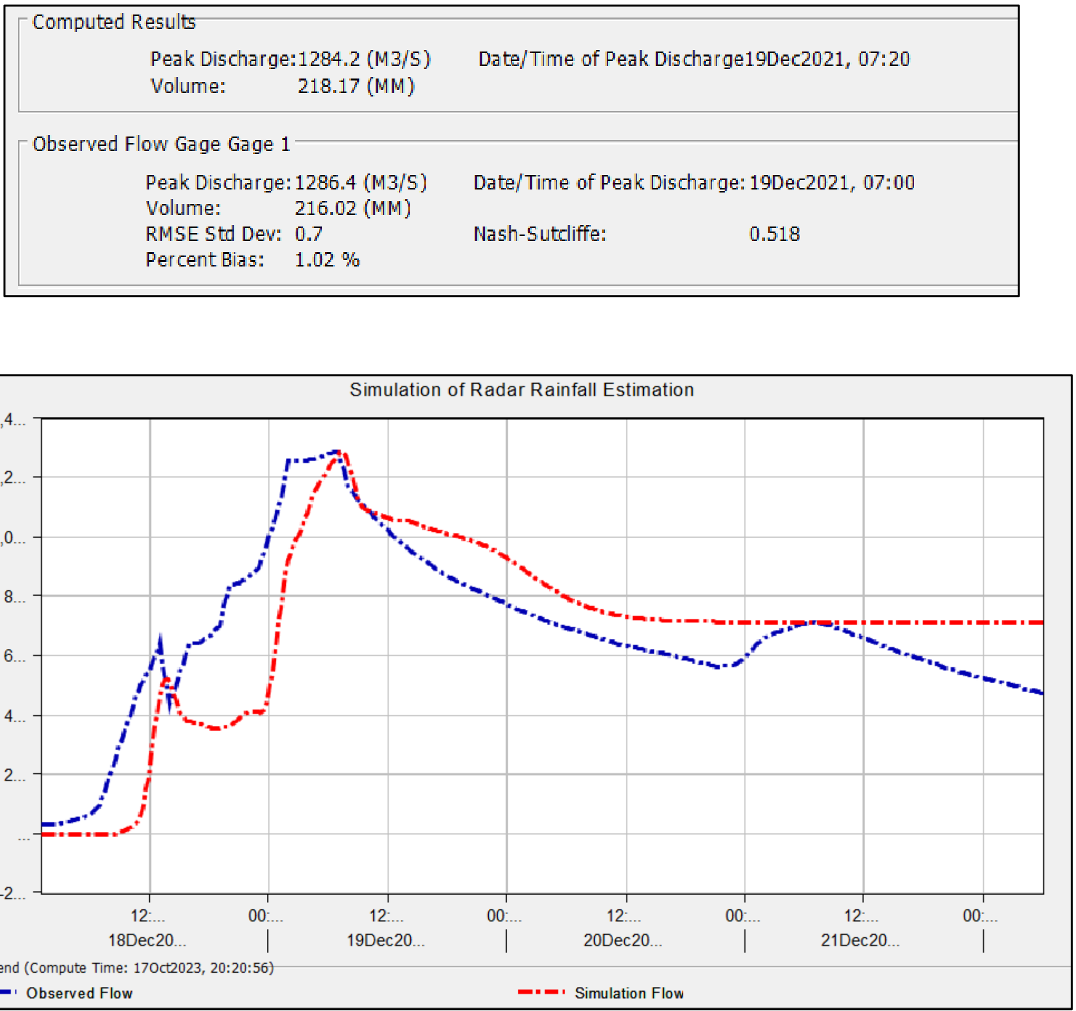

Figure 4.32 Simulated and Observed Hydrograph using Radar QPE after Calibration for Klang River Basin

Computed Results

Peak Discharge: 1304.0 (M3/S) Date/Time of Peak Discharge19Dec2021, 02:30

Volume: 216.20 (MM)

Observed Flow Gage Gage 1

Peak Discharge: 1286.4 (M3/S) Date/Time of Peak Discharge: 19Dec2021, 07:00

Volume: 216.02 (MM)

RMSE Std Dev: 0.6 Nash-Sutcliffe: 0.594

Percent Bias: 0.11 %

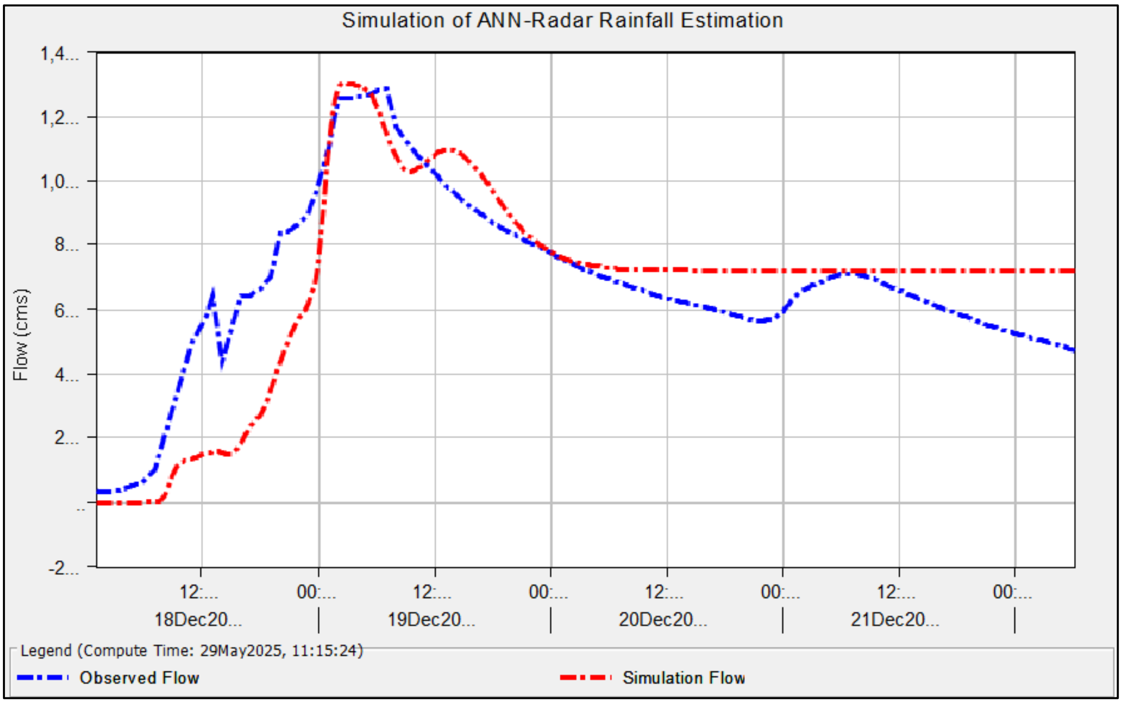

Figure 4.33 Simulated and Observed Hydrograph using ANN-Radar QPE after Calibration for Klang River Basin

Figures 4.34, 4.35, and 4.36 illustrate the hydrographs comparing runoff simulations using rain gauge data, radar QPE, and ANN-based radar QPE after model calibration for the Langat River Basin. The model accurately reproduced the hydrograph shape, with both the overall pattern and peak timing closely matching the observed data. As shown in Figure 4.34, the runoff simulation using rain gauge data produced a computed runoff volume of 81.3 mm, which is slightly lower than the observed volume of 92.8 mm. The observed peak discharge on 18 December 2021 was the same as the computed peak discharge, at approximately 643.2 m^3/s, resulting in a 0% error.

Figure 4.35 shows the runoff simulation using radar QPE, where the computed runoff volume was 81.1 mm, lower than the observed volume of 92.8 mm. The computed peak discharge of 730.4 m^3/s on 19 December 2021 was slightly overestimated compared to the observed peak discharge of 643.2 m^3/s, resulting in a percentage error of 13.5%. In contrast, Figure 4.36 presents the runoff simulation using ANN-based radar QPE. The computed runoff volume was 87.7 mm, which is close to the observed volume of 92.8 mm, corresponding to a percentage error of 5.5%. The computed peak discharge on 18 December 2021 was approximately 746.9 m^3/s, slightly higher than the observed peak discharge of 643.2 m^3/s.

Overall, the simulated hydrographs demonstrate that the HEC-HMS model effectively captures peak discharge behaviour by accounting for the spatial variability of meteorological parameters in distributed-mode simulations.

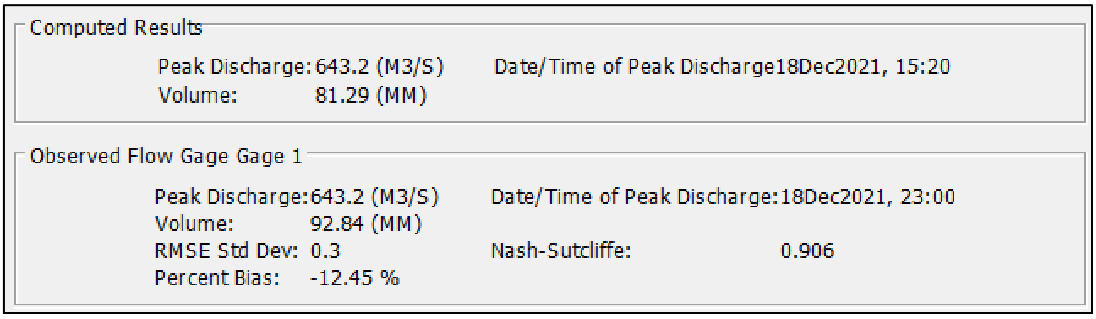

Computed Results

Peak Discharge: 643.2 (M3/S) Date/Time of Peak Discharge18Dec2021, 15:20

Volume: 81.29 (MM)

Observed Flow Gage Gage 1

Peak Discharge: 643.2 (M3/S) Date/Time of Peak Discharge: 18Dec2021, 23:00

Volume: 92.84 (MM)

RMSE Std Dev: 0.3 Nash-Sutcliffe: 0.906

Percent Bias: -12.45 %

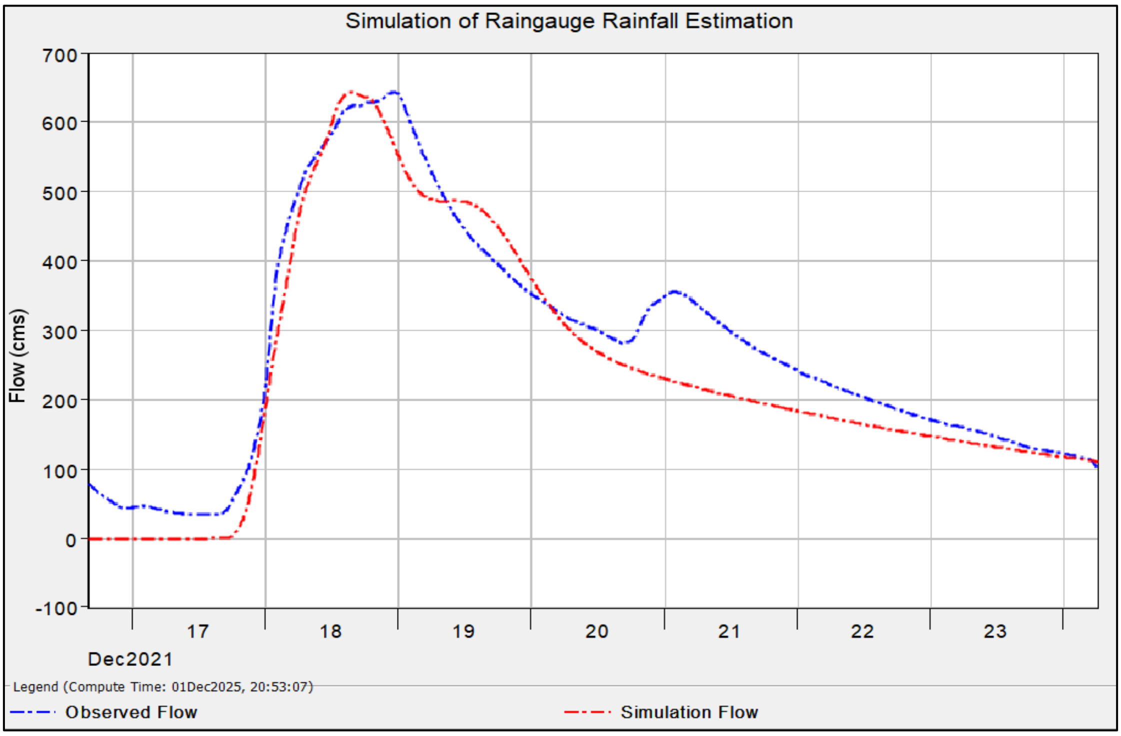

Figure 4.34 Simulated and Observed Hydrograph using Rain Gauge Data after Calibration for Langat River Basin

Computed Results

Peak Discharge:	730.4 (M3/S)	Date/Time of Peak Discharge	19Dec2021, 01:10
Volume:	81.12 (MM)		

Observed Flow Gage Gage 1

Peak Discharge:	643.2 (M3/S)	Date/Time of Peak Discharge:	18Dec2021, 23:00
Volume:	92.85 (MM)		
RMSE Std Dev:	0.5	Nash-Sutcliffe:	0.797
Percent Bias:	-12.64 %		

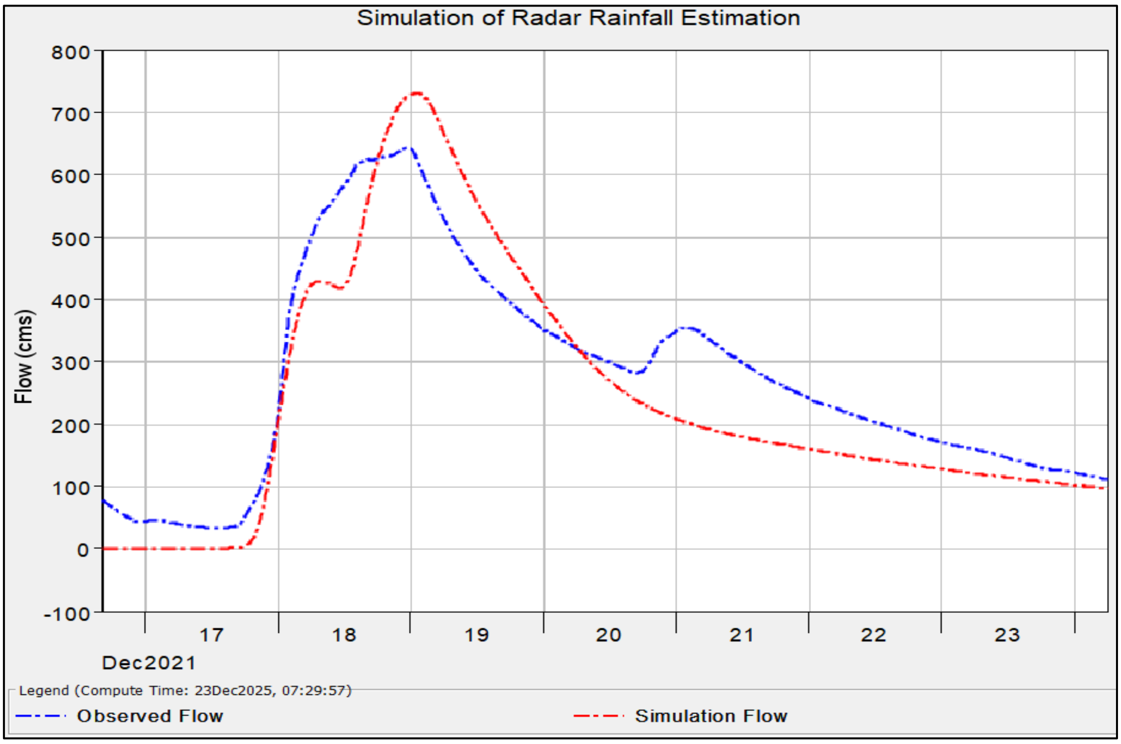

Figure 4.35 Simulated and Observed Hydrograph using Radar QPE after Calibration for Langat River Basin

Computed Results

Peak Discharge:	746.9 (M3/S)	Date/Time of Peak Discharge	18Dec2021, 10:50
Volume:	87.71 (MM)		

Observed Flow Gage Gage 1

Peak Discharge:	643.2 (M3/S)	Date/Time of Peak Discharge:	18Dec2021, 23:00
Volume:	92.85 (MM)		
RMSE Std Dev:	0.4	Nash-Sutcliffe:	0.857
Percent Bias:	-5.54 %		

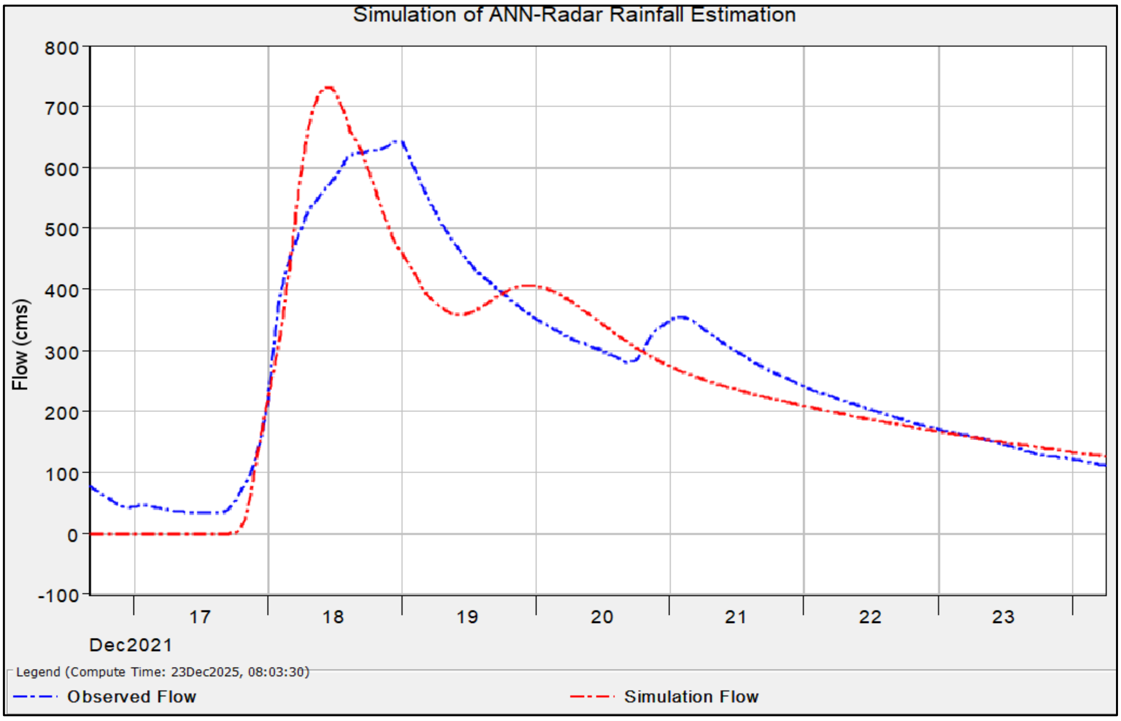

Figure 4.36 Simulated and Observed Hydrograph using ANN-Radar QPE after Calibration for Langat River Basin

Table 4.15

Simulated and Observed Peak Discharges, Total Volume, and their Evaluation Criteria after Calibration for Klang River Basin

	Total volume (mm)			Peak discharge (m^3/s)			R^2	NSE	PBIAS (%)	RSR
	Simulated	Observed	RE	Simulated	Observed	RE				
Rain gauge	216.3	216.0	0.1	1313.7	1286.4	2.1	0.8	0.7	0.1	0.6
Radar QPE	218.2	216.0	1.0	1284.2	1286.4	-0.2	0.6	0.5	1.0	0.7
ANN-Radar QPE	216.2	216.0	0.1	1304.0	1286.4	1.4	0.8	0.6	0.1	0.6

RE: relative error; R^2 : correlation coefficient; NSE: Sutcliffe Efficiency; PBIAS: percent bias; RSR: Root mean square error-standard deviation ratio

Table 4.16

Simulated and Observed Peak Discharges, Total Volume, and their Evaluation Criteria after Calibration for Langat River Basin

	Total volume (mm)			Peak discharge (m^3/s)			R^2	NSE	PBIAS (%)	RSR
	Simulated	Observed	RE	Simulated	Observed	RE				
Rain gauge	81.3	92.8	-12.5	643.2	643.2	0	0.9	0.9	-12.5	0.3
Radar QPE	81.1	92.8	-12.6	730.4	643.2	13.5	0.8	0.8	-12.6	0.5
ANN-Radar QPE	87.7	92.8	-5.5	746.9	643.2	16.1	0.9	0.9	-5.5	0.4

RE: relative error; R^2 : correlation coefficient; NSE: Sutcliffe Efficiency; PBIAS: percent bias; RSR: Root mean square error-standard deviation ratio

As shown in Table 4.15, after the optimization process, the relative error (RE) for rainfall estimation using rain gauge data in the Klang River basin decreased significantly, reaching 2.1% for peak flow and 0.1% for total runoff volume. For radar QPE, the RE was reduced to 0.2% for peak flow and 1.0% for total volume. Similarly, the ANN-based radar QPE method achieved RE values of 1.8% for peak flow and 0.1% for total volume, indicating substantial improvements in accuracy. Table 4.16 presents the optimization results for the Langat River basin. The RE for rain gauge data decreased to 12.5% for total runoff volume, while the RE for peak flow was reduced to 0%. For radar QPE, the RE improved to 13.5% for peak flow and 12.6% for total volume. Likewise, the ANN-based radar QPE method showed reduced RE values of 16.1% for peak flow and 5.5% for total volume. Overall, these improvements demonstrate the effectiveness of the optimization process in reducing discrepancies between observed and simulated values. According to Rizal et al. (2023), the obtained RE values are considered highly satisfactory, as they fall within the generally acceptable range of less than 20%.

The results indicate a strong correlation between the measured and predicted peak flow rates during the calibration period for rainfall estimated using rain gauge data and the ANN-based radar QPE ($R^2 = 0.8$) in the Klang River basin, compared to the radar QPE, which shows a lower correlation ($R^2 = 0.6$). For the Langat River basin, a strong correlation is also observed between the measured and predicted peak flow rates for rainfall estimated using rain gauge data and the ANN-based radar QPE ($R^2 = 0.9$) during the calibration period, compared to the radar QPE ($R^2 = 0.8$). According to Zou et al. (2003), correlation coefficients greater than 0.8 are classified as strong correlations.

In addition, the comparison between simulated and observed values based on the Nash–Sutcliffe Efficiency (NSE) criterion indicates reliable model performance. The Klang River basin model performed satisfactorily, with NSE values of 0.7 for rain gauge estimation, 0.6 for the ANN-based radar QPE, and 0.5 for radar QPE. In contrast, the Langat River basin model showed good to very good performance, with NSE values of 0.9 for rain gauge estimation, 0.9 for the ANN-based radar QPE, and 0.8 for radar QPE. The higher NSE values for the Langat River basin suggest that the model was better able to reproduce observed flows in this basin, possibly due to more consistent rainfall patterns, better data coverage, or simpler hydrological responses compared to the Klang River basin (Jaffar et al., 2024). According to Moriasi et al. (2007), model simulations with NSE values greater than 0.5 are considered satisfactory, values above 0.65 are considered good, and values exceeding 0.75 are regarded as very good. An NSE value of 1 indicates a perfect model prediction, with no difference between observed and simulated values.

Furthermore, the performance of simulation results for rain gauge rainfall estimation and ANN-based radar QPE models was better than that of the radar QPE model when evaluated using the ratio of the standard deviation of observations to the root mean square error (RSR) value. For the Klang River basin, the RSR values were 0.6 for rain gauge estimation, 0.6 for ANN-based radar QPE, and 0.7 for radar QPE. Similarly, for the Langat River basin, the RSR values were 0.3 for rain gauge estimation, 0.4 for ANN-based radar QPE, and 0.5 for radar QPE, indicating that the ANN-based model consistently provided more accurate simulations in both basins. The RSR value of 0.6 obtained in this study suggests that the models can be considered suitable if the RSR is below 0.7, as suggested by Bárdossy and Pegram (2017). In general, a decrease in RSR values indicates an improvement in the model's ability to replicate the hydrological characteristics of the basin.

Consequently, the rain gauge data exhibited strong simulation performance for the Klang River basin, as evidenced by four statistical assessment criteria: NSE = 0.7, R^2 = 0.8, PBIAS = 0.1, and RSR = 0.6, all indicating a good fit between estimated and observed values. Similarly, the ANN-enhanced radar QPE model also showed promising results, with NSE = 0.6, R^2 = 0.8, PBIAS = 0.1, and RSR = 0.6, demonstrating that the model predictions were dependable and consistent with observations. For the Langat River basin, the rain gauge data performed even better, with NSE = 0.9, R^2 = 0.9, PBIAS = 0.0, and RSR = 0.3. The ANN-based radar QPE model also achieved strong performance, with NSE = 0.9, R^2 = 0.9, PBIAS = 0.1, and RSR = 0.3.

The rain gauge data exhibited strong simulation performance for both the Klang and Langat River basins, with NSE, R^2, PBIAS, and RSR values indicating good to very good fits. Likewise, the ANN-based radar QPE models achieved comparable performance, with values closely matching those of the rain gauge data. This demonstrates that ANN-enhanced radar QPE can serve as a reliable alternative to traditional rain gauge measurements, particularly in regions where gauge coverage is limited. Overall, the results highlight the model's accuracy and reliability, reinforcing their usefulness for hydrological forecasting.

4.10 Summary

The radar QPE performance was assessed, revealing that some uncalibrated radar data tend to underestimate rainfall amounts. However, a strong correlation (r = 0.8) was found between radar QPE data and rain gauge measurements, indicating that despite the underestimation, both data sources generally align in capturing precipitation patterns. Next, feature extraction from radar images was performed to identify some of rainfall attributes, such as intensity, size, shape, and orientation. The extracted features were used to train a K-Nearest Neighbor (KNN) model, which achieved over 90% accuracy in rainfall classification. However, some misclassifications occurred in a few instances. Subsequently, the optimization of the Z/R relationship based on rainfall classification shows that the RMSE values for both rainfall types decreased, indicating a better fit and more accurate predictions.

An Artificial Neural Network (ANN) model was developed to improve radar QPE accuracy. The model showed promising results, with the RMSE approaching zero and a strong correlation between radar QPE and ANN-based radar QPE. The findings indicate significant improvement, with the ANN-enhanced radar QPE showing a positive relationship to rain gauge data and providing more accurate rainfall estimation.

To complete the analysis, the ANN-based radar QPE was integrated into a rainfall-runoff model within the HEC-HMS system for a case study of the Klang and Langat River basins. Statistical analysis revealed that the ANN-enhanced radar QPE, along with rain gauge data, provided more accurate streamflow predictions compared to the uncalibrated radar QPE with NSE>=0.6.

CHAPTER 5
CONCLUSION AND RECOMMENDATIONS

5.1 Introduction

This chapter presents the conclusion of the study by summarizing key findings and demonstrating how the research objectives have been met. It also outlines recommendations for future improvements and offers guidance for further research in the field.

5.1.1 Research Motivation

Accurate rainfall estimates play a crucial role in hydrological modeling, flood forecasting, and effective water resources management. Weather radar-based Quantitative Precipitation Estimation (QPE) systems offer wide spatial coverage, which is particularly valuable in areas with limited ground-based monitoring infrastructure. However, these systems often fall short in terms of accuracy, especially during extreme rainfall events as presented in Chapter 2. In contrast, rain gauges provide direct and highly accurate point-based rainfall measurements, serving as a reliable source of ground truth. The observed gap between radar and gauge data highlights the need for improved methodologies. This has led to the motivation behind this study which is to explore the use of advanced machine learning techniques, particularly Artificial Neural Network (ANN) in order to improve the accuracy of radar-based rainfall estimates.

5.2 Conclusion

Extracting convective and stratiform rainfall features from radar reflectivity and optimally developing a rainfall estimation model using machine learning techniques, remains both a challenging and novel task. This study aimed to enhance radar QPE and improve flood forecasting accuracy in the Klang and Langat River basins by integrating machine learning techniques and hydrological modeling. Objective 1 was achieved through the successful classification of rainfall types (stratiform and convective) using radar reflectivity images and the K-Nearest Neighbor (KNN) algorithm, which demonstrated high classification accuracy. Objective 2 was achieved by developing optimized Z–R relationships using Solver analysis to address the underestimation in radar QPE, resulting in reduced errors when validated against rain gauge measurements. Objective 3 was achieved by training an ANN model using 1,680 rain cell features (8×210) to enhance radar QPE rainfall estimation, which showed improved accuracy and a strong correlation with observed rainfall. The enhanced QPE was integrated into the HEC-HMS hydrological model, which simulated rainfall-runoff responses using three types of input: rain gauge data, uncalibrated radar QPE, and ANN-based radar QPE. Objective 4 was achieved, as the simulation results demonstrated that the ANN-based radar QPE produced more accurate streamflow predictions, particularly in terms of peak flow and total runoff volume. These findings supported the potential use of ANN-based radar QPE as a reliable input for flood forecasting systems and as an early warning tool to aid decision-making in emergency response operations.

5.2.1 New Model Development and Accuracy

This research developed and evaluated two key models to enhance the accuracy of radar-based QPE for hydrological applications. A KNN algorithm was employed to classify rainfall into convective and stratiform types using geometric features extracted from radar reflectivity data, such as rain cell location, area, intensity, and orientation. The KNN model achieved strong classification performance with an Area Under the Curve (AUC) exceeding 90%, despite some overlap in feature characteristics. To further improve rainfall estimation, an ANN model was trained using the Levenberg-Marquardt algorithm with rain gauge observations, significantly reducing the Root Mean Square Error (RMSE) from 11.40 mm/h to 4.76 mm/h.

5.2.2 Model Application and Certainty

The newly developed models were applied within an integrated flood forecasting framework to assess their practical utility and reliability. The enhanced ANN-radar QPE was incorporated into the HEC-HMS hydrological model using a novel approach that assigned gridded rainfall estimates to sub-basins within the Klang

River Basin. This allowed for more spatially representative runoff simulations compared to traditional rain gauge-based inputs. The integrated system showed strong performance during calibration, with the ANN-radar QPE yielding the highest correlation with observed discharge ($R^2 = 0.8$), significantly outperforming uncalibrated radar QPE ($R^2 = 0.6$). This demonstrates the improved certainty in flood predictions when using machine learning-enhanced radar data. Generally, the application of the hybrid model framework provides a more accurate and dependable tool for flood forecasting, offering valuable support for early warning systems and disaster risk reduction in flood-prone regions.

5.2.3 Summary

The objective of this study was to classify rainfall types, improve the accuracy of radar-based rainfall estimation, and enhance flood forecasting by integrating advanced machine learning techniques and hydrological modeling. This objective has been successfully met through a series of methodical approaches. The use of KNN algorithm for rainfall type classification yielded an overall accuracy of over 90%, demonstrating effective differentiation between convective and stratiform rainfall based on radar-derived features. Additionally, the development of optimized Z-R relationships significantly reduced the discrepancies between radar and rain gauge measurements, particularly lowering MAE and RMSE values for both rainfall types.

Further enhancement was achieved through the application of an ANN, which improved radar QPE accuracy, evidenced by a strong correlation with rain gauge data and minimal RMSE. In addition, the incorporation of the ANN-based radar QPE into the HEC-HMS rainfall-runoff model led to more accurate simulations of streamflow, especially when compared to observed data. This integrated system has shown its potential as a reliable hydrological forecasting tool, suitable for early flood warning and decision-making support for emergency response.

In summary, the combined use of classification algorithms, optimization techniques, and ANN modeling has led to notable advancements in rainfall estimation and flood prediction, thereby fulfilling the study's objective.

5.3 Recommendation

i) In future studies, expanding the dataset to include a wider variety of radar images from diverse geographical areas and different weather conditions could significantly enhance the model's robustness. Incorporating radar data from different river basins would enable the model to adapt more effectively to various environmental conditions.

ii) The inclusion of additional rainfall stations would further enhance the accuracy of rainfall estimation. With a larger network of stations, the spatial coverage of rainfall measurements would expand, offering a more comprehensive view of the precipitation patterns across a wider area. The integration of data from multiple stations would help to identify regional variations and improve the overall reliability of forecasts by reducing the uncertainty that can arise from relying on data from a limited number of stations.

iii) It is recommended that future applications incorporate an optimized Z–R relationship derived from classified rainfall into ANN modelling, as this approach better captures the variability of radar-derived rainfall intensities.

iv) The use of deep learning techniques, especially convolutional neural networks (CNNs), can enhance the model's ability to automatically detect complex patterns in radar images. CNNs excel at identifying spatial features like shape, texture, and orientation of precipitation structures, leading to more accurate rainfall type classifications. By learning directly from raw radar data, CNNs eliminate the need for manual feature extraction, enabling the model to adapt to different conditions without predefined input.

v) Integrating additional meteorological data, such as satellite imagery and surface weather observations, can enhance the model's accuracy. Satellite imagery provides insights into large-scale weather patterns, while surface data like temperature, humidity, and wind helps refine the model's understanding of local environmental factors. Combining these with radar information offers a more comprehensive view, leading to improved forecasting and more reliable predictions.

REFERENCES

Abdolrasol, M. G., Hussain, S. S., Ustun, T. S., Sarker, M. R., Hannan, M. A., Mohamed, R., ... & Milad, A. (2021). Artificial neural networks-based optimization techniques: A review. *Electronics*, *10*(21), 2689.

Abrahart, R. J., Anctil, F., Coulibaly, P., Dawson, C. W., Mount, N. J., See, L. M., ... & Wilby, R. L. (2012). Two decades of anarchy? Emerging themes and outstanding challenges for neural network river forecasting. *Progress in Physical Geography*, *36*(4), 480-513.

Ademe, F., Kibret, K., Beyene, S., Getinet, M., & Mitike, G. (2020). Rainfall analysis for rain-fed farming in the Great Rift Valley Basins of Ethiopia. *Journal of Water and Climate Change*, *11*(3), 812-828.

Adnan, N. A., Atkinson, P. M., Yusoff, Z. M., & Rasam, A. R. A. (2014, March). Climate variability and anthropogenic impacts on a semi-distributed monsoon catchment runoff simulations. In *2014 IEEE 10th International Colloquium on Signal Processing and its Applications* (pp. 178-183). IEEE.

Aghelpour, P., Bagheri-Khalili, Z., Varshavian, V., & Mohammadi, B. (2022). Evaluating three supervised machine learning algorithms (LM, BR, and SCG) for daily pan evaporation estimation in a semi-arid region. Water, 14(21), 3435.

Ahmad, F., Ushiyama, T., & Sayama, T. (2017). Determination of ZR relationship and inundation analysis for Kuantan river basin. *Malays. Meterol. Dep. Res. Publ*, *2*, 55.

Ahmed, S. I., Rudra, R., Goel, P., Khan, A., Gharabaghi, B., & Sharma, R. (2022). A comparative evaluation of using rain gauge and NEXRAD radar-estimated rainfall data for simulating streamflow. *Hydrology*, *9*(8), 133.

Aldrich .C (2002), “Exploratory Analysis of Metallurgical Process Data with Neural Networks and Related Methods”, Elsevier Science, British Library Cataloguing in Publication Data, Netherlands, Vol.1, pp.56-57.

Alfieri, L., Claps, P., & Laio, F. (2010). Time-dependent ZR relationships for estimating rainfall fields from radar measurements. *Natural Hazards and Earth System Sciences*, *10*(1), 149-158.

Ali, A., Deranadyan, G., & Umam, I. H. (2021). An enhancement to the quantitative precipitation estimation using radar-gauge merging. *International Journal of Remote Sensing and Earth Sciences (IJReSES)*, *17*(1), 65-74.

Alpers, W., & Melsheimer, C. (2004). Rainfall. *Synthetic Aperture Radar Marine Users Manual*, 353-372.

Alqudah, A., Chandrasekar, V., & Le, M. (2013). Investigating rainfall estimation from radar measurements using neural networks. *Natural Hazards and Earth System Sciences*, *13*(3), 535-544.

Anagnostou, E. N. (2004). A convective/stratiform precipitation classification algorithm for volume scanning weather radar observations. *Meteorological Applications*, *11*(4), 291-300.

ArcGIS website. Retrieved on 20 November 2021. https://www.arcgis.com/home/item.html?id=cfcb7609de5f478eb7666240902d4d3d.

Asmat, A., Hazali, N. A., Sahak, N., Tahir, W., & Ramli, S. (2021). Spatial Rainfall Rate Estimation from Multi-Source Data in Klang Valley, Malaysia. *International Journal of Geoinformatics*, *17*(2).

Aswin, S., Geetha, P., & Vinayakumar, R. (2018, April). Deep learning models for the prediction of rainfall. In *2018 International Conference on Communication and Signal Processing (ICCSP)* (pp. 0657-0661). IEEE.

Atlas, D. (1964). Advances in radar meteorology. Advances in geophysics, 10, 317-478.

Azad, W. H., Hassan, M. H., Ghazali, N. H. M., Weisgerber, A., & Ahmad, F. (2019, November). National flood forecasting and warning system of Malaysia: an overview. In *International Conference on Dam Safety Management and Engineering* (pp. 264-273). Singapore: Springer Singapore.

Azam, S. H. M. N., Tahir, W., & Abdullah, J. (2021, January). Assessment of SRTM, ASTER and IFSAR digital elevation model (DEM) in oil palm plantation river derivation and basin delineation. In *Proceedings of the international conference on civil, offshore and environmental engineering* (pp. 56-65). Singapore: Springer Singapore.

Bangsawan, L., Jatmiko, R. H., & Nurjani, E. (2022, September). The comparison of zr relation methods on convective and stratiform rain of quantitative precipitation estimation (QPE) in east java area. In *Proceedings of the International Conference on Radioscience, Equatorial Atmospheric Science and*

Environment and Humanosphere Science, 2021 (pp. 273-285). Singapore: Springer Nature Singapore.

Barbosa, J. H. S., Fernandes, A., Lima, A., & Assis, L. (2019). The influence of spatial discretization on HEC-HMS modelling: a case study. *International Journal of Hydrology*, *3*(5), 442-449.

Bárdossy, A., & Pegram, G. (2017). Combination of radar and daily precipitation data to estimate meaningful sub-daily point precipitation extremes. *Journal of Hydrology*, *544*, 397-406.

Barnolas, M., Rigo, T., & Llasat, M. C. (2010). Characteristics of 2-D convective structures in Catalonia (NE Spain): an analysis using radar data and GIS. *Hydrology and Earth System Sciences*, *14*(1), 129-139.

Batool, S., Frezza, F., Mangini, F., & Simeoni, P. (2020). Introduction to radar scattering application in remote sensing and diagnostics. *Atmosphere*, *11*(5), 517.

Battan, L. J. (1973). Radar observation of the atmosphere. *University of Chicago Press.*

Battan, L. J. (1975). Doppler radar observations of a hailstorm. *Journal of Applied Meteorology (1962-1982)*, 98-108.

Bech, J., Gjertsen, U., & Haase, G. (2007). Modelling weather radar beam propagation and topographical blockage at northern high latitudes. *Quarterly Journal of the Royal Meteorological Society: A journal of the atmospheric sciences, applied meteorology and physical oceanography*, *133*(626), 1191-1204.

Binetti, M. S., Campanale, C., Massarelli, C., & Uricchio, V. F. (2022). The use of weather radar data: Possibilities, challenges and advanced applications. *Earth*, *3*(1), 157-171.

Birkhead, A. L., & James, C. S. (2002). Muskingum river routing with dynamic bank storage. *Journal of Hydrology*, *264*(1-4), 113-132.

Biswas, S. K., Cifelli, R., & Chandrasekar, V. (2020). Improving Quantitative Precipitation Estimation by X-Band Dual-Polarization Radars in Complex Terrain Over the Bay Area in California, USA. In *IGARSS 2020-2020 IEEE International Geoscience and Remote Sensing Symposium* (pp. 5411-5414). IEEE.

Bonelli, P., & Marcacci, P. (2008). Thunderstorm nowcasting by means of lightning and radar data: algorithms and applications in northern Italy. *Natural Hazards and Earth System Sciences*, *8*(5), 1187-1198.

Boodoo, S., Hudak, D., Ryzhkov, A., Zhang, P., Donaldson, N., Sills, D., & Reid, J. (2015). Quantitative precipitation estimation from a C-band dual-polarized radar for the 8 July 2013 flood in Toronto, Canada. *Journal of Hydrometeorology*, *16*(5), 2027-2044.

Bringi, V. N., Chandrasekar, V., Hubbert, J., Gorgucci, E., Randeu, W. L., & Schoenhuber, M. (2003). Raindrop size distribution in different climatic regimes from disdrometer and dual-polarized radar analysis. *Journal of the atmospheric sciences*, *60*(2), 354-365.

Bringi, V. N., Rico-Ramirez, M. A., & Thurai, M. (2011). Rainfall estimation with an operational polarimetric C-band radar in the United Kingdom: Comparison with a gauge network and error analysis. *Journal of Hydrometeorology*, *12*(5), 935-954.

Brown, B. R., Bell, M. M., & Frambach, A. J. (2016). Validation of simulated hurricane drop size distributions using polarimetric radar. *Geophysical Research Letters*, *43*(2), 910-917.

Brown, R. A. (2013). Doppler weather radar. In *Encyclopedia of natural hazards* (pp. 188-188). Springer, Dordrecht.

Bruen, M., & O'Loughlin, F. (2014). Towards a nonlinear radar-gauge adjustment of radar via a piece-wise method. *Meteorological Applications*, *21*(3), 675-683.

Bukar, U. A., Sidi, F., Jabar, M. A., Nor, R. N. H. B., Abdullah, S., & Ishak, I. (2022). A multistage analysis of predicting public resilience of impactful social media crisis communication in flooding emergencies. *IEEE Access*, *10*, 57266-57282.

Buscema, M. (1998). Back propagation neural networks. *Substance use & misuse*, *33*(2), 233-270.

Byers, H. R., & Braham, R. R. (1949). *The thunderstorm: report of the Thunderstorm Project*. US Government Printing Office.

Calvetti, L., Beneti, C., Neundorf, R. L. A., Inouye, R. T., Santos, T. N. D., Gomes, A. M., ... & de Gonçalves, L. G. G. (2017). Quantitative precipitation estimation integrated by poisson’s equation using radar mosaic, satellite, and rain gauge network. *Journal of Hydrologic Engineering*, *22*(5), E5016003.

Cao, X., Yang, B., Shen, Y., Yuen, C., Zhang, Y., Han, Z., ... & Hanzo, L. (2022). Edge-assisted multi-layer offloading optimization of LEO satellite-terrestrial integrated networks. *IEEE Journal on Selected Areas in Communications*, *41*(2), 381-398.

Capsoni, C., D’Amico, M., & Locatelli, P. (2008). Statistical properties of rain cells in the Padana Valley. *Journal of Atmospheric and Oceanic Technology*, *25*(12), 2230-2244.

Caseri, A. N., Santos, L. B. L., & Stephany, S. (2022). A convolutional recurrent neural network for strong convective rainfall nowcasting using weather radar data in Southeastern Brazil. *Artificial Intelligence in Geosciences*, *3*, 8-13.

Chen, F., Zheng, X., Wen, H., & Yuan, Y. (2022). Microphysics of convective and stratiform precipitation during the summer monsoon season over the Yangtze–Huaihe River Valley, China. *Journal of Hydrometeorology*, *23*(2), 239-252.

Chen, H., Chandrasekar, V., Cifelli, R., & Xie, P. (2019). A machine learning system for precipitation estimation using satellite and ground radar network observations. *IEEE Transactions on Geoscience and Remote Sensing, 58(2),* 982-994.

Chen, J. Y., Chang, W. Y., & Chang, P. L. (2021). A synthetic quantitative precipitation estimation by integrating S-and C-band dual-polarization radars over northern Taiwan. *Remote Sensing*, *13*(1), 154.

Cheng, K. S., Lin, Y. C., & Liou, J. J. (2008). Rain-gauge network evaluation and augmentation using geostatistics. *Hydrological Processes: An International Journal*, *22*(14), 2554-2564.

Cheok H.S, (2005): Development of PC Based Tank Model Real Time Flood Forecasting System. Faculty of Civil Engineering, Universiti Teknologi Malaysia.

Choi, Y., & Kim, S. (2020). Rain-type classification from microwave satellite observations using deep neural network segmentation. *IEEE Geoscience and Remote Sensing Letters*, *18*(12), 2137-2141.

Chong, S.F. and Amin, M.Z.M (2001). Flood Forecasting Systems in Malaysia, National Conference on Hydraulics , Hydrology and Sustainable Water Resources Development, Bangi, Malaysia 24-26 September.

Chu, X., & Steinman, A. (2009). Event and continuous hydrologic modeling with HEC-HMS. *Journal of Irrigation and Drainage Engineering*, *135*(1), 119-124.

Chumchean, S. (2004). Improved estimation of radar rainfall for use in hydrological modelling.

Chumchean, S., Sharma, A., & Seed, A. (2006). An integrated approach to error correction for real-time radar-rainfall estimation. *Journal of Atmospheric and Oceanic Technology*, *23*(1), 67-79.

Ciach, G. J., & Krajewski, W. F. (1999). Radar–rain gauge comparisons under observational uncertainties. *Journal of applied meteorology*, *38*(10), 1519-1525.

Cifelli, R., Chandrasekar, V., Lim, S., Kennedy, P. C., Wang, Y., & Rutledge, S. A. (2011). A new dual-polarization radar rainfall algorithm: Application in Colorado precipitation events. *Journal of Atmospheric and Oceanic Technology*, *28*(3), 352-364.

Collier, C. G. (2000). Precipitation. In *Remote Sensing in Hydrology and Water Management* (pp. 111-132). Berlin, Heidelberg: Springer Berlin Heidelberg.

Cox, C. H., & Ackerman, E. I. (2022, March). Review of radar system needs, and performance of techniques, for STAR. In *2022 IEEE Radar Conference (RadarConf22)* (pp. 1-6). IEEE.

Cramer, S., Kampouridis, M., Freitas, A. A., & Alexandridis, A. K. (2017). An extensive evaluation of seven machine learning methods for rainfall prediction in weather derivatives. *Expert Systems with Applications*, *85*, 169-181.

D. J. Yik, Y. W. Sang, N. K. Chang, F. J. Fakaruddin, A. Dindang, & M. H. Abdullah, (2018). Analysis of the cyclonic vortex and evaluation of the performance of the radar integrated nowcasting system (RAINS) during the heavy rainfall episode which caused flooding in Penang, Malaysia on 5 November 2017. Tropical Cyclone Research and Review, 7(4), 217-229.

D. Wolfensberger, M. Gabella, M. Boscacci, U. Germann, & A. Berne, (2021). RainForest: a random forest algorithm for quantitative precipitation estimation over Switzerland. Atmospheric Measurement Techniques, 14(4), 3169-3193.

Daide, F., Afgane, R., Lahrach, A., Chaouni, A. A., Msaddek, M., & Elhasnaoui, I. (2021). Application of the HEC-HMS hydrological model in the Beht watershed (Morocco). In *E3S Web of Conferences* (Vol. 314, p. 05003). EDP Sciences.

Das, K., Jiang, J., & Rao, J. N. K. (2004). Mean squared error of empirical predictor.

Delrieu, G., Wijbrans, A., Boudevillain, B., Faure, D., Bonnifait, L., & Kirstetter, P. E. (2014). Geostatistical radar–raingauge merging: A novel method for the quantification of rain estimation accuracy. *Advances in Water Resources*, *71*, 110-124.

Deo, A., & Walsh, K. J. (2016). Contrasting tropical cyclone and non-tropical cyclone related rainfall drop size distribution at Darwin, Australia. *Atmospheric Research*, *181*, 81-94.

Dewangan, S. K., Nagarjuna, C., Jain, R., Kumawat, R. L., Kumar, V., Sharma, A., & Ahn, B. (2023). Review on applications of artificial neural networks to develop high entropy alloys: A state-of-the-art technique. *Materials Today Communications*, 107298.

Dhiram, K., & Wang, Z. (2016). Evaluation on radar reflectivity-rainfall rate (ZR) relationships for Guyana. Atmospheric and Climate Sciences, 6(4), 489-499.

Dixon, M., & Wiener, G. (1993). TITAN: Thunderstorm identification, tracking, analysis, and nowcasting—A radar-based methodology. *Journal of atmospheric and oceanic technology*, *10*(6), 785-797.

Djafri, A., & Haddad, B. (2014). Classification of Convective and Stratiform Cells in Meteorological Radar Images Using Svm Based on A Textural Analysis. *Journal of Electronic Science and Technology*, *12*(1), 130-133.

Doviak, R. J., & Zrnic, D. S. (2014). Doppler radar & weather observations. Academic press.

Doviak, R. J., Zrnic, D. S., & Schotland, R. M. (1994). Doppler radar and weather observations. Applied Optics, 33(21), 4531.

El Afandi, G., Morsy, M., & El Hussieny, F. (2013). Heavy rainfall simulation over Sinai Peninsula using the weather research and forecasting model. *International Journal of Atmospheric Sciences*, *2013*(1), 241050.

Falconi, M. T., & Marzano, F. S. (2019). Weather radar data processing and atmospheric applications: An overview of tools for monitoring clouds and detecting wind shear. *IEEE Signal Processing Magazine*, *36*(4), 85-97.

Féral, L., Mesnard, F., Sauvageot, H., Castanets, L., & Lemorton, J. (2000). Rain cells shape and orientation distribution in south-west of France. *Physics and Chemistry of the Earth, Part B: Hydrology, Oceans and Atmosphere*, *25*(10-12), 1073-1078.

Flach, P. (2019, July). Performance evaluation in machine learning: the good, the bad, the ugly, and the way forward. In *Proceedings of the AAAI conference on artificial intelligence* (Vol. 33, No. 01, pp. 9808-9814).

Fleming, M. (2004). Description of the hydrologic engineering center's hydrologic modeling system (HEC-HMS) and application to watershed studies.

Foth, A., Zimmer, J., Lauermann, F., & Kalesse-Los, H. (2021). Evaluation of micro rain radar-based precipitation classification algorithms to discriminate between stratiform and convective precipitation. *Atmospheric Measurement Techniques*, *14*(6), 4565-4574.

Fraile, R., & Fernández-Raga, M. (2009). On a more consistent definition of radar reflectivity. *Atmósfera*, *22*(4), 375-385.

Fulton, R. A., Breidenbach, J. P., Seo, D. J., Miller, D. A., & O'Bannon, T. (1998). The WSR-88D rainfall algorithm. Weather and forecasting, 13(2), 377-395.

Garba, J. N., Diasso, U. J., Waongo, M., Sawadogo, W., & Daho, T. (2023). Performance evaluation of satellite-based rainfall estimation across climatic zones in Burkina Faso. *Theoretical and Applied Climatology*, *154*(3), 1051-1073.

Gauthreaux, S., & Diehl, R. (2020). Discrimination of biological scatterers in polarimetric weather radar data: Opportunities and challenges. *Remote Sensing*, *12*(3), 545.

Gavin, H. P. (2019). The Levenberg-Marquardt algorithm for nonlinear least squares curve-fitting problems. *Department of Civil and Environmental Engineering Duke University August*, *3*.

Ghada, W., Casellas, E., Herbinger, J., Garcia-Benadí, A., Bothmann, L., Estrella, N., ... & Menzel, A. (2022). Stratiform and convective rain classification using machine learning models and micro rain radar. *Remote Sensing*, *14*(18), 4563.

Giangrande, S. E., Collis, S., Theisen, A. K., & Tokay, A. (2014). Precipitation estimation from the ARM distributed radar network during the MC3E campaign. *Journal of Applied Meteorology and Climatology*, *53*(9), 2130-2147.

Giannakos, A., & Feidas, H. (2013). Classification of convective and stratiform rain based on the spectral and textural features of Meteosat Second Generation infrared data. *Theoretical and applied climatology*, *113*, 495-510.

Gou, Y., Chen, H., & Zheng, J. (2019). An improved self-consistent approach to attenuation correction for C-band polarimetric radar measurements and its impact on quantitative precipitation estimation. *Atmospheric Research*, *226*, 32-48.

Gou, Y., Ma, Y., Chen, H., & Wen, Y. (2018). Radar-derived quantitative precipitation estimation in complex terrain over the eastern Tibetan Plateau. *Atmospheric Research*, *203*, 286-297.

Gu, J. Y., Ryzhkov, A., Zhang, P., Neilley, P., Knight, M., Wolf, B., & Lee, D. I. (2011). Polarimetric attenuation correction in heavy rain at C band. *Journal of Applied Meteorology and Climatology*, *50*(1), 39-58.

Guduru, J. U., Jilo, N. B., Rabba, Z. A., & Namara, W. G. (2023). Rainfall-runoff modeling using HEC-HMS model for Meki River watershed, rift valley basin, Ethiopia. *Journal of African Earth Sciences*, *197*, 104743.

Gunathilake, M. B., Panditharathne, P., Gunathilake, A. S., & Warakagoda, N. (2020). Application of a HEC-HMS model on event-based simulations in a tropical watershed. *Engineering and Applied Science Research*, *47*(4), 349-360.

Hagos, S., Feng, Z., Plant, R. S., & Protat, A. (2020). A machine learning assisted development of a model for the populations of convective and stratiform clouds. *Journal of Advances in Modeling Earth Systems*, *12*(3), e2019MS001798.

Han, H., Choi, C., Jung, J., & Kim, H. S. (2021). Deep learning with long short term memory based sequence-to-sequence model for rainfall-runoff simulation. *Water*, *13*(4), 437.

Hanchoowong, R., Weesakul, U., & Chumchean, S. (2012). Bias correction of radar rainfall estimates based on a geostatistical technique. *Sci. Asia*, *38*, 373-385.

Handoyo, M. F., Hadi, M. P., & Suprayogi, S. (2021, November). Application of Attenuation Correction to Quantitative Precipitation Estimation on C-Band Weather Radar in Bengkulu. In *IOP Conference Series: Earth and Environmental Science* (Vol. 893, No. 1, p. 012054). IOP Publishing.

Hasni, H., Tahir, W., Osman, N. S., & Haron, N. F. (2024). Calibration and Performance Evaluation of Radar QPE and QPF in Klang River Basin. International Journal of Sustainable Construction Engineering and Technology, 15(3), 324-334.

Hawkins, R. H., Ward, T. J., Woodward, D. E., & Van Mullem, J. A. (2009). *Curve number hydrology: state of the practice. American Society of Civil Engineers*.

Haykin, S. (1994). *Neural networks: a comprehensive foundation*. Prentice hall PTR.

He, X., Sonnenborg, T. O., Refsgaard, J. C., Vejen, F., & Jensen, K. H. (2013). Evaluation of the value of radar QPE data and rain gauge data for hydrological modeling. *Water Resources Research*, *49*(9), 5989-6005.

Hong, Y., & Gourley, J. J. (2017). *Radar Hydrology*. Oxford, UK:: Taylor & Francis Limited.

Houze Jr, R. A. (1997). Stratiform precipitation in regions of convection: A meteorological paradox?. *Bulletin of the American Meteorological Society*, *78*(10), 2179-2196.

Houze Jr, R. A. (2004). Mesoscale convective systems. *Reviews of Geophysics*, *42*(4).

Huang, Y., Wang, Y., & Cui, X. (2019). Differences between convective and stratiform precipitation budgets in a torrential rainfall event. *Advances in Atmospheric Sciences*, *36*(5), 495-509.

Huangfu, J., Hu, Z., Zheng, J., Wang, L., & Zhu, Y. (2024). Study on quantitative precipitation estimation by polarimetric radar using deep learning. *Advances in Atmospheric Sciences*, *41*(6), 1147-1160.

Hung, M. K., Tien, D. D., Quan, D. D., Duc, T. A., Dung, P. T. P., Hole, L. R., & Nam, H. G. (2023). Assessments of use of blended radar–numerical weather prediction product in short-range warning of intense rainstorms in localized systems (SWIRLS) for quantitative precipitation forecast of tropical cyclone landfall on Vietnam's Coast. Atmosphere, 14(8), 1201.

Husnoo, N., Darlington, T., Torres, S., & Warde, D. (2021). A neural network quality-control scheme for improved quantitative precipitation estimation accuracy on the UK weather radar network. *Journal of Atmospheric and Oceanic Technology*, *38*(6), 1157-1172.

Hydrologic Engineering Center. (2025). *Gridded precipitation*. U.S. Army Corps of Engineers.https://www.hec.usace.army.mil/confluence/hmsdocs/hmstrm/meteorology/precipitation/gridded-precipitation?

Hwang, S. H., Kim, K. B., & Han, D. (2020). Comparison of methods to estimate areal means of short duration rainfalls in small catchments, using rain gauge and radar data. *Journal of Hydrology*, *588*, 125084.

InfoBanjir JPS Selangor (2008). Bahagian Pengurusan Sumber Air dan Hidrologi JPS Negeri Selangor. Google Images. https://infobanjirjps.selangor.gov.my/iwpns.html

Islam, T., Srivastava, P. K., Dai, Q., Gupta, M., & Jaafar, W. Z. W. (2015). Stratiform/convective rain delineation for TRMM microwave imager. *Journal of Atmospheric and Solar-Terrestrial Physics*, *133*, 25-35.

Ismail, H., Kamal, M. R., Hin, L. S., & Abdullah, A. F. (2020). Performance of HEC-HMS and ArcSWAT Models for Assessing Climate Change Impacts on Streamflow at Bernam River Basin in Malaysia. *Pertanika Journal of Science & Technology*, *28*(3).

Jaffar, O., Hadri, A., Ait Naceur, K., Saidi, M. E., Tramblay, Y., & Chehbouni, A. (2024). Assessment of hydrological model performance in Morocco in relation to model structure and catchment characteristics. Journal of Hydrology: Regional Studies, 54, 101899.

Jamaluddin, A. F., Kamal, M. I. M., Abdullah, M. H., & Marodzi, A. N. (2022). Comparison between Satellite-Derived Rainfall and Rain Gauge Observation over Peninsular Malaysia. *Sains Malaysiana*, *51*(1), 67-81.

Jang, M., Lee, D. I., You, C. H., Kim, D. S., Maki, M., Jeong, J. H., & Uyeda, H. (2012). Quantitative precipitation estimates from radar reflectivity corrected by the SMA method. *Atmospheric research*, *104*, 111-118.

Johnson, A. E., Carmichael, O., Huber, D. F., & Hebert, M. (1998). Toward a general 3-d matching engine: Multiple models, complex scenes, and efficient data filtering.

Karbalaee, N., Hsu, K., Sorooshian, S., & Braithwaite, D. (2017). Bias adjustment of infrared-based rainfall estimation using passive microwave satellite rainfall data. *Journal of Geophysical Research: Atmospheres, 122(7),* 3859-3876.

Karklinsky, M. M. E., & Morin, E. (2006). Spatial characteristics of radar-derived convective rain cells over southern Israel. *Meteorologische Zeitschrift*, *15*(5), 513-520.

Kartik.(2025, January).K-Nearest Neighbor(KNN) Algorithm. GeeksforGeeks. https://www.geeksforgeeks.org/k-nearest-neighbours/

Kato, A., & Maki, M. (2009). Localized Heavy Rainfall Near Zoshigaya, Tokyo, Japan on 5 August 2008 Observed by X-band Polarimetric Radar—Preliminary Analysis—. *Sola*, *5*, 89-92.

Kevin L. Priddy and Paul E.Keller (2005), “Artificial Neural Networks An Introduction”, SPIE-The International Society of Optical Engineering, Washington.

Kim Loi, H. (1996). Flood mitigation and flood risk management in Malaysia. In *Proceedings of international workshop on floodplain risk management* (pp. 205-16).

Kirsch, B., Clemens, M., & Ament, F. (2019). Stratiform and convective radar reflectivity–rain rate relationships and their potential to improve radar rainfall estimates. *Journal of Applied Meteorology and Climatology*, *58*(10), 2259-2271.

Kou, L., Mao, Y., Lin, Z., Gao, H., Chu, Z., & Chen, A. (2024). Error modeling and hierarchical Bayesian fusion for spaceborne and ground radar rainfall data. *Journal of Hydrology*, *629*, 130599.

Kovalchuk, M., Zikesova, A., Albakawe, A., & Fiser, O. (2023, July). On Improved ZR Realtion Derived from Czech Distrometer Data. In *2023 Photonics & Electromagnetics Research Symposium (PIERS)* (pp. 2156-2160). IEEE.

Krajewski, W. F., Vignal, B., Seo, B. C., & Villarini, G. (2011). Statistical model of the range-dependent error in radar-rainfall estimates due to the vertical profile of reflectivity. *journal of hydrology*, *402*(3-4), 306-316.

Kumar, P., Singh, R., Sharma, A., Singh, G., Kumar, D., & Singh, A. K. (2021). Comparison of Different Interpolation Techniques for Mean Areal Rainfall Estimation of Uttarakhand using Geographical Information System. Journal of the New England Water Works Association, 135(3), 43-50.

Kumar, S., Amarnath, G., Ghosh, S., Park, E., Baghel, T., Wang, J., ... & Belbase, D. (2022). Assessing the performance of the satellite-based precipitation products (SPP) in the data-sparse Himalayan Terrain. *Remote Sensing*, *14*(19), 4810.

Kuok, K. K. (2010). *Parameter optimization methods for calibrating tank model and neural network model for rainfall-runoff modeling* (Doctoral dissertation, Ph. D. Thesis. University Technology Malaysia).

Kyznarová, H., & Novák, P. (2009). CELLTRACK—Convective cell tracking algorithm and its use for deriving life cycle characteristics. *Atmospheric research*, *93*(1-3), 317-327.

Lanza, L. G., Cauteruccio, A., & Stagnaro, M. (2022). Rain gauge measurements. In Rainfall (pp. 77-108). Elsevier.

Laskar, B. Z., & Majumder, S. (2015). Artificial Neural Networks and Gene Expression Programing based age estimation using facial features. *journal of king saud university-computer and information sciences*, *27*(4), 458-467.

Lavanya, S., & Kirankumar, N. V. P. (2021). Classification of tropical coastal precipitating cloud systems using disdrometer observations over Thumba, India. *Atmospheric Research*, *253*, 105477.

Lazri, M. and Ameur, S.: Combination of support vector ma chine, artificial neural network and random forest for improv ing the classification of convective and stratiform rain using spectral features of SEVIRI data, Atmos. Res., 203, 118–129, https://doi.org/10.1016/j.atmosres.2017.12.006, 2018.

Lee, H., & Kim, S. (2017). Ensemble classification for anomalous propagation echo detection with clustering-based subset-selection method. *Atmosphere*, *8*(1), 11.

Legates, D. R., & McCabe Jr, G. J. (1999). Evaluating the use of "goodness-of-fit" measures in hydrologic and hydroclimatic model validation. Water resources research, 35(1), 233-241.

Li, W., Chen, H., & Han, L. (2023). Polarimetric radar quantitative precipitation estimation using deep convolutional neural networks. *IEEE Transactions on Geoscience and Remote Sensing*, *61*, 1-11.

Li, W., Chen, H., & Han, L. (2024). Improving explainability of deep learning for polarimetric radar rainfall estimation. *Geophysical Research Letters*, *51*(11), e2023GL107898.

Liu, Y., Liu, D., Qin, Z., Liu, F., & Liu, L. (2016). Rainfall data feature extraction and its verification in displacement prediction of Baishuihe landslide in China. *Bulletin of Engineering Geology and the Environment*, *75*, 897-907.

Llasat, M. C., & Rigo, T. (2002, October). The use of automatic raingauges and/or meteorological radar for identifying convective rainfall. In *Proceedings of 4th Plinius Conference on Mediterranean Storms, Mallorca, Spain* (pp. 2-4).

Llasat, M. C., Ceperuelo, M., & Rigo, T. (2007). Rainfall regionalization on the basis of the precipitation convective features using a raingauge network and weather radar observations. *Atmospheric research*, *83*(2-4), 415-426.

Lu, X., Li, J., Liu, Y., Li, Y., & Huo, H. (2023). Quantitative precipitation estimation in the Tianshan mountains based on machine learning. *Remote Sensing*, *15*(16), 3962.

Ma, J., Cui, X., & Jiang, N. (2022). Modelling the ZR Relationship of Precipitation Nowcasting Based on Deep Learning. *Computers, Materials and Continua*, *72*(1), 1939-1949.

Mahdianpari, M., Salehi, B., Rezaee, M., Mohammadimanesh, F., & Zhang, Y. (2018). Very deep convolutional neural networks for complex land cover mapping using multispectral remote sensing imagery. *Remote Sensing*, *10*(7), 1119.

Mahyun, A. W., Chua, K. K., Salwa, M. Z. M., Seman, N. A., Hassan, Z., & Kamarudzaman, A. N. (2021). Derivation of ZR relationship parameter for Alor Setar radar using Traditional Matching Method (TMM). In *IOP Conference Series: Earth and Environmental Science* (Vol. 646, No. 1, p. 012043). IOP Publishing.

Majid, M. A., Omar, M. H., Noorani, M. S. M., & Razak, F. A. (2021, October). River-flood forecasting methods: the context of the Kelantan River in Malaysia. In *IOP Conference Series: Earth and Environmental Science* (Vol. 880, No. 1, p. 012021). IOP Publishing.

Malaymail (2021) https://www.malaymail.com/news/malaysia/2021/12/29/taman-sri-muda-floods-not-caused-by-construction-project-near-sluice-gate-s/2031905

Malaysian Meteorological Department (METMalaysia). Retrieved on 13 April 2024. https://www.met.gov.my/pencerapan/radar-malaysia/

Marshall, J. S., & Palmer, W. M. K. (1948). The distribution of raindrops with size. *Journal of Atmospheric Sciences*, *5*(4), 165-166.

Martin, O., Rugumayo, A., & Ovcharovichova, J. (2012). Application of HEC HMS/RAS and GIS tools in flood modeling: A case study for river Sironko–Uganda. *Glob J Eng Des Technol*, *1*(2), 19-31.

Martinaitis, S. M., Osborne, A. P., Simpson, M. J., Zhang, J., Howard, K. W., Cocks, S. B., ... & Kaney, B. T. (2020). A physically based multisensor quantitative precipitation estimation approach for gap-filling radar coverage. *Journal of Hydrometeorology*, *21*(7), 1485-1511.

Mat Taib, A. T., Tahir, W., Ramli, S., & Ahmad Mohtar, I. S. (2020). Hydro-Meteorological Flood Forecasting Using Tank Model with Satellite-Based Rainfall Input for Kemaman River Catchment. *International Journal of Civil Engineering and Technology*, *11*(1).

May, P. T., & Ballinger, A. (2007). The statistical characteristics of convective cells in a monsoon regime (Darwin, Northern Australia). *Monthly weather review*, *135*(1), 82-92.

McKee, J. L., & Binns, A. D. (2016). A review of gauge–radar merging methods for quantitative precipitation estimation in hydrology. *Canadian Water Resources Journal/Revue canadienne des ressources hydriques*, *41*(1-2), 186-203.

Mecklenburg, S., Jurczyk, A., Szturc, J., & Ośródka, K. (2005). Use of radar observation in hydrological and NWP models. *Quantitative precipitation forecasts (QPF) based on radar data for hydrological models, COST Action*, *717*.

Mehrotra, K., Mohan, C. K., & Ranka, S. (1997). *Elements of artificial neural networks*. MIT press.

Meischner, P. (Ed.). (2005). *Weather radar: principles and advanced applications*. Springer Science & Business Media.

Mekonnen, K., Velpuri, N. M., Leh, M., Akpoti, K., Owusu, A., Tinonetsana, P., ... & Munzimi, Y. (2023). Accuracy of satellite and reanalysis rainfall estimates over Africa: a multi-scale assessment of eight products for continental applications. *Journal of Hydrology: Regional Studies*, *49*, 101514.

Met Office. (2023). Weather radar factsheet. Met Office. https://www.metoffice.gov.uk/

Militino, A. F., Ugarte, M. D., & Pérez-Goya, U. (2018). Improving the quality of satellite imagery based on ground-truth data from rain gauge stations. *Remote Sensing*, *10*(3), 398.

Mishra, S. K., & Singh, V. P. (2013). *Soil conservation service curve number (SCS-CN) methodology* (Vol. 42). Springer Science & Business Media.

Mohamad Sukairi, S., Harun, S., Mohd Nasir, K. A., Jeevaragagam, P., & Mohd Salleh, M. R. (2023). Application of Geospatial and Hydrological Modeling for Runoff Estimation in Lebir River Basin, Malaysia. *The International Archives of the Photogrammetry, Remote Sensing and Spatial Information Sciences*, *48*, 231-235.

Montopoli, M., Roberto, N., Adirosi, E., Gorgucci, E., & Baldini, L. (2017). Investigation of weather radar quantitative precipitation estimation methodologies in complex orography. *Atmosphere*, *8*(2), 34.

Moriasi, D. N., Arnold, J. G., Van Liew, M. W., Bingner, R. L., Harmel, R. D., & Veith, T. L. (2007). Model evaluation guidelines for systematic quantification of accuracy in watershed simulations. *Transactions of the ASABE*, *50*(3), 885-900.

Mosavi, A., Ozturk, P., & Chau, K. W. (2018). Flood prediction using machine learning models: Literature review. *Water*, *10*(11), 1536.

Nasrullah, M. F., Saedudin, R. R., & Hamami, F. (2024). Comparison Accuracy of C4. 5 Algorithm and K-Nearest Neighbors for Rainfall Classification. *SITEKNIK: Information Systems, Engineering and Applied Technology*, *1*(2), 90-101.

Nielsen, J. M., van de Beek, C. Z. R., Thorndahl, S., Olsson, J., Andersen, C. B., Andersson, J. C. M., ... & Nielsen, J. E. (2024). Merging weather radar data and opportunistic rainfall sensor data to enhance rainfall estimates. *Atmospheric Research*, *300*, 107228.

Nogales, R. E., & Benalcázar, M. E. (2023). Analysis and evaluation of feature selection and feature extraction methods. *International Journal of Computational Intelligence Systems*, *16*(1), 153.

Olawoyin, R., & Acheampong, P. K. (2017). Objective assessment of the Thiessen polygon method for estimating areal rainfall depths in the River Volta catchment in Ghana. *Ghana Journal of Geography*, *9*(2), 151-174.

Oleyiblo, J. O., & Li, Z. (2010). *Application of HEC-HMS for flood forecasting in Misai and Wan'an catchments in China. Water Science and Engineering, 3 (1), 14–22*.

Orescanin, M., Petković, V., Powell, S. W., Marsh, B. R., & Heslin, S. C. (2021). Bayesian deep learning for passive microwave precipitation type detection. *IEEE Geoscience and Remote Sensing Letters*, *19*, 1-5.

Osman, N. S., & Tahir, W. (2024). Radar Quantitative Precipitation Estimation (QPE) Calibration Methods: A Systematic Literature Review. *Engineering, Technology & Applied Science Research*, *14*(5), 16185-16192.

Ośródka, K., Szturc, J., & Jurczyk, A. (2014). Chain of data quality algorithms for 3-D single-polarization radar reflectivity (RADVOL-QC system). *Meteorological Applications*, *21*(2), 256-270.

Ozkaya, A. (2023). Assessing the numerical weather prediction (NWP) model in estimating extreme rainfall events: A case study for severe floods in the southwest Mediterranean region, Turkey. *Journal of Earth System Science*, *132*(3), 125.

Pauthier, B., Debuisson, S., Descotes, A., Pergaud, J., & Maillard, S. (2018). Radar Quantitative Precipitation Estimation improvement in Champagne vineyard. In *E3S Web of Conferences* (Vol. 50, p. 02013). EDP Sciences.

Peleg, N., Marra, F., Fatichi, S., Molnar, P., Morin, E., Sharma, A., & Burlando, P. (2018). Intensification of convective rain cells at warmer temperatures observed from high-resolution weather radar data. *Journal of Hydrometeorology*, *19*(4), 715-726.

Penide, G., Protat, A., Kumar, V. V., & May, P. T. (2013). Comparison of two convective/stratiform precipitation classification techniques: Radar reflectivity texture versus drop size distribution–based approach. *Journal of Atmospheric and Oceanic Technology*, *30*(12), 2788-2797.

Peng, W., Bao, S., Yang, K., Wei, J., Zhu, X., Qiao, Z., ... & Li, Q. (2022). Radar Quantitative Precipitation Estimation Algorithm Based on Precipitation Classification and Dynamical ZR Relationship. Water, 14(21), 3436.

Poornima, S., & Pushpalatha, M. (2019). Prediction of rainfall using intensified LSTM based recurrent neural network with weighted linear units. *Atmosphere*, *10*(11), 668.

Powell, S. W., Houze Jr, R. A., & Brodzik, S. R. (2016). Rainfall-type categorization of radar echoes using polar coordinate reflectivity data. *Journal of Atmospheric and Oceanic Technology*, *33*(3), 523-538.

Rafieeinasab, A., Norouzi, A., Seo, D. J., & Nelson, B. (2015). Improving high-resolution quantitative precipitation estimation via fusion of multiple radar-based precipitation products. *Journal of Hydrology*, *531*, 320-336.

Raghavan, S. (2013). *Radar meteorology* (Vol. 27). Springer Science & Business Media.

Razeghi Haghighi, A., Salehi, H., Banikhedmat, A., Gharechelou, S., Mirabbasi, R., Pham, Q. B., & Torabi Haghighi, A. (2026). Comparative assessment of hydrological and deep learning models for runoff simulation and water storage in irrigated basins. Modeling Earth Systems and Environment, 12(1), 55.

Ramli, S. (2015). *The use of radar-rainfall inputs for quantitative precipitation estimation (QPE) in Klang River Basin* (Doctoral dissertation, Universiti Teknologi MARA).

Ramli, S., & Tahir, W. (2011). Radar hydrology: New Z/R relationships for quantitative precipitation estimation in Klang River Basin, Malaysia. *International Journal of Environmental Science and Development*, *2*(3), 223.

Ramly, S., & Tahir, W. (2016). Application of HEC-GeoHMS and HEC-HMS as rainfall–runoff model for flood simulation. In *ISFRAM 2015: Proceedings of the International Symposium on Flood Research and Management 2015* (pp. 181-192). Springer Singapore.

Ramly, S., Tahir, W., Abdullah, J., Jani, J., Ramli, S., & Asmat, A. (2020). Flood estimation for SMART control operation using integrated radar rainfall input with the HEC-HMS model. *Water Resources Management*, *34*(10), 3113-3127.

Ramly, S., Tahir, W., Jani, J., Sharifi, S., & Abdullah, J. (2022). Coupling of Cellular Automata Urban Growth Model and HEC-HMS to Predict Future Flood Extents in the Upper Klang Ampang Catchment. International Journal of Integrated Engineering, 14(5), 154-167.

Rigo, T., & Llasat, M. C. (2004). A methodology for the classification of convective structures using meteorological radar: Application to heavy rainfall events on the Mediterranean coast of the Iberian Peninsula. *Natural Hazards and Earth System Sciences*, *4*(1), 59-68.

Rizal, N. S., Umarie, I., Munandar, K., & Wardoyo, A. E. (2023). Calibration and validation of CN values for watershed hydrological response. *Civil Engineering Journal*, *9*(1), 72-85.

Robert Lamb (1970). "How Weather Works". Retrieved on 14 April 2024. HowStuffWorks.com. https://science.howstuffworks.com/nature/climate-weather/atmospheric/weather.htm

Romali, N. S., Yusop, Z., & Ismail, A. Z. (2018, March). Hydrological modelling using HEC-HMS for flood risk assessment of Segamat Town, Malaysia. In *IOP Conference Series: Materials Science and Engineering* (Vol. 318, No. 1, p. 012029). IOP Publishing.

Roshni, Y. (2014) Radar System . Google Images. https://electronicsdesk.com/radar-system.html

Roslan, N., Md Reba, M. N., Sharoni, S. M., & Hossain, M. S. (2021). The 3D Neural Network for Improving Radar-Rainfall Estimation in Monsoon Climate. Atmosphere, 12(5), 634. https://doi.org/10.3390/atmos12050634

Rosli, N.N. “Flood Modeling and Simulation for Different Landuse Pattern using Hec-Hms Model: Case Study of the Upper Catchments of the Kelantan River,” BE(Hons)(Civil), Dept. Civil. Eng., Univ. Tech. MARA.,Malaysia,2021.

Rulfová, Z., & Kyselý, J. (2013). Disaggregating convective and stratiform precipitation from station weather data. *Atmospheric research*, *134*, 100-115.

Saad, M. S. H., Ali, M. I., Razi, P. Z., & Ramli, N. I. (2024). Flood Risk Management in Development Projects: A Review of Malaysian Perspective within the Sendai Framework for Disaster Risk Reduction 2015-2030. *Construction*, *4*(2), 103-117.

Sadeghi, M., Asanjan, A. A., Faridzad, M., Nguyen, P. H. U., Hsu, K., Sorooshian, S., & Braithwaite, D. A. N. (2019). PERSIANN-CNN: Precipitation estimation from remotely sensed information using artificial neural networks–convolutional neural networks. *Journal of Hydrometeorology*, *20*(12), 2273-2289.

Sahu, M. K., Shwetha, H. R., & Dwarakish, G. S. (2023). State-of-the-art hydrological models and application of the HEC-HMS model: a review. *Modeling Earth Systems and Environment*, *9*(3), 3029-3051.

Salleh, N. S. A., Aziz, M. K. B. M., & Adzhar, N. (2019, November). Optimal design of a rain gauge network models. In *Journal of Physics: Conference Series* (Vol. 1366, No. 1, p. 012072). IOP Publishing.

Saltikoff, E., Friedrich, K., Soderholm, J., Lengfeld, K., Nelson, B., Becker, A., ... & Tassone, C. (2019). An overview of using weather radar for climatological studies: Successes, challenges, and potential. Bulletin of the American Meteorological Society, 100(9), 1739-1752.

Sang, Y. W., Yik, D. J., Chang, N., & Yunus, F. (2015). Analysis on the long term trends of consecutive dry and wet days and extreme rainfall amounts in Malaysia. *Malaysian Meteorological Department*.

Santos, L. B., Freitas, C. P., Bacelar, L., Soares, J. A., Diniz, M. M., Lima, G. R., & Stephany, S. (2023). A Neural Network-Based Hydrological Model for Very High-Resolution Forecasting Using Weather Radar Data. *Eng*, *4*(3), 1787-1796.

Sapountzis, M., Kastridis, A., Kazamias, A. P., Karagiannidis, A., Nikopoulos, P., & Lagouvardos, K. (2021). Utilization and uncertainties of satellite precipitation data in flash flood hydrological analysis in ungauged watersheds. *Glob. Nest J*, *23*, 388-399.

Sardoii, E. R., Rostami, N., Sigaroudi, S. K., & Taheri, S. (2012). Calibration of loss estimation methods in HEC-HMS for simulation of surface runoff (Case Study: Amirkabir Dam Watershed, Iran). *Adv. Environ. Biol*, *6*(1), 343-348.

Schleiss, M., Olsson, J., Berg, P., Niemi, T., Kokkonen, T., Thorndahl, S., ... & Pulkkinen, S. (2020). The accuracy of weather radar in heavy rain: a comparative study for Denmark, the Netherlands, Finland and Sweden. Hydrology and Earth System Sciences, 24(6), 3157-3188.

Schmidgall, S., Ziaei, R., Achterberg, J., Kirsch, L., Hajiseyedrazi, S., & Eshraghian, J. (2024). Brain-inspired learning in artificial neural networks: a review. *APL Machine Learning*, *2*(2).

Schumacher, C., & Houze Jr, R. A. (2003). The TRMM precipitation radar's view of shallow, isolated rain. Journal of Applied Meteorology, 42(10), 1519-1524.

Seed, A. W., Pierce, C. E., & Norman, K. (2013). Formulation and evaluation of a scale decomposition-based stochastic precipitation nowcast scheme. Water Resources Research, 49(10), 6624-6641.

Seela, B. K., Janapati, J., Kalath Unnikrishnan, C., Lin, P. L., Le Loh, J., Chang, W. Y., ... & Venkatrami Reddy, M. (2021). Raindrop size distributions of North Indian Ocean tropical cyclones observed at the coastal and inland stations in South India. *Remote Sensing*, *13*(16), 3178.

Sehad, M., Lazri, M., & Ameur, S. (2017). Novel SVM-based technique to improve rainfall estimation over the Mediterranean region (north of Algeria) using the multispectral MSG SEVIRI imagery. *Advances in Space Research*, *59*(5), 1381-1394.

Sen Jaiswal, R., M, S., M, R., & K, T. L. (2020). Characteristics of convective/stratiform dominance on surface rainfall over a few tropical locations. *Journal of Earth System Science*, *129*(1), 131.

Sene, K. (2024). Meteorological Observations. In *Hydrometeorology: Forecasting and Applications* (pp. 41-87). Cham: Springer Nature Switzerland.

Sezer, E. A., Pradhan, B., & Gokceoglu, C. (2011). Manifestation of an adaptive neuro-fuzzy model on landslide susceptibility mapping: Klang valley, Malaysia. *Expert Systems with Applications*, *38*(7), 8208-8219.

Sharma, M., & Sharma, S. R. (2025). Advanced Hydrological Simulation and Hybrid CNNLSTM Models for Sustainable Water Resource Management in Nepal. Journal of Information Systems Engineering and Management, 10, 393-414.

Shen, H., Zhai, G., Zhu, Y., & Xu, Y. (2012). Numerical study of a mesoscale vortex in the planetary boundary layer of the Meiyu front. *Acta Meteorologica Sinica*, *26*(6), 788-802.

Shin, J. Y., Ro, Y., Cha, J. W., Kim, K. R., & Ha, J. C. (2019). Assessing the applicability of random forest, stochastic gradient boosted model, and extreme learning machine methods to the quantitative precipitation estimation of the radar data:

A case study to Gwangdeoksan Radar, South Korea. Advances in Meteorology, 2019, 1–17

Shin, K., Song, J. J., Bang, W., & Lee, G. (2021). Quantitative Precipitation Estimates Using Machine Learning Approaches with Operational Dual-Polarization Radar Data. *Remote Sensing, 13(4),* 694.

Sidek, L. M., Basri, H., Mohammed, M. H., Marufuzzaman, M., Ishak, N. A., Ishak, A. M., ... & Hassan, M. H. (2021, March). Towards impact-based flood forecasting and warning in Malaysia: A case study at Kelantan river. In *IOP conference series: earth and environmental science* (Vol. 704, No. 1, p. 012001). IOP Publishing.

Simpson, J., Adler, R. F., & North, G. R. (1988). A proposed tropical rainfall measuring mission (TRMM) satellite. *Bulletin of the American meteorological Society*, *69*(3), 278-295.

Simpson, M. J., & Fox, N. I. (2018). Dual-polarized quantitative precipitation estimation as a function of range. *Hydrology and Earth System Sciences*, *22*(6), 3375-3389.

Skolnik, M. I. (2008). Radar handbook. IEEE Aerospace Electronic Systems Magazine, 23(5), 41-41.

Smith, J. A., Baeck, M. L., Villarini, G., Welty, C., Miller, A. J., & Krajewski, W. F. (2012). Analyses of a long-term, high-resolution radar rainfall data set for the Baltimore metropolitan region. *Water Resources Research*, *48*(4).

Sokol, Z., Szturc, J., Orellana-Alvear, J., Popova, J., Jurczyk, A., & Célleri, R. (2021). The role of weather radar in rainfall estimation and its application in meteorological and hydrological modelling—A review. *Remote Sensing*, *13*(3), 351.

Song, L., Chen, S., Li, Y., Qi, D., Wu, J., Chen, M., & Cao, W. (2021). The Quantile-Matching Approach to Improving Radar Quantitative Precipitation Estimation in South China. *Remote Sensing*, *13*(23), 4956.

Stepanian, P. M., Chilson, P. B., & Kelly, J. F. (2014). An introduction to radar image processing in ecology. *Methods in Ecology and Evolution*, *5*(8), 730-738.

Sun, S., & Huang, R. (2010, August). An adaptive k-nearest neighbor algorithm. In *2010 seventh international conference on fuzzy systems and knowledge discovery* (Vol. 1, pp. 91-94). IEEE.

Suprajitno, H. (2022). Experimental Analysis of Training Parameters Combination of ANN Backpropagation for Climate Classification. *Mathematical Modelling of Engineering Problems*, *9*(4).

Susmaga, R. (2004, May). Confusion matrix visualization. In *Intelligent Information Processing and Web Mining: Proceedings of the International IIS: IIPWM '04 Conference held in Zakopane, Poland, May 17–20, 2004* (pp. 107-116). Berlin, Heidelberg: Springer Berlin Heidelberg.

Tahir, W., Ariffin, M. A. M., Abdullah, J., Ibrahim, Z., Ramli, S., Deni, S. M., ... & Chang, N. K. (2022). Mean Field Bias Correction to Radar QPE as Input to Flood Modeling for Malaysian River Basins. International Journal of Integrated Engineering, 14(5), 168-177.

Tahir, W., Azad, W. H., Husaif, N., Osman, S., Ibrahim, Z., & Ramli, S. (2019). Climatological Calibration of ZR Relationship for Pahang River Basin. *Jurnal Teknologi (Sciences & Engineering)*, *81*(4).

Tahir, W., Ramli, S., Abdullah, J., Muhammad, N. S., & Rahim, N. F. H. M. (2022). Subang Radar CAPPI Data Processing and ZR Optimization for Quantitative Precipitation Estimates (QPE) Over Langat River Basin. *Jurnal Teknologi*, *84*(4), 113-122.

Tahir, Wardah (2024) *Forecasting the impending flood disasters / Wardah Tahir.* UiTM Press, Universiti Teknologi MARA (UiTM). ISBN 9786294960251

Tan, K. C. (2018, April). Trends of rainfall regime in Peninsular Malaysia during northeast and southwest monsoons. In *Journal of Physics: Conference Series* (Vol. 995, No. 1, p. 012122). IOP Publishing.

Tassew, B. G., Belete, M. A., & Miegel, K. (2019). Application of HEC-HMS model for flow simulation in the Lake Tana basin: The case of Gilgel Abay catchment, upper Blue Nile basin, Ethiopia. *Hydrology*, *6*(1), 21.

Taunk, K., De, S., Verma, S., & Swetapadma, A. (2019, May). A brief review of nearest neighbor algorithm for learning and classification. In *2019 international conference on intelligent computing and control systems (ICCS)* (pp. 1255-1260). IEEE.

Teng, K., Cai, H., Sun, X., & Chen, Q. (2022). Geometric and physical characteristics of precipitation clouds in tibetan plateau. *Advances in Meteorology*, *2022*(1), 9181219.

Teschl, R., Randeu, W. L., & Teschl, F. (2007). Improving weather radar estimates of rainfall using feed-forward neural networks. *Neural networks*, *20*(4), 519-527.

Theusner, M., & Hauf, T. (2004). A study on the small-scale precipitation structure over Germany using the radar network of the German Weather Service. *Meteorologische Zeitschrift (Berlin)*, *13*.

Tokay, A., & Short, D. A. (1996). Evidence from tropical raindrop spectra of the origin of rain from stratiform versus convective clouds. Journal of Applied Meteorology and Climatology, 35(3), 355-371.

Tranceto, A. E. (2015) "Comparison of Hydrologic Model Performance Statistics Using Thiessen Polygon Rain Gauge and NEXRAD Precipitation Input Methods at Different Watershed Spatial Scales and Rainfall Return Frequencies," *M.S. thesis*, Dept. Civil. Eng., Univ. of. North. Flori.,USA.

Trinh, T., Do, N., Trinh, L., & Carr, K. (2023). Flood forecasting by means of dynamical downscaling of global NWPs coupling with a hydrologic model at Nong Son-Thanh My River basins. *Journal of Water and Climate Change*, *14*(9), 3257-3279.

Ulbrich, C. W., & Lee, L. G. (2002). Rainfall characteristics associated with the remnants of Tropical Storm Helene in upstate South Carolina. *Weather and Forecasting*, *17*(6), 1257-1267.

Urban, G., & Strug, K. (2021). Evaluation of precipitation measurements obtained from different types of rain gauges. *Meteorol. Z*, *30*, 445-463.

Van den Heuvel, F., Foresti, L., Gabella, M., Germann, U., & Berne, A. (2020). Learning about the vertical structure of radar reflectivity using hydrometeor classes and neural networks in the Swiss Alps. *Atmospheric Measurement Techniques*, *13*(5), 2481-2500.

Varikoden, H., Preethi, B., Samah, A. A., & Babu, C. A. (2011). Seasonal variation of rainfall characteristics in different intensity classes over Peninsular Malaysia. *Journal of hydrology*, *404*(1-2), 99-108.

Villarini, G., & Krajewski, W. F. (2010). Review of the different sources of uncertainty in single polarization radar-based estimates of rainfall. Surveys in geophysics, 31(1), 107-129.

Vokoun, M., & Moravec, V. (2022). Measuring annual precipitation with a radar rain gauge in severe mountain conditions. Vodohospodářské technicko-ekonomické informace, 64(5), 39-45.

Vollrath, S. J. (1998). A seasonal and regional evaluation of a value added national radar data set for precipitation (Doctoral dissertation, Massachusetts Institute of Technology).

Voormansik, T., Cremonini, R., Post, P., & Moisseev, D. (2020). Use of dual-polarization weather radar quantitative precipitation estimation for climatology. *Hydrology and Earth System Sciences Discussions*, *2020*, 1-14.

Wallner, M., Haberlandt, U., & Dietrich, J. (2012). Evaluation of different calibration strategies for large scale continuous hydrological modelling. *Advances in Geosciences*, *31*, 67-74.

Wang, Y., & Chandrasekar, V. (2010). Quantitative precipitation estimation in the CASA X-band dual-polarization radar network. *Journal of Atmospheric and Oceanic Technology*, *27*(10), 1665-1676.

Wang, Y., Tang, L., Chang, P. L., & Tang, Y. S. (2021). Separation of convective and stratiform precipitation using polarimetric radar data with a support vector machine method. *Atmospheric Measurement Techniques*, *14*(1), 185-197.

Wang, Y., Zhang, P., Ryzhkov, A. V., Zhang, J., & Chang, P. L. (2014). Utilization of specific attenuation for tropical rainfall estimation in complex terrain. *Journal of Hydrometeorology*, *15*(6), 2250-2266.

Wardah, T., Abu Bakar, S.H.,Bardossy, A., Maznorizan, M., 2008. Use of geostationary meteorological satellite images in convective rain estimation for flash-flood forecasting. Journal of Hydrology 356 (3-4), pp. 283-298.

Wardah, T., Huda, S. S. N., Deni, S. M., & Azwa, B. N. (2011, December). Radar rainfall estimates comparison with kriging interpolation of gauged rain. In *2011 IEEE Colloquium on Humanities, Science and Engineering* (pp. 93-97). IEEE.

Wardah, T., Suzana, R., & Huda, S. S. N. (2012, December). Multi-sensor data inputs rainfall estimation for flood simulation and forecasting. In *2012 IEEE Colloquium on Humanities, Science and Engineering (CHUSER)* (pp. 374-379). IEEE.

Wardhana, A., Pawitan, H., & Dasanto, B. D. (2017, March). Application of hourly radar-gauge merging method for quantitative precipitation estimates. In *IOP Conference Series: Earth and Environmental Science* (Vol. 58, No. 1, p. 012033). IOP Publishing.

Weesakul, U., Kaewprapha, P., Boonyuen, K., & Mark, O. (2018). Deep learning neural network: A machine learning approach for monthly rainfall forecast, case study in eastern region of Thailand. *Engineering and Applied Science Research*, *45*(3), 203-211.

Wei, C. C., & Hsieh, P. Y. (2020). Estimation of hourly rainfall during typhoons using radar mosaic-based convolutional neural networks. *Remote Sensing*, *12*(5), 896.

Wei, D. D., & Liu, Y. (2022, July). Precipitation Characteristics on Weather Radar Images And Application In ZR Relationship of Wuhan City. In *IGARSS 2022-2022 IEEE International Geoscience and Remote Sensing Symposium* (pp. 6530-6533). IEEE.

Wijayarathne, D., Boodoo, S., Coulibaly, P., & Sills, D. (2020). Evaluation of Radar Quantitative Precipitation Estimates (QPEs) as an Input of Hydrological Models for Hydrometeorological Applications. *Journal of Hydrometeorology*, *21*(8), 1847-1864.

Wijayarathne, D., Coulibaly, P., Boodoo, S., & Sills, D. (2021). Use of radar quantitative precipitation estimates (QPEs) for improved hydrological model calibration and flood forecasting. Journal of Hydrometeorology, 22(8), 2033-2053.

Wong W.S (2006) Klang River Basin Flood Modeling and Forecasting System, River Protection and Watershed Modeling Seminar, Shah Alam, Malaysia.

Wood, S. J., Jones, D. A., & Moore, R. J. (2000). Accuracy of rainfall measurement for scales of hydrological interest. Hydrology and Earth System Sciences, 4(4), 531-543.

Wu, W., Zou, H., Shan, J., & Wu, S. (2018). A Dynamical Z-R Relationship for Precipitation Estimation Based on Radar Echo-Top Height Classification. *Advances in Meteorology*, *2018*(1), 8202031.

Wu, Z., Zhang, Y., Zhang, L., Zheng, H., & Huang, X. (2022). A comparison of convective and stratiform precipitation microphysics of the record-breaking Typhoon In-Fa (2021). *Remote Sensing*, *14*(2), 344.

Xiang, E. S. Z. (2020). *Evaluation and Inter-Comparison of Satellite Precipitation Estimations for Extreme Flood Events in Peninsular Malaysia* (Doctoral dissertation, University of Malaya (Malaysia)).

Xiao, R., & Chandrasekar, V. (1997). Development of a neural network based algorithm for rainfall estimation from radar observations. *IEEE Transactions on Geoscience and Remote Sensing*, *35*(1), 160-171.

Xie, H., Pan, P., Shi, H., Chen, J., & Wang, J. (2020). Observed Microphysical Characteristics of Stratiform and Convective Precipitation over an Inland Arid Region of the Qinghai–Tibet Plateau. *Water*, *12*(8), 2300.

Yabin, G. O. U., Liping, L. I. U., Dan, W. A. N. G., Lingzhi, Z. H. O. N. G., & Chao, C. H. E. N. (2015). Evaluation and analysis of the ZR storm-grouping relationships fitting scheme based on storm identification. *Torrential Rain and Disasters*, *34*(1), 1.

Yahya, S. N. H. S., Tahir, W., Ramli, S., Deni, S. M., Arof, H., & Saaid, M. F. M. (2012, September). Improved estimation of radar rainfall bias over Klang River Basin using a Kalman filtering approach. In *2012 IEEE Symposium on Business, Engineering and Industrial Applications* (pp. 368-373). IEEE.

Yang, L., Yang, Y., Liu, P., & Wang, L. (2016). Radar-derived quantitative precipitation estimation based on precipitation classification. *Advances in Meteorology*, *2016*.

Yang, X., Kuang, Q., Zhang, W., & Zhang, G. (2017). A terrain-based weighted random forests method for radar quantitative precipitation estimation. *Meteorological Applications*, *24*(3), 404-414.

Yang, Y., Chen, X., & Qi, Y. (2013). Classification of convective/stratiform echoes in radar reflectivity observations using a fuzzy logic algorithm. *Journal of Geophysical Research: Atmospheres*, *118*(4), 1896-1905.

Yang, Z., Liu, P., & Yang, Y. (2019). Convective/stratiform precipitation classification using ground-based Doppler radar data based on the K-nearest neighbor algorithm. *remote sensing*, *11*(19), 2277.

Yao, Q., Hu, X., & Lei, H. (2020). Multiscale convolutional neural networks for geospatial object detection in VHR satellite images. *IEEE Geoscience and Remote Sensing Letters*, *18*(1), 23-27.

Yin, H., Zheng, F., Duan, H. F., Savic, D., & Kapelan, Z. (2023). Estimating rainfall intensity using an image-based deep learning model. *Engineering*, *21*, 162-174.

Yo, T. S., Su, S. H., Chu, J. L., Chang, C. W., & Kuo, H. C. (2021). A deep learning approach to radar-based QPE. *Earth and Space Science*, *8*(3), e2020EA001340.

Yousefi, K. P., Yilmaz, M. T., Öztürk, K., Yucel, I., & Yilmaz, K. K. (2023). Time-independent bias correction methods compared with gauge adjustment methods in improving radar-based precipitation estimates. *Hydrological Sciences Journal*, *68*(14), 1963-1983.

Yuter, S. E., & Houze Jr, R. A. (1997). Measurements of raindrop size distributions over the Pacific warm pool and implications for Z–R relations. *Journal of Applied Meteorology*, *36*(7), 847-867.

Zakaria, S. F., Zin, R. M., Mohamad, I., Balubaid, S., Mydin, S. H., & MDR, E. (2017, November). The development of flood map in Malaysia. In *AIP Conference Proceedings* (Vol. 1903, No. 1). AIP Publishing.

Zelman, C. (2019, June 12). Convective versus stratiform rain [status update].Facebook. https://www.facebook.com/ChrisWALB/photos/convective-vs-stratiform-rain-in-the-summerwarm-months-we-are-dominated-by conve/2347819388611043/?_rdr

Zeng, Z., Wang, D., & Chen, Y. (2021). An investigation of convective features and ZR relationships for a local extreme precipitation event. *Atmospheric Research*, *250*, 105372.

Zhang, J., & Qi, Y. (2010). A real-time algorithm for the correction of brightband effects in radar-derived QPE. *Journal of Hydrometeorology*, *11*(5), 1157-1171.

Zhang, J., Langston, C., & Howard, K. (2008). Brightband identification based on vertical profiles of reflectivity from the WSR-88D. *Journal of Atmospheric and Oceanic Technology*, *25*(10), 1859-1872.

Zhang, J., Qi, Y., Langston, C., Kaney, B., & Howard, K. (2014). A real-time algorithm for merging radar QPEs with rain gauge observations and orographic precipitation climatology. *Journal of Hydrometeorology*, *15*(5), 1794-1809.

Zhang, J., Tang, L., Cocks, S., Zhang, P., Ryzhkov, A., Howard, K., ... & Kaney, B. (2020). A dual-polarization radar synthetic QPE for operations. *Journal of Hydrometeorology*, *21*(11), 2507-2521.

Zhang, Y., Bi, S., Liu, L., Chen, H., Zhang, Y., Shen, P., ... & Yao, S. (2021). Deep Learning for Polarimetric Radar Quantitative Precipitation Estimation during Landfalling Typhoons in South China. Remote Sensing, 13(16), 3157.

Zhao, Y., & Su, D. (2019, December). Research on Quantitative Precipitation Estimation Method based on Weather Radar in Leshan Area. In *2019 International Conference on Meteorology Observations (ICMO)* (pp. 1-4). IEEE.

Zou, J., Han, Y., & So, S. S. (2009). Overview of artificial neural networks. *Artificial neural networks: methods and applications*, 14-22.

Zou, K. H., Tuncali, K., & Silverman, S. G. (2003). Correlation and simple linear regression. *Radiology*, *227*(3), 617-628.

APPENDICES

APPENDIX A

Mean Areal Rainfall Comparison between Radar QPE and Raingauge Data

No	Station_Name	Longitude	Latitude	Thiessen Weight
1	Pulau Meranti	101.6394	2.969105	0.09
2	Puchong Drop	101.5974	3.019527	0.02
3	Ayer Hitam Puchong	101.5804	2.979611	0.05
4	Bandar Klang	101.4448	3.048056	0.08
5	Taman Sri Muda	101.5345	3.037722	0.06
6	Batu 3	101.5539	3.075611	0.02
7	Ioi Puchong Jaya	101.6214	3.04275	0.05
8	Taman Mayang	101.5964	3.112277	0.03
9	Ttdi Jaya	101.5542	3.096944	0.03
10	Kota Damansara	101.578	3.156392	0.03
11	Sg Penchala Jln 222	101.6344	3.09652	0.1
12	Kg Melayu Subang	101.5409	3.150055	0.03
13	Puncak Atheneum	101.7658	3.182472	0.08
14	Selayang Baru	101.6663	3.250222	0.08
15	Kg. Rantau Panjang	101.4132	3.049139	0.03
16	Batu 10	101.7267	3.267279	0.16
17	Bukit Antarabangsa	101.7727	3.183694	0.05

Date & Time	Mean Radar	Mean Gauge
2021-12-17 00:00	0.204	0.08
2021-12-17 01:00	0.267	0.135
2021-12-17 02:00	0.142	0.145
2021-12-17 03:00	0.042	0
2021-12-17 04:00	0.034	0.015
2021-12-17 05:00	0.404	0.135
2021-12-17 06:00	0.648	0.04
2021-12-17 07:00	0.757	0.55
2021-12-17 08:00	0.617	0.48
2021-12-17 09:00	0.579	0.175
2021-12-17 10:00	0.498	0.31
2021-12-17 11:00	0.669	0.385
2021-12-17 12:00	1.332	2.13
2021-12-17 13:00	1.104	2.705
2021-12-17 14:00	0.382	0.58
2021-12-17 15:00	0.261	0.405
2021-12-17 16:00	0.302	0.36
2021-12-17 17:00	0.427	0.835
2021-12-17 18:00	0.746	2.525
2021-12-17 21:00	1.958	4.68
2021-12-17 23:00	1.02	4.605
2021-12-18 00:00	1.417	4.875
2021-12-18 01:00	2.422	0

2021-12-18 02:00	1.906	0
2021-12-18 03:00	1.676	0
2021-12-18 04:00	1.604	0
2021-12-18 05:00	1.597	0
2021-12-18 06:00	0.502	0
2021-12-18 07:00	0.115	0.215
2021-12-18 08:00	0.181	2.12
2021-12-18 09:00	0.179	0.915
2021-12-18 10:00	0.561	4.745
2021-12-18 14:00	3.605	0
2021-12-18 16:00	1.487	5.265
2021-12-18 17:00	2.072	4.04
2021-12-18 18:00	2.221	0
2021-12-18 21:00	3.925	0
2021-12-18 22:00	3.141	2.275
2021-12-18 23:00	3.197	5.48

APPENDIX B
Radar Images Processing

200822_1700

200822_1800

200822_1900


230822_1700


230822_1800


080922_2100


080922_2200


080922_2300


131122_2000

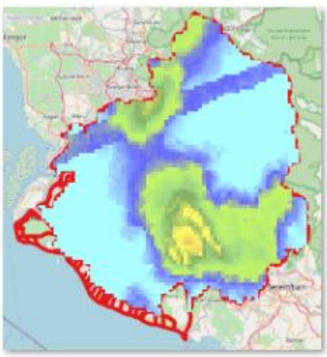
131122_2100


171122_0000


171122_0100

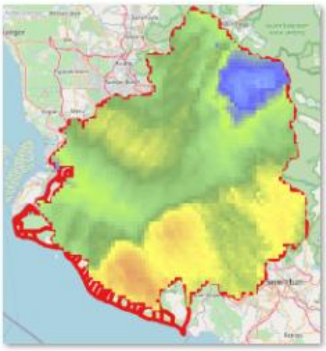
171122_0300

171122_0400

021222_2200

021222_2300
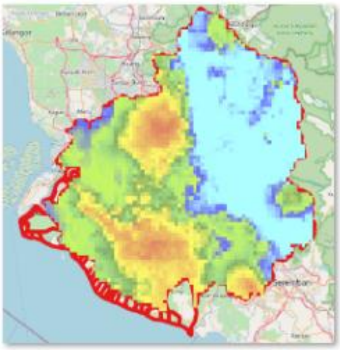
170123_0100

170123_0200
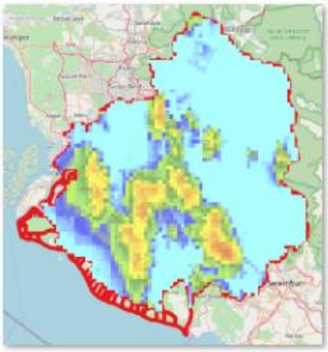
010223_1600
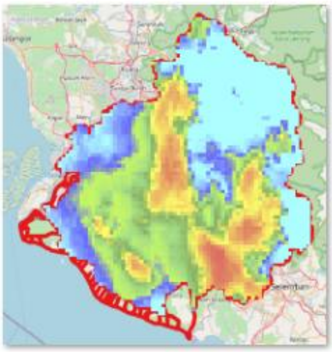
010223_1700

110223_0400

110223_1500
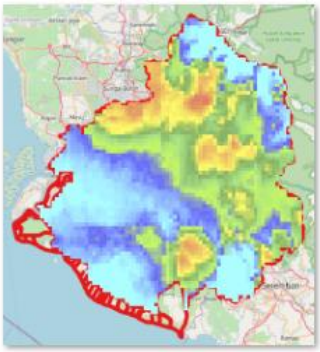
110223_1600

180223_1900

180223_2000

180223_2100

190223_1800

190223_1700

190223_1900

230623_1500

240623_1400

240623_1500

270623_1800

270623_1900

260623_1500

010723_0100

010723_0200

010723_0300

120723_1700

120723_1800

140723_0500

140723_0600

140723 0700

230723 1000

030823 0800

080823_1600

080823_1700

080823_1800

100823_0600

100823_0700

100823_0800

100823_0900

140823_0600

140823_0700

APPENDIX C
Feature Extraction of Radar Images


010223_1600

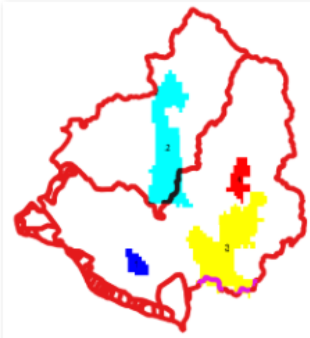
010223_1700


010723_0100

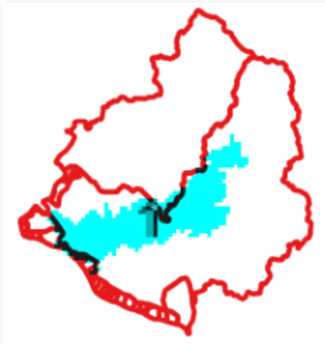
010723_0200

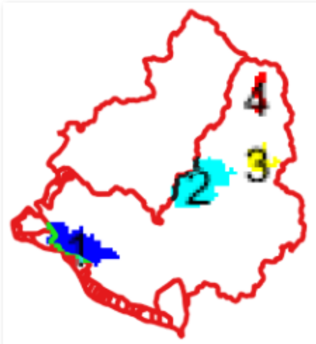
010723_0300

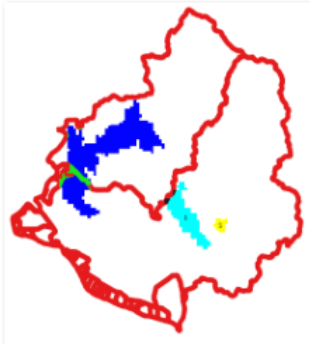
021222_2200

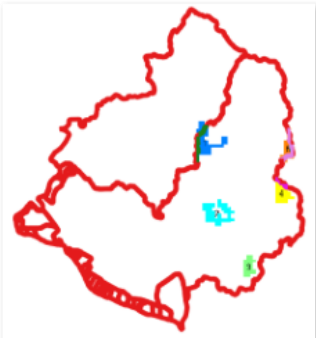
021222_2300


030823_0800


080823_1600

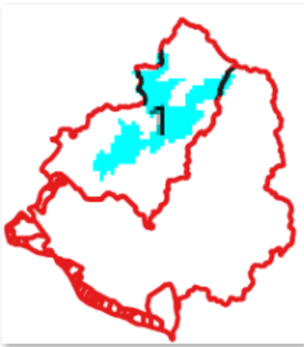
080823_1700


080823_1800


080922_2100

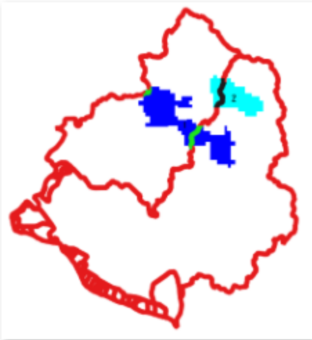
080922_2200


080922_2300


100823_0600


100823_0700

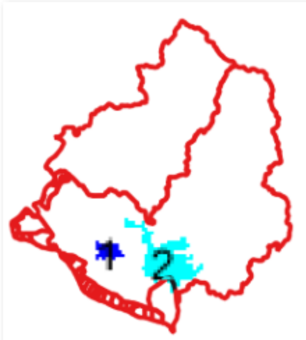
100823_0800


100823_0900

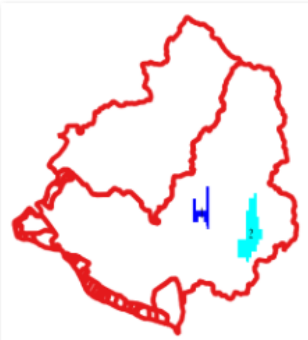
110223_0400

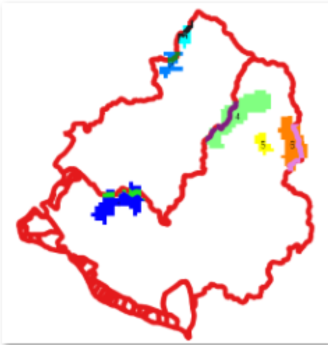
110223_1500

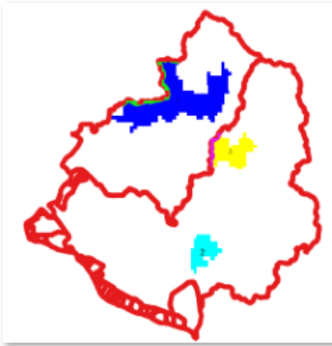
110223_1600


120723_1700


120723_1800


131122_2000

131122_2100

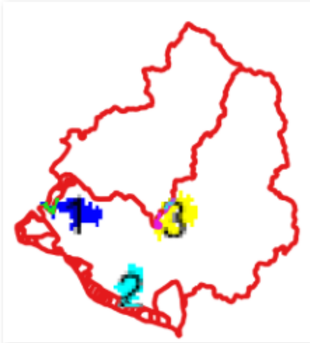

140723_0500

140723_0600

140723_0700

140823_0600


140823_0700

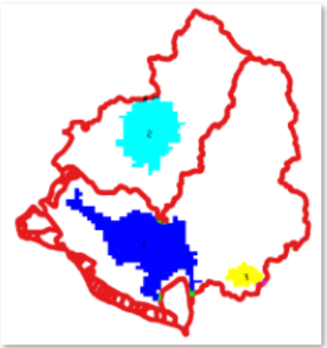
170123_0100

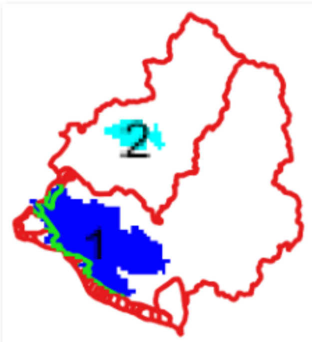

170123_0200

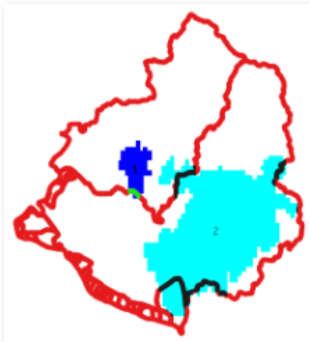
171122_0000


171122_0100

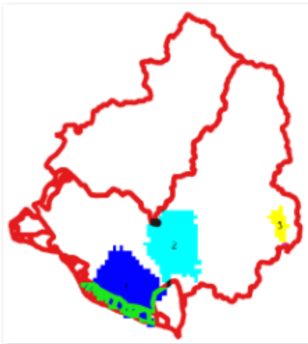
171122_0300


171122_0400

180223_1900

180223_2000

180223_2100

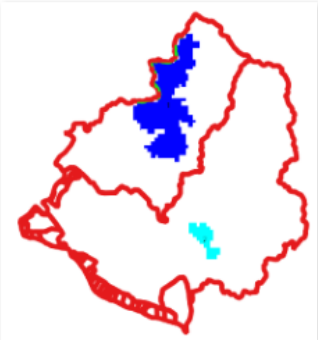

190223_1700

190223_1800

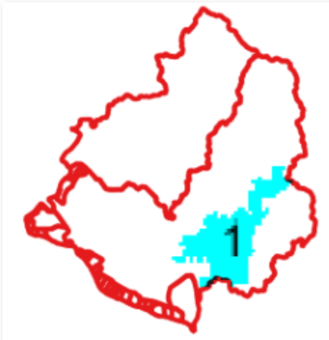

190223_1900

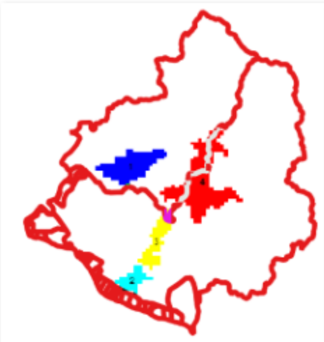

200822_1700

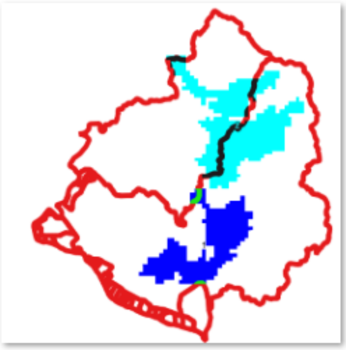

200822_1800

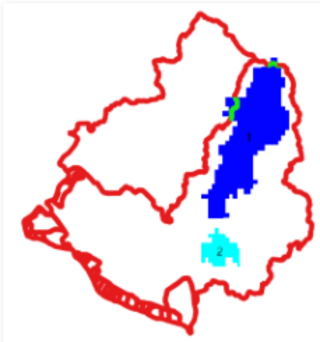

200822_1900

230623_1500

230723_1000

230822_1700

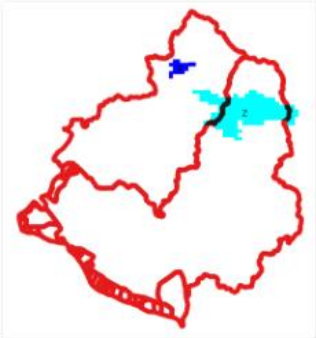

230822_1800

240623_1400

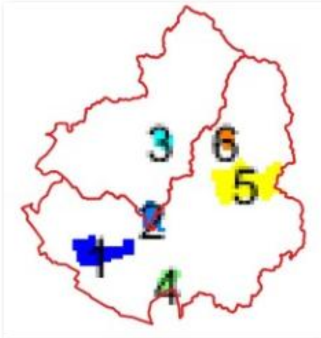

240623_1500

260623_1500

270623_1800

270623_1900

		Cell Features/ Input training								
Date	Time	Center X	Center Y	Area,km^2	Major Radius,km	Minor Radius,km	Orientation, degree	Max Intensity, mm	Mean gridded intensity,mm	Mean Rainfall data,mm / Output training
200822	17:00	23.81	42.22	100.00	17.59	8.02	20.45	20.86	11.31	33.9
		30.62	63.43	60.00	19.85	4.87	69.37	33.97	10.11	1.5
		42.59	46.59	191.00	26.78	15.60	77.92	34.76	11.98	8.2
	18:00	39.04	62.12	296.00	34.36	17.52	41.16	32.18	11.05	26.8
		47.64	30.48	468.00	32.64	28.84	-76.33	26.64	11.39	20.7
	19:00	58.13	30.55	358.00	36.84	14.18	57.81	21.85	10.80	22.3
		49.84	54.05	56.00	11.34	7.17	-6.74	13.31	8.66	4.2
230822	17:00	32.56	62.56	16.00	7.35	3.53	-53.37	15.56	9.32	3.5
		36.82	15.50	105.00	17.39	8.97	59.64	24.17	13.92	19.7
		56.89	29.94	53.00	13.31	5.33	-13.08	23.97	11.58	2.8
	18:00	38.22	17.72	18.00	7.03	4.23	16.92	9.59	7.22	17
		55.53	29.05	177.00	26.25	11.08	-2.22	22.06	10.55	28.9
080922	21:00	43.50	24.51	141.00	23.06	10.72	7.79	52.12	16.17	11.5
	22:00	42.52	31.72	197.00	36.08	10.09	-33.93	31.97	13.72	16.8
		56.32	24.53	95.00	17.17	7.62	-24.22	19.55	10.73	15.3
	23:00	36.95	32.23	86.00	11.46	10.38	-26.55	25.26	12.98	4.3
131122	20:00	46.70	54.33	87.00	12.37	10.38	78.90	22.38	11.61	11.3
	21:00	41.21	61.67	24.00	7.77	4.82	-41.59	11.72	8.32	11.5
171122	0:00	27.29	42.03	63.00	11.47	7.99	-86.68	8.05	7.05	62.8
		48.69	54.70	746.00	41.57	26.22	31.60	21.61	10.40	23.3
	1:00	54.22	59.46	585.00	36.51	21.52	-83.16	26.06	13.34	32.2

	3:00	26.36	72.47	205.00	19.83	14.05	-28.23	19.96	11.78	28.3
		38.54	63.01	173.00	16.59	14.07	-77.35	13.66	8.19	6.3
		65.77	58.69	26.00	8.73	4.35	-72.89	7.58	6.89	2
	4:00	39.61	63.76	666.00	49.27	18.78	29.95	18.02	9.41	7.9
		65.25	42.29	56.00	12.71	8.64	-76.08	18.67	9.46	9.5
021222	22:00	21.83	39.66	477.00	49.42	22.51	43.28	16.93	9.32	9.2
		50.95	61.92	128.00	26.24	8.09	-61.30	15.36	8.70	2.5
		63.13	64.81	16.00	5.31	4.55	77.04	10.81	8.12	9.3
	23:00	42.73	35.95	44.00	10.39	9.90	-5.19	11.20	7.51	8.5
		46.33	55.17	36.00	10.96	6.69	-7.88	8.12	7.03	4.8
		66.69	49.69	26.00	7.34	5.19	-58.55	12.47	8.93	2
		68.79	37.74	19.00	8.69	3.46	85.39	24.86	13.66	3
170123	1:00	29.51	65.56	381.00	34.23	18.23	-38.90	27.69	11.96	20.38
		30.90	33.55	226.00	20.78	14.37	78.94	28.24	12.77	12.78
		54.56	74.58	43.00	9.31	6.43	-11.61	22.04	11.01	4
	2:00	18.57	62.66	529.00	37.93	19.21	-35.70	44.51	19.03	41
		28.07	33.43	75.00	14.33	7.46	-12.72	14.26	9.38	28.43
010223	16:00	16.28	49.07	29.00	10.11	4.40	85.19	15.40	8.95	9
		25.94	63.90	51.00	15.47	4.97	-76.28	17.10	9.62	6.5
		33.19	27.24	21.00	8.90	3.33	86.17	16.76	11.19	5.5
		39.68	47.82	28.00	12.23	3.77	-61.05	17.78	10.57	7.5
		48.70	62.19	69.00	14.93	7.33	-69.62	24.43	12.50	7.5
	17:00	35.17	37.55	265.00	40.45	10.82	89.20	27.66	12.82	10.4
		52.66	64.05	305.00	29.67	19.00	59.39	45.72	17.26	5.13

		56.41	46.14	49.00	11.82	6.05	82.13	20.97	11.04	12.5
110223	4:00	41.94	57.59	17.00	8.61	6.07	14.20	9.56	7.69	12.5
		60.30	61.15	54.00	12.05	6.91	64.59	19.94	10.90	4
	15:00	20.69	51.94	67.00	16.01	7.48	21.92	12.40	8.46	2.25
		34.48	15.61	23.00	8.27	4.91	63.15	11.70	8.75	6.5
		38.38	8.06	16.00	7.28	3.22	70.57	12.72	9.01	5.5
		52.08	29.16	100.00	22.61	6.75	39.44	19.76	11.45	15.67
		66.54	36.43	67.00	14.34	6.62	-79.41	26.62	14.40	10.75
	16:00	35.26	23.25	267.00	35.38	15.36	15.60	34.93	12.53	26.5
		50.13	37.44	82.00	13.67	9.31	2.22	21.91	10.22	12.25
180223	19:00	50.92	23.12	76.00	14.10	7.56	69.24	28.13	14.38	8.5
		66.41	29.94	17.00	6.35	3.77	-52.14	19.65	12.47	0.5
	20:00	57.44	29.35	276.00	26.12	14.54	-15.58	36.40	13.86	24
	21:00	52.51	45.49	39.00	9.04	6.17	13.88	11.03	7.74	10.6
190223	17:00	34.70	24.27	321.00	37.23	14.88	78.72	24.92	11.07	8.8
	18:00	43.04	54.07	611.00	45.60	18.70	-59.98	82.60	19.93	17.9
	19:00	50.22	62.65	396.00	39.59	18.01	45.15	23.81	10.70	19.1
230623	15:00	17.16	32.81	37.00	10.02	4.95	66.68	25.97	14.28	22
		28.89	27.15	54.00	9.54	7.92	-11.00	21.80	11.39	9
		44.69	24.33	121.00	15.11	10.67	-64.63	31.38	16.60	27
		50.69	63.55	62.00	10.49	7.95	46.61	22.69	11.91	5.5
240623	14:00	20.38	62.13	16.00	9.45	2.60	-24.59	13.33	9.24	15.3
		36.28	63.50	149.00	18.07	12.53	80.84	34.59	14.91	14
		44.82	55.35	17.00	6.80	3.63	76.59	27.12	13.07	1

		61.29	49.76	42.00	11.10	7.46	55.08	14.76	9.69	3.3
	15:00	20.61	63.12	69.00	16.93	6.33	3.50	30.21	14.53	23
		34.00	54.69	32.00	8.22	5.62	-64.35	16.89	10.29	12.3
		36.90	34.90	20.00	5.85	4.57	-34.48	19.40	11.66	6.5
		38.17	70.09	23.00	7.22	4.58	44.05	24.19	11.62	2
		58.32	45.86	139.00	19.56	10.42	4.88	26.51	13.83	8.33
260623	15:00	58.63	36.78	360.00	25.06	20.33	37.11	38.18	13.96	11.7
270623	18:00	47.13	26.24	46.00	9.81	6.26	-83.09	36.36	16.47	25.7
	19:00	47.95	27.76	21.00	5.90	5.56	-81.29	14.38	9.85	13.8
		52.98	34.05	43.00	10.82	6.32	79.26	26.18	11.85	1.25
10723	1:00	20.56	62.29	333.00	30.81	15.69	-15.18	22.05	11.12	17.30
	2:00	29.92	54.59	601.00	59.53	18.07	23.40	22.78	11.29	27.3
	3:00	13.18	63.44	119.00	20.78	7.87	-23.72	16.73	9.94	9.5
		46.54	46.89	153.00	18.47	11.05	34.78	16.04	10.47	11.2
		63.00	40.59	39.00	8.92	7.58	-33.82	9.61	7.60	5
		62.70	22.04	27.00	12.87	3.89	88.03	10.56	7.51	2.5
120723	17:00	18.60	28.88	25.00	6.74	5.18	67.67	11.32	8.78	10.8
		37.18	23.44	131.00	14.23	13.61	-9.04	31.01	12.18	9.25
	18:00	58.88	45.52	48.00	12.05	6.32	4.72	19.67	11.27	0.5
140723	5:00	38.38	54.80	76.00	14.43	8.72	36.40	16.96	8.68	10
	6:00	43.67	42.75	484.00	59.62	14.95	25.13	25.66	12.29	8.5
	7:00	60.58	26.58	96.00	16.80	8.88	25.25	14.49	8.94	13.5
230723	10:00	48.78	61.57	206.00	39.09	9.06	45.50	20.85	9.56	5.75
030823	8:00	43.05	65.91	75.00	15.25	8.57	-47.41	15.41	9.60	12.7

		58.03	43.50	129.00	19.18	8.94	-43.13	24.66	13.60	6.5
		54.80	65.82	49.00	10.15	6.90	18.80	15.48	9.38	9.5
080823	16:00	29.61	29.30	294.00	34.58	12.95	43.89	38.85	15.49	14.1
	17:00	37.56	26.58	455.00	45.85	22.25	47.55	27.68	11.56	21.1
	18:00	38.21	31.69	58.00	16.72	4.82	40.32	18.23	9.94	8
100823	6:00	14.10	54.37	194.00	20.54	13.03	-6.18	26.09	12.12	12.5
	7:00	17.22	55.03	60.00	12.97	8.19	-73.79	13.25	9.20	5
		24.98	47.06	54.00	11.60	7.71	76.92	19.70	9.81	44.5
		32.90	52.78	40.00	10.41	5.67	42.80	14.33	9.33	4.5
		34.88	72.00	16.00	7.49	3.52	15.12	12.09	8.57	16
		52.62	75.27	26.00	7.21	5.03	-43.00	23.52	13.16	2
	8:00	21.32	64.74	34.00	9.32	5.45	-8.07	13.16	9.61	20.9
		38.73	67.15	182.00	23.80	13.56	-45.00	23.28	10.54	16.8
	9:00	67.45	54.89	97.00	12.64	10.04	53.43	26.34	13.65	2.5
140823	6:00	23.71	29.19	125.00	20.38	10.35	18.13	23.83	11.98	10.8
		32.72	17.44	25.00	8.43	4.41	-75.89	20.41	10.86	3
	7:00	51.94	10.88	16.00	5.95	3.73	35.23	14.00	9.56	10

AUTHOR'S PROFILE

Noor Shazwani Osman received her BSc in Electronic Systems Engineering from the Malaysian-Japan International Institute of Technology (MJIIT), Universiti Teknologi Malaysia. She obtained her MSc in Philosophy in 2018 from Universiti Teknologi Malaysia. From 2021 to 2025, she worked as a research assistant on a project funded by the Fundamental Research Grant Scheme (FRGS).

LIST OF PUBLICATIONS:

Shazwani, O. N., Wardah, T., & Nursalleh,C. K. (2024). Integrated Flood Modeling for Klang River Basin using HEC-HMS and Radar Rainfall Input. *International Journal of Environmental Science and Development* vol. 15, no. 4, pp. 176-184.

Osman, N. S., & Tahir, W. (2024). Radar Quantitative Precipitation Estimation (QPE) Calibration Methods: A Systematic Literature Review. *Engineering, Technology & Applied Science Research*, *14*(5), 16185-16192.

Osman, N. S., & Tahir, W. (2023, May). Feature Extraction of Rain Cell Using Weather Radar Imagery in Tropical Regions. In *2023 IEEE 13th Symposium on Computer Applications & Industrial Electronics (ISCAIE)* (pp. 209-213). IEEE.

Osman, N. S., & Tahir, W. (2023, December). Machine learning-based model for enhanced quantitative precipitation estimates (QPE) from radar images extracted features. In *2023 IEEE 8th international conference on recent advances and innovations in engineering (ICRAIE)* (pp. 1-5). IEEE.

Hasni, H., Tahir, W., Osman, N. S., & Haron, N. F. (2024). Calibration and Performance Evaluation of Radar QPE and QPF in Klang River Basin. *International Journal of Sustainable Construction Engineering and Technology,* 15(3), 324-334.

Ahbar, M. I., Tahir, W., & Osman, N. S. (2023, October). Performance Comparison Between S-Band And C-Band Radar In Quantitative Precipitation Estimation. In *2023 IEEE Symposium on Computers & Informatics (ISCI)* (pp. 70-75). IEEE.

Wardah, T., Shazwani, O.N., Jazuri, A., Azizi, M.A.M., Hafiz, H., Lariyah, M.S., Hidayah, B., Suzana, R., Nursalleh, K.C., & Yip, W.S. (2025). RaINS and HEC-HMS Applications for Flood Nowcasting in the Langat River Basin. International Journal of Environmental Science and Development vol.16, no. 5, pp. 364-373.